# GROWTH AND CHARACTERIZATION OF AlN AND InN THIN FILMS GROWN BY REACTIVE GAS-TIMING RF MAGNETRON SPUTTERING AND THEIR APPLICATIONS

NISAPORN PORNTHEERAPHAT

A THESIS SUBMITTED IN FULFILMENT
OF THE REQUIREMENT FOR THE DEGREE OF
DOCTOR OF PHILOSOPHY IN APPLIED PHYSICS
SCHOOL GRADUATE STUDENTS
KING MONGKUT'S INSTITUTE OF TECHNOLOGY LADKRABANG
2007

KMITL-2007-SC-D-030-077

| | |
|---|---|
| **หัวข้อวิทยานิพนธ์** | การปลูกและการตรวจวิเคราะห์สมบัติฟิล์มบางอลูมินัมไนไตรด์และอินเดียมไนไตรด์ที่ปลูกโดยระบบอาร์เอฟแมกนีตรอนสปัตเตอริงด้วยเทคนิคการควบคุมเวลาก๊าซไวปฏิกิริยาและการประยุกต์ใช้งาน |
| **นักศึกษา** | นางสาวนิศาพร พรธีระภัทร |
| **รหัสนักศึกษา** | 44065902 |
| **ปริญญา** | ปรัชญาดุษฎีบัณฑิต |
| **สาขาวิชา** | ฟิสิกส์ประยุกต์ |
| **อาจารย์ที่ปรึกษาวิทยานิพนธ์** | รศ.ดร.จิติ หนูแก้ว |

# บทคัดย่อ

งานวิจัยในวิทยานิพนธ์ฉบับนี้ เกี่ยวข้องความสำเร็จของเป้าหมายสำคัญหลักสามประการด้วยกันคือ ประการแรกเป็นการปลูกฟิล์มบางอลูมินัมไนไตรด์ ฟิล์มบางอินเดียมไนไตรด์ ฟิล์มบางอินเดียมทินออกไซด์ และฟิล์มบางอินเดียมออกซีไนไตรด์ ด้วยเทคนิคใหม่ที่คิดค้นขึ้นซึ่งเรียกว่าเทคนิคการควบคุมเวลาก๊าซไวปฏิกิริยา โดยใช้ระบบปลูกผลึกอาร์เอฟแมกนีตรอนสปัตเตอริง ประการที่สองเป็นการตรวจวิเคราะห์สมบัติทางโครงสร้าง สมบัติทางไฟฟ้าและสมบัติทางแสงของฟิล์มบางทั้งหมดที่ปลูกได้ด้วยเครื่องมือวิเคราะห์อันได้แก่ เครื่องสเปกโตรโฟโตมิเตอร์เทคนิคการเลี้ยวเบนของรังสีเอ็กซ์ กล้องจุลทรรศน์อิเล็กตรอนแบบเลื่อนกราด เครื่องวัดค่าความต้านทานเชิงแผ่นแบบสี่หัววัด เครื่องสเปกโตรสโคปีระบบยูวี-วิสสิเบิล และระบบโฟโตรีเฟล็กแตนท์สเปกโทรสโคปี ประการที่สามเป็นการทดลองประยุกต์ใช้ฟิล์มบางต่างๆ สร้างเป็นอุปกรณ์ได้แก่เซนเซอร์ตรวจวัดค่าความเป็นกรด-ด่างจากฟิล์มบางผลึกนาโนอลูมินัมไนไตรด์ ตัวตรวจวัดแสงจากฟิล์มบางผลึกนาโนอินเดียมไนไตรด์ ขั้วไฟฟ้าโปร่งใสจากฟิล์มบางผลึกอินเดียมทินออกไซด์สายอากาศพลาสติกจากฟิล์มบางผลึกอินเดียมทินออกไซด์ และอุปกรณ์กรองแสงจากฟิล์มผลึกอินเดียมออกซีไนไตรด์

ด้วยเทคนิคการปลูกฟิล์มบางแบบควบคุมเวลาก๊าซไวปฏิกิริยา สามารถปลูกฟิล์มบางอลูมินัมไนไตรด์ได้เป็นโครงสร้างผลึกแบบคิวบิกซิงค์เบลนด์ ในระนาบ (111) และ (200) โดยที่ค่าคงที่โครงผลึกและขนาดเม็ดผลึกจะลดลงเมื่ออัตราการไหลของก๊าซไนโตรเจนเพิ่มขึ้น และด้วยเทคนิคเดียวกันนี้สามารถปลูกฟิล์มบางอินเดียมไนไตรด์ ได้ทั้งโครงสร้างผลึกแบบเฮกซะโกนอลซึ่งมีการจัดเรียงตัวในระนาบ (101) และ (002) และแบบคิวบิกซึ่งมีการจัดเรียงตัวในระนาบ (111) โดยขึ้นอยู่กับคาบเวลาที่ใช้ในการควบคุมก๊าซไวปฏิกิริยาในระบบปลูกฟิล์มบาง จากการวิเคราะห์

พื้นผิวฟิล์มบางอลูมินัมไนไตรด์และอินเดียมไนไตรด์ทั้งหมด พบว่าขนาดของเม็ดผลึกอยู่ในระดับนาโนเมตร และจากการศึกษาแถบพลังงานต้องห้ามของฟิล์มบางด้วยระบบโฟโตรีเฟล็กแตนท์สเปกโทรสโคปีที่อุณหภูมิห้องพบว่า ฟิล์มบางอลูมินัมไนไตรด์มีค่าแถบพลังงานต้องห้าม 3.18 อิเล็กตรอนโวลท์ และจะมีค่าเพิ่มขึ้นเมื่อทำการลดอัตราการไหลของก๊าซไนโตรเจนที่ป้อนเข้าสู่ห้องปลูกฟิล์ม จากการตรวจวัดหาค่าแถบพลังงานต้องห้ามของฟิล์มบางอินเดียมไนไตรด์โดยระบบโฟโตรีเฟล็กแตนท์สเปกโทรสโคปีและระบบยูวีวิสสิเบิล พบว่าโครงสร้างผลึกแบบเฮกซะโกนอลและแบบคิวบิกมีค่าเป็น 1.18 และ 1.38 อิเล็กตรอนโวลท์ ตามลำดับ หลังจากนั้น ได้ทำการใช้ฟิล์มบางอลูมินัมไนไตรด์ สร้างเป็นชั้นตรวจจับไอออนของอุปกรณ์ตรวจวัดค่าความเป็นกรด-ด่าง ประยุกต์ใช้ฟิล์มบางอินเดียมไนไตรด์สร้างเป็นอุปกรณ์ตรวจวัดแสง ประยุกต์ใช้ฟิล์มบางอินเดียมทินออกไซด์สร้างเป็นขั้วนำไฟฟ้าโปร่งใสบนพลาสติก และเป็นสายอากาศชนิดพลาสติกโค้งงอได้ ท้ายที่สุดได้ใช้ฟิล์มบางอินเดียมออกซีไนไตรด์สร้างเป็นอุปกรณ์กรองแสงที่สามารถเลือกย่านที่ต้องการกรองได้ตั้งแต่ย่านยูวีจนถึงย่านใกล้แดง ซึ่งอุปกรณ์กรองแสงดังกล่าวได้นำไปประยุกต์ใช้งานทางด้านการแพทย์และการตรวจหาหลักฐานทางด้านนิติวิทยาศาสตร์

| | |
|---|---|
| **Thesis Title** | Growth and Characterization of AlN and InN Thin Films Grown by Reactive Gas-Timing RF Magnetron Sputtering and Their Applications |
| **Student** | Ms.Nisaporn Porntheeraphat |
| **Student ID.** | 44065902 |
| **Degree** | Doctor of Philosophy |
| **Program** | Applied Physics |
| **Thesis Advisor** | Associate Professor Dr.Jiti Nukeaw |

## ABSTRACT

The research conducted for this dissertation involved three tasks importance to the achievement of (1) aluminum nitride (AlN), indium nitride (InN) and related thin films including of indium tin oxide (ITO) and indium oxynitride (InON) grown by radio frequency (r.f.) magnetron sputtering with innovative technique called "reactive gas-timing", (2) the structural, electrical and optical properties of deposited films characterized by X-ray Diffraction (XRD), Field Emission Scanning Electron Microscope (FE-SEM), Four-Point Probe , Ultraviolet-Visible Spectroscopy (UV-VIS) and Photoreflectance Spectroscopy (PR), and (3) the experimental devices fabrications of pH-AlN sensor, InN photodetector, ITO plastic antenna, and InON optical filter.

By reactive gas-timing thin film growth technique, the XRD patterns of all deposited AlN films show orientation of cubic zincblende structure in (111) and (200) planes. The lattice constant and grain size of AlN films were decreased with decreasing flow rate of nitrogen gas. For InN thin films, the XRD patterns show the crystalline phase change from hexagonal-InN in orientation of (101) and (002) to cubic-InN in (111) planes depended on the difference of reactive gas-timing sequence. The surface morphologies observed by FE-SEM show all deposited AlN and InN films have the grain size in nanometer scale. Bandgap energy ($E_g$) of AlN and InN thin films was investigated by room-temperature photoreflectance spectroscopy (PR). PR results show the value about 3.18 eV for AlN thin films and increase with decreasing flow rate of $N_2$ fed into the sputtering chamber. Meanwhile, the PR peaks of InN thin films reveal the $E_g$ values of 1.18 and 1.38 eV for hexagonal-InN and cubic-InN, respectively. The pH-AlN sensor, nanocrystal-InN Photodetector, ITO flexible transparent electrode, ITO plastic antenna, and InON optical filters were fabricated as application devices. Finally, the InON optical filters take advantage for medical and crime scene investigation in forensic science.

# ACKNOWLEDGEMENT

I would like to express my sincere gratitude to my best advisor Assoc. Prof. Dr. Jiti Nukeaw for sharing his expert advice, in-dept knowledge and time on this research. His support has been tremendous, from the admission to the Ph.D.program to the submission of this thesis.

I am thankful to Assoc.Prof.Suwan Kusamran and Assoc.Prof.Anupong Songprapa for their insights and suggestions during my study at King Mongkut's Institute of Technology Ladkrabang (KMITL).

I must thanks to Win Bunjongpru, Annop Klumcheun, and Apichart Sungthong graduated students in Quantum and Optical Semiconductor Research Laboratory (QOSLAB.), Applied Physics, Science, KMITL, for acting as co-workers in some parts of my research. I would like to say thank you to all members; Nu, Don, Keng, Chart, Mo, Win, Yay, Jack, Ben, Pe, Aey, Kaj, Tong, Pex and Nop of QOSLab., and to Pakorn for helping and our friendship all the time that we have shared together; work, play, eat, sleep and something special. Sharing time with them has been a wonderful experience.

I am indebted to the first advisor in my work life, Dr.Wiriya Chupaween, Electro-Optics Lab, National Electronics and Computer Technology Center (NECTEC) who teach a lot of advantage thinking and how way of research work. Working with him has been a great experience. From the heaven, his words still brighten with my works everywhere. I would like to thanks to my work organization, NECTEC, NSTDA and colleague for giving me a chance to study. I would also like to thanks all my teachers from the beginning of my studying life until now, friends and all those who have directly or indirectly contributed to the successful outcome to my Ph.D.

I am very thankful to my parents and family members: Kait-Peng, Lek, Ohm-Eed, Sagut, Praew-Ploy and to my little daughter, Tonnam, who has understanding in my special life. Thank you for your encouragement and support. I cannot thank you enough for the love and encouragement you have given me.

A lot of thinks and thanks to "Zenze" who has making "Kokoro" know the human's real life. His spirit will go on with my breath.

With more appreciate,

Nisaporn (Supanit) Porntheeraphat

# LIST OF PUBLICATIONS

The following international publications, international conference presentations and patents have resulted from the research works associated to this thesis.

## PUBLICATIONS

### International Journals:

1. N. **Kietpaisalsophon**, W. Bunjongpru, W. Techitdheera, and J. Nukeaw, **"Photoreflectance Study of AlN Thin Films Grown by Reactive Gas-Timing RF Magnetron Sputtering"**, International Journal of Modern Physics B, Vol. 16, No. 28&29, pp. 4418-4422, Nov. 20, 2002.
2. Annop Klamchuen, **Nisaporn Pornteeraphat**, and Jiti Nukeaw, **"Characterization of ITO thin films on PET substrates prepared by gas-timing RF magnetron sputtering"**, e-Journal of Surface Science and Nanotechnology, Vol. 3, pp. 272-275, 2005.

### International Proceedings:

1. **N. Kietipaisalsophon**, W. Bunjongpru, W. Techitdheera, and J. Nukeaw, **"Structure properties of cubic-AlN grown by reactive gas-timing rf magnetron sputtering"**, Proceeding of IEEE ICIT' 02, Vol. 2 (2002), pp. 1365-1367.
2. **N. Kietipaisalsophon**, W. Bunjongpru, W. Techitdheera, and J. Nukeaw, **"Experimental Study of the pH-sensitive EIS for AlN Thin Film grown by Reactive Gas-Timing r.f. Magnetron Sputtering"**, Proceeding 5th of International Conference on Nitride Semiconductors, Physics Status Sodidy C, May 25-30, 2003.
3. P. Prajuabwan, **S. Porntheeraphat**, A. Klamchuen, and J. Nukeaw, **"ITO Thin Films prepared by Gas-Timing RF Magnetron Sputtering for Transparent Flexible Antenna"**, Proceeding of the 2nd IEEE International Conference on Nano/Micro Engineered and Molecular Systems, pp. 647-650, January 16-19, 2007, Bangkok, Thailand.

# LIST OF PUBLICATIONS (cont.)

4. **N. Porntheeraphat**, B. Tunhoo and J, Nukeaw, **"XRD Characterization of InN Thin Films grown by Reactive Gas-timing RF Magnetron Sputtering"**, Proceeding of International Conference on Smart Materials (SmartMat-'04), pp. 343-345, December 1-3, 2004, Chiang Mai, Thailand.
5. D. Klaitabtim, A. Klamcheun, **N. Porntheeraphat**, A. Tuantranont, and J. Nukeaw, **"A Study of Thin AlN Film for Piezoelectric MEMS Applications"**, Proceeding of The International Conference on Smart Materials (SmartMat-'04), pp. 99-101, December 1-3, 2004, Chiang Mai, Thailand.

## Conference and Presentations:

1. **N. Kietipaisalsophon**, W. Bunjongpru, and J. Nukeaw, **"Photoreflectance Study of AlN Thin Films Grown by Reactive Gas-Timing RF Magnetron Sputtering"**, The 8th International Conference on Electronic Materials (ICEM 2002), June 10-14, 2002, Xi'an China.
2. **N. Porntheeraphat**, B. Tunhoo, and J. Nukeaw, **"Photoreflectance Spectroscopy Study on Optical Property of InN Thin Films Grown by Reactive Gas-timing RF Magnetron Sputtering"**, International Conference on Materials for Advanced Technologies (ICMAT2003), December 7-12, 2003, Singapore.
3. **N. Porntheeraphat**, B. Tunhoo, T. Tiwawong, and J. Nukeaw, **"Photoreflectance Study of AlN and InN Thin Films Grown by Reactive Gas-Timing RF Magnetron Sputtering"**, Proceeding of The First Electrical Engineering/Electronic, Computer, Telecommunication, and Information Technology Annual Conference (ECTI-CON2004), pp.149-152, May 13-14, 2004, Pattaya, Thailand.
4. B. Tunhoo, **N. Porntheeraphat** and J. Nukeaw, **"Structure and Optical Properties of CuPc Organic Thin Film Grown by Electron-Beam Evaporation"**, NSTDA Annual Conference (NAC2005) S&T in Thailand: Towards the Molecular Economy, March 28-30, 2005, Bangkok, Thailand.

# LIST OF PUBLICATIONS (cont.)

5. **S. Porntheeraphat** and J. Nukeaw, **"Photomodulated Reflectance Study on Optical Property of InN Thin Films Grown by Reactive Gas-Timing RF Magnetron Sputtering"**, 9th international Conference on Atomically Controlled Surfaces, Interfaces and Nanostructures November 11-15, 2007, Komaba Research Campus of The University of Tokyo, Tokyo, Japan.
6. A. Sungthong, **S. Porntheeraphat**, and J. Nukeaw, **"An Extreme Change in Structural and Optical Properties of Indium Oxynitride Deposited by Reactive Gas-Timing RF Magnetron Sputtering"**, 9th international Conference on Atomically Controlled Surfaces, Interfaces and Nanostructures November 11-15, 2007, Komaba Research Campus of The University of Tokyo, Tokyo, Japan.

## PATENTS

### U.S. Patents:

1. **"Gas-timing Method for Depositing Oxynitride Films by Reactive RF Magnetron Sputtering"**, Jiti Nukeaw, **Supanit Porntheeraphat**, Surachart Kamoldilok, Apichart Sungthong, Submitted No. 11/878270.
2. **"Nanocrystal Indium Oxynitride Thin Films Optical Filter"**, Jiti Nukeaw, Supanit Porntheeraphat, Apichart Sungthong, Submitted No. 11/826162.

### Thai Patents:

1. **"อุปกรณ์ตรวจรับแสงฟิล์มบางอินเดียมไนไตรด์** (Indium Nitride Photodetector)", รศ.ดร. จิติ หนูแก้ว, **น.ส.นิศาพร พรธีระภัทร**, นายเบญจพล ตันฮู้, เลขที่คำขอ 098819.
2. **"วิธีการจัดเตรียมขั้วไฟฟ้าโปร่งใสบนพลาสติกจากฟิล์มบางอินเดียมทินออกไซด์ และอุปกรณ์ดังกล่าว** (Indium Tin Oxide Transparent Electrode on Plastic)", รศ.ดร.จิติ หนูแก้ว, **น.ส.นิศาพร พรธีระภัทร**, นายกาจปัญญา สุวรรณสุโข, นายอรรณพ คล้ำชื้น, เลขที่คำขอ 095890.

# LIST OF PUBLICATIONS (cont.)

3. **“อุปกรณ์กรองแสงฟิล์มบางนาโนคริสตัลอินเดียมออกซีไนไตรด์** (Nanocrystal Indium Oxynitride Thin Film Optical Filter)”, รศ.ดร. จิติ หนูแก้ว, **น.ส.ศุภนิจ (นิศาพร) พรธีระภัทร**, นายอภิชาติ สังข์ทอง, เลขที่คำขอ 0701004000.
4. **“วิธีการปลูกฟิล์มออกซีไนไตรด์โดยควบคุมเวลาก๊าซในระบบรีแอคทีฟอาร์เอฟแมกนีตรอนสปัตเตอริง** (Gas-timing Method for Depositing Oxynitride Films by Reactive RF Magnetron Sputtering)”, รศ.ดร.จิติ หนูแก้ว, **น.ส.ศุภนิจ (นิศาพร) พรธีระภัทร**, นายสุรชาติ กมลดิลก, นายอภิชาต สังข์ทอง, เลขที่คำขอ 0701004105.
5. **“วิธีการเตรียมฟิล์มบางอินเดียมทินออกซีไนไตรด์และอุปกรณ์กรองแสงนำไฟฟ้าดังกล่าว** (Preparation of Indium Tin Oxynitride Films and Applied to Conductive Optical Filter)” รศ.ดร.จิติ หนูแก้ว, นายดอน คล้ายทับทิม, **น.ส.ศุภนิจ (นิศาพร) พรธีระภัทร**, ดร.สิรพัฒน์ ประโทนเทพ, เลขที่คำขอ 0701004105.

# TABLE OF CONTENTS

PAGE

# TABLE OF CONTENTS (cont.)

PAGE

# TABLE OF CONTENTS (cont.)

PAGE

# TABLE OF CONTENTS (cont.)

PAGE

# TABLE OF CONTENTS (cont.)

**PAGE**

# LIST OF TABLES

**TABLE** **PAGE**

# LIST OF FIGURES

**FIGURE** **PAGE**

# LIST OF FIGURES (cont.)

**FIGURE** **PAGE**

# LIST OF FIGURES (cont.)

# LIST OF FIGURES (cont.)

# LIST OF FIGURES (cont.)

**FIGURE** **PAGE**

# LIST OF FIGURES (cont.)

**FIGURE** **PAGE**

# LIST OF FIGURES (cont.)

**FIGURE** **PAGE**

# LIST OF FIGURES (cont.)

# CHAPTER 1

# INTRODUCTION

## 1.1 Motivation

The III-nitride such as (Aluminum Nitride (AlN), Gallium Nitride (GaN) and Indium Nitride (InN) are promising materials for the application to optoelectronic devices. They span a range of direct band gaps from near-Infrared (near-IR), green, blue to Ultra-Violet (UV). III-nitrides are more attractive because short wavelength is beneficial to high capacity optical digital data storage. Characteristics such as high drift velocity, high breakdown voltage, high thermal conductance and thermal stability make them good candidates for the application of high speed, high power, and high temperature devices.

Group III-nitrides extended the field of semiconductor applications to the limits where classical semiconductors such as Si and GaAs fail. The theoretical ability to tailor the direct bandgaps of this system from 0.7-6.2 eV makes it suitable for light emission and detection applications ranging from the red to the deep ultra-violet (UV) regions of the electromagnetic spectrum. LEDs based on III-nitride materials emitting from green to UV have been commercialized over the last decade. The visible LEDs are well suited to indicator applications such as automotive light and traffic signals as well as in the development of full color displays. These applications demand the improved materials quality and better device design, which turn require the knowledge of nitride material parameters. The new results from the intensive research on properties and device applications of III-nitrides require revision of the importance parameters of these materials, the energy gap of InN being a dramatic example.

During the last 6 years evolution and rise of III-nitride semiconductors has been phenomenal due to their various potential applications [1]. Authored books, and edited books have been published on these semiconductors and on the device fabricated using them. Reviews on the III-nitrides have been written by Akasaki and co-workers [2], by Nakamura [3] and more recently by Pearton et al. [4]. Morkoc and co-workers have written comprehensive reviews covering several aspects of the nitride semiconductors [5]. There are many areas where conventional III-V semiconductors (GaAs based) cannot be used. III-nitride devices have significant market potential. There are five major market segments that benefit from III-nitride devices, including optical storage, laser printing, high brightness LEDs, general illumination, and wireless base stations.

The bandgap of a semiconductor material is the most important parameter that determines the transport, optical properties, and other phenomena. The large variation in the nature of the chemical bonding has brought up a wide range in energy gap covered by the nitride semiconductors. The recent studies, it has been determined that the bandgap of InN is 0.7 eV instead of 1.9 eV value from earlier studies [6-8]. The widest bandgap of 6.2 eV in the nitride family is possessed by AlN. Thus, the group III-nitrides could potentially be fabricated into optical devices which are active at wavelengths ranging from the infra-red well into the deep ultraviolet.

Growth improvements in device performance were enabled mainly by the growth of high quality epilayers and heterostructures. The development of substrates (including introduction of new substrates and substrate preparation) and growth process are still the challenges to the researchers. The crystalline microstructure, which influences important physical properties of a material, is directly related to the growth process. Improvement of the growth techniques of III-nitrides will therefore yield improved film quality, a better understanding of their properties, and certainly more reliable III-nitride based devices.

Independent of the substrate choice and regardless of the growth method employed, another important concern of the epitaxial growth of good quality III-nitride films arises from incorporating stoichiometric quantities of nitrogen into the fabricated film. Nitrogen vacancies in nitride films are thought to be responsible for the n-type conductivity and the large carrier concentration observed in these films. A recent study by Butcher *et al.* [9] ascribes the high carrier concentrations in radio frequency sputtered InN films to high levels of excess nitrogen incorporation. The large carrier concentrations are also attributed to the presence of impurities (Oxygen) in the films. Thus an impurity-free atmosphere and a high purity source material are essential for the growth of high quality nitride films. The difficulty in the growth of InAlN alloy is mainly caused by thermal instability resulting from spinodal phase separation. This effect leads to problems with solubility between AlN and InN. Among III-nitrides, the fabrication of single crystalline InN films is still not esily attainable due to the low dissociation temperature (550 °C) and stoichiometric instability of InN. As a result, incorporation of Indium (In) in In-rich alloys is very difficult. Temperatures lower than ~ 550 °C must be used to prevent InN from dissociation but at the same time temperatures should be high enough for epitaxial growth. These difficult and the attempt to overcome them are addressed differently by different deposition techniques.

In order to grow good quality III-nitrides; research groups have tried several deposition techniques. The more common growth methods are metalorganic chemical vapor deposition (MOCVD), molecular beam epitaxy (MBE), and reactive sputtering. However these methods are limited in their capabilities to produce high quality wide band gap semiconductor thin films. The growth temperature for MOCVD is generally higher than 1000 °C. MOCVD reactor design for III-nitrides growth is a complex issue because it must cope with the problems presented by the gas phase reaction, high temperature, and film non-uniformity. Threading dislocations stemming from the interface tend to deteriorate the electrical properties of the material. H. Amano *et al.* [10] and S. Nakamura *et al.* [11] reported that low temperature grown AlN and GaN buffer layers, respectively, could improve the crystalline structure substantially, as well as electrical and optical characteristics. The lower growth temperature compared to the CVD counterpart makes MBE attractive for the preparation of GaInN quantum wells, which are necessary for blue/green display devices, because lower growth temperature is required for the growth of GaInN. The reaction process involved during growth is simpler with the case of MBE. The fine growth sequence control and lower growth rate are another benefits to the growth of layer structure such as laser diodes. However, the lower MBE growth temperature compared to MOCVD is a disadvantage for surface diffusion.

Radio frequency reactive sputtering (RF-sputtering) is a relatively simple growth technique. Using on-axis reactive sputtering AlN films have been deposited on different substrates such as glass, Si (100), Si (111), $SiO_2$ and sapphire. The c-axis AlN films are easier obtained at lower pressure (0.75-8 mTorr) and lower pressure [12-17] In Chien-Chuan Cheng's study [18], it is provided that the full width of half maximum intensity (FWHM) of AlN (002) was decrease with increase the $N_2$ concentration. It is widely studied growth technique for InN thin films, see for example Foley and Tansley [19], Tansley and Foley [20] and Butcher *et al.* [21]. Importantly, film growth typically occurs at low temperature, below 100°C, which is important for the growth of InN films. Low temperature growth allows the use of substrates other than temperature resistant materials such as sapphire. These alternative substrates, including glass and Si, are less-expensive. Hence, the growth of InN films using the RF-sputtering technique is relatively cost-effective. InN films grown by Butcher et al. (2004), columnar structures are clearly visible suggesting polycrystalline materials were obtained for RF-sputtering growth technique. The width of these columns is about 50 nm. Even though AlN and InN is a difficult material to study, radio frequency rf magnetron sputtering has been achieved with a polycrystalline structure.

Today there are still major obstacles to obtaining high quality thin films for device structures, such as the lack of lattice and thermally matched substrate, the narrow growth window, adduct formation, material characterization, and ability to obtain high quality p-type doping. In addition, challenges still remain to reduce interface defect densities, high impurity levels and surface roughness.

This research is focused on the issues relating to the growth of thin films by reactive r.f. magnetron sputtering including of four important semiconductor compounds; aluminum nitride (AlN), indium nitride (InN), indium tin oxide (ITO) and indium oxynitride (InON) with the innovative growth technique called "reactive gas-timing". The X-ray Diffraction (XRD) and Field Emission Scanning Electron Microscope (FE-SEM) are proposed to characterize crystalline structures and surface morphologies of thin films. The photoreflectance spectroscopy and UV-Visible spectroscopy (UV-VIS) are conducted to investigate the band gap energies of thin films. The Four Point Probe is used to measure sheet resistance of ITO thin films. Finally, the thin films of AlN, InN, ITO and InON were fabricated as application devices.

## 1.2 Objective

The objective of this research work has been the study of

1.2.1 the thin film growth process of AlN, InN, ITO and InON thin films by reactive gas-timing rf magnetron sputtering system.

1.2.2 the physical properties and breakdown characreistics of AlN, InN, ITO and InON thin films with various growth parameters.

1.2.3 the fabrication of AlN, InN, ITO and InON devices and their applications.

## 1.3 Scope of This Study

The scope of this research is as follows,

1.3.1 study the background of AlN, InN, ITO and InON thin films

1.3.2 study the theory of the rf magnetron sputtering growth system.

1.3.3 study the characterization systems;

- X-ray diffraction spectrometer (XRD)
- Scanning electron microscope (SEM)
- Photoreflectance spectroscopy (PR)
- UV-VIS measurement (UV-VIS)
- Four point probes measurement
- Current-Voltage measurement (I-V)
- Wavelength response measurement

1.3.4 experiment of AlN thin films grown with varying parameters.

1.3.5 experiment of InN thin films grown with varying parameters.

1.3.6 experiment of ITO thin films grown with varying parameters.

1.3.7 experiment of InON thin films grown with varying parameters.

1.3.8 set up the photoreflectance spectroscopy, wavelength response and pH-measurement experiment.

1.3.9 employ the characterization systems including XRD, SEM, Four Point Probe, PR, UV-VIS to investigate crystallization, surface morphology, sheet resistance and band gap energy of AlN, InN, ITO and InON thin films, respectively.

1.3.10 fabrications of AlN, InN, ITO and InON devices for some applications.

## 1.4 Expected Results

1.4.1 Important physical meaning; i.e, crystalline structure, thin film morphology and band gap energy of AlN, InN, ITO and InON will be clearly understood.

1.4.2 Effects of substrate distance, reactive gas-timing, gas flow rate, thin film thickness, and r.f. sputtering power on the growth of AlN, InN, ITO and InON thin films by using r.f. magnetron sputtering will be acknowledged.

1.4.3 Potential advantages of AlN, InN, ITO and InON thin films will be fabricated as devices including the pH-AlN sensor, nanocrystal-InN Photodetector, ITO flexible transparent electrode, ITO plastic antenna, and InON optical filters.

## 1.5 Dissertation Outline

This dissertation consists of three major parts, the first part dealing with the background of AlN, InN and related thin films (ITO, InON), sputtering system and characterization methods, the second part dealing with the growth and characterization experiments, results and discussions of AlN, InN, ITO, InON and the third part dealing with the devices applications of aluminum nitride, indium nitride and related thin films.

Chapter 2, 3 and 4 provide the fundamental knowledge of AlN, InN, ITO, InON and r.f. magnetron sputtering system, respectively. The new innovation method call "reactive gas-timing" was proposed in chapter 4. Chapter 5 presents the thin film characterization methods including x-ray diffraction, scanning electron microscope, photoreflectance spectroscopy, UV-VIS measurement, and four point probe measurement used in the thesis experiments.

Chapter 6 concerns experimental growth and analytical studies of structural and optical properties of AlN thin films. This chapter provides the characterizations of crystalline structure, surface morphology, and bandgap energy of AlN thin films and reports experimental results and discussion regarding the effects of growth parameters, including rf sputtering power, gas-timing, gas-flow rate, and film thickness.

Chapter 7 presents an experimental study on InN, ITO and InON thin films. The growth and characterizations of thin films affected by r.f. sputtering power, gas-timing, gas-flow rate, and film thickness were addressed.

Chapter 8 provides the applications of AlN, InN, ITO and InON thin films including AlN-pH sensor, InN photodetector, ITO plastic electrode, ITO plastic antenna and InON optical filters. The introduction, experiment, results and discussion of each application was addressed in this Chapter. The thesis conclusion and future perspective of area study addresses in Chapter 9.

## References

[1] F. Bertram, S. Srinivasan, R. Liu, L. Geng, F. A. Ponce, T. Riemann, J. Christen, S.Tanaka, H. Omiya, Y. Nakawaka, **"Spatial Variation of Luminescence of InGaN Alloys Measured by Highly-Spatially-Resolved Scanning Cathodoluminescence"**, Mater. Sci. & Eng. (b) 93, 19, 2002.

[2] I. Akasaki and H. Amano, **"In Properties of Group III Nitrides"**, ed. By J. H. Edgar, EMIS Data Reviews Series, p. 222, IEEE, London, 1994.

[3] S. Nakamura, T. Mukai, and M. Senoh, **"Candela-Class High Brightness InGaN/AlGaN Double Heterostructure Blue Light Emitting Diodes"**, Appl. Phys. Lett. 64, pp. 1687, 1994.

[4] S.J. Pearton, F. Ren, A.P. Zhang, and K.P. Lee, **"Fabrication and Performance of GaN Electronic Devices"**, Material Science and Engineering, Vol. R30, pp. 55-212, 2000.

[5] H. Morkok, S. Strite, G. Gao, M. Lin, B. Sverdlov, and M. Burns, **"Large Band-Gap SiC, III-V nitride, and II-VI ZnSe-based Semiconductor Devices Technologies"**, J. Appl. Phys, Vol. 76, No. 3, pp. 1363-1396, Aug. 2001.

[6] Y. Nanishi, Y. Saito, T. Yamaguchi, Japan J. Appl. Phys., 42 (2003) 2549.

[7] V. Yu Davydov, A.A. Klochikhin, V.V. Emtsev, S.V. Ivanov, V.V. Vekshin, F. Bechstedt, J. Furthmuller, H. Harima, A.V. Mudryi, A. Hashimoto, A. Yamamoto, A.J. Aderhold, J. Graul, E.E. Haller, Phys. Status Solidi b 230 (2002) R4.

[8] J.Wu, W. Walukiewicz, K.M. Yu, J.W. Ager III, E.E. Haller, H. Lu, W. Schaff, Y. Saito, Y. Nanishi, Appl. Phys. Lett. 80 (2002) 3967.

[9] K.S.A. Butcher, H. Dou, E.M. Goldys, T.L. Tansley, S. Srikeaw, **"Ultraviolet Raman and Optical Transmission Studies of RF Sputtered Indium Nitride"**, Physica Status Solidi (c). Vol. 0, Issue 1, 373-376, 2002.

[10] H. Amano, N. Sawaki, I. Akasaki, Y. Toyoda, **"Metalorganic vapor phase epitaxial growth of a high quality GaN film using an AlN buffer layer"**, Applied Physics Letters 48(5), 353,1986.

[11] S. Nakamura *et al.*, **"Characteristics of Room Temperature-cw Operated InGaN Multi-Quantum –Well-Structure Laser Diodes"**, MRS International J. Nitride Semicond. Res., 2 (5), 1997.

[12] L. Wu, S. Wu, and H. T. Song, **"Influence of Sputtering Pressure on Physical Structure of AlN Thin Films Prepared on Y-128$^{\circ}$ LiNbO$_3$ by RF Magnetron Sputtering"**, J. Vac. Sci. Technol. A Vol. 19, No. 1 (2001) 167.

[13] M. Akiyama, T. Harada, C.N Xu, K. Nonka, and T. Watanabe, **"Preparation of Highly Oriented AlN Thin Films on Glass Substrates by Helicon Plasma Sputtering and Design of Experiments"**, Thin Solid Films 350 (1999) 85.

[14] B. Wang, Y. N. Zhao, and Z. He **"The Effects of Deposition Parameters on The Crystallographic Orientation of AlN Films Prepared by RF Reactive Sputtering"**, Vaccum. Vol. 40, No.5 (1997) 427.

[15] F. Engelmark, G. Fucntes, I. V. Katardjiev, A. Harsta, U. Smith, and S. Berg **"Synthesis of Highly Oriented Piezoelectric AlN Films by Reactive Sputter Deposition"**, J. Vac. Sci. Technol. A Vol. 18, No. 4, (2000) 1609.

[16] H. L. Kao, P. J. Shih, and Chun-His Lai, **"The Study of Preferred Orientation Growth Aluminum Nitride Thin Films on Ceramic and Glass Substrate"**, Jap. J. Appl. Phys. 38 (1999) 1526.

[17] C. H. Wu, W. Y. Chiu, and H. L. Kao, **"Texture and Smooth AlN Films Prepared by Helicon Sputtering System for SAW Device Applications"**, Electronics.

[18] J. W. Soh, and W. J. Lee, **"SAW Characteristics of AlN Films Deposited on Various Substrates Using ERC Plasma Enchanced CVD and Refractive RF Sputtering"**, IEEE Ultrasonic Symposium (1996) 299.

[19] Foley C.P. & Tansley T.L. (1985).,**"Morphology and structure of indium nitride films"**, Appl. Surf. Sci. 22-23, 663-669.

[20] Tansley T.L. & Foley C.P. (1984), **"Electron Mobility in Indium Nitride"**, Electron. Lett. 20(25-26), 1066-1068.

[21] K.S.A. Butcher, **"InN, an Historic review from Obscurity to Controversy In"**: Q. Guo, Editor, Advanced Material in Electronics, Research Signpost (2004), p. 1.

# CHAPTER 2

# BACKGROUND OF ALUMINUM NITRIDE (AlN)

## 2.1 Introduction to AlN

As a member of nitride system, aluminum nitride (AlN) is one of the most promising III/V binary materials in these acoustical, optoelectronic, and microwave applications. In binary form and alloyed with GaN and InN, AlN has the unique capability of serving as a cladding, active, buffer or window layer in short wavelength optoelectronic devices. The crystal AlN structure is shown in Fig. 2.1.

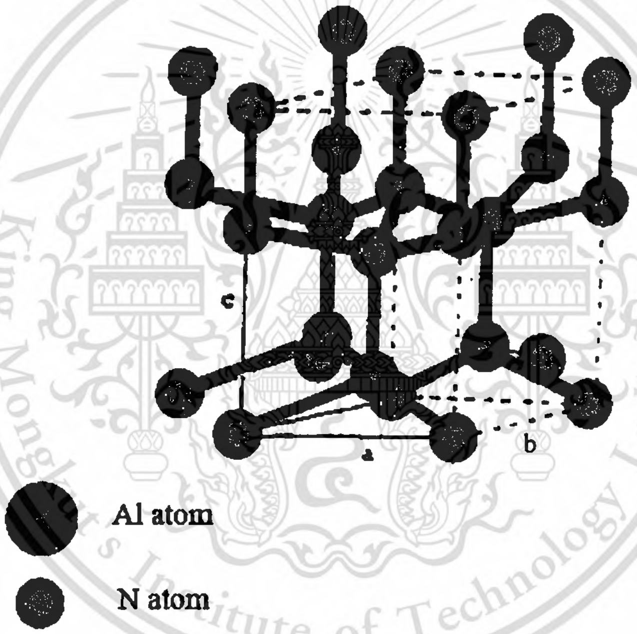

**Fig. 2.1** The crystal structure of AlN: (a) the structure of distorted tetrahedron (b) unit cell.

Due to its wide band gap of 6.2 eV at room temperature, AlN is of interest for devices, which operate at wavelength well into the UV regime of the spectrum. As compared to GaAs, Si, Ge, GaN, SiC and other commonly used semiconductors for devices. Due to its low dielectric constant (ε = 9) and good lattice match (less than 1% mismatch) to SiC, AlN is a prime dielectric alternative to $SiO_2$ in high temperature, high power SiC technology. With high surface acoustic velocities and piezoelectric properties, AlN has also been investigated for surface acoustic wave delay lines. Therefore, in order to realize the full potential of AlN and Al based nitrides, it is essential to understand the growth of high quality AlN and device implications in the progression of nitride technology.

In the late 1950's and early 1960's, many investigations were conducted to grow and characterize AlN. These studies mostly fabricated small metallic aluminum crystals or AlN powder samples. The earliest reports of synthesized AlN growth were by Tiede *et al.* [1]. Who used a metallic Al source in a stream of $NH_3$. For powder samples of AlN, a flow of ammonia over a source material in a furnace was also used. Investigations of AlN single crystal growth continued with Edwards [2], Cox [3], and Kawabe [4] using sintering compacted AlN powder and sublimed pressed AlN powder under a nitrogen flow, respectively. As progress in AlN thin film growth continued, researchers found reactive sputtering to be inexpensive and simple. These Al sputtered films using argon ions tended to be polycrystalline or amorphous, however, there was some improvements in crystallinity using Ne ions.

Early difficulties in obtaining high quality single crystal AlN stemmed from the reactivity of Al with oxygen, the lack of thermal and lattice compatible substrate, the need for high quality source materials, and the absence of an oxygen free environment. In an effort to address some of these growth issues, researchers in 1970's used many popular epitaxial growth techniques, such as chemical vapor deposition (CVD), molecular beam epitaxy (MBE), and hydride vapor phase epitaxy (HVPE). High quality AlN was achieved in early investigations by using vapor transport CVD, but the films had very high background contaminations. Not until the late 1970's have results of high quality AlN been reported on sapphire ($Al_2O_3$) and silicon carbide (SiC). Chu et al. [5] reported growing a 25 micron thick monocrystalline AlN layer on hexagonal SiC at 1200 to 1250 °C. In 1979 Yoshida used MBE to grow on Si (111) and sapphire (0001) at 1000 to 1200 °C. Source materials for many of these studies were trimethylaluminum and ammonia, diethylaluminum azide and hydrazine, triethylamine and ammonia, or triethylaluminum and ammonia. Different substrates for these investigations included Si, SiC, and sapphire. As the optimization of AlN continues today, researchers are investigating using two very common growth techniques, the MOCVD and MBE processes.

## 2.2 The Growth of AlN

Because of the outstanding properties of AlN, high quality AlN thin films are potential candidates for use in the fabrication of corrosion resistant [6], SAW, short wavelength laser and UV light detector [7]. About the optical properties, the AlN thin films were transparent in visible and infrared region, and have high refractive index (~2.1). For most optical application such as anti-reflection coating, the high hardness, high refractive index (n) and lower extinction coefficient (k) are required. The refractive index is much related to packing density and crystalline of the film. The extinction coefficient was affected by the impurity and defects. Therefore, the optical constants and quality are very important for optical application. Moreover, the optical constants of AlN were varied by different deposition methods. The table 2.1 shows the optical constants in the different deposition systems.

**Table 2.1** The optical constants of AlN prepared by different deposition systems.

| Method | Refractive index | Structure | References |
|---|---|---|---|
| CVD | 2.18(589nm) | Single crystalline(wurizite) | J.Pastrnák and L.Roskovcová. [8] |
| CVD | 1.99(550nm) | Polycrystalline | Chu and Kelm [9] |
| PECVD | 1.85(375nm) | Hexagonal (002) | Bauer et al [10] |
| LPCVD | 1.9-2.2(632.8nm) | Polycrystalline | Interrante et al [11] |
| DC Magnetron sputtering | 1.7-1.8(632.8nm) | _ | E.V. Gerova et al [12] |
| DC Magnetron sputtering | 2.075(632.8nm) | Hexagonal (002) | A. Cachard et al [13] |
| R.F sputtering | 1.9-2.1(550nm) | Polycrystalline | Hirofumi et al [14] |
| R.F sputtering | 1.95-2.05(633nm) | Hexagonal (002) | Han et al [15] |
| Dual ion beam sputtering | 1.96-2.10(632.8nm) | Hexagonal (002) | H.Windischmann [16] |
| RLVIP | 2.10~2.15(550nm) | Hexagonal (002) | N.Q.Danh et al [17] |

### 2.2.1 Epitaxial Growth

High quality nitride thin films are grown almost exclusively using molecular beam epitaxy (MBE), metalorganic chemical vapor deposition (MOCVD) and hydride vapor phase epitaxy (HVPE). Since MBE requires ultra high vacuum and the growth rate in MBE is about 10 times smaller than in MOCVD, it cannot be scaled up from research to production of commercial devices easily. Bulk-like nitride is often grown by HVPE due to the high growth rate that can be achieved using this technique. However, crystal quality is not as good as that of MOCVD grown layers.

MOCVD technique has been widely used in research from early 1970s and in commercial production from 1990s for epitaxial growths of single crystal thin films of III-V, II-VI, IV-VI semiconductors. The major attractions of MOCVD relative to other techniques are its versatility and suitability for larger scale production. Nevertheless, a few problems remain, including the need of expensive precursors, and a larger number of parameters that must be precisely controlled to obtain uniformity and reproducibility. In 1986, Amano *et al.* [18] develop the "two step processes" for nitride growth for the first time. This involves deposition of a thin nucleation layer (NL) at low temperature prior to high temperature (HT) GaN growth. The crystal quality of the NL itself is poor due to the low atomic mobility at low deposition temperature, followed by deposition of device quality overlayers at higher temperature. It has been proposed that the high island densities obtained in the NL after annealing at HT provide attachment sites for the HT GaN adatoms, resulting in enhanced lateral growth of the GaN film [19-21]. This technique paved the way for practical applications of nitride-based devices by greatly improving the film crystal quality.

### 2.2.2 Sputtering Growth

Sputtering is a very versatile process for the fabrication of thin solid films. Even though AlN is a difficult material to study, radio frequency rf magnetron sputtering has been achieved with a polycrystalline structure. Today there are still major obstacles to obtaining high quality thin films for device structures, such as the lack of lattice and thermally matched substrate, the narrow growth window, adduct formation, material characterization, and ability to obtain high quality p-type doping. In addition, challenges still remain to reduce interface defect densities, high impurity levels and surface roughness. Fabrication of good AlN films is possible at considerably lower temperatures using reactive sputtering [22-24] as compared to MOCVD.

This study, AlN thin films were grown by reactive rf magnetron sputtering with a new technique called reactive gas-timing using various growth conditions and parameters. In the process of establishing the growth conditions, other influences, such as substrate cleaning and chamber contamination, were also investigated. To provide the high quality AlN thin films, the XRD, FE-SEM, AFM, and PR were used to characterize all the samples and feedback to enhance the growth process. Finally, this study will demonstrate such potential applications of AlN thin film in pH-sensitive devices.

## 2.3 The Properties of AlN

### 2.3.1 Crystal Structure of AlN

The group III atoms form compounds with $N$ that have four covalent bonds for each atom. AlN can crystallize in two crystal structures [25]; Wurtzite and Zinc blende with the stable one being the wurtzite structure. The wurtzite structure has a hexagonal unit cell with two lattice parameters $a$ and $c$ with an ideal ratio of $c/a = \sqrt{8/3} = 1.633$. Four nitrogen atoms surround every group III atom, and four group III atoms, which are arranged at the edges of a tetrahedron, surround every nitrogen atom. For an actual nitride, the structure is distorted from the ideal hexagonal packing of the basic molecule oriented along the stacking direction (c-axis). Because of this small distortion, there are two slightly different bond lengths in the wurtzite structure given by:

$$B_{\parallel} = u \cdot c$$

$$B_{\perp} = \sqrt{\frac{a^2}{3} + \left(\frac{1}{2} - u\right)^2 \cdot c^2} \tag{2.1}$$

where $u$ represents the cell-internal structural parameter (ideal value is 3/8), $a$ and $c$ denote the length of the lattice vectors of the structure. $B_{\parallel}$ represents the length of bonds parallel to the c-axis and $B_{\perp}$ represents the length of bonds pointing in any other direction. The wurtzite structure with greater $c/a$ value than the ideal value of 1.633 is unstable, while less than 1.633 is stable.

In a perfect hexagonal wurtzite structure, the bond lengths between atoms in any tetrahedral cell are all the same and the angle between any two bond directions is also the same (the standard tetrahedral angle of $109.6^{\circ}$).

In AlN, this structure is slightly distorted [26-28] with two different bond lengths and two different angles. X-ray experiments performed on AlN [29, 30] to measure lattice parameters $a$, $c$ and $u$ gave 3.1115, 4.9798 and 0.3821 respectively. Upon using these values in equations 2.1, the two different bond lengths in AlN were found to be 1.9028 (parallel to the c-axis) and 1.8899 (otherwise). This leads to two different angles between bond directions that can be calculated using simple geometry rules (see figure 2.2 below). There got $108.10^{\circ}$ for the angle between the two bonds when one of them is along the symmetry axis and $110.81^{\circ}$ otherwise.

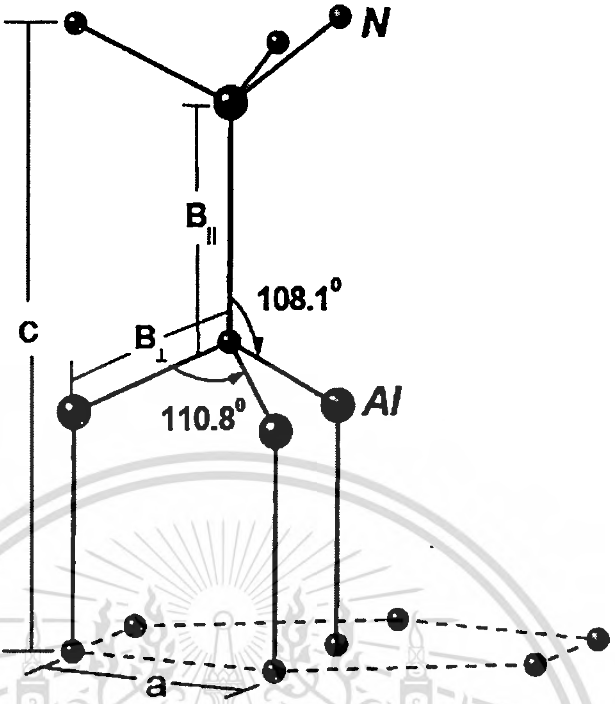

**Fig. 2.2** Part of the AlN wurtzite structure showing the two different bond lengths and the angles between bond directions.

The deviation of the c/a ratio from that of the ideal wurtzite crystal is probably due to lattice stability and ionicity. While the theoretical estimate of the lattice parameter of zincblende structured AlN is a = 4.38 Å, the rocksalt structure has a value of a = 4.043-4.045 Å at room temperature. Figure 2.3 represents the stick and ball stacking model of AlN crystals orientations.

The cubic zincblende AlN is easier to dope, cleave (for laser facets), and make contact with silicon due to its higher symmetry. Also zincblende structured AlN is believed to have decreased photon scattering and higher ballistic electron velocities, thermal conductivity and acoustic velocity due to its higher symmetry.

The crystal structure can be modified into a variety of polytypes with the addition of impurity elements such as oxygen, carbon, and silicon. At 1.00 atm of pressure, AlN does not melt, but dissociates significantly above 2230°C. AlN does not occur naturally; therefore, it must be synthesize by high-temperature reaction.

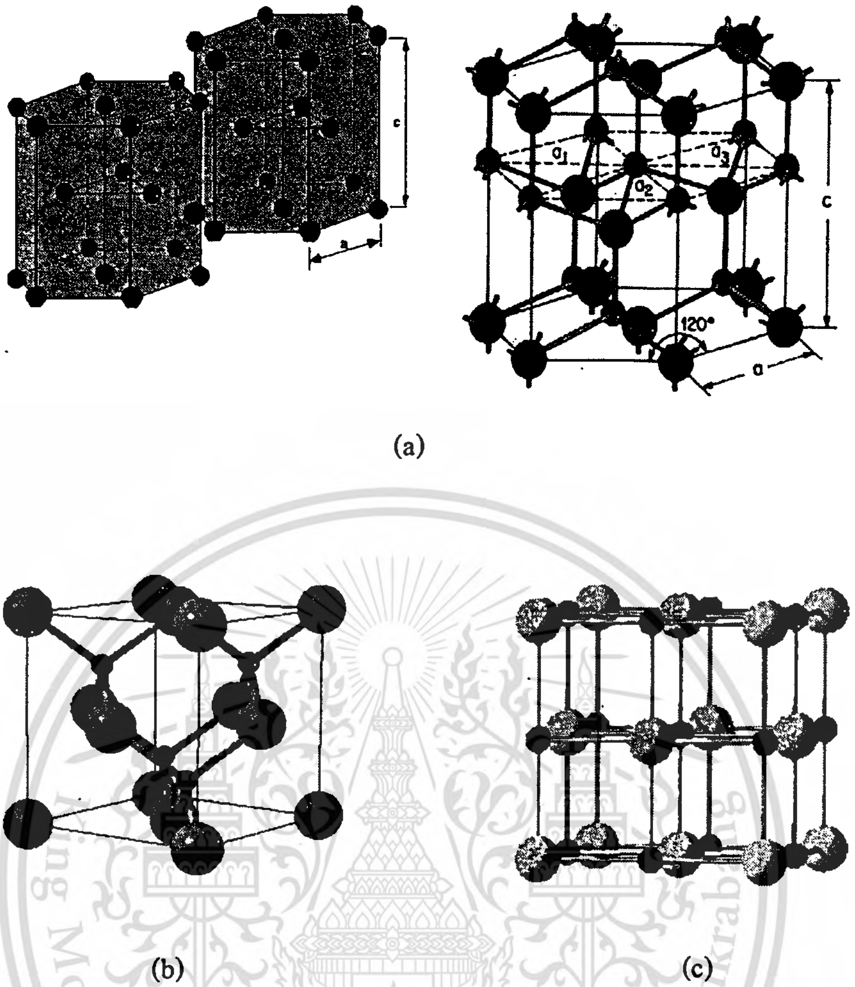

**Fig. 2.3** Stick and ball stacking model of AlN crystals with wurtzite (a), zincblendee (b) and rocksalt (c) orientations.

### 2.3.2 Thermal and Chemical Properties of AlN

The properties of hexagonal wurtzite structured AlN have been much more often reported due to its stability. Hex-AlN is an extremely hard ceramic material with a melting point higher than 2000 $^{o}$C. The thermal conductivity *k* of AlN at room temperature has been predicted at ≈ 3.2 Wcm$^{-1}$K$^{-1}$ [31]. Values of *k* measured at 300 K are 2.85 Wcm$^{-1}$K$^{-1}$ [32]. The measured thermal conductivity as a function of temperature is plotted in Fig. 2.3. It has high resistivity (1013 Ωm) and high breakdown voltage (14 kV/mm).

Using X-ray techniques across a broad temperature range (77–1269 K), it was noted by Slack and Bartram [31] that the thermal expansion of AlN is isotropic with a room temperature value of 2.56x10$^{-6}$ K$^{-1}$. The thermal expansion coefficients of AlN measured by Yim and Paff [33] have mean values of $\Delta a/a$ = 4.2x10$^{-6}$ K$^{-1}$ and $\Delta c/c$ = 5.3x10$^{-6}$ K$^{-1}$. The dependence of the thermal expansion coefficient in the c plane and in the c direction is shown in Fig. 2.4, which can be fitted by the following polynomials

$$\Delta a/a_0 = - 8.679\mathrm{x}10^{-2} + 1.929\ \mathrm{x}10^{-4}T + 3.400\ \mathrm{x}10^{-7}T2 - 7.969\ \mathrm{x}10^{-11}T3$$

and

$$\Delta c/c_0 = - 7.006\mathrm{x}10^{-2} + 1.583\ \mathrm{x}10^{-4}T + 2.719\ \mathrm{x}10^{-7}T2 - 5.834\ \mathrm{x}10^{-11}T3$$

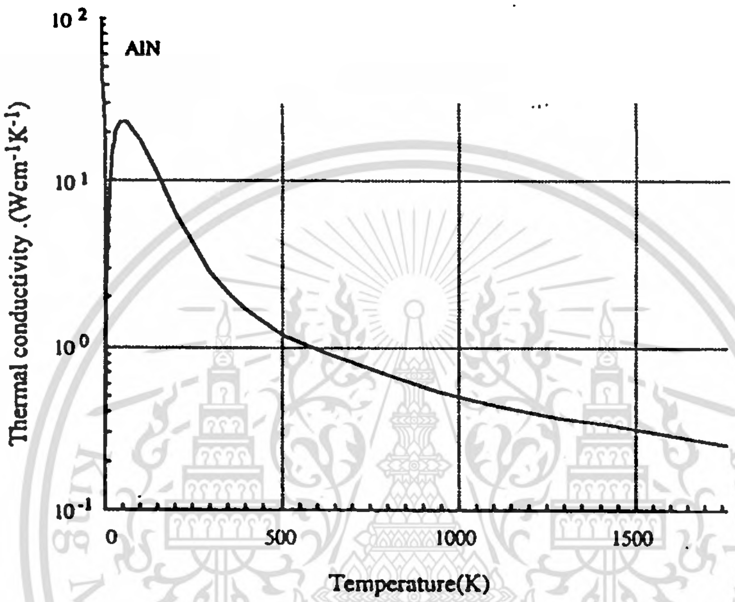

**Fig. 2.4** Thermal conductivity of single-crystal AlN

The equilibrium $N_2$-vapor pressure above AlN is relatively low compared to that above GaN which makes AlN easier to synthesize. The calculated temperatures at which the equilibrium $N_2$ pressure reaches 1, 10, and 100 atmospheres are 2836 K, 3088 K, and 3390 K, respectively.

Similar to GaN but even more so, AlN exhibits inertness to many chemical etches. A number of AlN etches have been reported in the literature. However, none of these etches have performed on high-quality single-crystal AlN. The surface chemistry of AlN has been investigated by numerous techniques, including Auger electron spectroscopy, X-ray and Ultraviolet Photoemission Spectroscopy (XPS, UPS), ultraviolet photoelectron spectroscopy, and electron spectroscopy. One of these investigations by Slack and McNelly [34] indicated that the AlN surface grows an oxide 50-100 angstrom thick when exposed to ambient air for about a day. However, this oxide layer was protective and resisted further decomposition of the AlN samples.

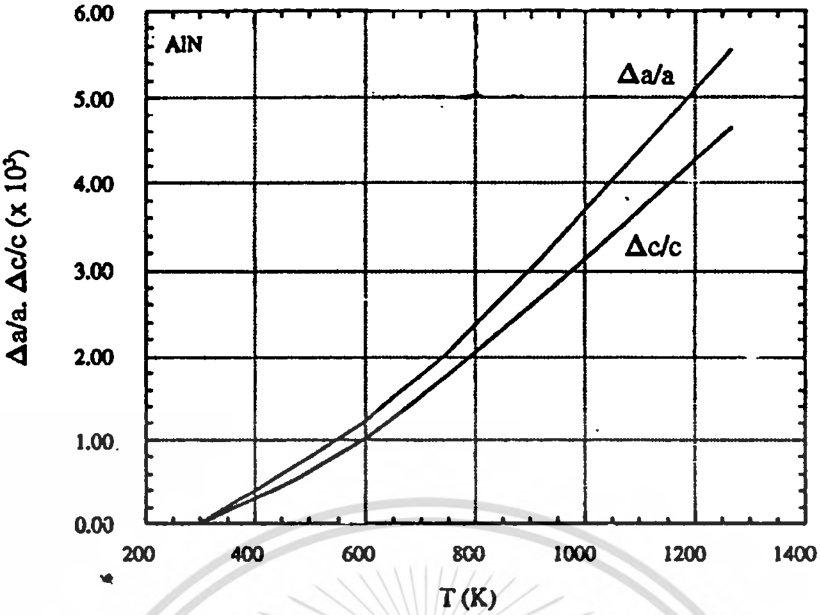

**Fig. 2.5** Variation of the thermal expansion coefficient of AlN on temperature in and out of the c-plane.

### 2.3.3 Mechanical Properties of AlN

Early investigations of the elastic properties of AlN were carried out on sintered polycrystalline specimens, due to the unavailability of large single crystals. This, however, paved the way to more refined measurements as single crystalline AlN became available.

The hardness of AlN has been measured to be ~ 12 GPa on the basal plane (0001) using a Knoop diamond indenter. Some anisotropy in Knoop hardness has been observed with the indent direction perpendicular to the c axis with measured values in the range of 10-14 GPa.

### 2.3.4 Electrical Properties of AlN

Due to the low intrinsic concentration, and the deep native defect and impurity energy levels, the electrical characterization of AlN has usually been limited to resistivity measurements. One such measurement by Kawabe and co-workers on transparent AlN single crystals yielded resistivities ρ = 1011-1013 Ωcm, a value consistent with other reports. However, it was found that impure crystals, which exhibited a bluish color possibly due to the presence of $Al_2OC$, have much lower resistivities ρ = 103-105 Ωcm. These resistivity values are much lower than those according to Chu et al. who were able to obtain both n- and p-type AlN by introducing Hg and Se, respectively, but failed to determine the net carrier concentrations due to very high resistivities.

The n-AlN films grown by Rutz [19] had a quite low resistivity ($\rho$ = 103 Ωcm), which is comparable to those of Kawabe et al. Although Rutz did not determine the source of the electrons, Rutz et al. observed an interesting transition in their AlN films in which the resistivity abruptly decreased by two orders of magnitude with an increase in the applied bias. This observation found applications to switchable resistive memory elements that are operated at 20 MHz.

The insulating nature of these early films hindered meaningful studies of their electrical transport properties. With the availability of refined growth techniques, AlN is presently grown with much improved crystal quality and shows both n- and p-type conductions. This has rejuvenated efforts to measure both the electron and hole Hall mobilities. Edwards et al., and Kawabe et al. carried out some Hall measurements in p-type AlN, which produced a very rough estimate of the hole mobility $\mu p$ = 14 $cm^2/Vs$ at 290 K. Not all the parameters needed for the calculations are known precisely, which somewhat reduce the confidence in predicted values. As is the case for GaN, the room temperature mobility is dominated by the polar optical photon scattering.

### 2.3.5 Optical Properties of AlN

Since an AlN lattice has a very large affinity to oxygen, it is almost impossible to eliminate oxygen contamination in AlN. Currently, commercially available AlN contains about 1-1.5 at. % oxygen. Some oxygen is dissolved in the AlN lattice while the remainder forms an oxide coating on the surface of each power grain. Harris and Youngman have recently reviewed photoluminescence and cathodoluminescence characteristics of AlN. After irradiation with ultraviolet light, AlN doped with oxygen was found to emit a series of broad luminescence bands at the near-ultraviolet frequencies at room temperature, no matter whether the sample was powdered, single crystal, or sintered ceramic. Pacesova and Jastrabik observed two broad luminescence lines centered in the vicinity of 3.9 and 4.2 eV and more than 0.5 eV wide for samples contaminated at about 1 to 1.5 at. % oxygen. Youngman and Harris, and Harris et al. investigated the luminescence characteristics of polycrystalline sintered AlN samples and noted a continuous shift of the peak position in the ultraviolet luminescence line as a function of oxygen content up to a critical concentration of about 0.75 at. %. The luminescence lines beyond this limit of oxygen concentration remained stationary.

Yim et al. characterized high-quality AlN by optical absorption and determined the room-temperature bandgap to be direct with a value of 6.2 eV. Several groups have reported comparable values whereas others have produced questionable values considerably below 6.2 eV, probably due to oxygen contamination. Oxides formed with Ga are not stable at GaN-growth temperatures and are easily desorbed. However, the same fortuity does not hold for AlN. Both MOCVD and MBE films show oxygen contamination. Yim et al. also observed a broad emission-spectrum range of 2-3 eV with a peak at 2.8 eV. Other investigations confirmed the presence of a 2.8 eV peak which Slack and McNelly have attributed to oxygen impurities. Samples grown at the H. Morkoc's laboratory by MBE and measured at the Honeywell Technology Center revealed a broad peak at 4 eV as well as the band-edge or near-band-edge signal in the emission spectrum. These observations are common to MOCVD samples as well. Perry and Rutz performed temperature-dependent optical absorption; measuring a bandgap of 6.28 eV at 5 K compared to their room temperature value of 6.2 ± 0.1 eV. In the only optical study of AlN impurities, Karel and coworkers reported on the luminescence of Mg and rare-earth center in AlN. Measurements of the refracvtive index of AlN have been carried out in amorphous, polycrystalline, and single epitaxial thin films. The values of the refractive index are in the $n = 1.99$-$2.55$ range with several groups reporting $n = 2.15 \pm 0.05$. These values are found to increase with increasing structural order, varying between 1.8 to 1.9 for amorphous films, 1.9 to 2.1 for polycrystalline films, and 2.1 to 2.2 for single crystal epitaxial films. The spectral dependence and the polarization dependence of the index of refraction has been measured and showed a near-constant refractive index in the wavelength range of 400-600 nm. Some of these measurements also indicate that, in the long-wavelength range, the dielectric constant ($\varepsilon_0$) of AlN lines in the range of 8.3-11.5, and that most of the values fall within $\varepsilon_0 = 8.5 \pm 0.2$. Other measurements in the high-frequency range produced dielectric constants of 4.68 and $\varepsilon_\infty = 4.84$. AlN has also been examined for its potential for second-harmonic generation.

Synchrotron radiation studies of AlN single crystal out to 40 eV have been performed, which resulted in the observation of 8 eV luminescence peak. The same peak was also found in vacuum-ultraviolet reflection measurements. Recently, photoluminescence determinations using excimer-laser excitation were performed and the results are displayed in Fig. 2.5 for MBE samples grown at 800 $^{\circ}$C and 850 $^{\circ}$C. The samples were grown on sapphire substrates and exhibit broad peaks at a wavelength of 320 nm. Table 2.2 summarizes the observed structural and optical properties of AlN.

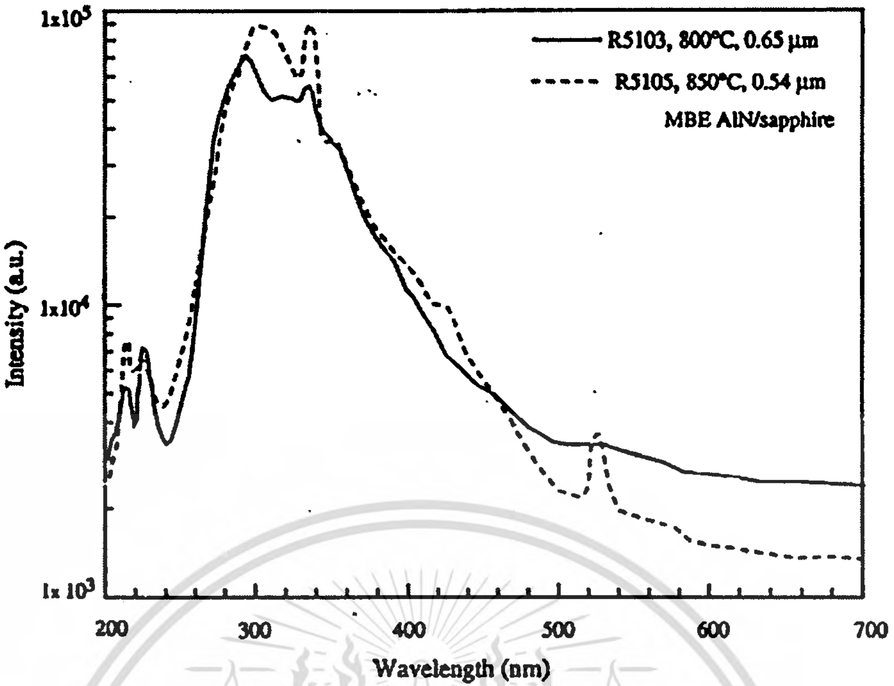

Fig. 2.6 Intensity versus wavelength curves of the photoluminescence spectra of AlN grown on sapphire.

**Table 2.2** A summarizes the observed structural and optical properties of AlN

| | | |
|---|---|---|
| **Wurzite polytype** | | |
| Bandgap energy | $E_g$(300 K) = 6.2 eV | $E_g$(5 K) = 6.28 eV |
| Lattice constant | a = 3.112 Å, c = 4.982 Å, | |
| Thermal expansion | $\Delta a/a = 4.2\text{x}10^{-6}$/K | Δc/c = 5.3x10-6/K |
| Thermal conductivity | k = 3.2 W/cm K | |
| Index of refraction | n(3eV) = 2.15 ±0.05 | n(3.42eV) = 2.85 |
| Dielectric constant | $\varepsilon_r$=8.5±0.2 | $\varepsilon\infty$=4.68±4.84 |
| **Zincblende polytype** | | |
| Bandgap energy | $E_g$(300 K) = 5.11 eV; theory | |
| Lattice constant | a = 4.38 Å | |

### 2.3.6 Band Structures of AlN

AlN is a wide band gap material, and can crystallize in both wurtzite and zincblende polytypes. Hexagonal wurtzite structured AlN has a direct room temperature bandgap of 6.2 eV. Cubic (zincblende) structured AlN has a bandgap of ~4 eV and hard to obtain.

Well-known $Al_xGa_{1-x}N$ band structure calculations are performed by the methods of orthogonalized linear combinations of atomic orbitals [35], by linear-muffintin- orbitals [36], by the first-principle pseudopotential calculation based on the theory of density functional [37], and by other methods. The band structure of AlN is also calculated by the local model pseudopotential method. A modified virtual crystal approximation [38] accounting for the existence of antisite defects created during the formation of substitutional solid solution is used to explain the nonlinear concentration dependence of the energy gap. Temperature dependence of the energy gap is considered in the context of the Brooks-U theory [39]. The dynamics of the chemical bond in the compounds is investigated by analyzing the spatial distribution of the valence electron charge.

In 1999, V. G. Deibuk et al. [40] were studied the AlN epitaxial layers of 0.5–20 μm thickness grown by pyrolytic deposition on the (0001) sapphire substrates from complex ammonium compounds of Al halides [41]. Electron diffraction and X-ray diffraction studies confirm that as-grown structure is single-crystal. The composition of solid solution is determined by X-ray diffraction analysis using a JXA microanalyzer. The energy gap ($E_g$) of the samples is found from the optical absorption long-wavelength edge. The dependence of optical absorption coefficient $\alpha$ on the photon energy $h\nu$ is approximated by the well-known relation for direct interband transitions

$$\alpha(h\nu) = \alpha_0(E_g - h\nu)^{1/2}, \tag{2.2}$$

Where $\alpha_0$ is the parameter which does not depend on $h\nu$. According to (1), the dependence $\alpha^2(h\nu)$ of is linear within six orders of magnitude, and extrapolation of $\alpha^2$ until it intersects the energy axis yields the values of *Eg* which are in reasonably good agreement with well-known published data.

Their calculations are based on the local model pseudopotential method [38] developed in [42, 43] for hexagonal binary compounds. One-electron pseudopotential Hamiltonian is expressed by the relation

$$\hat{H} = -\frac{\hbar^2}{2m}\nabla^2 + V(\mathbf{r}), \tag{2.3}$$

where $V(\mathbf{r})$ is total crystal pseudopotential, which is written for periodic lattice as

$$V(\mathbf{r}) = \sum_{G \leq G_0} V(\mathbf{G}) \exp(i\mathbf{G} \cdot \mathbf{r}), \tag{2.4}$$

The influence of temperature on solid-solution band structure is considered in the context of the Brooks-U theory. The calculation band structure of wurtzite-AlN from V. G. Deibuk et al. is shown in Fig. 2.7.

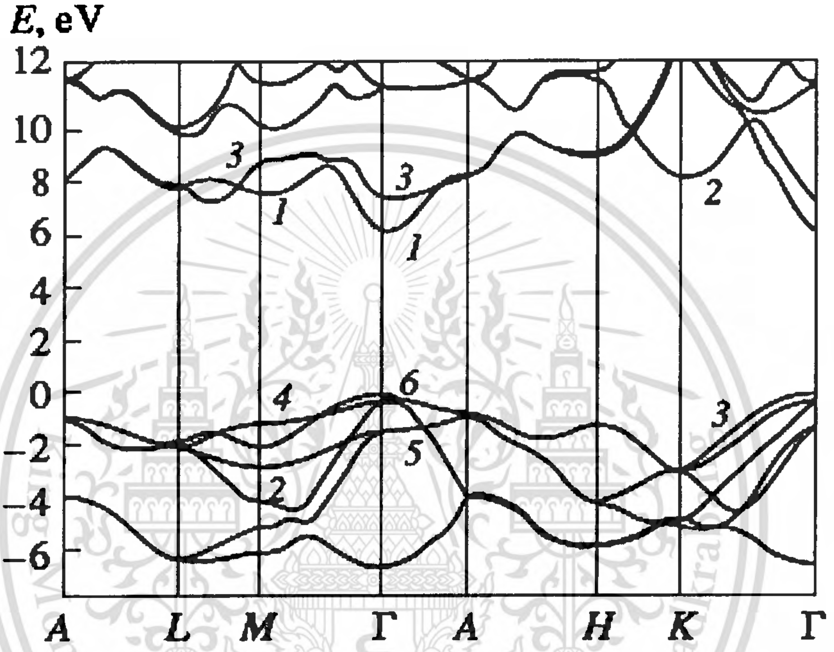

Fig. 2.7 Calculation band structure of wurtzite-AlN

## 2.4 Chapter Summary

Among the Nitrides, GaN films have been investigated extensively in the last thirty years, however, few studies on AlN growth have been reported. AlN can crystallize in two crystal structures; Wurtzite and Zincblende. High quality AlN thin films are grown almost exclusively using MBE, MOCVD, and HVPE. Sputtering is a very versatile process for the fabrication of thin solid films. Even though AlN is a difficult material to study, radio frequency rf magnetron sputtering has been achieved with a polycrystalline structure. Hexagonal wurtzite structured AlN has a direct room temperature bandgap of 6.2 eV. Cubic (zincblende) structured AlN has a bandgap of ~4 eV and hard to obtain. Moreover, the optical constants of AlN were varied by different deposition methods.

Today there are still major obstacles to obtaining high quality thin films for device structures, such as the lack of lattice and thermally matched substrate, the narrow growth window, adduct formation, material characterization, and ability to obtain high quality p-type doping. In addition, challenges still remain to reduce interface defect densities, high impurity levels and surface roughness.

## References

[1] E. Tiede, M. Thimann, and K. Sensse, **"Uber phosphorescenzfahiges, durch Silicium aktiviertes Aluminumnitrid "**, Chem. Berichte 61, pp.1568, 1928.

[2] M. D. Bremser, W. G. Perry, T. Zheleva, N.V. Edwards, O.H. Nam, N. Parikh, D.E. Aspnes, and Robert F. David, **"Growth, Doping and Characterization of $Al_xGa_{1-x}N$ Thin Film Alloys on 6H-SiC(0001) Substrates"**, MRS Internet J. Nitride Semicond. Res. 1, 8, 1996.

[3] R.L. Lichti, Y.G. Celebi, K.H. Chow, B. Hitti, and S.F.J. Cox, **"Trapping of Mobile Mu Centers in Single Crystal AlN"**, Physica B, pp. 340-342, 2003.

[4] K. Kawabe, R. H. Tredgold, Y. Inuishi, **"Electrical and Optical Properties of AlN-Thermo Stable Semiconductor"**, Electrical Engineering Japan, **62**, 1967.

[5] Chu P.K., Gao. Y., and Erickson. J.W., **"Characterization of III Nitride Materials and Devices by Secondary Ion Mass Spectroscopy"**, Journal of Vacuum Science and Technology B, **16(1)**, pp. 197-203, 1998.

[6] Y. Pauleau, J.J. Hantzpergue, and J.C. Remy, Bull. Soc Chim. Fr., I, pp. 199-214, 1979.

[7] M.A. Khan, J.N. Kuznia, D.T. Olson, J.M. Hove, and M. Blasingame, Appl. Phys. Lett. **60**, pp. 2917, 1992.

[8] J. Pastmak and L. Roskovcova, Phys. Stat. Sol., **14**, K5, 1996.

[9] T.L. Chu, and R.W. Kelm, J. Electrochem. Soc. (USA), Vol. **122**, pp.995, 1975.

[10] J. Bauer, L. Biste, and D. Bolze, Phys. Status Solidi (Germany), Vol.**39**, 1973.

[11] L.V. Interrante, W. Lee, M. McConnell, N. Lewis, and E. Hall, J. Electrochem. Soc., Vol. **36**, pp.472, 1989

[12] E.V. Gerova, N.A. Ivanov, and K. I. Kirov, Thin Solid Films 81, pp.201, 1981.

[13] A. Cachard, R. Fillit, I. Kadad, and J.C. Pommier, Vacuum **41**, pp. 1151, 1990.

[14] H. Takikawa, N. Kawakami, and T. Sakakibara, **"Synthesis of a-axis-Oriented AlN Films by a Shield Reactive Vacuum arc Deposition Method"**, Surface Coating Technology, pp.120-121, 1993.

[15] H.Y. Joo and H.J. Kim, **"Spectrophotometric Analysis of Aluminum Nitride Thin Films"**, J. Vac. Sci. Technol. A 17, No.3, pp.862, 1999.

[16] H. Windischmann, Thin Solid Films, **154**, pp.159, 1987.

[17] N. Q. Danh, K.H. Monz, and H.K. Pulker, **"Reactive Low Voltage Ion Plating of Aluminum Nitride Films and Their Characteristics"**, Thin Solid Films, pp.257, 1995.

[18] H. Amano, N. Sawaki, I. Akasaki, Y. Toyoda, **"Metalorganic Vapor Phase Epitaxial Growth of A High Quality GaN Film Using an AlN Buffer Layer"**, Applied Physics Letters **48(5), 353**,1986.

[19] R.F. Rutz, **"Ultraviolet Electroluminescence in AlN"**, Appl. Phys. Lett. **28**, pp. 379-381, 1976.

[20] T.L. Tansley. C.P. Folley, **"Optical Band Gap of Indium Nitride"**, J. Appl. Phys. **59**, pp. 3241, 1986.

[21] K. Osamura, K. Nakajima, Y. Murakami, P.H. Shingu, and A. Ohtsuki, **"Fundamental Absorption Edge in GaN, InN and Their Alloys"**, Solid State Commun. **11**, pp. 617-621, 1972.

[22] C. R. Aita, J. Appl. Phys, **53**(3), 1807, 1982.

[23] T. Shiosaki, T. Yamamoto, T. Oda and A. Kawabana, Appl, Phys. Lett. **36(8)**, 643, 1980.

[24] S.V. Krishnaswamy, W.A. Hester, J.R. Szedon and M.H. Francombe, Thin Solid Films **125**, 191, 1985

[25] P. Jonnard, N. Capron, F. Semond, J. Massies, E. Martinez-Guerrero and H. Mariette, Eur. Phys. J. B: Condensed Matter Physics **42**, 351-359 (2004).

[26] Kwiseon Kim, Walter R. L. Lambrecht, and Benjamin Segall, Phys. Rev. B **53**, 16310 (1996).

[27] T. Mattila and Alex Zunger, J. Appl. Phys. 85, 160 (1999).

[28] P.E. Van Camp, V.E. Van Doren and J.T. Devreese, Phys. Rev. B **44**, 9056 (1991).

[29] W.M. Yim and R.J. Paff, J. Appl. Phys. **45**, 1456 (1974).

[30] H. Schultz and K.H. Thiemann, S. S. Commun. **23**, 815 (1977).

[31] G.A. Slack and T.F. McNelly, **“AlN Single Crystal”**, Journal of Crystal Growth 42, 560, 1977.

[32] G.A. Slack and S.F. Bartram, **“Thermal Expansion of Some Diamond-Like Crystals”**, Journal of Applied Physics 46, 89, 1975.

[33] W.M. Yim and R.J. Paff, **“Thermal Expansion of AlN, Sapphire, and Silicon”**, Journal of Applied Physics, V. 45, I. 3, pp. 1456-1457, 1974.

[34] G.A. Slack and T.F. McNelly, **“Growth of High Purity AlN Crystals”**, Journal of Crystal Growth 34, 263, 1976.

[35] Yong-Nian Xu and W. Y. Ching, Phys. Rev. B: Condens. Matter **48**, 4335 (1993).

[36] E. A. Albanesi, W. R. L. Lambrecht, and B. Segall, Phys. Rev. B: Condens. Matter **48,** 17841 (1993).

[37] M. Malachowski, I. R. Kityk, and B. Sahraoui, Phys. Status Solidi B **207**, 405 (1998).

[38] A. P. Dmitriev, N. V. Evlakhov, and A. S. Furman, Fiz. Tekh. Poluprovodn. (St. Petersburg) **30,** 106 (1996).

[39] M. L. Cohen and J. R. Chelicowsky, Electronic Structuresand Optical Properties of Semiconductors (Springer, Berlin, 1998).

[40] V.G. Deibuk, A.V. Voznyi, and M.M. Sletov, **“Band Structure and Spatial Charge Distribution in $Al_xGa_{1-x}N$”**, Semiconductors, Vol. 34, No. 1, 2000, pp. 35–39.

[41] A. V. Dobrynin, M. M. Sletov, and V. V. Smirnov, Zh. Prikl. Spektrosk. **55**, 861 (1991).

[42] S. Bloom, J. Phys. Chem. Solids **32**, 2027 (1971).

[43] M. Schluter, J. R. Chelikowsky, S. G. Lui, *et al.*, Phys. Rev. B: Condens. Matter **12**, 4200 (1975).

# CHAPTER 3

# BACKGROUND OF INDIUM NITRIDE (InN) AND RELATED THIN FILMS

## 3.1 Introduction to Indium Nitride

In recent year, indium nitride (InN) has emerged as a potential material for optical and electronic devices. InN has similar to GaN in many respects. For example, both are III-nitride semiconductors and the thermodynamically stable crystal structure is wurtzite. The cubic zicnblende structure has also been obtained for both GaN and InN by growing thin films on the (001) crystal planes of cubic substrates such as Si and GaAs (Mohadmad & Mokoc, 1996). Figure 3.1a shows the hexagonal wurtzite structure of InN. Each indium atom is coordinated by four nitrogen atoms and vice versa. The lattice parameters of InN and GaN are given in Table 3.1. The hexagonal structure of InN is also evident from the SEM image shown in Fig. 3.1b [1]. InN is predicted to have the lowest effective mass for electron among all the nitride semiconductors [2]. This would result in a high mobility and a high saturation velocity of the electrons [3].

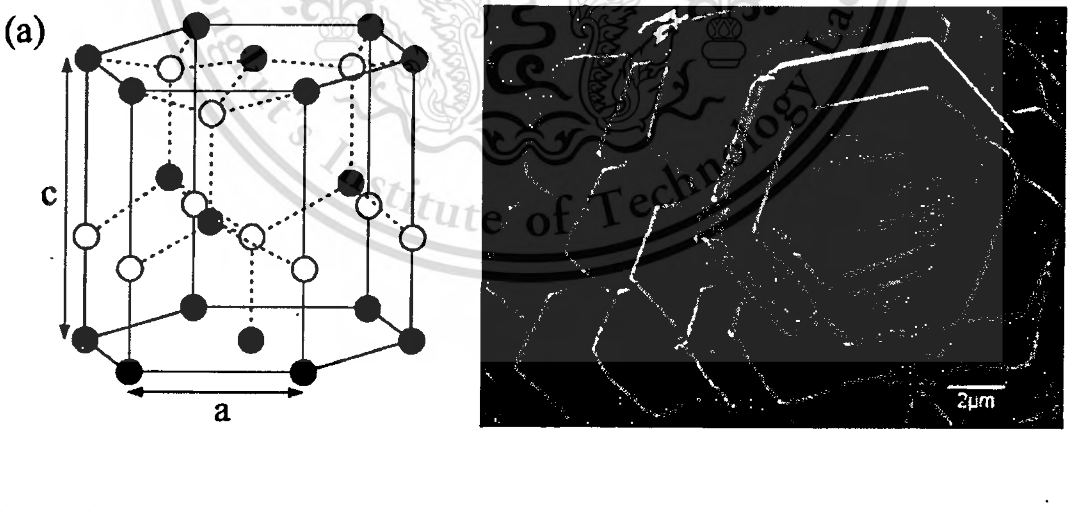

**Fig. 3.1** (a) Schematic illustration showing the lattice structure of InN. The dashed lines show the bonds. (b) SEM image of an InN crystal grain including its hexagonal lattice structure.

Based on Monte Carlo simulations, O'Leary *et al.* (1998) predict that the peak drift velocity at room temperature in InN is $4.3 \times 10^7 cms^{-1}$, which is considerably larger than that of

GaN for which it is estimated to be 3.1x$10^7$ $cms^{-1}$. The electron mobility in InN is also predicted to be much higher than in GaN. Using the variational principle method, Chin *et al.* (1994) have calculated that the maximum room temperature mobility in InN is 4400 $cm^2V^{-1}s^{-1}$ and it is 1000 $cm^2V^{-1}s^{-1}$ in GaN. In fact, the highest mobility measured at room temperature is 2700 $cm^2V^{-1}s^{-1}$ [4]. This value is three times larger than that obtained for GaN which is reported to be 900 $cm^2V^{-1}s^{-1}$ [5]. Thus, it is expected that InN based high speed and high frequency devices should perform better than GaN based devices.

However, compared with the intensively studied GaN, GaInN and other nitride semiconductors, InN, which is also an important component of the III-nitride system, is less studied. This is mainly due to the difficulty in preparing high quality InN epilayer. There is no suitable substrate material for InN. The lattice mismatch between InN and $Al_2O_3$ (001), which is widely used, is about 25%. Even if an AlN or GaN buffer is used, the lattice mismatch between InN and GaN buffer is still more than 10%. Table 3.1 shows physical and electrical properties of InN compared to GaN. The lattice parameters given here are the average value of the data for wurtzite InN given by Mokoc & Mohadmad, 1996.

**Table 3.1** Physical and electrical properties of wurtzite GaN and InN.

| **Parameters** | **GaN** | **InN** | **Unit** | **References** |
|---|---|---|---|---|
| **Lattice constant, $a_0$** | **3.189$^a$** | **3.55$^a$** | **Å** | **$^a$Mohammad & Morkoç (1996)** |
| **Lattice constant, $c_0$** | **5.185$^a$** | **5.78$^a$** | **Å** | **and references therein** |
| **Effective mass** | **0.20$^a$** | **0.11$^a$** | **$m_0$** | **$^b$Chin *et al.* (1994)** |
| **Mobility** | | | | **$^c$Binari & Dietrich (1997)** |
| **Theoretical** | **1000$^b$** | **4400$^b$** | **$cm^2V^{-1}s^{-1}$** | **$^d$Tansley & Foley (1984)** |
| **Experimental** | **900$^c$** | **2700$^d$** | **$cm^2V^{-1}s^{-1}$** | **$^e$O'Leary *et al.* (1998)** |
| **Peak drift velocity** | **3.1$^e$** | **4.3$^e$** | **$10^7$ $cms^{-1}$** | **$^f$Maruska & Tietjen(1969)** |
| **Band gap** | **3.39$^f$** | **1.89$^g$** | **eV** | **$^g$Tansley & Foley (1986*b*)** |
| | | **1.55$^h$** | **eV** | **$^h$Butcher *et al.* (2005)** |
| | | **0.9$^i$** | **eV** | **$^i$Davydov *et al.* (2002*b*)** |
| | | **0.7$^j$** | **eV** | **$^j$Wu *et al.* (2002)** |

The early measurements of the electronic band gap of InN gave 1.89 eV [6] which was long accepted as the nominal value. Consequently, InN has been proposed to be a top cell material for a two-junction tandem solar cell [7]. The combination of 1.98 eV for InN and 1.1 eV for Si would give a conversion efficiency of over 30%.

Recently, there have been reports suggesting the electronic band gap of InN material may be lower around, 0.7-1.0 eV [8-10]. This is very interesting since the newly reported band gap values are compatible with the wavelength of optical fiber [3]. If a low value around 0.7 eV is confirmed, InN might be used to fabricate high speed laser diodes and photodiodes in optical and infrared communication system. It is further suggested that the ternary compound $In_{1-x}Ga_xN$ $(0 \leq x \leq 1)$ may be tuned by changing x to cover the whole of the visible spectrum [8], from infrared to deep ultraviolet. This is schematically illustrated in Fig. 3.2. This would allow the manufacture of light emitting diodes which emit all colors of the visible spectrum. Importantly, this compound would also be suitable for new types of photovoltaic cells. In fact, solar cells made of multilayer of this material are expected to provide high conversion efficiency. Indium (In) and gallium (Ga) used in solar cells are much less toxic than arsenic (As) used in Ga-As based solar cells.

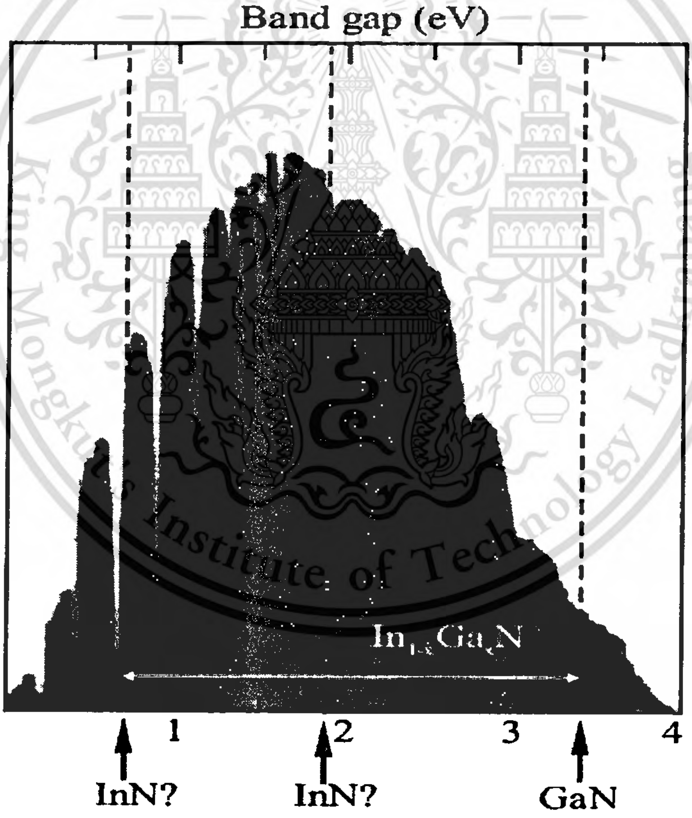

**Fig. 3.2** Solar spectrum and the electronic band gap of GaN and illustrating band gap debate for InN.

Due to the large and diverse spectrum of possible applications of InN, the correct band gap assignment for InN is the focus of much current research and debate.

## 3.2 The Growth of InN

The growth technology of InN is the least developed of the group III nitrides and compound is thus the least understood. Stoichiometry is one of the key issues: thermal dissociation of the equilibrium binary compound becomes significant about 550 °C and there is strong circumstantial evidence, currently without unequivocal proof, that nitrogen vacancies provide shallow donor centres leading to high electron concentration. Good crystallinity in thin film materials requires sufficient adatom mobility during growth for lattice sites to adopt their preferred species. The particularly acute conflict in the case of InN is between growth temperatures low enough to avoid dissociation, yet high enough for crystalline evolution. There is a clear correlation in the literature between lower electron concentrations and higher mobilities in films of imperfect crystallinity, and, in better crystals, concentrations around $10^{20}$ $cm^{-3}$ with commensurately low mobility.

Another difficulty in growing InN is the low dissociation temperature of InN as well as the high equilibrium $N_2$ pressure over the InN film. Therefore, the preparation of InN requires a low growth temperature. Meanwhile, for common III-nitride epitaxy techniques, such as OMVPE and MBE, low growth temperature means a short surface migration distance of group-III atoms. That is, many group-III atoms will have less energy to travel long enough on the growing surface to locate their minimum energy sites before they react with N to form small less-mobile nitride islands. As a result, InN film with high density defects will form.

### 3.2.1 Growth Techniques of InN Films

The growth of InN thin film has been studied since 1970's. Hovel and Cuomo grew InN films by RF-sputtering. The resulting films were reported to be wurtzite polycrystalline. In the 1980's extensive work on InN was carried out by Transley and Foley. Using RF-sputtering, they produced polycrystalline InN films with the highest mobility and the lowest background carrier concentration reported to date. Their material was said to show room temperature Hall mobility more than 2700 $cm^2V^{-1}s^{-1}$ with $5.3x10^{16}$ $cm^3$. The progress in epitaxial film growth has been slow due to the low dissociation temperature of InN (~550°C), the steep rise of the equilibrium $N_2$

pressure with growth temperature and the poor pyrolysis efficiency of the $NH_3$ reactant at low growth temperatures [11].

The growth of InN using MOVPE was pioneered by Wakahara and Yoshida (1989). The films were grown on sapphire ($Al_2O_3$) substrates in the temperature range of 400-600°C. The quality of the films was improved by nitridation of the substrate surface before growth [12-13]. This may be as a result of the formation of AlN, since the lattice mismatch is reduced from 25 % for InN and $\alpha$-$Al_2O_3$ to 13% for InN and AlN.

The growth of InN with MBE only began in the early 1990's following the successful development of this technique for the growth of GaN. The films has been improved with various approaches such as the use of AlN [14], InN [15] and GaN [16] buffer layer between film and substrate. It may be speculated that the improvement in film quality is related to the reduced lattice mismatch. The lattice mismatch between InN and GaN is about 10%. Lu *et al.* (2001) have shown that the electrical and structural properties of InN films improve with the thickness of the AlN buffer layer. The mechanism for the improvement has not been explained, but it is speculated that the quality of the AlN buffer improves with thickness, with then provide a better foundation for the InN film.

Figure 3.3(a) and Figure 3.3(b) show several measurements of electron mobility and carrier concentration in InN films from growth techniques. All the films were grown un-doped. It is clear from the figure that the quality of InN films, in the term of electron transport, has significantly improved over the last few years with an increase in the electron mobility and a decrease in the carrier concentration. However, the highest mobility and lowest background carrier concentration has been measured for the material grown 20 years ago by RF-sputtering. Lately the MBE-grown films have shown significant improvements, with mobilities close to the highest value reported.

Therefore, in order to test the theoretical predications are provided guidance for device design, there is an urgent need to synthesis high quality InN to extract or verify its fundamental parameters.

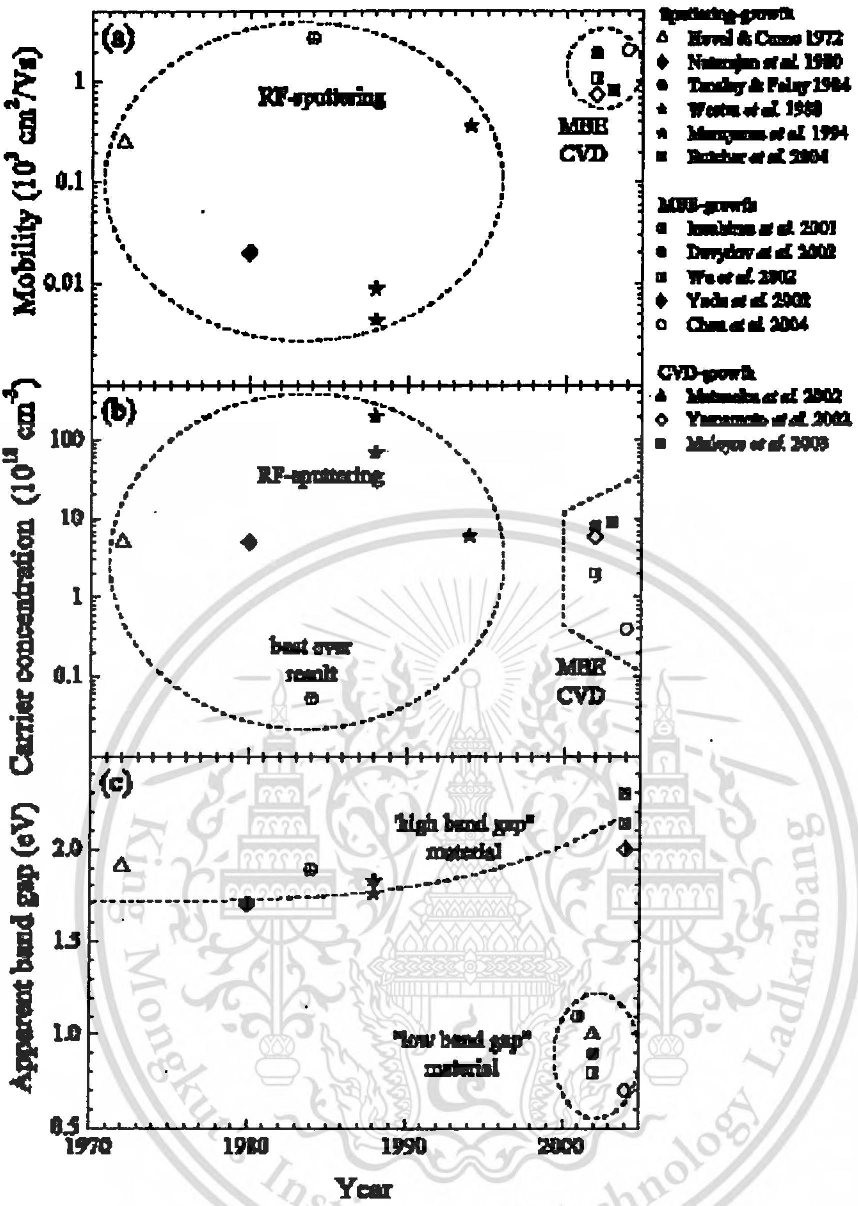

**Fig. 3.3** Electron mobility, carrier concentration and electronic band gap measurements for InN films. Dashed curves are for illustration.

### 3.2.2 Radio Frequency Reactive Sputtering

Radio frequency reactive sputtering (RF-sputtering) is a relatively simple growth technique. It is widely studied growth technique for InN thin films, see for example Hovel & Cuomo (1972), Foley (1984), Tansley & Foley (1984, 1986*b*) and Butcher *et al.* (2004). Importantly, film growth typically occurs at low temperature, below 100°C, which is important for the growth of InN films. Low temperature growth allows the use of substrates other than temperature resistant materials such as sapphire. These alternative substrates, including glass and

Si, are less-expensive. Hence, the growth of InN films using the RF-sputtering technique is relatively cost-effective. InN film in Fig. 3.4 was grown by Butcher *et al.* (2004). Columnar structures are clearly visible suggesting polycrystalline materials were obtained for RF-sputtering growth techniq

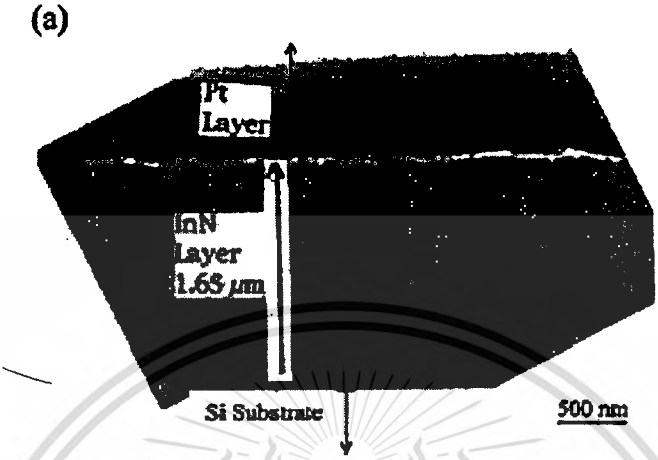

**Fig. 3.4** A typical transmission electron microscope image of a film grown by RF-sputtering.

For the RF-sputtering InN films studied in this thesis were grown with a new technique developed in our laboratory called "reactive gas-timing" which is difference from the other researchers such as Tansley and Foley (1984, 1986b), Motlan *et al.* (2002) and Butcher *et al.* (2004). The films growth technique detail is described in experiments. Briefly, thin films are grown by sputtering a metallic indium (99.999% In) target with energetic ions from argon and nitrogen plasma which are controlled timing of flow rates inflected to the chamber. The r.f. source was operated at a frequency of 13.56 MHz. The films were grown on glass slides cleaned with PIRANHA process. In this research, no substrate heating were used, however, the substrate temperature may have been as high as 60°C due to plasma heating.

### 3.2.3 Metal Organic Chemical Vapor Deposition

Metal Organic Chemical Vapor Deposition (MOCVD) is a common method of growing high quality GaN films. In this growth technique, the films are deposited by chemical reactions occurring between the precursors. In the case of InN, trimethyllindium (TMIn) and $NH_3$ are used as precursors of indium and nitrogen, respectively. Nitrogen is used as the carrier gas for the TMIn. When these precursor gases come into contact with a heated substrate, they decompose and react to form InN on the substrate.

Both the substrate temperature and the ratio of the precursor flow rates (V/III) are critical to film quality. At high temperature the decomposition rate of $NH_3$ increases, however, this also results in the decomposition or thermal etching of the already grown InN film. Alternatively, growth at a temperature below 400°C can result in the formation of metallic indium droplets due to the shortage of reactive nitrogen as the decomposition rate of $NH_3$ is low at such a low temperature [3]. Moreover, growth below 550°C has been found to produce columnar structures. Two-dimensional growth has been achieved for a growth temperature higher than 600°C [17]. Importantly, an increase in mobility and a reduction in carrier concentration have been reported. Growth temperatures in the range of 500-600°C have been suggested as suitable for the growth of InN [3].

For low temperature growth, formation of indium droplets has been reported for V/III ratio $<1.63\text{x}10^4$ [18]. The number of indium droplets was shown to decrease with this ratio increasing, and for a V/III ratio $>1.63\text{x}10^5$ no droplets was observed. For film growth temperature above 650°C, a low V/III ratio is suggested due to enhanced decomposition of $NH_3$. Importantly, an increase in the $NH_3$ decomposition rate also increases the $H_2$ partial pressure, which prevents the film growth [19].

### 3.2.4 Remote Plasma Enhanced Chemical Vapor Deposition

Remote Plasma Enhanced Chemical Vapor Deposition (RPECVD) is an improved version of CVD in which reactive nitrogen radicals are produced by plasma dissociation independent of the growth temperature. This allows the low temperature growth of InN. TMIn and neutral nitrogen plasma species were used as indium and nitrogen precursors, respectively. $N_2$ was used as the carrier gas for the TMIn. TMIn is introduced to the substrate through a shower head above the substrate holder. The substrate is heated to a desired temperature by a heater attached to the substrate holder. The growth of InN occurs because of reactions between thermally decomposed. TMIn and nitrogen radicals produced in the nitrogen plasma. The plasma itself is generated by 2.45 GHz microwaves. The plasma is produced away from the substrate so that high energy ions, which are also generated in the plasma, do not reach the substrate. Hence, the substrate and the grown film are protected from possible ion-induced damage. This is the advantage of RPECVD over plasma enhanced CVD growth. A typical SEM image of a film grown by RPECVD is shown in Fig. 3.5 [20].

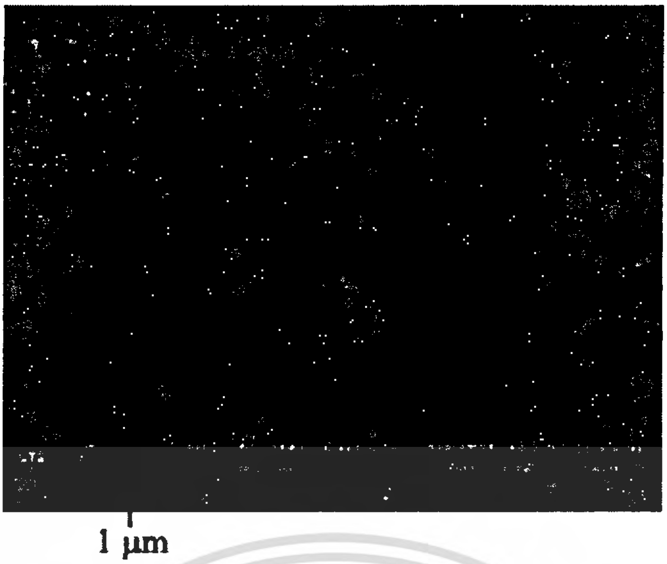

**Fig. 3.5** A typical SEM image of a film grown by RPECVD

### 3.2.5 Molecular Beam Epitaxy

Molecular Beam Epitaxy (MBE) growth of InN, indium and nitrogen, in the form of molecular beams, are deposited on a substrate heated to a desired temperature. In gas-source MBE, a solid source is used for indium, whereas a gas source for nitrogen, typically, $N_2$ or $NH_3$. In contrast, a metal organic chemical beam is used as a source of indium in metal organic MBE (MOMBE). In both types of MBE-growth, the dissociation of the nitrogen source is a major issue, since the dissociation energy of $N_2$ molecular is relatively high (9.5 eV). Reactive atomic nitrogen is generally obtained by applying radio-frequency to dissociate $N_2$ molecules. Alternatively, reactive nitrogen can be obtained by electron cyclotron resonance (ERC) microwave plasma source. However, the energetic ions generated in the plasma can produce damage in the films. Oxygen and carbon contaminations are other issues associated with the plasma. The use of electric or magnetic fields has been used attempted to reduce the ion induced damage [21]. In case of ECR source, the damage can be reduced by operating the plasma at a low power, however, it results in a lower growth rate [2].

Growth temperatures in the range of 450-550°C are suggested to be suitable for the growth of InN by MBE [3]. It is reported that the growth rate of InN above this temperature range is very low, or that film growth may not occur at all due to the dissociation of the film. Film growth below this temperature range results in poor quality films. Studies have shown that the crystal quality and electric properties of InN films improve with growth temperature [22, 23]. Lu *et al.* have reported that a growth temperature of ~500°C is optimum to achieve good quality films.

Figure 3.6 shows X-ray diffraction spectra for films from RF-sputtering, RPE-CVD, MBE and MOCVD studied by Butcher *et al.* (2002), Lu *et al.* (2003), Bhuiyan *et al.* (2003) and Maleyre *et al.* (2004), respectively. In all cases the (002) and the (004) reflections are clearly evident confirming the hexagonal wurtzite structure of InN films. The dominance of the (002) reflection indicates that the c-axis of the hexagonal InN structure is perpendicular to the substrate.

In the case of the film grown by MOCVD, in addition to the peaks corresponding to InN, a peak due to metallic indium is also evident; see Fig. 3.6 (d). Moreover, a split in the (002) reflection can be observed (see inset). This may suggest strain in the InN lattice, possibly due to the inclusion of indium clusters in the film. In all cases a strong reflection from the (002) plane is observed indicating the wurtzite structure of InN films. In (d) a metallic indium signal and a split in the InN peak are evident which is also shown in the inset.

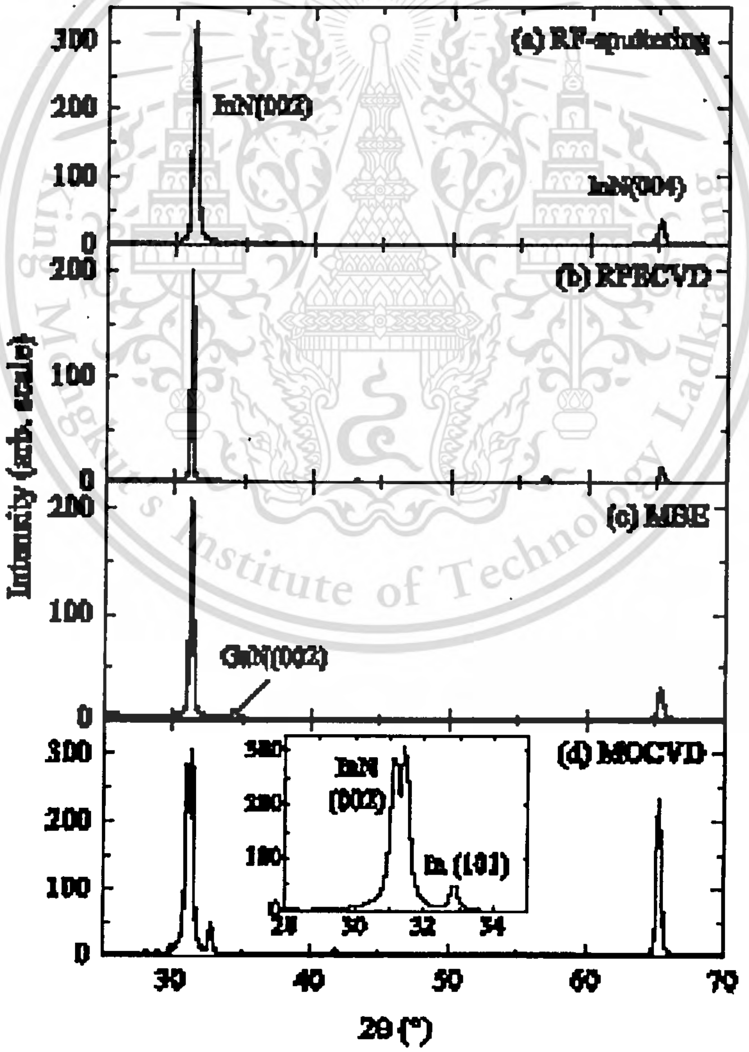

**Fig. 3.6** Typical X-ray diffraction spectra for InN films grown by difference techniques.

## 3.3 The Properties of Indium Nitride

### 3.3.1 Crystal Structure of InN

InN normally crystallizes in the wurtzite (hexagonal) structure. The zincblende (cubic) form has been reported to occur in films containing both polytypes. Due to absence of good-quality single crystal films, the crystal structure of InN has been measured mainly in non-ideal thin films, particularly the ordered polycrystalline films with crystallites in the range of 50-500 nm. The end results of the measurement indicate that, although InN normally crystallizes in the wurtzite structure, occasionally it also crystallizes in the zincblende (cubic) polytype. Table 3.2 lists values of the basal-plane and out-of-basal-plane lattice constants, $a_0$ and $c_0$, deduced from a series of experiments as well as other basic properties.

**Table 3.2** The basal plane and perpendicular-axis lattice constants along with other basic parameters of InN.

| **Wurtzite polytype of InN** | |
|---|---|
| Bandgap energy | $E_g(300\ K) = 1.89$ eV |
| Temperature coefficientt | $dE_g/dT = -1.80\times10^{-4}$ eV/K |
| Lattice constant | a = 3.548 Å, c = 5.760 Å |
| Index of refraction | n = 2.80-3.05 |
| Dielectric constant | $\varepsilon_r=15.3$, $\varepsilon_\infty=8.4$ |
| **Zincblende polytype of InN** | |
| Bandgap energy | $E_g(300\ K) = 2.2$ eV; theory |
| Lattice constant | a = 4.98 Å |

The value of $c_0/a_0$ data from various measurements is about 1.615 ± 0.008. This is close to the more optimistic value of 1.633 determined from layers specially grown under significant precautions, best possible growth conditions, and presumably with reduced nitrogen vacancies. An examination of the tabulated data indicates an unacceptably large scatter. This may possibly be due to nitrogen deficiency, since nitrogen atoms are closely packed in (0001) planes. While the cubic polytype of InN yields a molecular cell volume of 30.9 Å$^3$, the hexagonal polytype gives a molecular cell volume of 31.2 ± 0.2 Å$^3$.

### 3.3.2 Mechanical and Thermal Properties of InN

The experimental density of InN deduced from Archimedean-displacement measurements is 6.89 g/cm$^3$ at 25 °C. This is comparable to 6.81 g/cm$^3$ estimated from X-ray data. The bulk modulus determined from first-principles calculations by a local-density approximation method and by the linear muffin-tin orbital method is B = 165 GPa. In a hexagonal structure, the second-order elastic moduli are $C_{11}$, $C_{12}$, $C_{13}$, $C_{33}$, and $C_{44}$, but there are no reports of these parameters yet. Since these figures depend on the lattice constants which are within some 10%, values of other nitrides can be used as a first approximation when absolutely needed. InN has twelve photon modes at the zone centre (symmetry group: $C_{6V}$), three acoustic and nine optical ones with acoustic branches near zero at k = 0. The infrared active modes are of the $E_1$ (LO), $E_1$(TO), $A_1$(LO), and $A_1$(TO) type. Moreover, a transverse optical mode has been observed at 478 cm$^{-1}$ (59.3 meV) by reflectance and 460 cm$^{-1}$ (57.1 meV) by transmission measurements.

The linear thermal expansion coefficients measured at five different temperatures between 190 K and 560 K, indicate that both along the parallel and perpendicular directions to the c axis of InN these coefficients increase with increasing temperature. Deriving thermal conductivity data from the Leibfried-Schloman scaling parameter and assuming that the thermal conductivity is limited by intrinsic photon-photon scattering, the thermal conductivity is about 0.80 ± 0.20 Wcm$^{-1}$ K$^{-1}$. While the heat capacity of InN is (9.1 ±2.9) 10$^{-3}$ (cal/mol K) at temperatures between 298 and 1273 K, the entropy is 10.4 cal/(mol K) at 298.15 K. The equilibrium partial pressure of $N_2$ above InN is about 1 atm at 800 K, and it increases exponentially with temperature to 105 atm at 1100 K.

### 3.3.3 Electrical Properties of InN

It is fair to state that no reliable experimental data for the electron mobility in InN have yet to be obtained. InN suffers from the lack of a suitable substrate material and the atomic radii of In and N is an additional contributing factor to the difficulty to obtain InN of good quality. As a result, nitrogen vacancies are thought to lead to large background electron concentrations in InN. Because of all these factors, the electron mobility obtained from various films have varied very widely. The electron mobility in InN can be as high as 3000 cm$^2$/Vs at room temperature. A recent study of the electron mobility of InN as a function of the growth temperature indicates that the mobility of Ultra-High-Electron Cyclotron Resonance-Radio-Frequency Magnetron

Sputtering (UHV-ECR-RMS) grown InN can be as much as much as four times the mobility of conventionally grown (vacuum deposition) InN.

### 3.3.4 Optical Properties of InN

Recently, the value of the optical band gap energy $E_g$ for InN has come under intense reinvestigation due to a disagreement between the generally accepted value of 1.9 eV [24-26] and recently reported values in the range of 0.7–1.1 eV [27-29]. The higher values of $E_g$ (1.8-2.1 eV) have been determined from optical absorption spectra on polycrystalline or (002)-textured InN thin films deposited by reactive sputtering techniques. Band-edge photoluminescence peaks with energies ranging from 1.81 to 2.15 eV have also been observed for InN films grown on Si substrates by molecular beam epitaxy (MBE). On the other hand, optical absorption and photoluminescence measurements on high-quality InN thin films gown on (001) sapphire substrates by MBE and MOVPE have revealed the lower $E_g$ values (0.7-1.0 eV). Thus, the lower reported band gap values (< 1 eV) are thought to be associated with improvements in the thin film fabrication techniques leading to higher quality InN films with relatively less disorder, and are more consistent with values predicted by theoretical calculations.

It is well known that first-principles density-functional calculations using the local density approximation (LDA) typically understimate the band gaps of materials. Although the generalized gradient approximation (GGA) has been found to give a better description of many properties connected with the total energies of atoms and solids, the GGA does not any significant improvement in the calculation of band gap energies. For example, the calculation band gaps in the LDA (GGA) are 24% (32%) and 47% (55%) smaller than the measured gaps for AlN and GaN, respectively. Moreover, InN is found to be metallic in both the LDA and GGA with respective band gaps of –0.3 eV and –0.4 eV. However, a full GW calculation using a dielectric matrix calculated in the random-phase approximation has been shown to correct underestimations in the band gap calculated from the LDA and GGA. Likewise, a GW calculation using a good model dielectric function is just as satisfactory for many materials. Such a model dielectric function calculation has led to good agreement between the corrected and experimental band gap values for AlN and GaN. For wurzite InN, a calculation using the GW approach with a recent model dielectric function results in a corrected band gap of 0.8-0.9 eV. Although this result agrees with the lower experimental values for $E_g$, there is some uncertainty in this calculation due to difficulties in properly accounting for the pd repulsion arising from In 4d electrons in LDA-based calculations such as this one.

The correct value of the band gap for this material is crucial, as the usefulness of InN for a particular application depends sensitively upon it. The reasons for the observed variation in the apparent band gap are not well understood. Several possibilities are suggested, of which the important ones are discussed below.

### 3.3.5 The Possibility Suggestions

#### 3.3.5.1 Moss-Burstein Effect

A Moss-Burstein effect occurs when carrier concentrations are such that electrons partly fill the conduction band. As a result the band gap, when measured by optical absorption spectroscopy, is overestimated due to the additional energy required to excite electrons from the top of the valence band to the Fermi level within the conduction band. This effect was first observed for InN by Trinor & Rose (1974) and later it was studied in detail by Tansley & Foley (1986*b*) for film grown by RF-sputtering. The increase in the absorption edge was empirically described as

$$E_g^{(m)} = E_g + 2.1\times10^{-8} n^{1/3} eV \qquad (3.1)$$

where $E_g^{(m)}$ is the measured apparent band gap and $n$ is the carrier concentration in $cm^{-3}$.

This formulation is based on the assumption that the correct value of the band gap energy is $E_g$ = 1.89 eV. This equation suggests a significant shift of the observed band gap value for material with carrier concentrations higher than $10^9$ $cm^{-3}$.

Figure 3.7 shows the apparent band gap as a function of carrier concentration for InN films grown by different techniques. The solid curve represents the expected value greater than 1.9 eV, however, it can not explain the observed lower values around 0.7 eV. Recently Walukiewicz *et al.* (2004) have attempted to describe the differences in the measured band gap with an alternate model. This is shown by the dashed curve in Fig. 3.7. It is evident that this model cannot explain those data point below $10^{19}$ $cm^{-3}$ which have high band gap values around 2 eV. This suggests that other effects might be important.

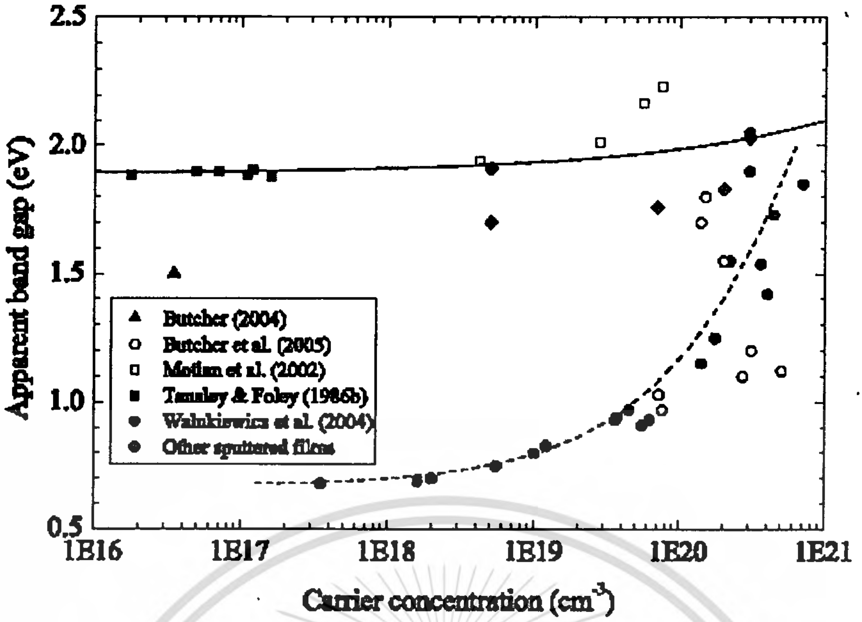

Fig. 3.7 Apparent band gap of InN films as a function of carrier concentration.

The solid and the dashed curves in Fig. 3.7 represent the theoretical Moss-Burstein effects suggested by Tansley and Foley (1986*b*) and Walukiewicz *et al.* (2004), respectively. The other sputtered films are from Hovel & Cuomo (1072). Trainer & Rose (1974), Natarajan *et al.* (1980) and Westra *et al.* (1988).

#### 3.3.5.2 The Role of Oxygen

The band gap values around 2 eV observed for the polycrystalline material, as obtained primarily from RF-sputtering, are also suggested to be possibly due to high oxygen incorporation in these types of films [30, 31]. It has been proposed that the high oxygen incorporation in these sputtered films leads to the formation of an InN-$In_2O_3$ alloy. Such as alloy could have a higher band gap than the value for InN. This is because of the high band gap value of $In_2O_3$ which is 3.75 eV [32].

Figure 3.8 shows Vegard's diagram for the InN-$In_2O_3$ alloy system. The solid lines represent the expected increase of the band gap energy of InN with oxygen content assuming an InN-$In_2O_3$ alloy system. It can be derived that an oxygen content of 39 at.% (43%$In_2O_3$) is required to increase the band gap from 0.7 eV to 2 eV. Alternatively, only 8 at.% oxygen (6% $In_2O_3$) is required to increase the band gap from 1.89 eV to 2 eV. Both cases are indicated by dashed lines in Fig. 3.8. Some preliminary measurements of oxygen content of InN exist, however, no accurate quantification has been carried out in a comprehensive fashion for InN films from the important growth techniques.

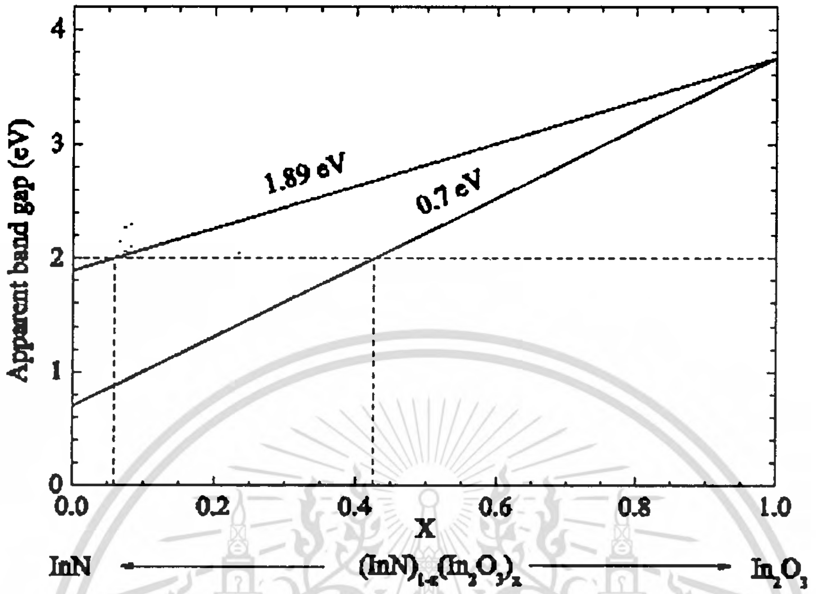

Fig. 3.8 Vegard's diagram for an InN-$In_2O_3$ alloy system.

The expected increase in the band gap with oxygen alloying is shown assuming the band gap of InN to be 0.7 eV or 1.89 eV. The two vertical dashed lines indicate the compositions of a hypothetical InN-$In_2O_3$ alloy, for which the band gap is 2 eV, assuming the band gap of InN to be 0.7 eV or 1.89 eV, respectively.

### 3.3.5.3 Mie-Resonance

The presence of metallic indium in InN films is suggested to obscure band gap measurements with optical absorption spectroscopy. In a recent paper by Shubina *et al.* (2004) it was proposed that photoluminescence emission at 0.7-0.8 eV from films grown by MOCVD and MBE, may be due to Mie scattering from metallic indium clusters in the films. These clusters can form during film growth, which is particularly likely when a film is grown above 500 °C (Shubina *et al.* 2004). Importantly, the energy value of the absorption edge was shown to decrease with the amount of indium clusters in the film. For a film without such clusters, an absorption edge near 1.4 eV was reported.

The presence of metallic indium clusters in an InN film would suggest that the film is indium-rich, reducing the value of the nitrogen-to-indium ratio $\eta$ below unity. Additionally, the possibility of metallic indium inclusions has been investigated at the microscopic level with Perturbed Angular Correlation (PAC). The observed variation in the electronic and optical properties of InN films produced by different growth techniques may suggest that their microscopic structure is different. Local microscopic structure can be probed using hyperfine interactions methods. PAC spectroscopy is a suitable technique to study local structure as well as defects and annealing behavior at the atomic scale. For PAC spectroscopy a radioisotope is introduced into a host material as a probe which is sensitive to the local electric field gradients or magnetic fields. The directional correlation of the probe's emitted radiation can then be defected which may provide information about local electromagnetic fields in the immediate vicinity of the probe nucleus.

#### 3.3.5.4 Quantum Size Effects

It has been suggested in a report of a lower InN band-gap that the observed higher band-gaps may result from quantum size effects related to polycrystallinity. This suggestion remains open, although there has been no instance where the presence of quantum size effects has been positively identified in InN thin films. Lan *et al.* produced CVD grown InN-based nanorods and observed that with rod diameters of 30–50 nm the InN was brown with 1.9 eV photoluminescence (PL) being evident, whereas nanorods of more than 50 nm diameter were observed to be black with 0.77 eV photoluminescence. Great care must, however, be used in interpreting these results solely in terms of quantum confinement effects. Undefined differences in growth temperature existed between the two materials (the brown nanorods being grown at lower temperature) and the impurity concentrations in both types of material (as determined by X-ray diffraction) were large. A chemical origin for the observations of Lan et al. cannot therefore be excluded. It is instructive that a discrete change from 0.77 to 1.9 eV PL was observed and that a continuous change in PL energy, as might be expected in a situation where quantum confinement is evident, was not observed as the rod diameters shrank.

Other groups have ~0.7 V PL in polycrystalline material. Anderson *et al.* grew polycrystalline InN with ~0.8 eV luminescent present but did not identify the size of polycrystalline grains; similarly, Kuball *et al.* observed ~0.85 eV PL from polycrystalline RPECVD grown InN, while, as shown in Fig. 3.9 a weak room temperature ~0.7 eV PL emission has been observed for a polycrystalline RF sputtered InN sample with a band-gap, measured by absorption techniques, of 1.9 eV. It has also recently been shown that for polycrystalline samples (with crystal grain diameters of ~100nm) that a large variation in band-gap could be achieved, for material containing less than 1% oxygen concentration, through a variation in In:N ratio. Finally, Cimalla *et al.* have calculated only a 0.03 eV shift for a 20 nm InN film, which would exclude the presence of a strong quantum size effect for almost all thick sputtered films, since grains tend to be larger then 20 nm, and in thin epitaxial layers. While these results do not exclude the possibility of quantum size effects, they certainly indicate that other mechanisms are probably considerably more important.

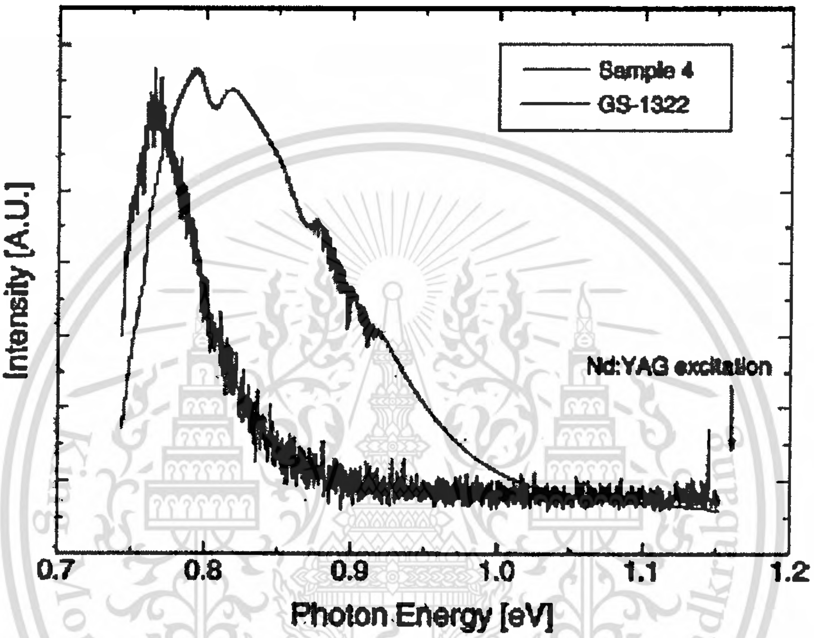

**Fig. 3.9** Room temperature photoluminescence spectra for an older Cornell MBE sample (GS-1322) and for an RF sputtered InN sample.

The spectral intensities have been normalised for comparison (the intensity for the RF sputtered sample being much less). Both spectra are clipped at the lower energy side due to the response of the Ge detector used.

The properties of genuine InN quantum dots differ from those observed in InN films, and much smaller dimensions than those typical of the grain size of polycrystalline material have been achieved. The possibility of InN quantum dot formation in InGaN layers has had a long and controversial history of its own that need not be addressed here. The first intentional growth of InN quantum dots has only recently been reported but no quantum confinement effects have yet been identified. For high indium content intentionally grown InGaN quantum dots, however, quantum confinement has been evident through blue shifted PL emission. In that case the dot height was 1.2 nm, much smaller than the grain sizes typical of sputtered InN.

### 3.3.6 As-Grown Indium Nitride

Except for one report of p-type material, as-grown InN has high n-type carrier concentrations resulting from native defects [3]. This has widely been attributed to nitrogen vacancies in the InN lattice [33]. Other possible sources are oxygen atoms on nitrogen sites or silicon atoms on indium sites [34] or the hydrogen incorporation into the film [35-36].

The existence of nitrogen vacancies in InN suggests that material may be nitrogen-poor with the nitrogen-to-indium ratio $\eta < 1$. In the present study, this proposition has been tested with measurements of the nitrogen-to-indium ratio of InN films from different growth techniques. Additionally, the possibility of defects at the microscopic level has been investigated with the PAC method.

### 3.3.7 Implantation and Annealing Study

Future devices based on InN will require the availability of both n-type and p-type material. In the case of GaN, p-type material has been obtained by doping Mg as an acceptor impurity during growth, followed by low-energy electron-beam irradiation [37], or by thermal annealing of the film in a $N_2$-ambient at a temperature above 700 °C [38]. In general, p-type characteristic is often achieved by introducing dopants using ion implantation. Ion implantation is also widely employed in device processing, for example to provide electrical isolation between layers.

When an energetic projectile ion penetrates a material, it deposits its energy in the material. The deposited energy can result in the displacement of lattice atoms. Both the ion and the displaced atoms can continue their motion and create a damage cascade. Hence, the original crystal lattice structure of the material will be perturbed to a disordered state. If the implanted dose of the incident ions is sufficiently large, complete amorphization of the material can occur. High temperature annealing can remove the lattice defects and thus is an important processing tool. Although both ion implantation and annealing will be important for future device procession of InN, only limited information is available.

### 3.3.8 Optical Data for Nanostructured InN

Optical data for InN nanostructures present an interesting reference to the discussion of the bandgap of the bulk InN semiconductor, since specific energy shifts compared to the bulk case are expected, due to confinement of electrons. InN quantum dots (QDs) of nanometer dimensions have been prepared by MOCVD growth [39, 40]. An example of a PL spectrum for such structures is shown in Fig. 10, where the PL from a QD sample is compared with an ordinary MOCVD grown InN film [41]. Two observations are interesting here. The bulk InN film shows a PL peak at about 0.76 eV, often observed in the case of an electron concentration of about 1 x$10^{19}$ cm$^{-3}$, as was the case here. The QD structure has an emission substantially upshifted in energy, peaking at about 0.95 eV (Fig. 3.10). Also, this QD PL is much more temperature stable than the bulk spectrum. Although it is not clear whether the QDs have a similar electron density to that of the bulk layer, these data support the observation of a confinement induced shift to higher energies in the QD structure. This means that the bulk InN bandgap of about 0.7 eV would be consistent with these observations.

InN quantum rods have also been reported recently [42]. They may be grown by an Au catalyst CVD technique, with diameters 30–100 nm. Apparently two different species of rod ensembles may be produced: "brown" InN rods with a broad PL band about 2.0 eV and no observed IR PL, and "black" InN rods with an IR PL band at 0.77 eV at 20 K. The latter would again be consistent with a bulk InN PL spectrum for a shallow donor doping density of about 1 x$10^{19}$ cm$^{-3}$; indeed the large diameters of these rods would make the properties bulk-like. The reason for the quite different optical properties of the "brown" rod ensembles is so far unclear.

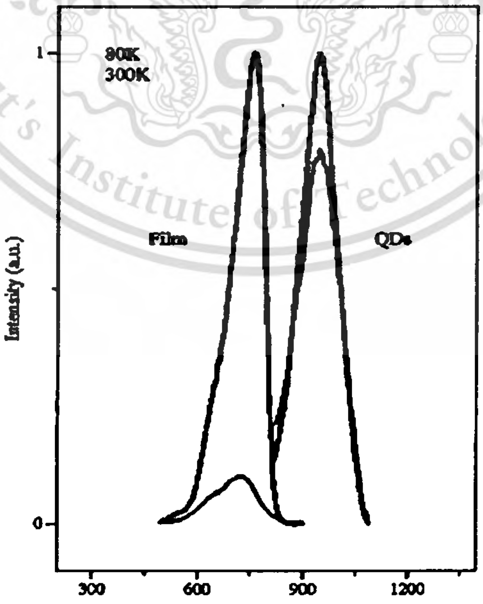

**Fig. 3.10** Photoluminescence spectra obtained for an MOCVD grown InN quantum dot sample, compared with the corresponding data an ordinary InN film, at two different temperatures.

The strong upshift in the peak position for the QD sample is suggested to be partly due to quantum confinement.

### 3.4 The Quality and Reproducibility of InN

Accurate information on the stoichiometry of gas-grown InN and the amount of impurity contaminations is limited. What are acceptable levels of impurities and defects in InN films will be determined by specific future device applications. At this stage little is known about the minimum concentrations possibly achievable for oxygen and other impurities. Compositional analysis is often performed with sputter depth profiling techniques such as Secondary Ion Mass Spectrometry (SIMS), or X-ray Photoelectron Spectroscopy (XPS) which are, however, reliant on calibration samples.

Studies of Maruyama and Morishita (1994) [43] have shown that the composition of InN films grown by RF-sputtering can be sensitive to the growth conditions (temperature, RF power and total pressure). Interestingly, for all the films analyzed the nitrogen-to-indium ratio $\eta$ was always less than unity indicating indium-rich material was obtained. Motlan *et al.* (2002) [44] it can be calculated that the nitrogen-to-indium ratio $\eta$ of films from a non-nitrided target was as low as 0.36. This ratio increased with target nitridation to the maximum value of $\eta = 0.73$, again indicating that all the films were highly indium-rich. It should be noted, however, that in both of the above cases the composition was measured with XPS, a technique which can only provide qualitative information on the elemental composition. The determination of the composition relies on correct calibration, which is difficult for InN due to the lack of standard samples.

Kumar *et al.* (1996) [45] have compared the composition of films grown by RF-sputtering as obtained with XPS and Rutherford Backscattering Spectroscopy (RBS). Significantly different values have been obtained. The authors argue that XPS underestimates the nitrogen-to-indium ratio $\eta$ due to preferential sputtering of the N atoms by the $Ar^+$ ion gun used for the sputter cleaning and depth profiling of the sample. It may be also possibly due to the redeposition of the sputtered indium on the sample surface. Hence, RBS was suggested to be a better used by Yoshimoto *et al.* (2003*a*) [46] to measure the composition of a film grown by MBE. Both of the above two studies suggested that the films were non-stoichiometric ($\eta \neq 1$) and that the films had oxygen contamination. Kumar *et al.* (1996) [45] reported the film to be nitrogen-rich ($\eta = 1.1$), whereas the film analyzed by Yoshimoto *et al.* (2003a) [46] was measured to be indium-rich with $\eta = 0.9$.

Figure 3.11 shows simulated 4 MeV $^4$He RBS spectra for InN films grown on silicon and sapphire substrates. For the simulation, stoichiometric InN ($\eta$ = 1) with carbon and oxygen impurities assumed to be at the 5% level, has been used. The simulation has been performed using the program SIMNRA (Mayer 1997) [47]. The calculation for the 300 nm film grown on silicon (Fig. 3.11*a*) shows that the carbon, nitrogen and oxygen signals are fairly separated, though these signals are obscured by the large signal from the silicon substrate. As film thickness increases, these signals start to overlap as shown in Fig. 3.11*b* for a 500 nm film. Thus, the determination of film composition becomes very difficult. The situation becomes even worse when RBS is applied to the analysis of InN films grown on sapphire substrates. This is shown in Fig 3.11*c*. In principle, the extraction of individual signals from the experimental data may be attempted using simulation routines such as SIMNRA (Mayer 1997) or Data Furnace. However, because of the complexity of the data, accuracy is certainly compromised. Thus, using this technique reliable stoichiometric information of InN films is not readily obtained unless the film is grown on a low-z substrate such as glassy carbon. Even then the InN film has to be rather thin (<200 nm). The use of resonant backscattering could enhance the light element signals, but it is cumbersome and quantification is difficult, since it would rely on measured nuclear cross-sections.

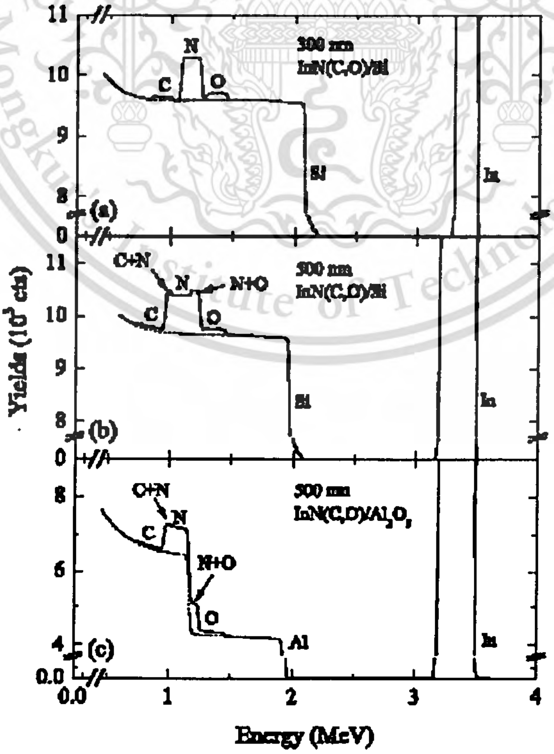

**Fig. 3.11** Simulated RBS spectra for InN films with 5% carbon and 5% oxygen grown on silicon and sapphire substrates.

In Fig. 3.11(a) the carbon, nitrogen and oxygen signals are separated. However, they overlap in Fig. 3.11(b) and Fig. 3.11(c). In all cases these signals are obscured by large signals from the substrate. This is particularly so when measurement statistics are also considered.

It is noteworthy that the RBS spectra presented in both cases are for films less than 200 nm thick and even then the nitrogen and oxygen signals are not fully separated. Thus, the determination of the nitrogen and oxygen contents of the film is not accurate. Moreover, the films were grown on uncommonly used glassy carbon substrate to permit the RBS measurements. Hence, any information on the carbon content in the film is not ready available. If the RBS technique were used on InN films grown on more common substrate, such as silicon or sapphire, the carbon, nitrogen and oxygen signals from the film would be obscured by those from precisely measured.

## 3.5 The Related Thin Films

### 3.5.1 Indium Tin Oxide (ITO)

Indium Tin Oxide or tin doped indium oxide (ITO) is an *n*-type, highly degenerated, wide band gap semiconductor with relatively low resistivity and high transmittance in visible range region [48]. Due to these properties, it has been widely used as transparent electrodes in various displays, including liquid-crystal display (LCD), electro luminescent display (ELD), and organic light-emitting diode (OLED) [48]. It has been reported that r.f magnetron sputtering yields ITO thin films with low resistivity and good reproducibility. For the crystallization of ITO thin films, the heating process at an elevated temperature during the film deposition or an addition post-annealing treatment at around 150°C is required [49]. The substrate temperature is an important parameter for several applications, particularly when organic polymer substrates are used [50-51].

#### 3.5.1.1 Physical Structure and Properties of ITO

Indium Tin Oxide is essentially formed by subsititutional doping of $In_2O_3$ with Sn which replaces the $In^{3+}$ atoms from the cubic bixbyte structure of indium oxide [52]. Sn thus forms an interstitial bond with oxygen and exists either as SnO or $SnO_2$accordingly it has a valency of +2 or +4 respectively. This valency state has a direct bearing on the ultimate conductivity of ITO. The lower valence state results in a net reduction in carrier concentration since a hole is created which acts as a trap and reduces conductivity. On the other hand, predominance of the $SnO_2$ state means $Sn^{4+}$ acts as a n-type donor releasing electrons to the conduction band. However, in ITO, both substitutional tin and oxygen vacancies contribute to the high conductivity and the material can be represented as $In_{2-x}Sn_xO_{3-2x}$. ITO films have a lattice parameter close to that of $In_2O_3$ and lie in the range 10.12 to 10.31Å [53].

A summary of electrical and optical properties of typical ITO films deposited using various techniques is shown in Table 3.3. Variations in film properties can be easily noted; these are attributable to both pre- and post-deposition treatments as well as the techniques themselves.

**Table 3.3** Typical electrical and optical properties of ITO deposited by various techniques.

| Deposition Technique | Thick [Å] | Hall Mobility $\mu_H$ [$cm^2V^{-1}s^{-1}$] | Carriers N [$cm^{-3}$] | Resistivity $\rho$ [$\Omega cm$] | Transmit. $T_r$ [%] | Ref. No. |
|---|---|---|---|---|---|---|
| r.f. Sputtering | 7,000 | 35 | $6 \times 10^{20}$ | $3 \times 10^{-4}$ | 90 | [5] |
| r.f. Sputtering | 5,000 | 12 | $12 \times 10^{20}$ | $4 \times 10^{-4}$ | 95 | [6] |
| r.f. Sputtering | 4,000 | 25 | $3 \times 10^{20}$ | $8 \times 10^{-4}$ | - | [7] |
| Magnetron Sputtering | 800 | 26 | $6 \times 10^{20}$ | $4 \times 10^{-4}$ | 85 | [8] |
| d.c. Sputtering | 1,000 | 35 | $9 \times 10^{20}$ | $2 \times 10^{-4}$ | 85 | [9] |
| Reactive Evaporation | 2,500 | 30 | $5 \times 10^{20}$ | $4 \times 10^{-4}$ | 91 | [10] |
| Ion Beam Sputtering | 600 | 26 | $2 \times 10^{20}$ | $12 \times 10^{-4}$ | - | [11] |
| Spray Pyrolysis | 3,000 | 45 | $5 \times 10^{20}$ | $3 \times 10^{-4}$ | 85 | [12] |

The high conductivity, $\sigma$, of ITO films is said to be due to high carrier concentration, N, rather than high Hall mobility, $\mu H$ [1] bearing in mind that resistivity, $\rho = 1/\sigma = 1/(qN\mu H)$ according to Ohm's law. The observed low mobility of ITO, compared to bulk In2O3, and its dependence on carrier concentration and substrate temperature has been explained in terms of scattering mechanisms due to ionized impurities or grain boundaries. Mobility is said to increase due to enhanced crystallinity of films deposited at higher substrate temperatures [54]. TEM and electron diffraction studies of r.f. sputtered ITO films on glass substrates by Sreenivas *et al.* suggest that films grown at room temperature have large stacking faults and represent an amorphous structure [55]; increasing this temperature to 200°C leads to a polycrystalline structure and finally annealing results in near single crystallinity with uniform grain size which leads to increased conductivity. The authors further suggest that deposition of ITO on single crystal substrates, rather than amorphous glass, can enhance the grain growth process.

The direct optical bandgap of ITO films is generally greater than 3.75 eV although a range of values from 3.5 to 4.06 eV have also been reported in the literature [56-57]. The high optical transmittance, Tr, of these films is a direct consequence of their being a wide bandgap semiconductor. The fundamental absorption edge generally lies in the ultraviolet of the solar spectrum and shifts to shorter wavelengths with increasing carrier concentration, N. This is because the bandgap exhibits an $N^{2/3}$ dependence due to the Moss-Burstein shift [58]. The band structure of ITO is assumed to be parabolic as shown in Figure 3.12.

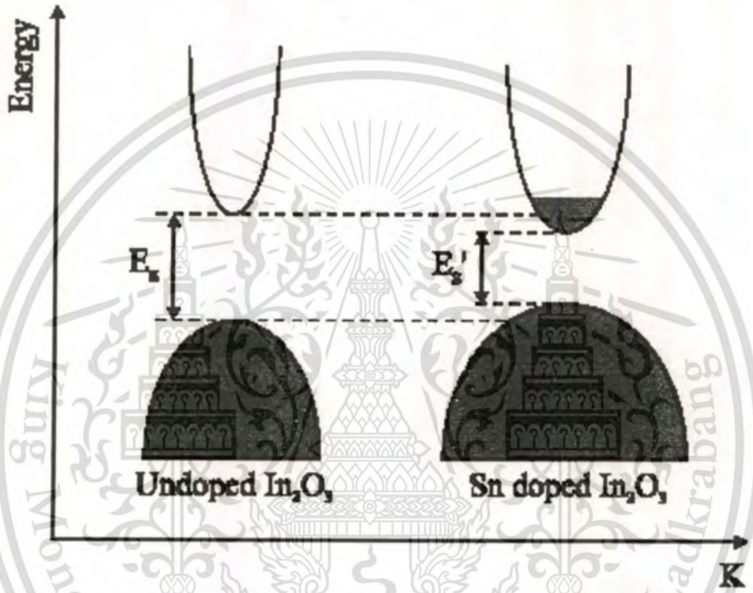

**Fig. 3.12** Assumed parabolic band structure of undoped $In_2O_3$ and the effect of tin doping; (After Gupta *et al.* [58]).

The conduction band is curved upwards, the valence band is curved downwards and the Fermi level is located at mid bandgap for the undoped material; addition of Sn dopants results in the formation of donor states just below the conduction band. As the doping density is increased, these eventually merge with the conduction band at a critical density, nc, which was calculated to be $2.3 \times 10^{19}$ $cm^{-3}$ by Gupta *et al.* [58]. Free electron properties are exhibited by the material when the density of electrons from the donor atoms exceeds this value. Hence all ITO films are expected to be degenerate in nature. Once the material becomes degenerate, the mutual exchange and coulombic interactions shift the conduction band downwards and the valence band upwards - effectively narrowing it from $E_g$ to $E_g'$ - as shown in Figure 3.12 earlier. The bandgap increase by the Burstein-Moss shift is partially compensated by this effect.

The reported value for the refractive index of ITO is 1.96 [59]. The transmittance of ITO films is also influenced by a number of minor effects which include surface roughness and optical inhomogeneity in the direction normal to the film surface. Inadvertently grown dark brown (effectively translucent) metallic films of ITO have also been reported. This opaqueness has been attributed to unoxidised Sn metal grains on the ITO surface as a result of instability due to absence of sufficient oxygen during deposition [52, 55].

#### 3.5.1.2 ITO Deposition Techniques

Sputtering, of one form or another, is by far the most extensively used technique for the deposition of ITO. This is closely followed by thermal evaporation - which can also be achieved using several different techniques. ITO has also been prepared by other methods such as Spray Pyrolysis and Screen Printing. The choice of deposition technique is dictated by a number of factors such as quality and reproducibility of the ITO film, homogeneity over a wide cross section, capacity, ease and cost of use as well as detrimental side effects and limitations specific to each technique. In addition, since the properties of ITO depend strongly on the microstructure, stoichiometry and the nature of the impurities present, it is inevitable that each deposition technique with its associated controlling parameters should yield films with different characteristics. Some of these issues will now be discussed briefly.

#### 3.5.1.3 Sputtering

Sputtering involves knocking an atom or molecule out of a target material by accelerated ions from an excited plasma and condensing it on the substrate. When this modification is induced by a chemical reaction during the transit from the target to the substrate, the process is referred to as reactive sputtering. In general, most ITO sputter sources consist of hot pressed 90% $In_2O_3$ : 10% $SnO_2$ compound targets. The sputtering can be achieved by a number of ways which include accelerating the plasma ions by a d.c field [60] or a d.c field combined with a magnet (to direct the high velocity emitted electrons away from the substrate), r. f. (with its self induced bias) as well as by ion beams [61]. Hence names such as magnetron [62] and reactive r.f sputtering reflect on the process that has been used for the deposition of the ITO film.

The technique used in the course of this study involves reactive r. f. sputtering with reactive gas-timing method. This method is reputed for its excellent uniformity, high conductivity and high transparency. The r.f field ensures that sputtering of non-conductive materials can also be achieved at a practical rate. Parameters known to influence ITO quality include sputtering pressure, pre-conditioning, film thickness and r. f. power amongst others. The control of oxygen partial pressure is particularly critical in determining the conductivity and transmittance. However, without the ability to direct unwanted high velocity electrons away from the substrate, damage is associated with this technique; on the other hand magnetron sputtering yields high deposition rates and minimizes this damage.

### 3.5.2 Indium Oxynitride (InON)

The presence of oxygen has been suggested as a cause of the higher band-gap observed for some InN-based material (e.g. [27]), though proponents of a lower band-gap have provided little cited work and even less experimental evidence on the actual role of oxygen. Many misconceptions have consequently arisen regarding the role of oxygen in InN. In particular, InN–$In_2O_3$ alloy formation has been suggested as a possible explanation for the higher band-gap [27]. There are two ways in which sufficient quantities of oxygen in InN may affect the band-gap. The first requires oxygen to form optically active centers, which, in high densities, modify a notional oxygen-free band-gap by the band filling (Moss–Burstein) effect or by impurity banding within the forbidden band. These effects will increase or decrease the apparent band-gap respectively. The second requires the formation of a semiconducting pseudo-binary alloy phase, $InO_xN_y$, with a band-gap different from InN. It seems to be a common misconception that an InN–$In_2O_3$ alloy system should exist and that its presence should intuitively explain the higher band-gap.

However, the physical evidence does not support the existence of InN–$In_2O_3$ alloys; in fact it has been known for a number of years that when oxygen is present in InN films in large quantities it forms discrete well segregated compounds [63]. It has also been shown that even if InN–$In_2O_3$ alloys were to occur and we re-iterate that the weight of evidence does not support their existence the amounts of oxygen present in available films have been insufficient to explain the difference in observed band-gap.

Examination of the relevant crystallography provides an explanation as to why the InN–$In_2O_3$ pseudo-binary alloy is not observed. The group III metal (M) oxides, of the form $M_2O_3$, most readily crystallise in the corundum structure. Group III metal nitrides most commonly form a wurtzite hexagonal structure with fewer atoms per unit cell. There is no continuous geometric transformation between the two structures and thus no continuous pseudo-binary analogous to familiar III–V intermetallics such as InGaAs. In particular, the equimolecular pseudo-binary $M_3O_3N$ (i.e. $MN+M_2O_3$) does not exist for any group III metal M, although there is a compositionally adjacent spinel in the $AlO_xN_y$ system. Other complex crystal structures appear at specific AlON compositions, but this is attributable to the strong Al–O bond. The familiar AlON range, commercially available in high quality optical components, is a sintered mixture of nanocrystalline AlN and $Al_2O_3$ powders with optical properties governed by effective-medium theory. There is no published evidence of an indium analogue to any of the $AlO_xN_y$ phases and a compositionally continuous crystalline pseudo-binary alloy of InN–$In_2O_3$ may be presumed not to exist. Nevertheless, effective-medium theory also dictates that sufficiently fine admixtures of two segregated phases will show optical absorption edges intermediate between those of the components.

Westra *et al.* [64] proposed a convincing model for the role of oxygen in indium nitride back in 1988. They produced polycrystalline material with carrier concentrations between $7x10^{19}$ and $2x10^{20}$ $cm^{-3}$ and low mobilities of 4–10 $cm^2/V$ s. Rutherford backscattering measurements showed oxygen oncentrations of about 11 at.%, but with indium to nitrogen ratios slightly above 1. However, there was no evidence of oxygen-related phases in their X-ray diffraction spectra, allowing them to propose that the oxygen in their films was surface-bound as an amorphous indium oxynitride. This oxide surface phase had previously been observed by Foley and Lyngdal [65] using XPS measurements. Such a structure maintains near-stoichiometry between nitrogen and indium, while the oxygen adsorbate is invisible in X-ray diffraction spectra. An $NO_2$-related contribution has also been observed in samples containing a higher oxygen content [45]. Kumar *et al.* [45] suggested that the grain boundaries of their columnar polycrystalline indium nitride acted as a site for the incorporation of such an oxygen–nitrogen species. They also saw no oxide contribution to X-ray diffraction spectra or to infrared absorption spectra.

Similar behavior has been demonstrated in polycrystalline GaN grown at low temperature (570 °C) [66] where it has been shown that large amounts of oxygen can be incorporated at the grain boundaries, and indeed and that the available concentration determines the eventual GaN crystal size. The reported amorphous oxynitride contribution [33] thus appears to be resident at the grain boundaries. Raman data for sputtered InN with 10% atomic oxygen concentration reveals only broad InN-related phonon peaks [67], also supporting the model.

#### 3.5.2.1 Oxygen and Other Potential Dopant Sources

Theory predicts that oxygen substitutional on a nitrogen site in InN should be a donor [36,34]; however, there has been no experimental confirmation of this. Other donor species have been identified as playing a more significant role for some forms of InN [36]. Early experimental evidence taken from sputtered samples suggested that there is at least one donor species resonant with or extremely close to the conduction band of InN [33], while other, deeper donor levels at 40–50 meV and 150 meV have also been identified [33]. The recent work of Haddad et al. [68] on nominally undoped MBE grown material of varying carrier concentration also shows the dominant donor to be resonant with the conduction band. These workers also observed deeper dopant energy levels using high temperature Hall effect measurements and found activation energies of 40, 81 and 114 meV. Additional energy levels at 17 and 66 meV were observed for Si-doped material, again with high carrier concentration and therefore likely to be influenced by both impurity banding and band-tailing. The energy separation between the conduction band and these deeper dopant levels may be affected by band-tailing for some of the heavily doped material. Interestingly, experimental evidence does not support oxygen as a dominant donor in InN. The work of Look et al. [36] suggests that hydrogen or possibly a native defect may have been the dominant donor in the 3.5 $\times 10^{18}$ $cm^{-3}$ MBE material they studied, since oxygen levels of only 3 $\times 10^{16}$ $cm^{-3}$ and silicon levels of $2\times 10^{16}$ $cm^{-3}$ were found to be present. The SIMS study of Specht *et al.* [69] also does not support the assignment of oxygen as an important donor in InN, with measured oxygen and donor concentrations showing no correlation. The recent work of Yoshimoto *et al.* [45], on films grown by MBE at 500 °C, showed electron concentrations of about $10^{20}$ $cm^{-3}$, corresponding to a donor concentration of 0.3% in InN with oxygen concentrations of 1–6 at.%. If oxygen is the donor in their films, then only 5% is electrically active, but it is not clear whether solubility limits have been reached. Carrier concentrations as high as $10^{21}$ $cm^{-3}$ have been recorded, and since very high oxygen concentrations do not yield these concentrations, other shallow donor impurities must be suspected. Nevertheless, oxygen substitutional on nitrogen sites may create a deeper donor state in InN, while segregated amorphous phases appear likely to be electrically neutral complexes.

#### 3.5.2.2 Oxynitride Crystal Structure

Materials based upon oxygen hold special potential because of low reactivity with the atmosphere. In the case of the metal dioxide ($M\mathrm{O}_2$), it is very likely that as the metal coordination increase so does the bulk modulus. The highest coordination in the metal dioxides is the cotunnite structure in which the metal atom is coordinated by nine oxygens. Several metal dioxides have now been observed in the orthorhombic cotunnite form with $\mathrm{ZrO}_2$, $\mathrm{HfO}_2$, $\mathrm{CeO}_2$, $\mathrm{PbO}_2$, $\mathrm{UO}_2$, $\mathrm{TbO}_2$, $\mathrm{TeO}_2$, and $\mathrm{ThO}_2$, all currently known dioxides include into this phase by pressure.

In fact it may be that the cotunnite phase of the metal oxides is the highest coordination phase that can be achieved in the $M\mathrm{O}_2$ series and therefore could represent the hardest possible structure. Given the great potential of the highly coordinated $M\mathrm{O}_2$ contunnite phase as an ultrahard material, the possibility of changing the chemical nature of this phase through incorporation of other elements may lead to another potentially important series of ultrahard materials. In this suggestion the possible direct incorporation of N into the cotunnite structure giving an oxynitride structure of the form $M$ON. The N is assumed to directly occupy a site in the 14-atom unit cell of the cotunnite lattice that has the lowest energy structure and do not to be randomly distributed through the oxygen sublattice as previously supposed for other oxynitride structure is shown in Fig. 3.13.

J. E. Lowther *et al.* make a comparison of this phase with a similar $M\mathrm{O}_2$ phase and especially compare the elastic properties as measured by the bulk modulus. Lattice parameters for each $M$ON cotunnite structure are also obtained. They have used the local density approximation (LDA) function of Ceperley and Alder [70] as parametrized by Perdew and Zunger [71], to obtain accurate exchange and correlation energies for a particular ionic configuration. A plane-wave basis is used [72] which is sampled over a reduced set of eight special $k$ points. A criterion of at least $10^{-4}$ eV/atom was placed on the self-consistent convergence of the total energy and all of the calculations reported here used a plane-wave cut off of 870 eV (64 Ry) with soft Troullier-Martins pseudopotentials [73].

In conclusion a correlation has been established between the number of electrons in the metal and the overall compressibility of the cotunnite structure as measured by a bulk modulus for the metal oxides and oxynitrides. They find that the $d$ orbitals make an important positive contribution to the bulk modulus through a sensitive reduction in the volume of the unit cell. The presence of N into the structure has affected the density of states at the Fermi energy and also introduced a series of sharp states lying below the Fermi level. A special enhancement of the bulk modulus has been found in the case of NbON and TaON, suggesting that such a cotunnite material could exhibit considerable hardness.

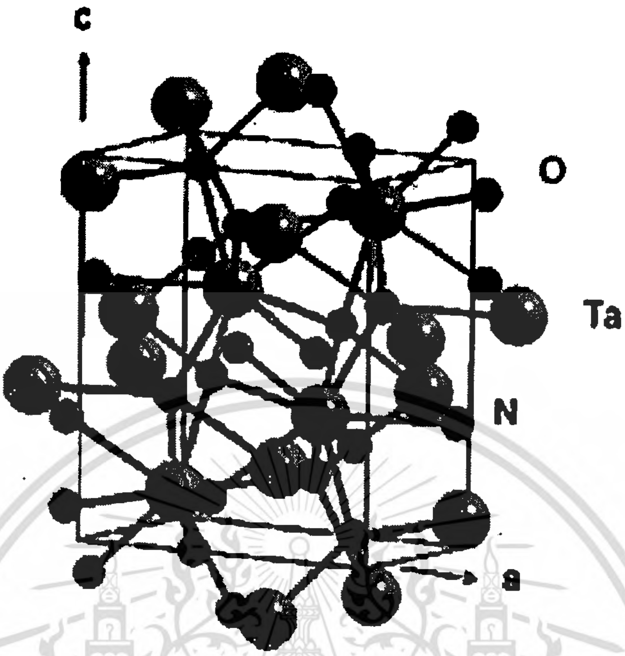

**Fig. 3.13** Typical crystal structure of a cottunite metal-Ta-Oxynitride.

The increase of the oxygen percentage is followed by a significant loss of crystallinity, being the films with the highest oxygen contents (34 and 43 at.%) practically amorphous. This amorphization of the films is related with the increase of the oxygen content promoted by the increase in the gas flow keeping in mind that oxygen is more reactive than nitrogen. The increase of the available oxygen over supersaturation level w15x reduces the possibility of crystallization (mostly that of TiN). The extended deformation of the titanium nitride structure, resulting from the incorporation of oxygen (referred here as Ti–N–O phase), increases the number of defects, and then facilitates the amorphization. This oxygen doping explains the broadening of the diffraction peaks, as it can be evidenced for intermediate and highest oxygen contents, where the peak broadening indicates the existence of microstrains and nanometer grain size. The asymmetricpr ofile may be related to peak overlap corresponding to phase structures with different lattice parameters. In-depth structural inhomogeneities assumption may be rejected since RBS results indicate homogeneous

A combination of beneficial properties of indium nitride and indium oxide results in a new material-indium oxynitride-with variable composition and functionality. Changing the oxygen-to-nitrogen ratio in In-O-N in a wide range offers a possibility to tune the film properties by controlling the progress parameters.

#### 3.5.2.3 InON Deposition Technique

The reactive magnetron sputtering system, which used for experimental growth of AlN, InN and ITO thin films in this thesis, was also used to deposit indium oxynitride thin films. The InON thin films were achieved by mixed-gas and reactive gas-timing techniques. A detail of experiment was presented in Chapter 8. With our technique, the bandgap of ION thin films were obtained in range between ultraviolet to near-IR depended on gas flow control.

## 3.6 Chapter Summary

InN is a key material of the III-nitride system. It has emerged as a potential material for optical and electronic devices. Due to the large and diverse spectrum of possible applications of InN, the correct band gap assignment for InN is the focus of much current research and debate. In this chapter mainly presented on the background of indium nitride which including of the growth techniques such as MBE, MOCVD and RF sputtering, the properties such as crystal structure, electrical, mechanical and optical properties, in addition of the quality and reproducibility of InN films. The related InN film, furthermore, ITO and InON films are also briefly here in order to using these films for device applications discussed in Chapter 8.

Recently, the value of the optical band gap energy $E_g$ for InN has come under intense reinvestigation due to a disagreement between the generally accepted value of 1.9 eV and recently reported values in the range of 0.7–1.0 eV. The lower reported band gap values (<1 eV) are thought to be associated with improvements in the thin film fabrication techniques leading to higher quality InN films with relatively less disorder, and are more consistent with values predicted by theoretical calculations. The correct value of the band gap for this material is crucial, as the usefulness of InN for a particular application depends sensitively upon it. The reasons for the observed variation in the apparent band gap are not well understood.

## References

[1] Angus J.C. (2005), www.cwru.edu/cse/eche/people/faculty/angus/plate.html.

[2] Mohammad S.N. & Morko_c H. (1996), **“Progress and Prospects of Group-III Nitride Semiconductors; Prog”**, Quantum Electron. 20(5-6), 361-525.

[3] Bhuiyan A.G., Hashimoto A. & Yamamoto A. (2003), **“Indium Nitride (InN): A Review on Growth, Characterization, and Properties”**, J. Appl. Phys. 94(5), 2779, 2808.

[4] Tansley T.L. & Foley C.P. (1984), **“Electron Mobility in Indium Nitride”**, Electron. Lett. 20(25-26), 1066-1068.

[5] Binari S.C. & Dietrich H.C. (1997), **“GaN and Related Materials, Gordon and Breach”**, New York, pp. 509-534.

[6] Tansley T.L. & Foley C.P. (1986a), **“Infrared Absorption in Indium Nitride”**, J. Appl. Phys. 60(6), 2092-2095.

[7] Yamamoto A., Tsujino M., Ohkubo M. & Hashimoto A. (1994a). **“Metalorganic Chemical Vapor Deposition Growth of InN for InN/Si Tandem Solar Cell”**, Sol. Energy Mater. Sol. Cells 35(1-4), 53-60.

[8] Wu J., Walukiewicz W., Yu K.M., Ager III J.W., Haller E.E., Lu H., Scha_W.J., Saito Y. & Nanishi Y. (2002). **“Unusual Properties of the Fundamental Bandgap of InN”**, Appl. Phys. Lett. 80(21), 3967-3969.

[9] Matsuoka T., Okamoto H., Nakao M., Harima H. & Kurimoto E. (2002). Optical bandgap energy of wurtzite InN, Appl. Phys. Lett. **81(7)**, 1246-1248.

[10] Davydov V.Yu., Klochikhin A.A., Seisyan R.P., Emtsev V.V., Ivanov S.V., Bechstedt F., Furthmuller J., Harima H., Mudryi A.V., Aderhold J., Semchinova O. & Graul J. (2002b). **“Absorption and Emission of Hexagonal InN Evidence of Narrow Fundamental Band Gap”**, phys. stat. sol. (b) 229(3), R1-R3.

[11] Ruterana P, Albrecht M & Neugebauer J, eds (2003). Nitride Semiconductors, WILEY-VCH, Weinheim.

[12] Yamamoto A., Tsujino M., Ohkubo M. & Hashimoto A. (1994b). **“Nitridation Effects of Substrate Surface on The Metalorganic Chemical Vapor Deposition Growth of InN on Si and alpha-$Al_2O_3$ Substrates”**, J. Cryst. Growth 137(3-4), 415-420.

[13] Tsuchiya T., Yamano H., Miki O., Wakahara A. & Yoshida A. (1999). **"Improvement of the Crystalline Quality of InN Layers Grown on Sapphire (0001) by Surface Nitridation"**, Jpn. J. Appl. Phys. 38(4A), 1884-1887.

[14] Mamutin V.V., Vekshin V.A., Davydov V.Yu., Ratnikov V.V., Shubina T.V., Ivanov S.V., Kopev P.S., Karlsteen M., Soderwall U. & Willander M. (1999). **"MBE Growth of Hexagonal InN Films on Sapphire with Different Initial Growth Stages"**, phys. stat. sol. (a) 176, 247-252.

[15] Saito Y., Teraguchi N., Suziki A., Araki T. & Nanishi Y. (2001). **"Growth of High Electron-Mobility InN by RF Molecular Beam Epitaxy"**, Jpn. J. Appl. Phys.40(2A), L91-L93.

[16] Higashiwaki M. & Matsui T. (2002). **"High-quality InN Film grown on A Low Temperature-grown GaN Intermediate Layer by Plasma-assisted Molecular Beam Epitaxy"**, Jpn. J. Appl. Phys. 41, L540-L542.

[17] Yamamoto A., Murakami Y., Koide K., Adachi M. & Hashimoto A. (2001). **"Growth Temperature Dependences of MOVPE InN on Sapphire Substrates"**, phys. stat. sol. (b) 228(1), 5-8.

[18] Matsuoka T., Okamoto H., Nakao M., Harima H. & Kurimoto E. (2002). **"Optical Bandgap Energy of Wurtzite InN"**, Appl. Phys. Lett. 81(7), 1246-1248.

[19] Koukitu A., Taki T., Takahashi N. & Seki H. (1997). **"Thermodynamic Study on The Role of Hydrogen During the MOVPE Growth of Group III Nitrides"**, J. Cryst. Growth 197, 97-105.

[20] Chen P.P.-T. (2002), **"Remote Plasma Enhanced Chemical Vapour Deposition Growth and Characterization of Gallium Nitride Films"**, Master's thesis, Macquarie University, Sydney, Australia.

[21] Molnar R.J. & Moustakas T.D. (1994). **"Growth of Gallium Nitride by Electroncyclotron Resonance Plasma-assisted Molecular-Beam Epitaxy"**,: The role of charged species, J. Appl. Phys. 76(8), 4587-4595.

[22] Lu H., Scha_ W.J., Hwang J., Wu H., Yeo W., Pharkya A. & Eastman L.F. (2000)., **"Improvement on Epitaxial grown of InN by Migration Enhanced Epitaxy"**, Appl. Phys. Lett. 77(16), 2548-2550.

[23] Saito Y., Harima H., Kurimoto E., Yamaguchi T., Teraguchi N., Suzuki A., Araki T. & Nanishi Y. (2002), **"Growth Temperature Dependence of Indium Nitride Crystalline Quality grown by RF-MBE"**, phys. stat. sol. (b) 234(3), 796-800.

[24] T.L. Tansley. C.P. Folley, **"Optical Band Gap of Indium Nitride"**, J. Appl. Phys. 59, pp. 3241, 1986.

[25] K. Osamura, K. Nakajima, Y. Murakami, P.H. Shingu, and A. Ohtsuki, **"Fundamental Absorption Edge in GaN, InN and Their Alloys"**, Solid State Commun. 11, pp. 617-621, 1972.

[26] H.J. Hovel, J.J. Cuomo, Appl. Phys. Lett. 20 (1972) 71.

[27] V. Yu Davydov, A.A. Klochikhin, V.V. Emtsev, S.V. Ivanov, V.V. Vekshin, F. Bechstedt, J. Furthmuller, H. Harima, A.V. Mudryi, A. Hashimoto, A. Yamamoto, A.J. Aderhold, J. Graul, E.E. Haller; Phys. Status Solidi b 230 (2002) R4.

[28] J.Wu, W. Walukiewicz, K.M. Yu, J.W. Ager III, E.E. Haller, H. Lu, W. Schaff, Y. Saito, Y. Nanishi, Appl. Phys. Lett. 80 (2002) 3967.

[29] T. Inushima, V.V.Mamutin, V.A. Vekshin, S.V. Ivanov, T. Sakon, M. Motokawa, S. Ohoya, J. Cryst. Growth 227–228 (2001) 481.

[30] Davydov V.Yu., Klochikhin A.A., Emtsev V.V., Kurdyukov D.A., Ivanov S.V., Vekshin V.A., Bechstedt F., Furthmuller J., Aderhold J., Graul J., Mudryi A.V., Harima H., Hashimoto A., Yamamoto A. & Haller E.E. (2002a), **"Band Gap of Hexagonal InN and InGaN Alloys"**, phys. stat. sol. (b) 234(3), 787-795.

[31] Chen F., Cartwright A.N., Lu H. & Scha_ W.J. (2004). **"Ultrafast Carrier Dynamics in InN Epilayers"**, J. Cryst. Growth 269, 10-14.

[32] Hamberg I. & Granqvist C.G., **"Evaporated Sn-doped $In_2O_3$ Films: Basic Optical Properties and Applications to Energy-Efficient Windows"**, J. Appl. Phys. 60(11), R123-59, (1986).

[33] T.L. Tansley and R.J. Egan, *Phys. Rev. B* **45** (1992), p. 10942.

[34] C. Stampfl, C.G. Van De Walle, D. Voggel, P. Krugger and J. Pollman, *Phys. Rev. B* **61** (2000), p. R7846.

[35] Limpijumnong S. & Van de Walle C.G. (2001). **"Passivation and Doping due to Hydrogen in III-Nitrides"**, phys. stat. sol. (b) 228(1), 303-307.

[36] Look D.C., Lu H., Scha_ W.J., Jasinski J. & Liliental-Weber Z. (2002). **"Donor and Acceptor Concentrations in Degenerate InN"**, Appl. Phys. Lett. 80(2), 258-260.

[37] Amano H., Kito M., Hiramatsu K. & Akasaki I. (1989). **"p-type Conduction in Mg-doped GaN Treated with Low-Energy Electron Beam Irradiation (LEEBI)"**, Jpn. J. Appl. Phys. 28(12), L2112-L2114.

[38] Nakamura S., Mukai T., Senoh M. & Iwasa N. (1992). **"Thermal annealing effects on p-type Mg-doped GaN films"**, Jpn. J. Appl. Phys. 31(2B), L139{L142.

[39] B.Maleyre, O. Briot, S. Ruffenach, B. Gil, Proc. of Int. Conf. on Nitride Semicond., ICNS-2004, Pittsburgh, 19–23 July 2004, Phys. Status Solidi c, **2** (2005) 2309.

[40] O. Briot, B. Maleyre, S. Ruffenach, Appl. Phys. Lett., **83** (2003) 2919.

[41] S. Ruffenach, B. Maleyre, O. Briot, B. Gil, Phys. Status Solidi c, **2** (2005) 826.

[42] Z.H. Lan, W.M. Wang, C.L. Sun, S.C. Shi, C.W. Hsu, T.T. Chen, K.H. Chen, C.C Chen, Y.F. Chen, L.C. Chen, J. Cryst. Growth, **269** (2004) 87.

[43] Maruyama T. & Morishita T., **"Indium nitride thin films prepared by radio-frequency reactive sputtering"**, J. Appl. Phys. 76(10), 5809-5812 (1994).

[44] Motlan, Goldys E.M. & Tansley T.L., **"The effect of target nitridation on structural properties of InN grown by radio-frequency reactive sputtering"**, Thin Solid Films 422, 28-32 (2002).

[45] Kumar S., Mo L., Motlan & Tansley T.L. (1996). **"Elemental composition of reactively sputtered indium nitride thin films"**, Jpn. J. Appl. Phys. 35(4A), 2261-2265.

[46] Yoshimoto M., Yamamoto H., Huang W., Harima H., Saraie J., Chayahara A. & Horino Y. (2003a). **"Widening of optical bandgap of polycrystalline InN with a few percent incorporation of oxygen"**, Appl. Phys. Lett. 83(17), 3480-3482.

[47] Mayer M, SIMNRA User's Guide, Max-Planck-Institut fur Plasmaphysik, Garching, Germany (1997).

[48] K. L.Chopra, S. Major , D. K. Pandya, Thin Solid Films 102, 1 (1983).

[49] E. Terzini, P. Thilakan, C. Minarini, Mater. Sci. Eng. B 77, 110 (2000).

[50] A. A. Karim, C. Deshpandey, H. J. Doerr, R. F. Bunshah, Thin Solid Films **172,** 111 (1989).

[51] B. Chiou, S. Hsieh, Thin Solid Films **229**, 146 (1993).

[52] J. C. C. Fan and J. B. Goodenough, **"X-Ray Photoemission Spectroscopy Studies of Sndoped Indium Oxide Films"**, Journal of Applied Physics, **48**(8), 1977, pp. 3524 – 3531.

[53] P. Nath and R. F. Bunshah, **"Preparation of $In_2O_3$ and Tin-Doped $In_2O_3$ Films by a Novel Activated Reactive Evaporation Technique"**, Thin Solid Films, **69**, 1980, pp. 63 - 68.

[54] N. Balasubramanian and A. Subrahmanyam, **"Effect of Substrate Temperature on The Electrical and Optical Properties of Reactively Evaporated Indium Tin Oxide Films"**, Materials Science and Engineering, **B1**, 1988, pp. 279 – 281.

[55] K. Sreenivas, T. Sundarsena Rao, A. Mansnigh and S. Chandra, **"Preparation and Characterization of r.f. Sputtered Indium Tin Oxide Films"**, Journal of Applied Physics, **57**(2), 1985, pp. 384 – 392.

[56] J. C. C. Fan and J. B. **Goodenough,** "X-Ray Photoemission Spectroscopy Studies of Sn doped Indium Oxide Films", Journal of Applied Physics, **48**(8), 1977, pp. 3524 – 3531.

[57] N. Balasubramanian and A. Subrahmanyam, **"Electrical and Optical Properties of Reactively Evaporated Indium Tin Oxide (ITO) Films - Dependence on Substrate Temperature and Tin Concentration"**, Journal of Physics D: Applied Physics, **22**, 1989, pp. 206 – 209.

[58] L. Gupta, A. Mansingh and P. K. Srivastava, **"Band Gap Narrowing and the Band Structure of Tin Doped Indium Oxide Films"**, Thin Solid Films, **176**, 1989, pp. 33 – 44.

[59] J. Szczyrbowski, A. Dietrich and H. Hoffmann, **"Optical and Electrical Properties of r.f. Sputtered Indium-Tin Oxide Films"**, Phys Stat Sol (a), **78**, 1983, pp. 243 – 252.

[60] M. Higuchi, S. Uekusa, R. Nakano and K. Yokogawa, **"Post-Deposition Annealing Influence on Sputtered Indium Tin Oxide Film Characteristics"**, Japanese Journal of Applied Physics, **33**, 1994, pp. 302 – 306.

[61] J. Bregman, Y. Shapira and H. Aharoni, **"Effects of Oxygen Partial Pressure During Deposition on the Properties of Ion-Beam-Sputtered Indium-Tin Oxide Thin Films"**, Journal of Applied Physics, **67**(8), 1990, pp. 3750 – 3753.

[62] M. Buchanan, J. B. Webb and D. F. Williams, **"The Influence of Target Oxidation and Growth Related Effects on the Electrical Properties of Reactively Sputtered Films of Tin-Doped Indium Oxide"**, Thin Solid Films, **80**, 1981, pp. 373 – 382.

[63] K.S.A. Butcher, **"InN, A Historic review from obscurity to controversy"**, in: Q. Guo (Ed.), Advanced Material in Electronics, Research Signpost, 2004, p. 1.

[64] Westra K.L., Lawson R.P.W. & Brett M.J., **"The Effects of Oxygen Contamination on the Properties of Reactively Sputtered Indium Nitride Films"**, J. Vac. Sci. Technol. A 6(3), 1730-1732 (1988).

[65] C.P. Foley and J. Lyngdal, J. Vac. Sci. Technol. A **5** (1987), p. 1708.

[66] K.S.A. Butcher, H. Timmers, Afifuddin, P.P.-T. Chen, T.D.M. Weijers, E.M. Goldys, T.L. Tansley, R.G. Elliman and J.A. Freitas Jr., J. Appl. Phys. **92** (2002), p. 3397.

[67] M. Wintrebert-Fouquet, K.S.A. Butcher, P.P.T. Chen, J. Cryst. Growth 269 (2004) 134.

[68] D.B. Haddad, H. Dai, R. Naik, C. Morgan, V.M. Naik, J.S. Thakur, G.W. Auner, L.E. Wenger, H. Lu, W.J. Schaff, Mater. Res. Soc. Symp. Proc. 798 (2004) Y12.7.1.

[69] P. Specht, R. Armitage, J. Ho, E. Gunawan, Q. Yang, X. Xu, C. Kisielowski, E.R.Weber, J. Cryst. Growth 269 (2004) 111.

[70] D. M. Ceperley and B. J. Alder, Phys. Rev. Lett. **45**, 566 (1980).

[71] J. P. Perdew and A. Zunger, Phys. Rev. B **23**, 5048 (1981).

[72] A. Kley, J. Neugebauer, M. Bockstedte, and M. Scheffler, Comput. Phys. Commun. **107**, 187 (1997).

[73] J. K. Dewhurst and J. E. Lowther, Phys. Rev. B **64**, 014104 (2001).

# CHAPTER 4

# INNOVATION TECHNIQUE OF REACTIVE GAS-TIMING RF MAGNETRON SPUTTERING

## 4.1 Background of Sputtering System

### 4.1.1 Overview

The process of sputtering may be defined as the ejection of particles from a condensed-matter target due to the impingement of energetic projectile particles. The sputter deposition process involves a target and plasma of a neutral working such as argon. The target material transferred to the vapor phase by positive ion bombardment from the plasma via momentum transfer from the ions to the target atoms. The most important parameters controlling the growth and the properties of the films by sputter deposition processes are:

1. target voltage and current,
2. reactant partial pressure and flow rate, and
3. substrate temperature and substrate bias.

Similar to PACVD process, these variables affect both process parameters as well as plasma parameters. For example, in conventional diode sputtering using either d.c or r.f, the deposition rate is dependent on target voltage and current as well as on pressure. However, these same parameters also determine the average energy of the secondary electrons, which in turn influences the floating potential and hence the bombardment of the growing film.

### 4.1.2 RF Sputtering

A d.c methods cannot be used to sputter nonconducting targets because of charge accumulation at the target surface. This difficulty can be overcome by using radio frequency (r.f) sputtering. A single r.f sputtering apparatus can be used to deposit electrically conducting, semiconducting, and insulating coatings. Consequently, r.f sputtering has found wide application in the electronics industry. Nonconducting and semiconducting materials which have been deposited by r.f sputtering include elemental semiconductors: Si and Ge; III-V compounds: GaAs, GaSb, GaN, and AlN; II-VI compounds: CdSe and CdS; IV-VI compounds: PbTe; refractory semiconductors: SiC; ferroelectric compounds: $Bi_4Ti_3O_{12}$; Oxides: $In_2O_3$, $SiO_2$, $Al_2O_3$,

$Ta_2O_5$, $Y_2O_3$, $TiO_2$, $ZrO_2$, $SnO_2$, PtO, $Bi_2O_3$, ZnO and CdO; pyrex glass and plastics. Often several targets are placed within a common vacuum enclosure so that multiplier coating can be deposited without breaking vacuum [1].

The usefulness of r.f methods for sputtering nonconducting materials is based upon the fact that a self-bias voltage, negative with respect to the plasma floating potential, develops on any surface that is capacitively coupled to a glow discharge. The basis for this potential, which forma as a consequence of the difference in mobility between electrons and ions, illustrated schematically in Fig. 4.1. The current-voltage characteristic for an electrode immersed in a plasma is given in Fig. 4.1a. The floating potential is negative relative to the plasma potential by an amount that depends upon the gas species and plasma electron energy distribution function, but is typically –20 to –50 V and therefore too low to produce significant sputtering of most materials. When an alternating voltage is applied to such an electrode, more electron current flows when the electrode is positive relative to the floating potential than ion current flows when the electrode is negative relative to the floating potential (Fig. 4.1b).

Capacitive coupling requires that there be no d.c current flow; i.e., the net current to the electrode in each r.f cycle must be zero. Accordingly, a negative bias must form such that the electron current on the positive side of the cycle becomes equal to the ion current on the negative side. The negative bias is approximately equal to half the peak-to-peak voltage of the r.f signal and therefore can be made large enough to produce sputtering.

The behavior illustrated in Fig. 4.1 applies strictly to the case where the electrode is passive; i.e., is not responsible for sustaining the plasma discharge. The planar diode shown schematically in Fig 4.2 is the most commonly used apparatus for r.f sputtering. The electrodes sustain the discharge and therefore have slightly different current-voltage characteristics than the one shown in Fig. 4.1, particularly at negative voltages. However, the overall effect when an r.f potential is superimposed on the I-V characteristic is essentially identical.

Figure 4.3 shows a schematic drawing of a typical r.f planar-diode sputtering configuration in which a nonconducting target is placed over one electrode and substrate are placed on the other one. The electrodes reverse cathode-anode roles on each half cycle. The discharge is operated at a frequency that is sufficiently high that significant ion charge accumulation does not occur during the cycle time when an electrode is serving as a cathode. Frequency in the low MHz range are required. Most systems are operated at a frequency of 13.56 MHz, since this has been allocated by the Faderal Communications Commission (FCC) for industrial-scientific-medical purposes.

Operation at other frequencies requires careful shielding to assure compliance with FCC regulations on radio interference.

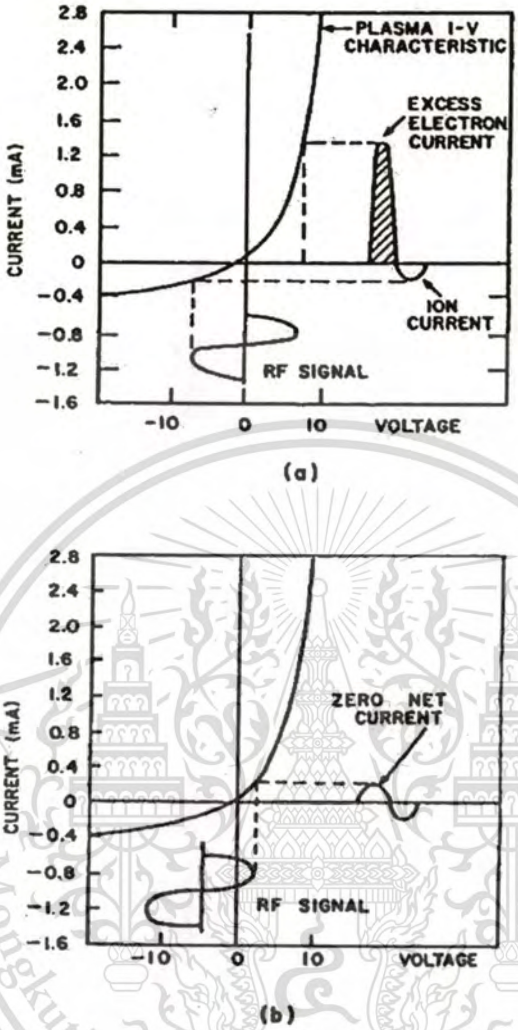

**Fig. 4.1** Schematic illustration of the development of a negative bias when an r.f potential is capacitively coupled to a probe immersed in a plasma.

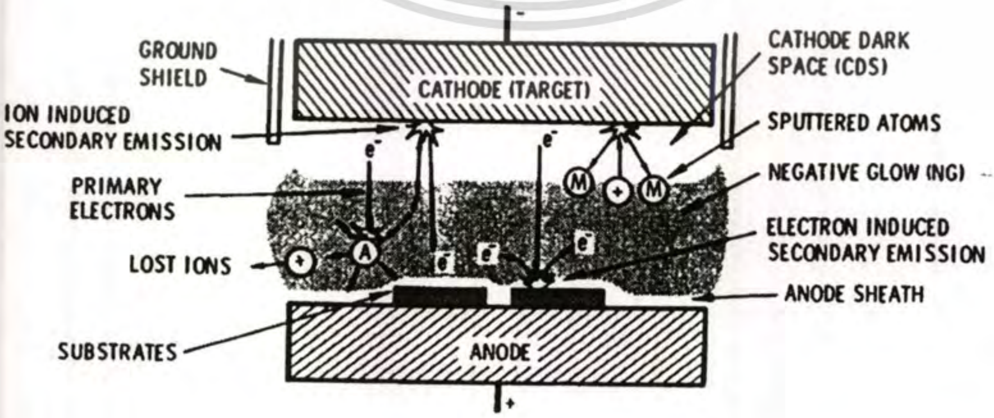

**Fig. 4.2** Schematic representation of the plasma in the planar diode sputtering source.

At MHz operating frequencies, massive ions can not follow the temporal variations in the applied potential. However, the electron can. Thus the cloud electrons in the negative glow plasma can be pictured as moving back and forth at the applied frequency in a sea of relatively stationary ions. As electron cloud approaches one electrode, it uncovers ions at the other electrode to form a positive ion sheath. This sheath takes up nearly the entire applied voltage, the same as in the d.c case.

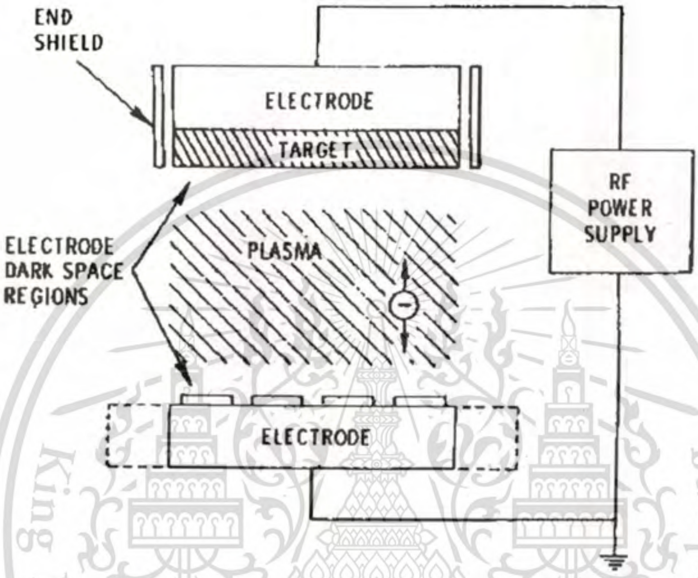

**Fig. 4.3** Schematic drawing of a planar r.f diode sputtering device.

A non-conducting target constitutes a capacitor in the electrical circuit between the electrodes (an external capacitor would have the same effect). Thus there can be no d.c component to the current flow. The total ion and electron charge flow to a given electrode during an r.f cycle must balance to zero. However, a large electron current flows to a given electrode as the electron cloud makes a contact. Thus the electron cloud need approach a given electrode for only a small fraction of a half cycle for purposes of supplying sufficient electrons to fulfill the anode requirement; i.e., to balance the entire ion flux to the cycle. Accordingly, in the steady state both electrodes develop a negative d.c bias relative to the plasma potential, such that the electrodes approach or exceed the plasma potential (and become anodes) for only very short portions of their r.f cycle as indicated in Fig. 4.4.

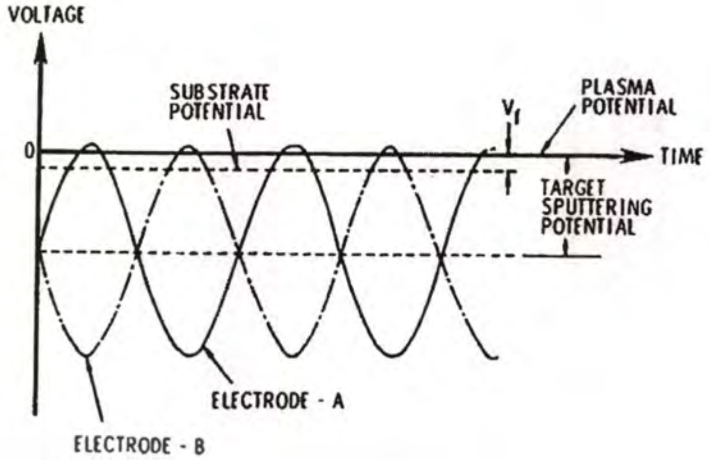

**Fig. 4.4** Approximate representation of target voltage waveforms relative to the plasma potential for a balance r.f system with two equal-area sputtering electrodes. $V_f$ is the floating potential.

The motion of the ions, because of their inertia, can be thought of as responding to the d.c potential and passing to both electrodes throughout the cycle. The electron cloud spends most of its time near the center position between the electrodes. Visually, the discharge appears a d.c discharge with a cathode dark space over each electrode. Functionally, sputtering occurs continually at both electrodes.

The r.f discharges in planar diode systems can be operated at considerably lower pressures than can d.c discharges. Typical operating pressures are 5 to 15 mTorr. There are two reasons: a reduction in the loss of primary electrons, and at high frequencies, an increase in the volume ionization efficiency. A fraction of lower-energy primary electrons are repelled from the electrode toward which they are accelerated and thus remain in the discharge longer to make additional ionizing collisions. In addition, electron can gain energy from the r.f field by making in-phase collisions with gas atoms. That is, if an electron, accelerated in one direction during the given half-cycle, makes an elastic collision in which its direction is reversed near the end of the half-cycle, it maintains most of its velocity (due to the large mass mismatch between electron and ions) and will again be accelerated during the next half-cycle and thus have gained by energy during the complete cycle.

The versatility of r.f sputtering is not achieved without drawbacks. Implementation of the process is complicated. A typical electron circuit is shown schematically in Fig. 4.5. It consists of an r.f power supply, an inductive coupling to the load, and a matching network.

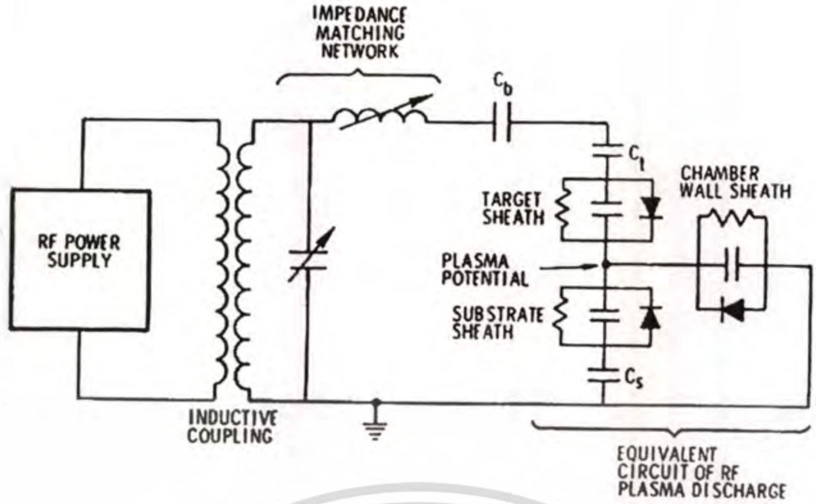

**Fig. 4.5** Schematic circuit of single-ended r.f discharge system including an equivalent circuit for the plasma discharge.

An equivalent circuit for an r.f glow discharge is also shown in Fig. 4.5. The equivalent circuit assumes that both electrodes and chamber walls are in contact with the plasma, and that the impedance is dominated by the plasma sheaths. The sheath capacitances result from the charge separation across the dark space. These capacitors are shunted to the electrode surface by resistor to account for the ion current, and by diode to account for the high electron current that can flow from the plasma to an electrode that is biased positive relative to the plasma potential. The capacitor $C_t$ accounts for capacitance of the target. $C_b$ is a blocking capacitor that is added to make the system independent of variations in the target capacitance.

The r.f current through the plasma is principally an electron current caused by the relative motion of the electron cloud. To the extent that there is no volume power transfer from the oscillating electrons to the gas, this current is out of phase with the applied voltage. The primary power transfer occurs via the relatively small ion and electron current component that are in phase with the voltage. Thus, in the equivalent circuit approximation, the power transfer to produce sputtering occurs as the ion currents pass through the sheath resistances. Efficient power transfer requires that the r.f power supply operate into a resistive load. Therefor a matching network is used to introduce inductance, and often capacitance, into the circuit in such a way that, in combination with the load, they form a resonant circuit. However, the power supply sees only the resistive component of the load, the current passing from the power supply to the current circuit is in phase with the load and represents the power passing to the load. Many commercial sputtering source monitor the reflected power from the load as an index of how effectively the matching network is adjusted. The reflected power should be minimized.

The ion current, and thus the sputtering rate at a given electrode, is determined by the average difference in potential between the electrode and the plasma. Thus it is useful to consider the plasma potential as a zero-point reference voltage in examining the performance of r.f sputtering systems. The electrical character of r.f sputtering systems can be classified in general as being either balanced or single-ended. In a balanced system, both electrodes are configured as identical sputtering targets and their potentials are 180° out of phase. The average sputtering voltage is about equal the peak-to-peak applied r.f potential. The link center trap is placed at ground potential to stabilize the system and the chamber walls and substrates are connected to the center trap ground, as shown in Fig.4.6. Science this point is at zero potential relative to the r.f voltage, no r.f current will flow to these elements. Furthermore, because of the capacitance in series with each of electrodes, there is no d.c current path from the plasma to the wall and substrates and then back through the electrodes into the plasma. Thus a charge will develop on the capacitors such that the substrates float at a potential slightly negative with respect to the plasma, just like a floating electrode in a d.c plasma.

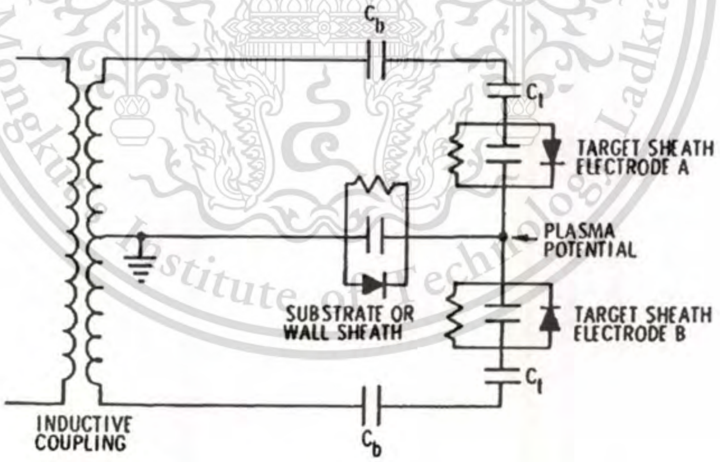

**Fig. 4.6** Schematic representation of an equivalent circuit for a balanced r.f system with two equal-area sputtering electrodes and center-trap ground. The matching network is not shown.

In an unbalanced r.f system, the electrode on which the substrates are placed is made considerably larger than the target electrode. This makes the sheath capacitance large, and the r.f voltage drop across the substrate electrode small, as shown schematically in Fig. 4.7. The chamber and one side of the link are generally grounded (Fig. 4.5). Again, the capacitance in both electrode circuits prevents a d.c current flow to the chamber, and a negative bias develops relative to the plasma potential. A potential relative the plasma potential will exist on the substrates and chamber wall unless the substrate electrode area is large enough to reduce this potential to essentially zero and to move the r.f balance point to the grounded end of the link. It is important that these voltage drops be small so that sputtering from uncontrolled surfaces does not introduce contamination into the coatings. An impedance may be added to the substrate electrode circuit so that the potential of this electrode relative to the plasma can be controlled for purposes of bias sputtering.

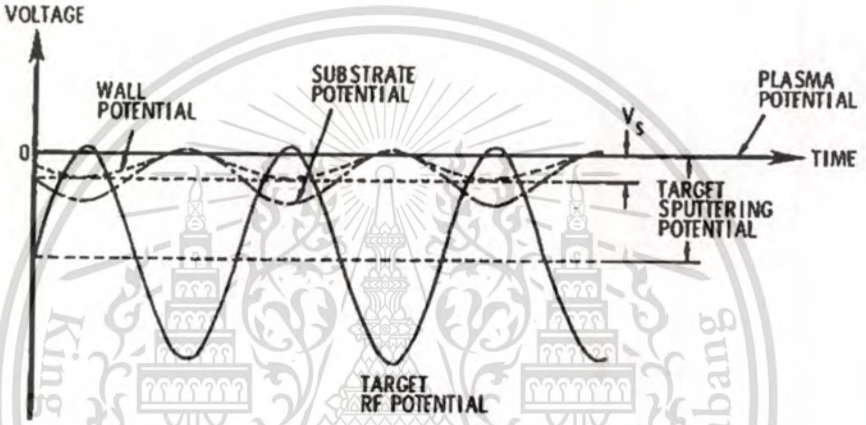

**Fig. 4.7** Approximate representation of voltages (as functions of time) relative to the plasma potential for a single-ended r.f sputtering system in which the wall area is much larger than target area. $V_s$ is the substrate ion bombardment potential.

The above discussion has been presented in the context of planar diode sputtering systems. Magnetron sputtering source can also be used for r.f sputtering. Cylindrical-post, planar, and gun-type magnetrons have all been successfully operated with r.f power. However, some problems are encountered. Magnetron sputtering technology is basically a d.c concept. The cathodes are shaped such that, in concert with the magnetic field, they form electron traps with specific symmetry. Anodes are placed to collect electrons which diffuse out of the trap.

Effective double-ended r.f magnetrons can be provided for some geometries. These configuration provide independent traps for both electrodes but allow magnetic coupling between them so that the electrons leaving one trap can diffuse freely to the vicinity of the others. However, most magnetron configurations must be operated with single-ended arrangements. The magnetic confinement produces gradients in the plasma density, so that special care is required to minimize the voltage and therefore the sputtering rate at the counter electrode. Furthermore, in the planar magnetron case, the current-density concentration under the plasma ring requires that the power level be limited to avoid cracking when using targets with low thermal conductivities. When magnetron sources are driven single-ended, they generally operate in hybrid modes with current voltage characteristics with are not representative of true magnetron behavior. Nevertheless, they provide deposition rates that are typically a factor of three greater than those achieved with r.f planar diodes. (This is to be compared to the factor of twenty-to-thirty improvement in deposition rate which d.c magnetrons provide over d.c diodes when sputtering metals). Reduced electron bombardment and substrate heating are other advantages of magnetrons, as opposed to planar diodes, for r.f sputtering.

### 4.1.3 Magnetrons

The lower limit of operating pressure in the planar-diode sputtering plasma was imposed by the need for the beam electrons ejected from the cathode to undergo enough ionizing collisions with the gas to sustain the plasma before they reach the anode are removed there. The magnetron has been a major advance in sputtering technology, and greatly improves upon this situation. Basically, it incorporates a crosswise magnetic field over the cathode, which traps the beam electrons in orbits in that location and thus greatly increases their path length before they finally escape to the anode by collisional scattering. Because the electron's travel path is now much longer than the electrode gap, the minimum pressure to sustain the plasma is much lower for the magnetron than for the planar diode. The sputtered particles retain most of their kinetic energy upon reaching the substrate, so one obtains the beneficial effects of this energy on film structure. Also, deposition rate is increased because of reduced scattering and redeposition is still measurable. Finally, the increased efficiency of electron usage means that lower applied voltage (typically 500 V) is needed to sustain plasma of a given density, $n_e$, and that the voltage increases even less steeply with power than it does in the planar diode. Unfortunately, the magnetic field can not be made strong enough to deflect the problematic cathode-sheath voltage of a magnetron target is highly nonuniform across the surface, as we will see below. This pattern becomes imprinted on films deposited on stationary substrates when negative ions are affecting the film, because of the beam nature of these ions. Deposition-rate nonuniformity is less sharply imprinted, because the sputtered particles are neural and are emitted in more or less the broad cosine distribution. Both magnetrons and planar diodes can be operated using r.f excitation when one needs to couple power through insulating targets.

Many configurations of magnetic field and cathode shape have been developed for various applications, but here shows magnetron operating principles with reference to the planar, circular configuration of Fig. 4.8 [2]. The target material to be sputtered in a disc 3 to 10 mm thick which is bonded for good thermal contact to a water-cooled Cu backing plate. Bonding is best done by soldering, although epoxy bonding or clamping onto a coating of thermally conductive vacuum grease can be employed instead at moderate plasma power densities. The cooling water is best deionized to prevent electrolytic corrosion between the electrically biased backing plate and the grounded water supply. The entire cathode assembly is floated off ground by a ceramic insulating ring which can also form part of vacuum wall by employing O-ring seals. The adjoining grounded metal vacuum wall then acts as the anode, although grounded shields are often added to confine the sputtered material. The anode is spaced closely enough to the edge of the cathode so that plasma cannot ignite between them. The crosswise magnetic field is established by a ring of bar magnets plus one central one, and these are connected on the back by an Fe "field-return" plate to complete the magnetic circuit and to confine the field. Using the strongest (Nd-Fe-B) magnets, the field over the target can approach one kilogauss, or 0.1 T in SI units.

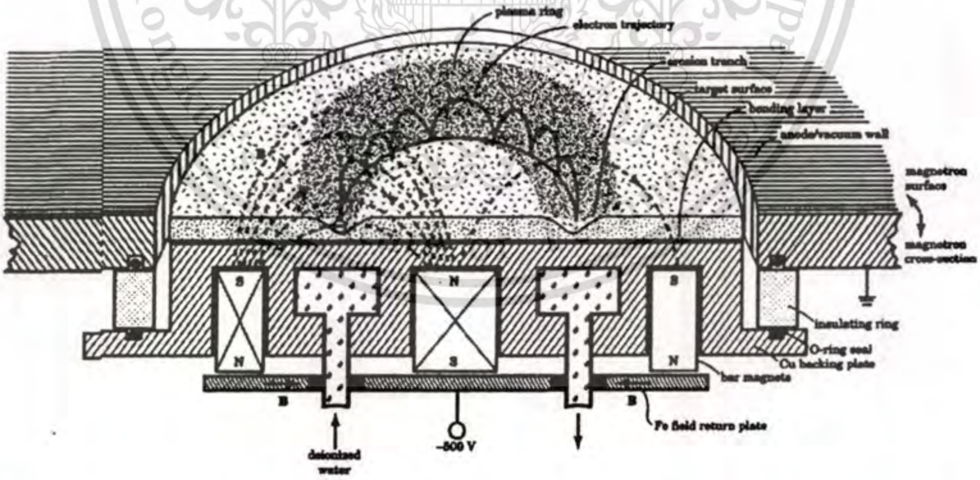

**Fig. 4.8** Planar-magnetron structure and behavior. The electron-orbit radius is shown much larger than actual size for clarity.

The film thickness nonuniformity that results from plasma compression in magnetrons can be avoided by moving the substrates around during deposition, as was done in dealing with point sources of evaporant. Common deposition geometry utilizes the rectangular magnetron, a variation of the Fig. 4.8. Localization of the plasma over the target by magnetron's transverse magnetic field results in a much lower plasma density over the substrate than in the case of the planar diode. This is desirable when the neutral sputtered particles alone carry sufficient kinetic energy to optimize film structure or when one wants to minimize the substrate heating that results from ion bombardment. In other cases, however, one may want to further increase film bombardment while retaining the low operating pressure of the magnetron. One way to do this is by "unbalancing" the magnets, as shown in Fig. 4.9. There, the central bar magnet has been replaced by a smaller one that cannot pull in all the field lines emanating from the magnets in the ring. Some of these lines then curve away toward the substrate. Since electrons traveling parallel to B are not acted on by B, they can escape along these field lines and toward the substrate, pulling positive ions along with them by ambipolar diffusion and thus increasing ion flux to the substrate. The bombardment energy may then be increased if necessary by negatively biasing the substrate.

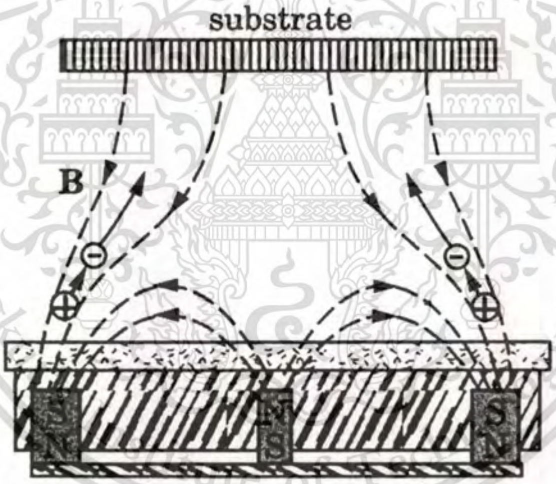

**Fig. 4.9** Plasma flow toward the substrate along magnetic field lines in an unbalanced magnetron.

### 4.1.4 Reactive Sputtering

Reactive Sputtering is a process in which a fraction of at least one of the coating species enters the deposition system in the gas phase. The target is typically either a pure metal (or metal alloy) or a compound containing volatile species. In the former case, the high vapor-pressure species, e.g., N in TiN, S in CdS, or O in $VO_2$, is provided entirely in the gas phase (via $N_2$, $H_2S$, and $O_2$, respectively) while in the latter case (e.g., GaAs in $As_4$) a considerably smaller partial pressure of the reactive gas is added to the discharge to account for the less than unity sticking probability of that species at the growing film surface. The advantages of reactive sputtering are: (i) compound can be formed using relatively easy-to-fabricate metallic targets, (ii) insulating compounds can be deposited using d.c power supplies, and (iii) films with graded compositions can be formed. The difficulty in the reactive-sputtering process is the complexity which accompanies its versatility.

Chemical reactions occur at the target, at the substrate, and in cases of very high working pressures, in the gas phase. When sputtering with a reactive-gas/Ar mixture, the relationship between film properties and the reactive gas injection rate is generally very nonlinear. The condensing films can be considered as an additional pump for the reactive gas. The nonlinearity occurs because the sticking probability (or getter-pump speed) of the condensing coating depends in a complex way on its growth rate, composition, film structure, and temperature. The composition dependence is shown in Fig. 4.10 for $N_2$ incident on a growing Ti film. Note that as the number of $N_2$ molecules adsorbed per Ti atom deposited approaches 0.5 (i.e., a stoichiometric TiN film), the sticking probability $\alpha$ drops by more than two orders of magnitude. The decrease in $\alpha$ occurs as the number of unoccupied surface adsorption sites decreases. Thus, for example, when sputtering in an $N_2$/Ar mixture at low reactive-gas injection rates, virtually all of the injected gas can react with the film. Consequently, the nitrogen is largely removed from the working gas, and the cathode process becomes primarily one of simple Ar sputtering of a metal. The coatings deposited under such conditions are generally metallic in nature.

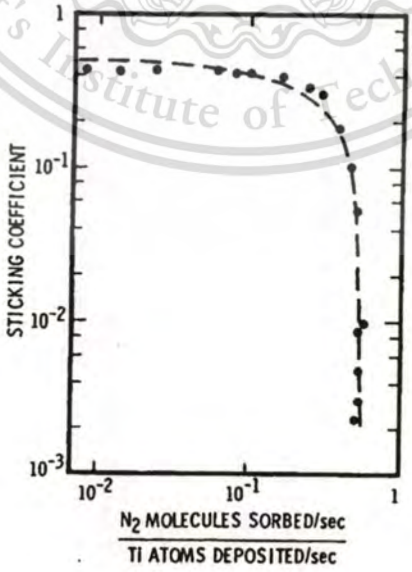

**Fig. 4.10** Sticking coefficient of $N_2$ measured during the continuous deposition of Ti as a function of the ratio of the getter-pumped nitrogen flux to the Ti deposition flux.

observed in planar diodes, planar magnetrons, and cylindrical magnetrons. Many papers have been written concerning the transition mechanism. It is important to realize that the reactive sputtering process is dependent on the total system; i.e., its geometry, the accumulation of coating on walls and fixtures and the positions of gas injection. All these parameters must be carefully controlled in order for reactive sputtering to effectively use on a production basis.

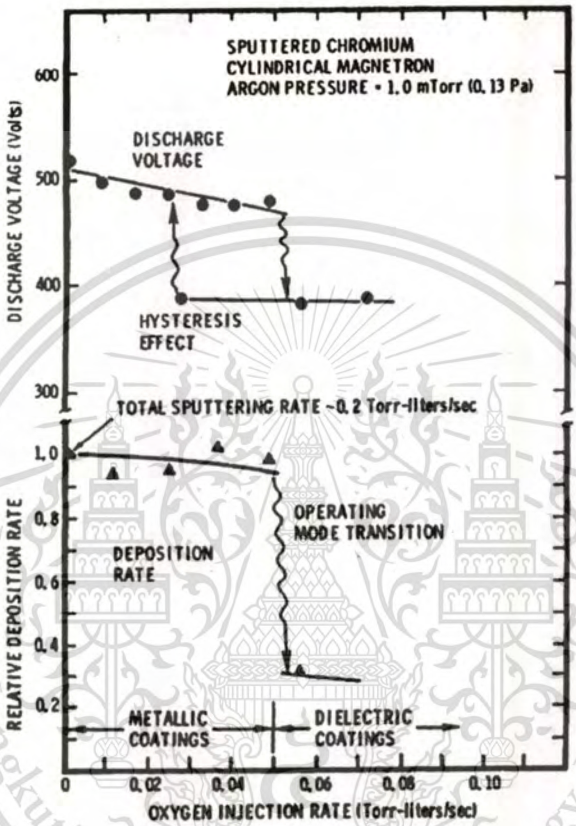

**Fig. 4.11** Transitions in the steady-state operating mode of a Cr cylindrical-post magnetron sputtering source due to injection of oxygen.

Several techniques have been developed to increase the deposition rate during reactive planar magnetron sputtering which take advantage of the nonuniform cathode current densities in these devices. For reactive sputtering in $N_2$, where the hysteretic behavior is more gradual than in $O_2$, Sproul has developed feedback control techniques which allow film deposition rates of transition-metal nitrides such as TiN, ZrN, and HfN at value very nearly equal to those of the pure metals. The feedback controls maintain constant target power, total pressure, and $N_2$ partial pressure [3].

### 4.1.5 RF Bias

The low impedance of capacitors in the high-frequency regime allows r.f power to be coupled to the driven electrode through a series capacitor as shown in Fig. 4.12a. This is an importance and widely used technique, which greatly improves plasma control. Consider the typical "asymmetric" plasma geometry of Fig. 4.12a, in which the area of grounded "electrode" is much larger than that of the driven electrode because it includes not only the substrate and its platform but also all of the vacuum-wall surface that is reached by the plasma. Now, recall that the ion flux or current density, $j_+$, injected into the sheath and arriving at the surface is determined only by plasma density and $T_e$. If these two quantities are reasonable uniform throughout the plasma, then the electrode of smaller area, A, will receive less ion current, $I_+ = j_+A$, than will the larger electrode. Conversely, electron current to a surface is determined by the plasma potential, $V_p$, relative to that surface When the driven electrode tries to become more positive than $V_p$ on its positive swing, the plasma instantly floats above it by discharging electrons into that electrode. Similarly, when the driven electrode tries to pull $V_p$ below ground on its negative swing, the plasma remains above ground by discharging electron into the substrate and the wall.

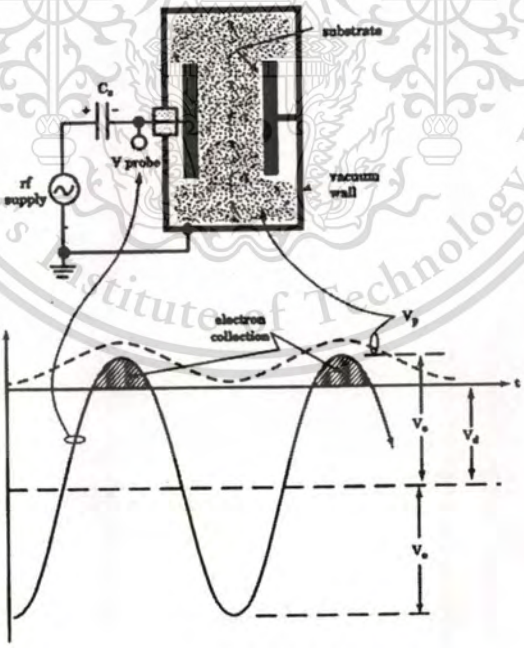

**Fig. 4.12** A d.c self-biasing of a capacitively coupled r.f waveform due to plasma-electrode asymmetry.

Thus electron current is not governed by electrode area, whereas ion current is. This means that the driven electrode in the asymmetric reactor of Fig. 4.12a receives less ion current than electron current, averaged over time. Because the coupling parameter blocks this net dc current, the electrode and capacitor proceed to charge up negatively. Without the capacitor (dc coupling), this dc current would flow around the circuit, and the plasma would behave as a dc plasma in parallel with an r.f one. A d.c plasma leads to many problems when insulating surface are in the circuit.

As the coupling capacitor of the asymmetric r.f plasma continues to charge negatively, the r.f waveform at the electrode shifts downward as shown in Fig. 4.12b; that is, it develops a negative dc self-bias voltage, $V_d$. This bias reduces both the potential across which electrons are being collected from the plasma and the length of the time intervals during which this collection takes place, as represented by the shaded portion of the biased waveform.

r.f bias may also be applied to insulating substrates the same circuitry. This is useful for ion-bombardment cleaning of the substrate ("backsputtering") prior to film deposition, or for increasing the energy of film ion bombardment during deposition to produce structural modification. When the substrate is being transported past the target or other vapor source to obtain good deposition uniformity, the r.f must be coupled to it through a metal backing plate which must carry the very high r.f displacement current mentioned in the previous subsection. Sliding or rolling electrical contact is usually insufficient, but the current can be capacitively couple from an r.f-driven spaced closely behind the moving backing plate.

A magnetic field applied perpendicular to the electrodes also reduces effective area by inhibiting the radial diffusion of electrons across the field lines. In the low-frequency regime, plasma spreading is further reduced because the perpendicularly directed beam electrons dominate plasma excitation. r.f bias may be hard to predict, but it is easy to measure using a high-impedance, high-voltage r.f oscilloscope probe on the cathode vacuum feedthrough as shown in Fig. 4.12a. It is useful to measure both $V_0$ and $V_d$ in this way so that the fraction bias may be determined. Alternatively, $V_d$ alone can be measured with the circuit of Fig. 4.13. The resistive divider reduces $V_d$ to a conveniently measured level. At the conventional r.f frequency of 13.56 MHz, the impedance of L and C shown are 3.4 kΩ and 12 Ω, respectively, so that only 0.4 percent of the r.f voltage appears across the capacitor and resistive divider.

For maximum bias where $V_d = V_0$, an upper limit on ion current, $I_+$, to the biased electrode can be estimated by assuming that all of the applied power, P, goes into ion acceleration across the cathode-sheath voltage drop, $V_b$; that is,

$$P = I_+V_b \sim I_+V_d \sim I_+V_0$$

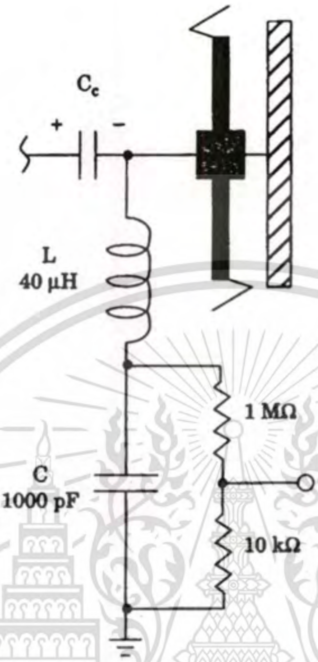

**Fig. 4.13** d.c-bias probe with L and C size for 13 MHz operation

This assumption is most reasonable for monatomic gases at low pressure and high power, where the fraction of power dissipated in other ways is smallest.

## 4.2 Reactive Gas-Timing RF Magnetron Sputtering

### 4.2.1 Magnetron Sputtering

Magnetron sputtering technology developed in the 1970s [4] has also been used for selective coatings with improved some performances, in particular, lower emittance and less environmental pollution than the electrochemical methods. The sputtering is a complicated process with several operation parameters being correlated. In a simple dc sputtering system the target serves as source material to be deposited. Argon is the most commonly used sputtering gas which serves as the medium where a glow discharge is initiated and sustained. Microscopically, argon ions in the discharge strike the target plate and eject neutral target atoms through energetic collisions. These atoms enter and pass through the discharge region and they eventually deposit on the substrate as growing film. The magnetron was developed in the 1970s by placing magnets behind the target. The magnetic field concentrates and intensifies the plasma in the space close to the target, as a result of trapping of electrons near the target surface. This leads to larger discharge current, increased sputter deposition rates, and reduced electron bombardment of substrates. Magnetron sputtering is presently the most widely, commercially practiced sputtering method. The chief reason for its success is the high deposition rates achieved. Figure 4.14 shows a schematic drawing of the process in dc planar magnetron sputtering.

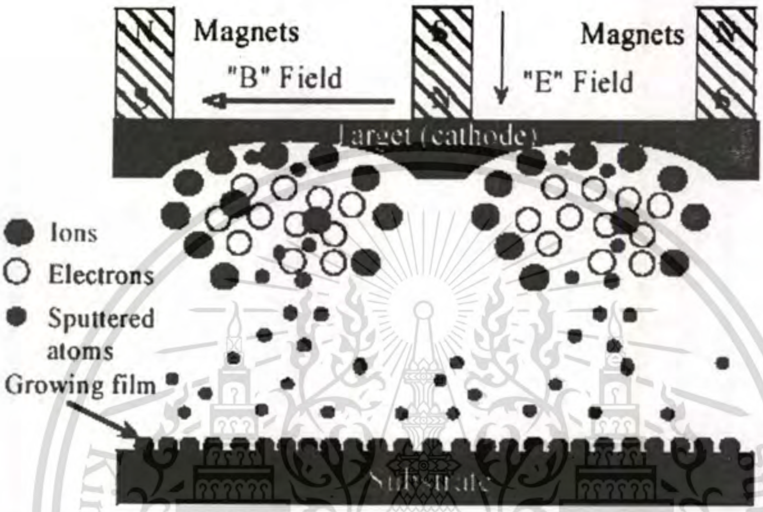

**Fig. 4.14** Schematic drawing of process under dc planar magnetron sputtering.

### 4.2.2 Reactive RF Sputtering

Reactive sputtering is a method to deposit films which have a chemical composition different from that of the target, by adding a gas to react with the target material. The most common reactive gas is oxygen, usually mixed with argon to produce an oxide film. An important phenomenon in reactive sputtering is the hystersis behavior. A general hysteresis process is illustrated by the change of system pressure with varying flow rate of the reactive gas, say oxygen. Typically, the curve measured by increasing oxygen flow does not coincide with that measured by decreasing oxygen flow. There is a critical point along the increasing oxygen flow with two target modes. When the oxygen flow is smaller than the critical oxygen flow, the target is metallic, therefore metallic atoms are sputtered and a compound is formed on the substrate. So this is called the 'metallic mode'. When the oxygen flow is bigger than the critical, the metallic target surface is 'poisoned' by formation of oxide on its surface, therefore it is called the 'compound mode'. For metal targets, the target voltage after the critical point is dropped due to higher secondary-electron emission yields in the 'compound mode'. The target voltage versus oxygen flow is used in our study to identify the critical oxygen flow. Figure 4.15 shows the target voltage for both increasing and decreasing oxygen flow. For increasing oxygen flow, target voltage shows a sudden drop at a critical oxygen flow down to lower voltage value. For decreasing oxygen flow, target voltage keeps low as oxygen decreases pass the critical oxygen flow, and the voltage rises somewhere at oxygen flow which is lower than that critical value. Critical oxygen flow depends on operation conditions. Figure 4.16 shows schematic r.f sputter.

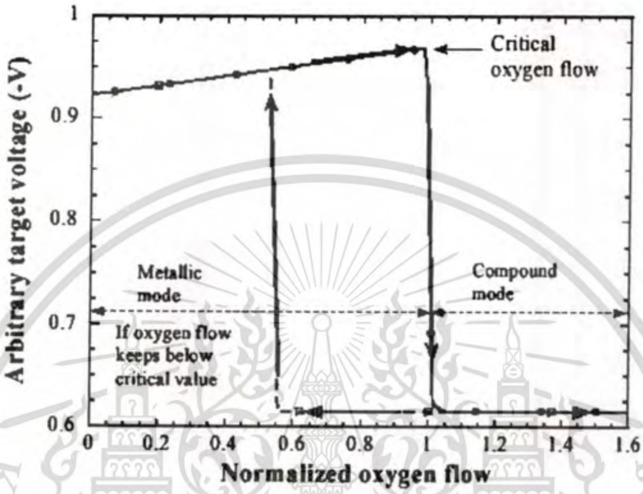

**Fig. 4.15** Scheme of target voltage versus oxygen flow rate showing hysteresis behavior.

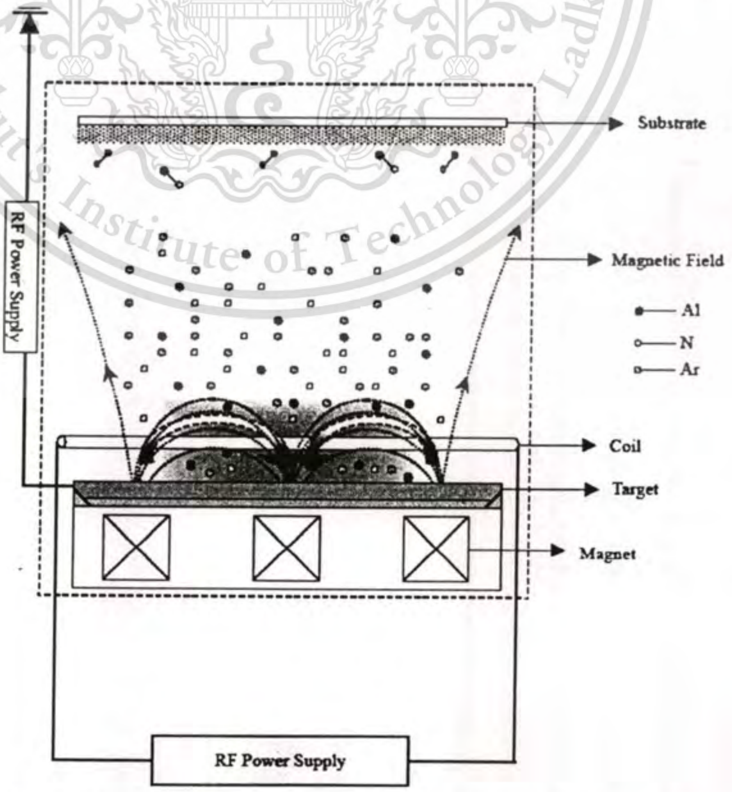

**Fig. 4.16** A schematic arrangement of r.f sputtering system.

### 4.2.3 Gas-Timing Method

This is the first time purposed for depositing thin films by sputtering process with this invention method, called **"gas-timing"**, to deposit III-nitride and oxynitride materials without substrate heating during and/or post deposition. More particularly, this method effectively to deposit various nitride films on many types of substrates. The method comprising loading a substrate into a vacuum chamber having the target, introducing the process gas controlled with gas-timing technique comprising argon, nitrogen and oxygen alternately and/or intermittently into the chamber and forming plasma of the process gas in the chamber to deposit nitride film on the substrate. The gas-timing method is also desirable to obtain a stable, easy to control plasma during the sputtering process with high deposition rate.

Driven by improvements in deposition techniques, these thin films materials are becoming common-place in many vacuum coating applications. Reactive sputtering continues to emerge as one of the most economical methods for depositing compound thin films. With properly configured power delivery and process control measures, high rate, arc free deposition of many oxides and nitrides is now possible. As reactive sputtering methods have matured, interest in extending the technique beyond simple binary compounds has been growing. As material complexity increases however, so do the challenges of process control as we propose in this invention.

The control of three sputtering gases in the sputtering process adds significant complexity and presents the issue of competing reactions. Since three sputtering gases can affect the state of the target surface and the plasma conditions. In this invention, the timing control of sputtering gas flow rate (gas-timing control) was used to control the deposition of nitride thin films. The gas – timing method is effectively technique for depositing films on various substrates such as glass, plastic or other flexible substrates without substrate heating by using reactive r.f magnetron sputtering system with a good deposition rates. It is also desirable to obtain a stable and easy to control plasma during the sputtering process. The method of gas-sequence control is basically used in epitaxy growth systems such as MOCVD and MOVPE for deposition of thin films.

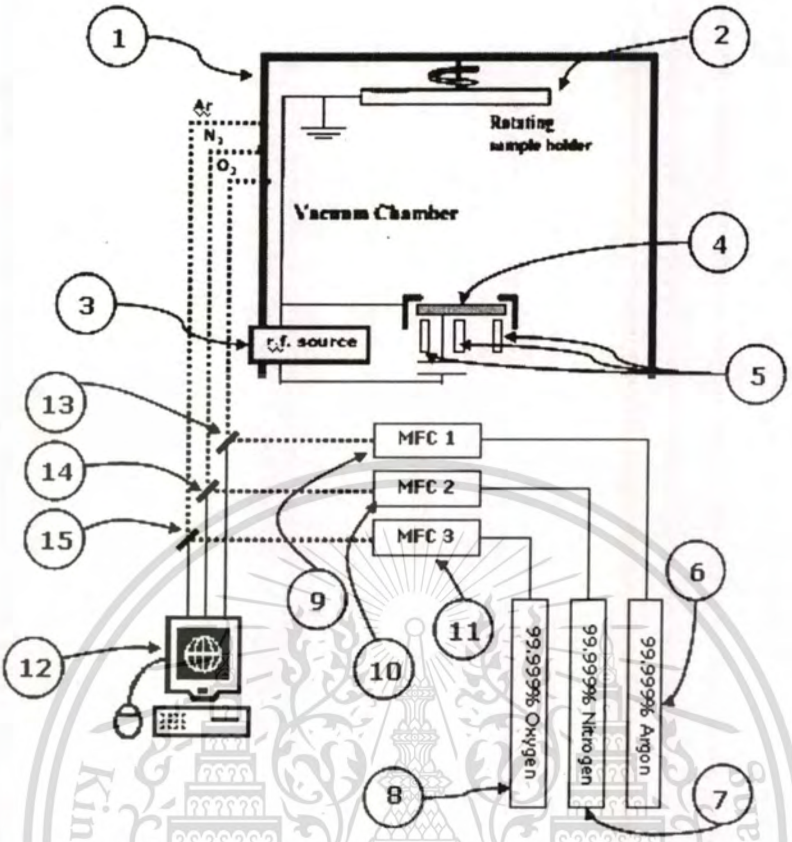

**Fig. 4.17** A schematic of vacuum and control apparatus used for three gases in the sputtering process.

The schematic of our growth system as shown in Fig. 4.17 comprises a sputtering chamber, the substrates, the targets, three mass flow controllers controlled flow rate of argon, nitrogen and oxygen gases alternately and intermittently into the sputtering chamber, radio frequency generator with 13.56 MHz which irradiated in the sputtering chamber to decompose sputtering gases.

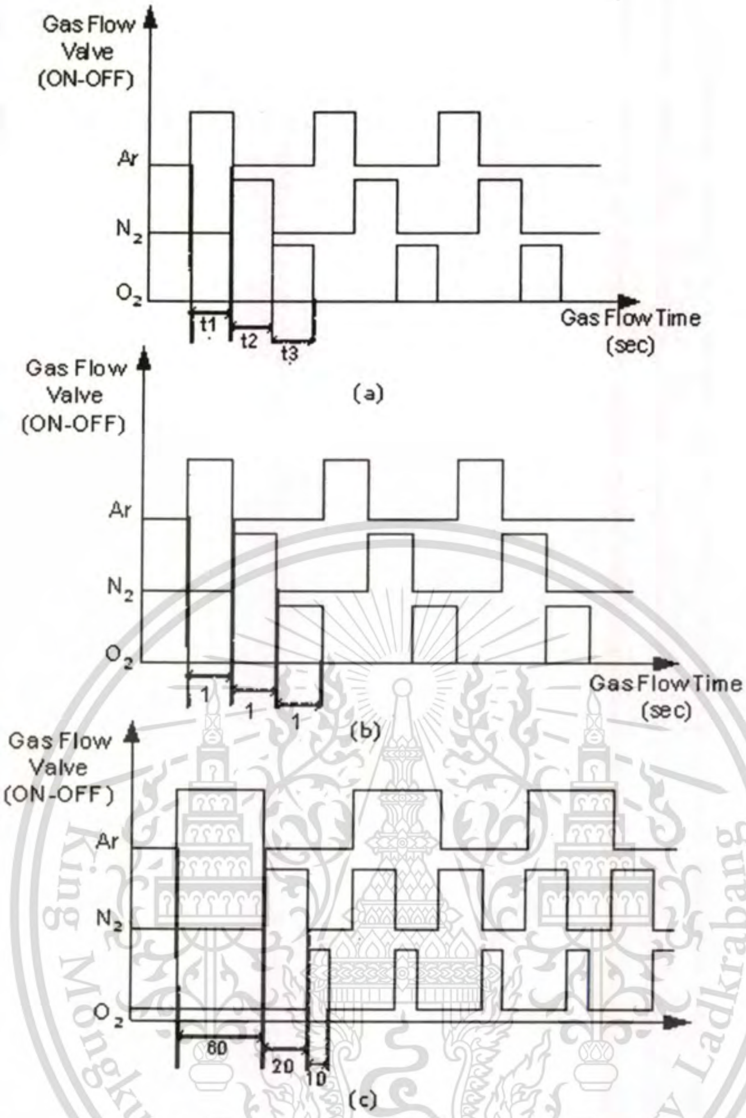

**Fig. 4.18** Diagram of gas-timing sequence of Ar (t1), $N_2$ (t2), and $O_2$ (t3) fed into sputtering chamber alternately at least 1 second (sec).

The gas-timing technique which uses to control gas (Ar, $N_2$, $O_2$) flow rate feeding into the sputtering chamber includes of three sequence processes as shown in Fig. 4.18, 4.19 and 4.20.

Figure 4.18 depicts the gas-timing sequence of Ar (t1), $N_2$ (t2), and $O_2$ (t3) which are fed into the sputtering chamber in sequence respectively (Fig. 4.18(a)) but the sequence of $N_2$ and $O_2$ can be interchangeable. The technique comprises the steps of depositing thin film layer on the substrate, which the following sequence timing;

Firstly; flow Ar at least 1 second (Fig. 4.18(b)), or 60 seconds (Fig. 4.18(c)) into the chamber in order to bombard the target, the duration of bombardment can be varied to any number less or more than 60 seconds. Second; flow $N_2$ at least 1 second (Fig. 4.18(b)), or 20 seconds (Fig. 4.18(c)) into the chamber as reactive ions, the duration of $N_2$ flow can be varied to any number less or more than 20 seconds. Third; flow $O_2$ at least 1 sec (Fig. 4.18(b)), or 10 sec (Fig. 4.18(c)) into the chamber as reactive ions, the duration of $O_2$ flow can be varied to any number less or more than 10 seconds.

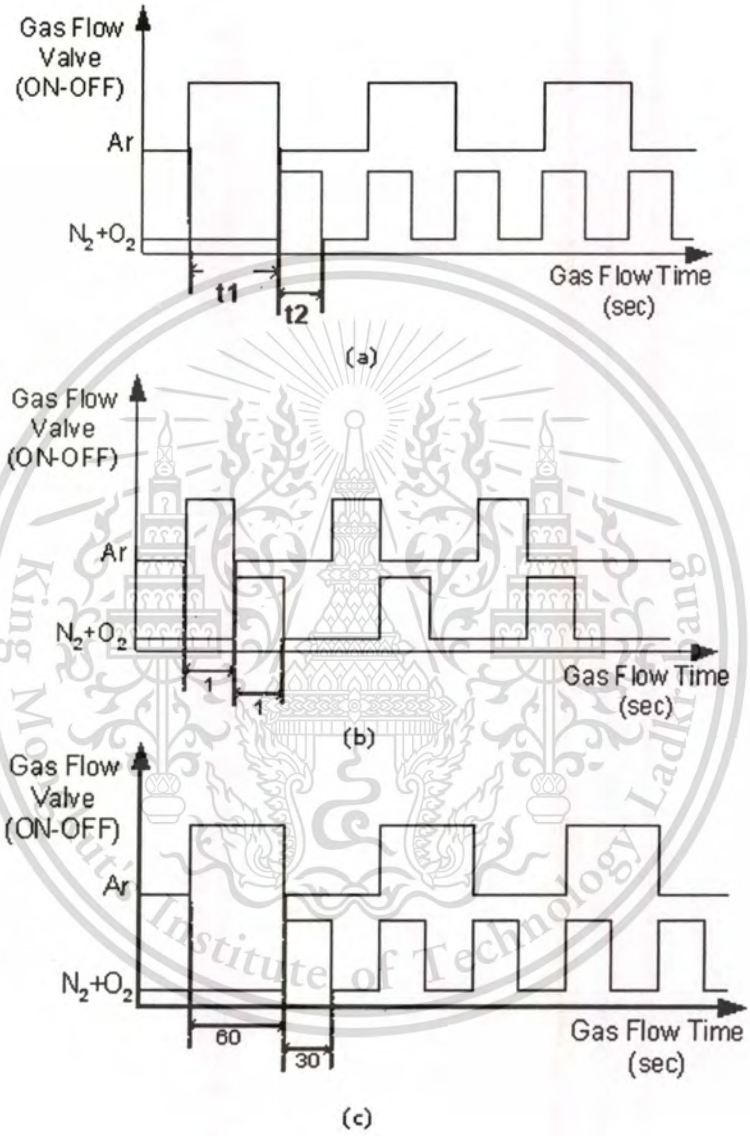

**Fig. 4.19** Diagram of gas-timing sequence of Ar (t1) and mixed $N_2+O_2$ (t2) fed into sputtering chamber alternately at least 1 second (sec).

Figure 4.19 depicts the gas-timing sequence of Ar (t1) and mixed $N_2+O_2$ (t2) as shown in Fig. 4.19(a), alternatively fed into sputtering chamber. As shown in Fig. 4.19, the invention comprises the steps of depositing thin film layer on the substrate, wherein;

Firstly; flow Ar at least 1 sec (Fig. 4.19(b)), or 60 sec (Fig. 4.19(c)) into the chamber for bombarding the target, the duration of bombardment can be varied to any number less or more than 60 seconds. Second; flow $N_2$+$O_2$ at least 1 sec (Fig 4.19(b)), or 30 sec (Fig. 4.19(c)) into the chamber as reactive ions. The duration of mixed $N_2$+$O_2$ can be varied to any number less or more than 30 seconds.

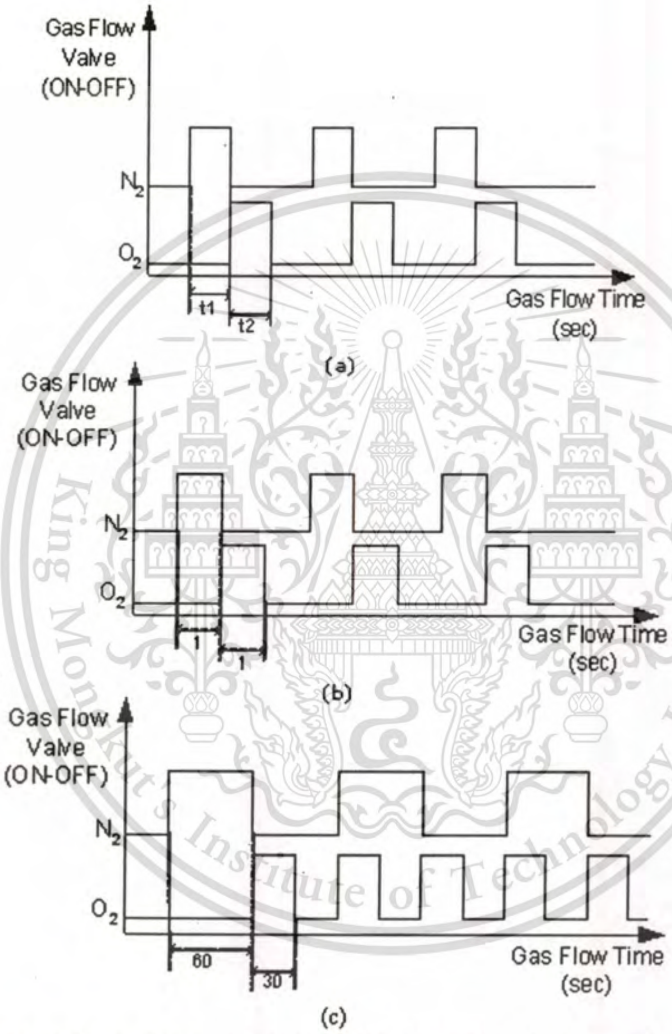

**Fig. 4.20** Diagram of gas-timing sequence of $N_2$ (t1) and $O_2$ (t2) flow into sputtering chamber alternately at least 1 second (sec).

Figure 4.20 depicts the gas-timing sequence of $N_2$ (t1) and $O_2$ (t2) as shown in Fig. 4.20(a), alternatively fed into sputtering chamber. As shown in Fig. 4.20, the process comprises the steps of depositing thin film layer on the substrate, wherein;

Firstly; flow $N_2$ at least 1 sec (Fig. 4.20(b)), or 60 sec (Fig. 4.20(c)) into the chamber as ion bombarding and reactive ions, The duration of $N_2$ flow can be varied to any number less or more than 60 seconds. Second; flow $O_2$ at least 1 sec (Fig. 4.20(b)), or 30 sec (Fig. 4.20(c)) into the chamber as reactive ions. The duration of $O_2$ flow can be varied to any number less or more than 30 seconds.

### 4.2.4 The Edwards Auto 500 Reactive RF Magnetron Sputtering System

Figure 4.22 shows the r.f magnetron sputtering system used to grow AlN, InN, ITO and InON thin films in this research. It is a model of Edwards Auto 500, made from BOC Edwards Company, ENGLAND. For this system, the r.f frequency is 13.56 MHz and the maximum r.f power is 600 watts. There are two mass flow controllers and a thickness monitor. The rotary and diffusion pumps are used to achieve high vacuum, $10^{3}$-$10^{-3}$ mbar for rotary pump and $10^{-3}$-$10^{-8}$ mabr for diffusion pump, as shown in Fig 4.22. The target holder used for 3-inch diameter target material and substrate holder in vacuum chamber also shown in Fig. 4.23.

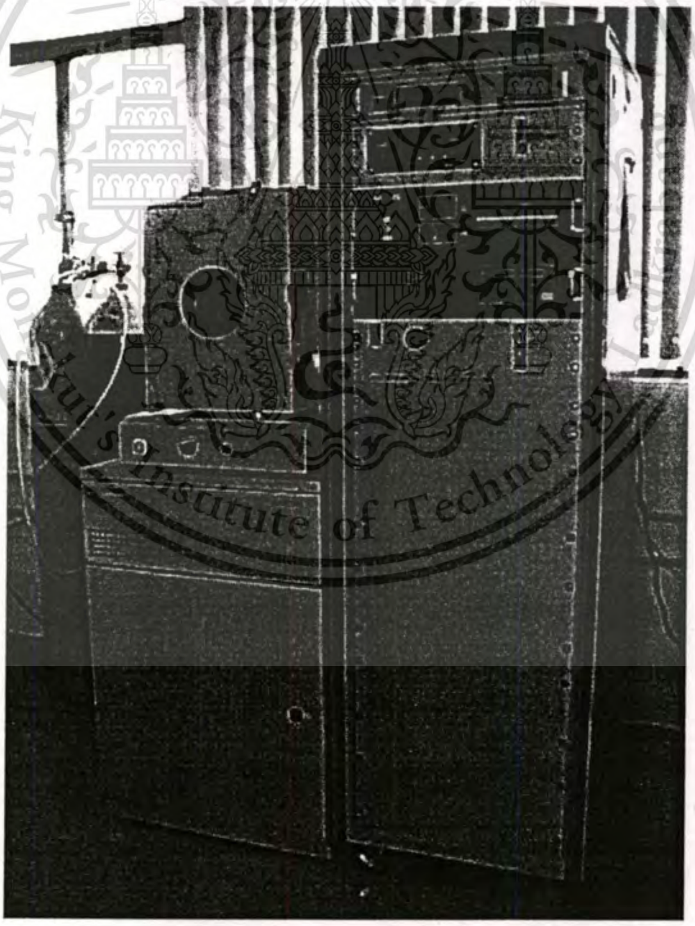

**Fig. 4.21** The r.f magnetron sputtering system used in this experiment.

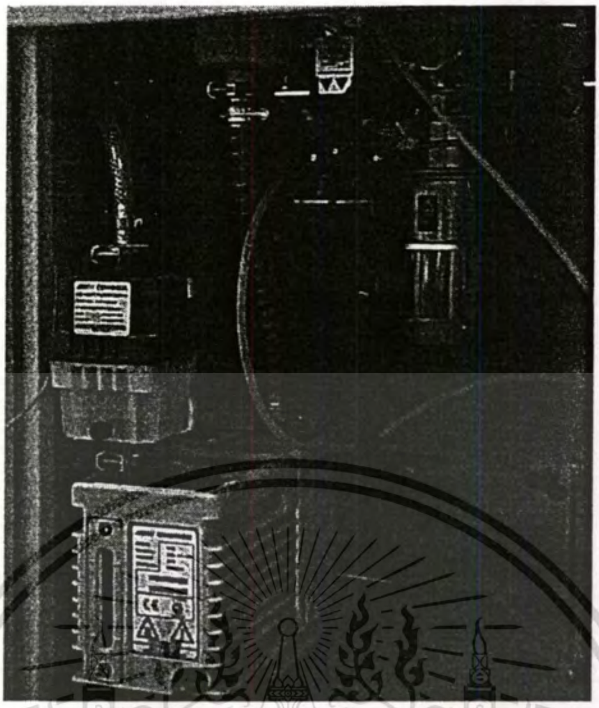

**Fig. 4.22** Rotary and diffusion pumps in sputtering system.

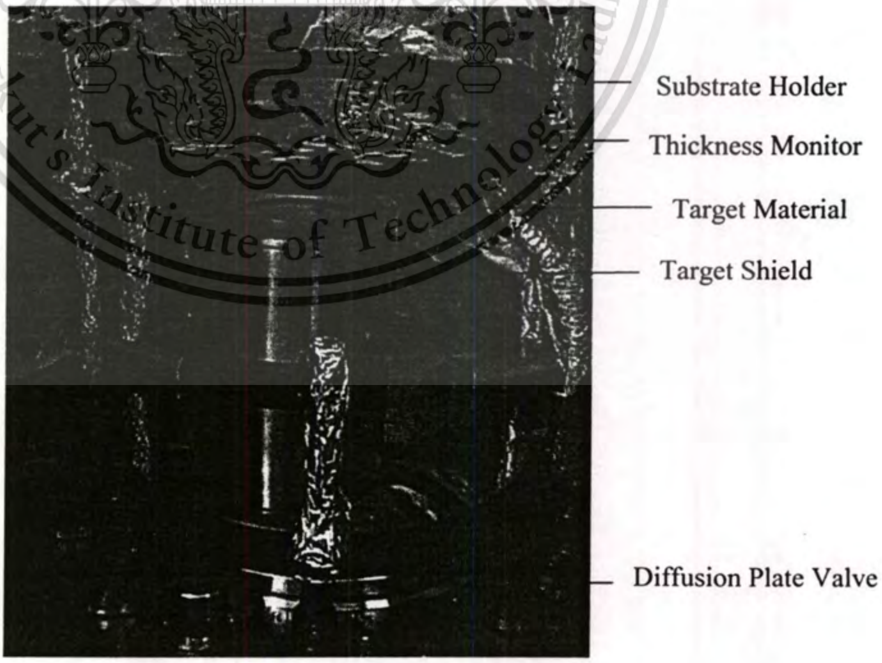

**Fig. 4.23** Target and substrate holder in vacuum chamber.

## 4.3 Chapter Summary

The sputter process has almost no restrictions in the target materials, ranging from pure metals where a d.c-power supply can be used to semiconductors and isolators which require a r.f-power supply or pulsed dc. Deposition can be carried out in either non reactive (inert gas only) or reactive (inert & reactive gas) discharges with single or multi-elemental targets. During the sputter process a magnetic field can be used to trap secondary electrons close to the target. The electrons follow helical paths around the magnetic field lines undergoing more ionizing collisions with neutral gaseous near the target than would otherwise occur. This enhances the ionisation of the plasma near the target leading to a higher sputter rate. It also means that the plasma can be sustained at a lower pressure. The sputtered atoms are neutrally charged and so are unaffected by the magnetic trap.

The use of radio frequency, r.f to sputter material was investigated in the 1960's. Davidse and Maiseel used r.f sputtering to produce dielectric films from a dielectric target in 1966. In 1968 Hohenstein co-sputtered glass using r.f and metals (Al, Cu, Ni) with d.c, to form cermet resistor films. The r.f sputter deposition is not used extensively for commercial PVD for several reasons. The major reasons are it is not economic to use large r.f power supplies due to their high cost and the fact that you introduce high temperatures, due to the high self-bias voltage associated with r.f power, into insulating materials.

The term reactive sputtering was introduced by Veszi in 1953. Reactive sputter deposition of tantalum nitride for thin film resistors was an early application. However it wasn't until the mid-1970s that reactively sputter-deposited hard coatings on tools began to be developed and they became commercially available in the early 1980s. Although the concept of reactive sputtering is quite simple, the art of employing it effectively to produce high quality insulating films at maximum rates can be a real challenge. The nature of forming insulating layers in a dc sputter deposition is inherently disruptive to the process. In recent years the issue of arcing in reactive sputtering has been effectively managed using one of several power delivery techniques. The most common of these are pulsed-dc in a single magnetron system and low frequency ac power in a dual magnetron system. In both cases a voltage reversal at the cathode is used to effectively eliminate charge built up on the target surface and thus avoid the breakdown event. Many modern power supplies also posses arc detection and arc handing circuitry designed to quickly extinguish an arc should one occur.

In this research, the innovation technique called **"reactive gas-timing"** will be purposed to grow AlN, InN and their compounds thin films by r.f magnetron sputtering at room temperature. Gas-timing technique is a process to control timing sequence of feeding gases (Ar, $N_2$ and $O_2$) into the sputtering process. The period of time sequence depends on thin film thickness requirement.

## References

[1] R.V. Stuart, **"Vacuum Technology, Thin Films, and Sputtering: An Introduction"**, Academic Press, New York, 1983.

[2] Donald L. Smith, **"Thin Film Deposition: Principles and Practices"**, McGraw-Hill, New York, 1995.

[3] David A. Glocker, Ismat Shah, editors, **"Handbook of Thin Film Process Technology"**, Institute of Physics Publishing, Bristol, 1995.

[4] Musil J, and Vleek, J. Surface and Coatings Technolog., 112: 162-169, 1999.

# CHAPTER 5

# THIN FILM CHARACTERIZATIONS

## 5.1 Structural Characterization Methods

### 5.1.1 X-Ray Diffraction (XRD)

X-ray diffraction was discovered by Max von Laue in 1912. It has provided a wealth of important information to science and industry [1, 2] for example, much that is known about the arrangement and the spacing of atoms in crystalline materials has been directly deduced from diffraction studies. In addition, such studies have led a much clearer understanding of the physical properties metals, polymeric materials, and other solids. X-ray diffraction is currently of prime importance in elucidating the structure of such complex natural products as steroids, vitamins, and antibiotics. X-ray diffraction also provides a convenient and practical means for the qualitative identification of crystalline compounds. This application is based upon the fact that an X-ray diffraction pattern is unique for each crystalline substance. Thus, if an exact match can be found between the pattern of an unknown and an authentic sample, chemical identity can be assumed. In addition, diffraction data sometimes yield quantitative information in concerning a crystalline compound in a mixture. The method may provide data that are difficult or impossible to obtain by other means as, for example, the percentage of graphite in a graphite-charcoal mixture.

X-rays are electromagnetic radiation with typical photon energies in the range of 100 eV-100 keV. For diffraction applications, only short wavelength x-rays (hard x-rays) in the range of a few angstroms to 0.1 angstrom (1 keV-120 keV) are used. Because the wavelength of x-rays is comparable to the size of atoms, they are ideally suited for probing the structural arrangement of atoms and molecules in a wide range of materials. The energetic x-rays can penetrate deep into the materials and provide information about the bulk structure.

X-rays are produced generally by either x-ray tubes or synchrotron radiation. In a x-ray tube, which is the primary x-ray source used in laboratory x-ray instruments, x-rays are generated when a focused electron beam accelerated across a high voltage field bombards a stationary or rotating solid target. As electrons collide with atoms in the target and slow down, a continuous spectrum of x-rays are emitted, which are termed Bremsstrahlung radiation. The high energy electrons also eject inner shell electrons in atoms through the ionization process. When a free electron fills the shell, a x-ray photon with energy characteristic of the target material is emitted. Common targets used in x-ray tubes include Cu and Mo, which emits 8 keV and 14 keV x-rays with corresponding wavelengths of 1.54 Å and 0.8 Å, respectively.

In recent years synchrotron facilities have become widely used as preferred sources for x-ray diffraction measurements. Synchrotron radiation is emitted by electrons or positrons travelling at near light speed in a circular storage ring. These powerful sources, which are thousands to millions of times more intense than laboratory x-ray tubes, have become indispensable tools for a wide range of structural investigations and brought advances in numerous fields of science and technology.

**Lattice Planes and Bragg's Law:**

X-rays primarily interact with electrons in atoms. When x-ray photons collide with electrons, some photons from the incident beam will be deflected away from the direction where they original travel, much like billiard balls bouncing off one anther. If the wavelength of these scattered x-rays did not change (meaning that x-ray photons did not lose any energy), the process is called elastic scattering (Thompson Scattering) in that only momentum has been transferred in the scattering process. These are the x-rays that we measure in diffraction experiments, as the scattered x-rays carry information about the electron distribution in materials. On the other hand, In the inelastic scattering process (Compton Scattering), x-rays transfer some of their energy to the electrons and the scattered x-rays will have different wavelength than the incident x-rays.

Diffracted waves from different atoms can interfere with each other and the resultant intensity distribution is strongly modulated by this interaction. If the atoms are arranged in a periodic fashion, as in crystals, the diffracted waves will consist of sharp interference maxima (peaks) with the same symmetry as in the distribution of atoms. Measuring the diffraction pattern therefore allows us to deduce the distribution of atoms in a material.

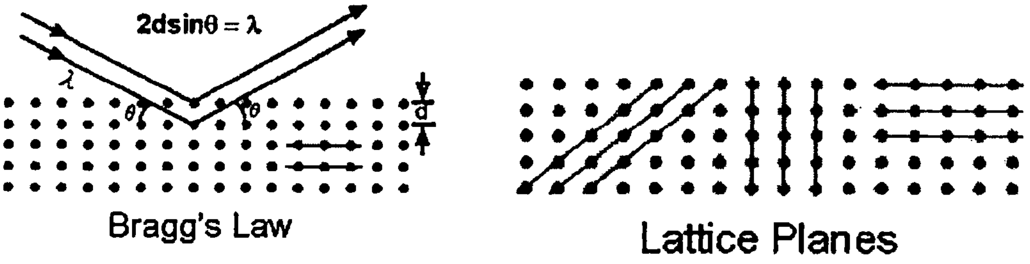

**Fig. 5.1** Schematic illumination of x-ray diffraction in the lattice plane.

The peaks in a x-ray diffraction pattern are directly related to the atomic distances. Let us consider an incident x-ray beam interacting with the atoms arranged in a periodic manner as shown in 2 dimensions in the following illustrations. The atoms, represented as green spheres in the graph, can be viewed as forming different sets of planes in the crystal (colored lines in graph on left). For a given set of lattice plane with an inter-plane distance of d, the condition for a diffraction (peak) to occur can be simply written as

$$m_B\lambda = 2d_B \sin\theta \qquad (1)$$

where $m_B$ is an integer representing the order of diffraction peak, $\lambda$ is the wavelength of the x-ray, $d_B$ the distance between parallel consecutive atomic planes and θ is the angle between these planes and the incident beam. Different elements or compounds are then identified by analysis of the $d_B$ values that are characteristic for the crystalline phase.

Equation 1 is known as the **Bragg's law**, after W.L. Bragg, who first proposed it. The Bragg's Law is one of most important laws used for interpreting x-ray diffraction data. It is important to point out that although we have used atoms as scattering points in this example, Bragg's Law applies to scattering centers consisting of any periodic distribution of electron density. In other words, the law holds true if the atoms are replaced by molecules or collections of molecules, such as colloids, polymers, proteins and virus particles.

and lattice constant:

$$a = \frac{\lambda}{2\sin\theta}\sqrt{h^2 + k^2 + l^2} \qquad (2)$$

where a is lattice constant and h, k,l are diffraction planes

XRD measurements for AlN, InN, ITO and InON thin films were performed by using a D8-Bruker model-XRD diffractometer, as shown schematically in Fig. 5.2, operating with a grazing incidence angle of one degree in parallel beam geometry using CuK radiation using wavelength 1.540598 Å. The effective grain size, i.e. the diameter of assumed spherical particle, was determined from the full width at half maximum (FWHM) of the X-ray diffraction peaks using the Scherrer equation [3] [80]:

$$FWHM(2\theta) = \frac{0.9\lambda}{L\cos(\theta)} \qquad (3)$$

where *L* is the effective grain size. The *FWHM* was determined by fitting each peak by a Lorentzian curve. Broadening caused by internal strain was not taken into account.

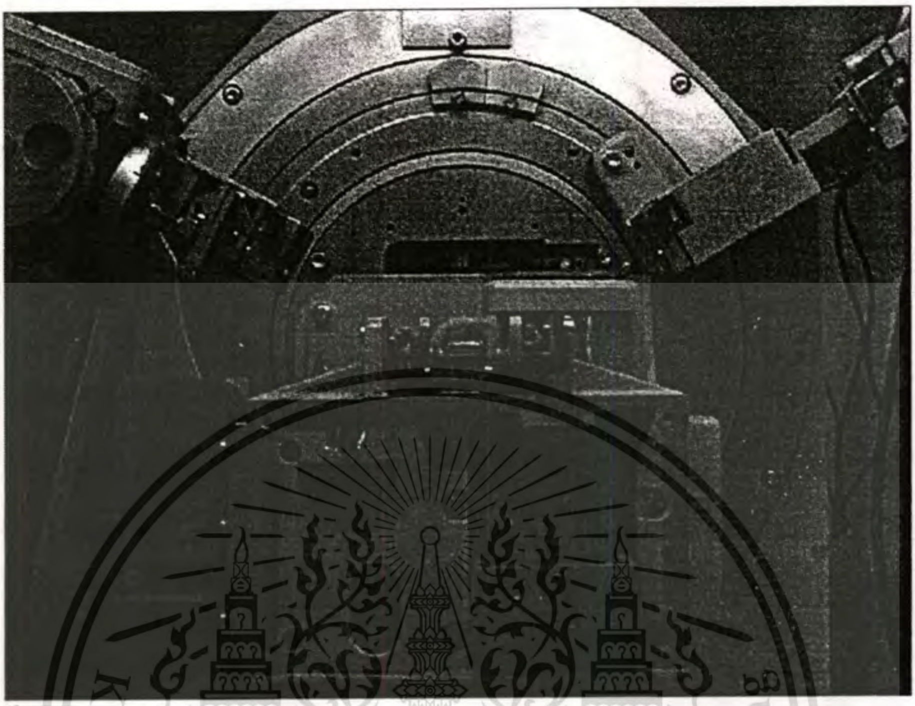

**Fig. 5.2** A photograph of D8-Bruker-XRD used to investigate crystalline structure of all thin films.

### 5.1.2 Field-Emission Scanning Electron Microscope (FE-SEM)

The Scanning Electron Microscope (SEM) uses electrons rather than light to form an image. In a scanning electron microscope, a beam of electrons is produced at the top of the microscope by heating a metallic filament. The electron beam follows a vertical path through the column of the microscope. It makes its way through electromagnetic lenses which focus and direct the beam down towards the sample. Once it hits the sample, other electrons (backscattered or secondary) are ejected from the sample. Detectors collect the secondary or backscattered electrons, and convert them to a signal that is sent to a monitor producing an image. The advantage of using the SEM includes higher magnification, larger depth of focus, greater resolution, and ease of sample observation which makes the SEM one of the most heavily used instruments in many research areas today.

SEM is surface imaging of solids using electron-beam generated secondary electrons [2, 3]. Fig. 5.3 illustrates the electron beam interaction with a solid. The primary beam may be focused to a spot < 50 Å in diameter. Upon interaction with the solid, secondary electrons are generated which are utilized to image the surface. As the high energy primary electrons penetrate the solid, they undergo scattering which increases the interaction volume. Some of the primary electrons will be backscattered toward the surface with little or no loss in energy. Energetic primary electrons ionize atoms in the solid producing x-ray which are characteristic of the elements that are present. With suitable detectors, the x-rays may be detected to provide elements that are present. With suitable detectors, the x-ray may be detected to provide elemental analysis.

The peak in the energy distribution is below 5 eV. In order to efficiently collect the secondary electrons, a high potential bias is applied to a scintillator tube which is positioned in proximity to the sample. The signal was converted to light and fed out through a light pipe to a photomultiplier tube as shown in Fig. 5.4. SEM images at less than 20 Å resolution have been obtained higher magnification with greater depth resolution than optical microscopes. SEM images may become distorted by the surface potential that builds up on insulators or edge effects at sharp contours. Insulators may be coated with a thin (~100 Å) conductive layer to dissipate the surface charge.

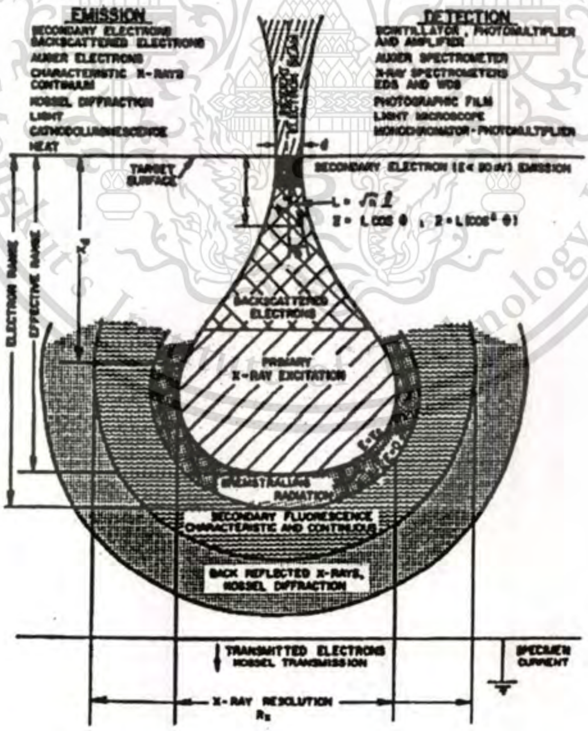

**Fig. 5.3** Diagram illustrating the interaction of the primary electron beam with a solid surface in the production of secondary and backscattered electrons, x-rays, and other secondary radiation.

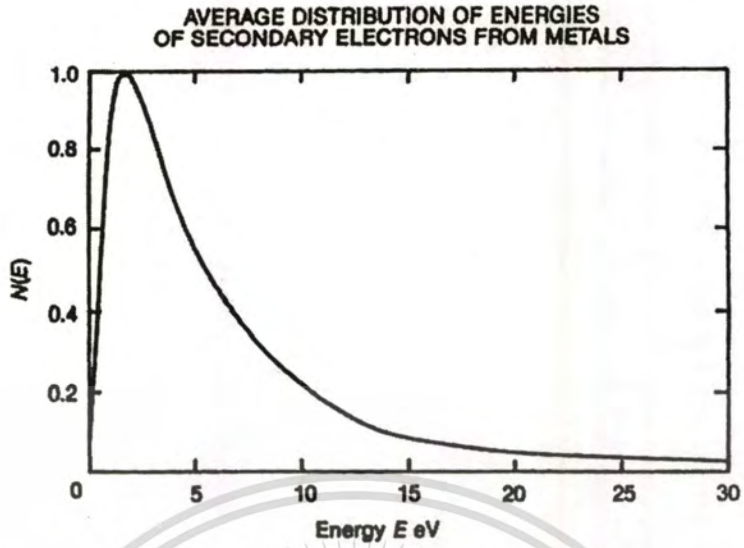

**Fig. 5.4** Plot of the average intensity of secondary electrons from metals as a function of energy.

Secondary electrons are low energy even though the primary electron beam is several keV or higher. Fig. 5.5 shows the average energy distribution of secondary electrons from metals.

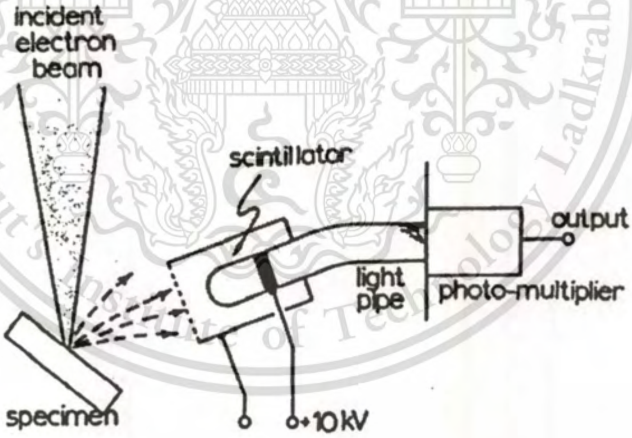

**Fig. 5.5** Schematic diagram of a scintillator tube used for the detection of secondary electrons.

A high resolution FE-SEM of JEOL 6301F with a field emission gun was used to examine grain size, surface and cross-sectional morphologies of different coatings of thin films on substrates.

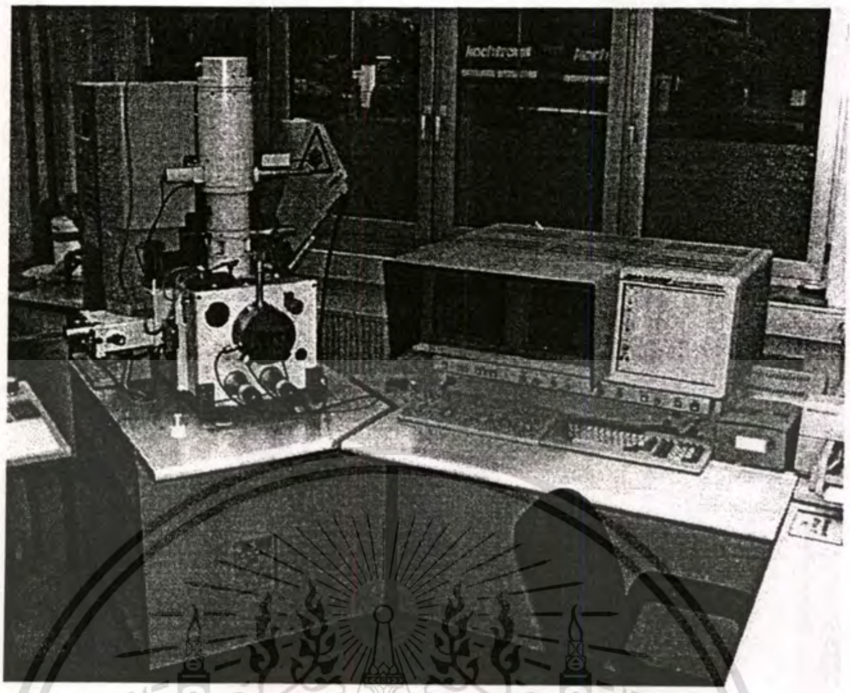

(a)

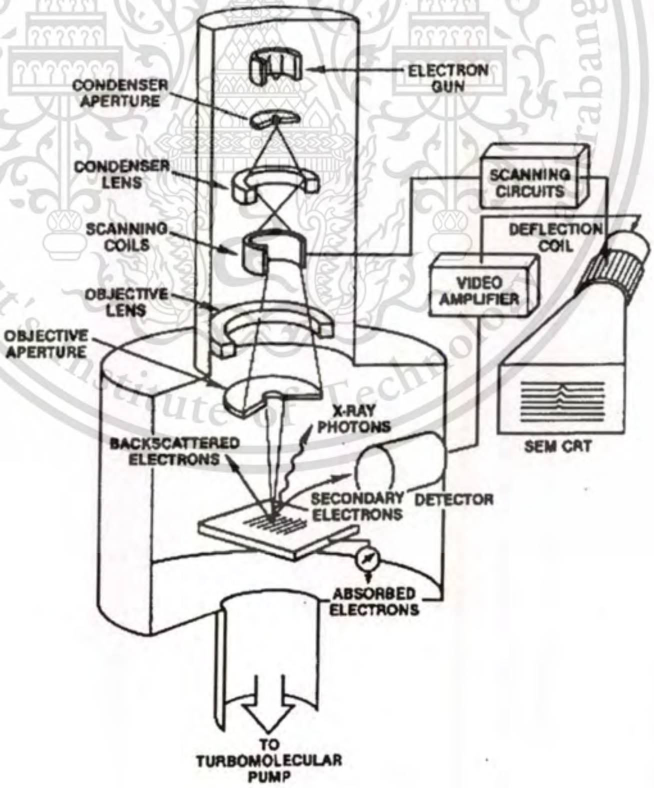

(b)

**Fig. 5.6** The photograph (a), and schematic (b) of FE-SEM system used to investigate surface morphologies of all thin films.

## 5.2 Optical Characterization Methods

### 5.2.1 Photoreflectance Spectroscopy (PR)

The photoreflectance technique is a modulation spectroscopy based on very general principles of experimental physics. Instead of directly measuring the optical spectrum (reflectance or transmittance), the derivative with respect to some parameter is evaluated. This can easily be accomplished periodically modulating some parameter applied to the sample (external modulation) or some internal material parameter (internal modulation) in a periodic fashion and measuring the corresponding change in the reflectance. Examples of the perturbations, which correspond to different modulation methods, are changes in the electric or magnetic field, heat pulse, or uniaxial stress [4, 5]. Such repetitive perturbations modify the spectral response of sample, giving rise to differential-like spectra in the region where optical excitation processes occur. Because of this derivative-like nature, a large number of sharp spectral features can be observed in modulated reflectance spectra of semiconductors even at room temperature. With these sharp, well-resolved spectra, it is possible to analyze and directly yield the properties of material under study. The vary small changes in reflectance can be observed using phase-sensitive techniques. The ability to perform a lineshape fit is one of the great advantages of photoreflectance modulation spectroscopy. Since, for the modulated signal, the features are localized in photon energy, it is possible to account for the lineshapes to yield accurate values of important parameters such as energies and broadening functions of interband (intersubband) transitions. For example, even at 300 K it is possible to obtain the energy of a particular feature to within a few meV. The extensive fundamental experimental and theoretical work in the area of modulation spectroscopy during the last 25 years, particularly the electroreflectance and photoreflectance methods, have provided the necessary framework to develop the technique into a powerful tool for material, device and processing characterization.

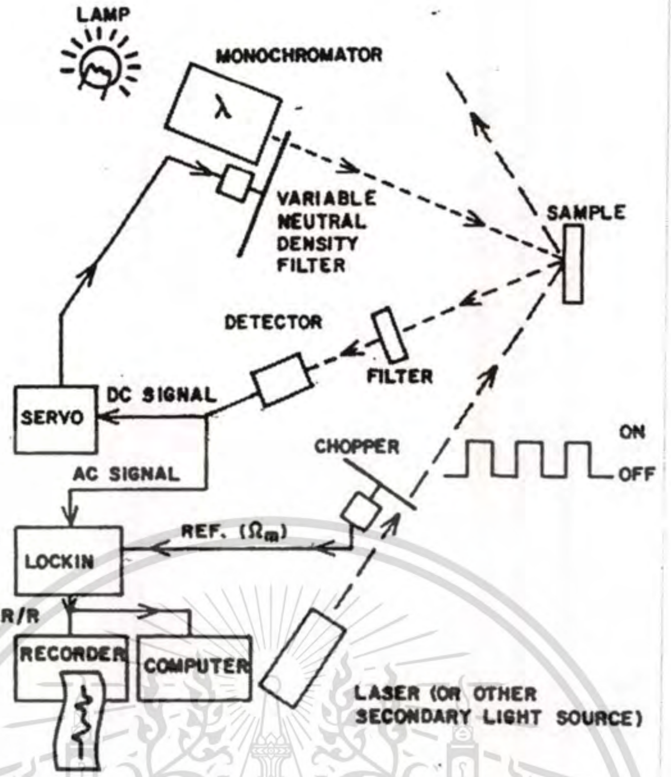

**Fig. 5.7** Schematic representative of a photoreflectance apparatus.

Shown in Fig. 5.7 is the schematic representative of a photoreflectance apparatus. Modulation of the electric field in the sample is caused by photo-excited electron-hole pairs created by the pump source (laser or other light source) which is chopped at frequency $\Omega_m$. Most PR experiments have utilized a mechanical chopper with maximum $\Omega_m \approx 5$ kHz. The photon energy of the pump source is generally above the bandgap of the semiconductor microstructure under investigation. A typical pump is He-Ne laser (except at high temperatures where a more power beam must be used).

In Fig. 5.7 the normalization is performed by a variable neutral density filter (VNDF) connected to a servo mechanism. The DC signal from the detector, which is proportional to $I_0(\lambda)\Delta R(\lambda)$, is introduced into the servo which moves the VNDF in such a manner as to keep $I_0(\lambda)\Delta R(\lambda)$ as a constant, i.e., $I_0(\lambda)R(\lambda) = C$. Under these conditions the AC signal $I_0(\lambda)\Delta R(\lambda) = C\Delta R(\lambda)/R(\lambda)$. Thus, the signal to the lock-in-amplifier is proportional to the quantity of interest, i.e., $\Delta R(\lambda)/R(\lambda)$. By changing the wavelength of the pump beam in PR it is possible to perform non-destructive depth profiling.

The vast majority of PR experiments measure features due to interband (intersubband) transitions between valence and condition bands (subbands) in semiconductors and semiconductor microstructures, i.e., probe monochromator wavelength in the near infrared to visible region. However, it is also possible to study the photoinduced transitions between quantized electron subbands in quantum wells by using an infrared probe beam and visible laser.

A drawback of PR is the spurious modulated background signal reaching the detector because of (a) luminescence from the sample and/or (b) scattering light from the pump source. Luminescence can sometimes be a problem for measurements near the fundamental gap, particularly at low temperatures. Scattered pump light can be reduced by means of an appropriate low pass filter in front of the detector. If the overall spurious background signal is not too large in relation to ΔR/R it can be subtracted by the normalization method of Fig. 5.8 The spurious background signal also can be reduced or eliminated by approaches such as the use of a double monochromator, a tunable dye laser probe beam, sweeping PR or differential PR.

The differential changes in reflectivity can be related to the perturbation of the complex dielectric function ($\varepsilon = \varepsilon_1 + i\varepsilon_2$) expressed as [6];

$$\Delta R/R = a(\varepsilon_1, i\varepsilon_2)\,\Delta\varepsilon_1 + b(\varepsilon_1, \varepsilon_2)\,\Delta\varepsilon_2, \qquad (4)$$

where $a$ and $b$ are the Seraphin coefficients, related to the unperturbed dielectric function, and $\Delta\varepsilon_1$ and $\Delta\varepsilon_2$ are the changes in the complex dielectric function due to the perturbation.

The quantities $\Delta\varepsilon_1$ and $\Delta\varepsilon_2$ are related by a Kramers-Kronig inversion. Near the fundamental gap of bulk materials $b \approx 0$ (Aspnes 1980) so that $\Delta R/R = a\Delta\varepsilon_1$ is the only term that is important. However, in multilayer structures interference effects are important so that both $\Delta\varepsilon_1$ and $\Delta\varepsilon_2$ may have to be considered. The functional form of $\Delta\varepsilon_1$ and $\Delta\varepsilon_2$ can be calculated for a given perturbation provided that the dielectric function critical point is known.

The PR was used to investigate the bandgap energies of AlN and InN thin films. Figure 5.8 and 5.9 illustrate experimental set up and schematic diagram of PR measurement, respectively.

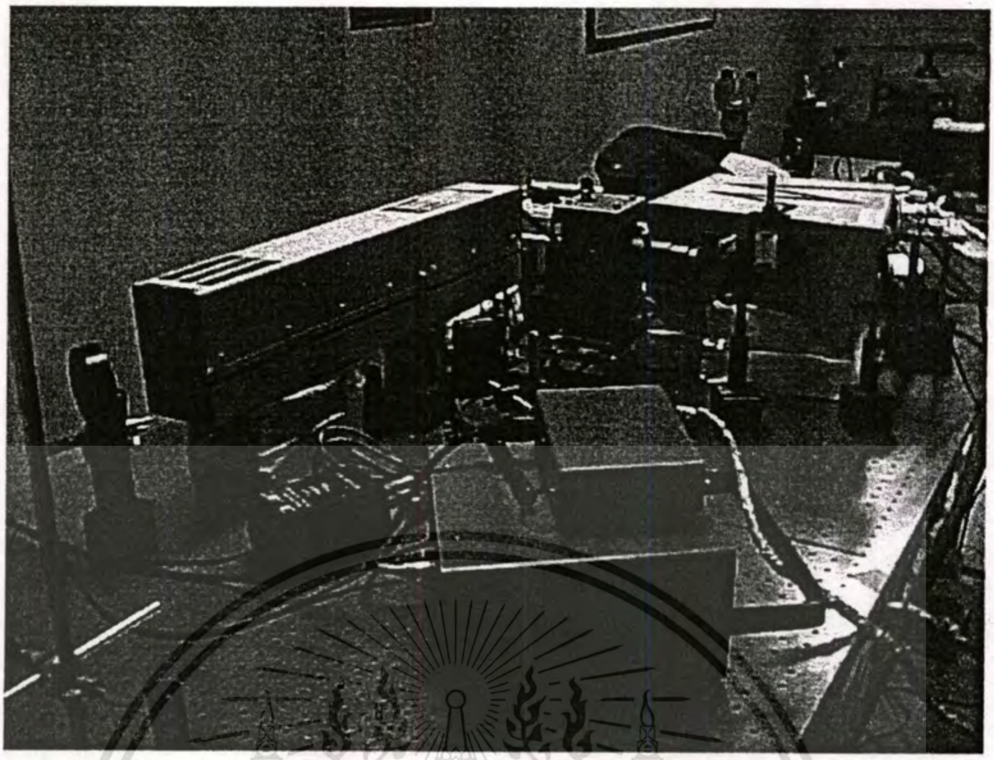

**Fig. 5.8** A photograph of room temperature PR set up used to investigate the bandgap energies of thin films in our laboratory.

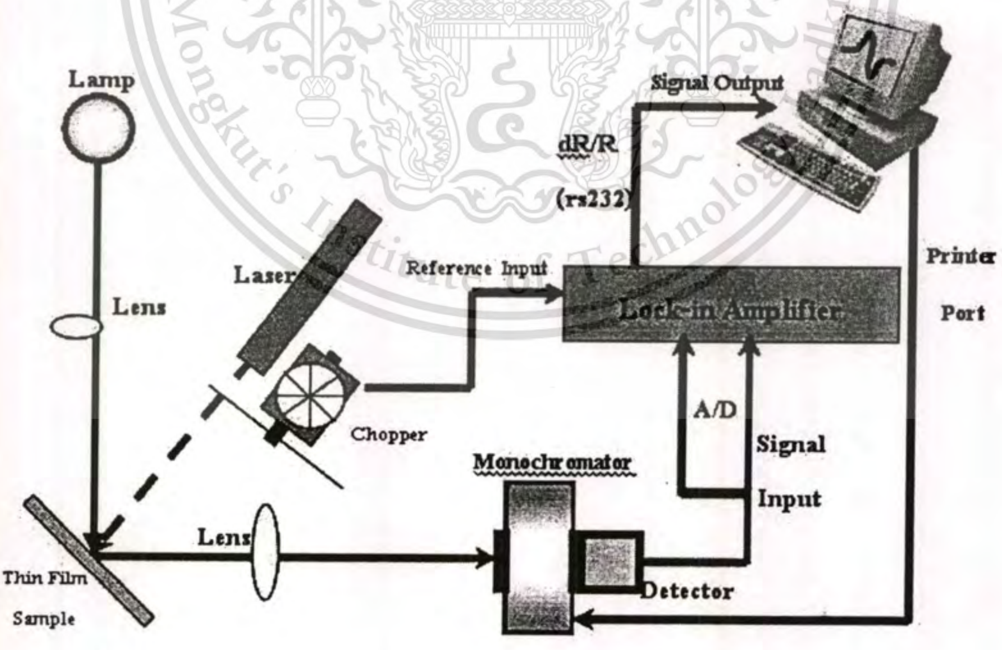

**Fig. 5.9** Schematic diagram of PR experimental set up.

### 5.2.2 UV-VIS Spectroscopy (UV-VIS)

Transmission measurements or absorption spectroscopy can be used to determine the optical quality of thin films. Absorption spectroscopy responds to processes that have large density of states, such as the absorption edge, and provides a measure of the bulk properties of the crystal. This technique is quick and non-destructive and is therefore a good complementary tool to the photoluminescence measurements. Two different types of light sources are used in the instrument in order to cover the whole spectral range. A tungsten/halogen lamp can provide visible and near IR light and a deuterium lamp is the UV light source. A photomultiplier (PMT) tube is used to detect signals in the UV and visible range (200-800 nm). A lead sulfide detector is used to detect infrared light.

The UV-VIS system used for transmittance measurement in this research is shown in Fig. 5.11

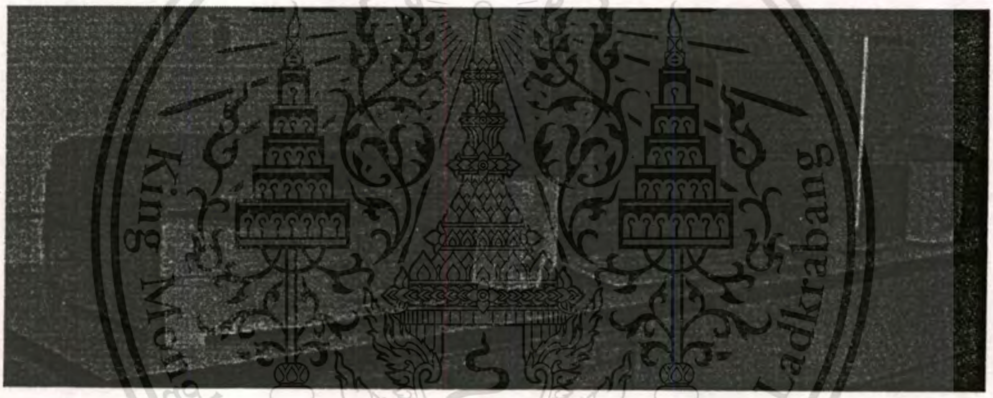

**Fig. 5.10** The photograph of UV-VIS system used in this research (Thermo electron; Helios α).

## 5.3 Other Measurements

### 5.3.1 Resistance Measurement

The electrical d.c conductivity of ITO sputtered films is deduced from resistance $R_f$ measured by using a square-probe which directly touches on the sample surface with a curtain pressure. The probe consists of two parallel rows of four pin type contacts. The four contacts in a row are electrically connected and work as one pole, so the measure distance is kept the same. Figure 5.11 shows a photograph of linear 4 point probes instrument (OmniMap r-RS35, Prometrix) used in this research.

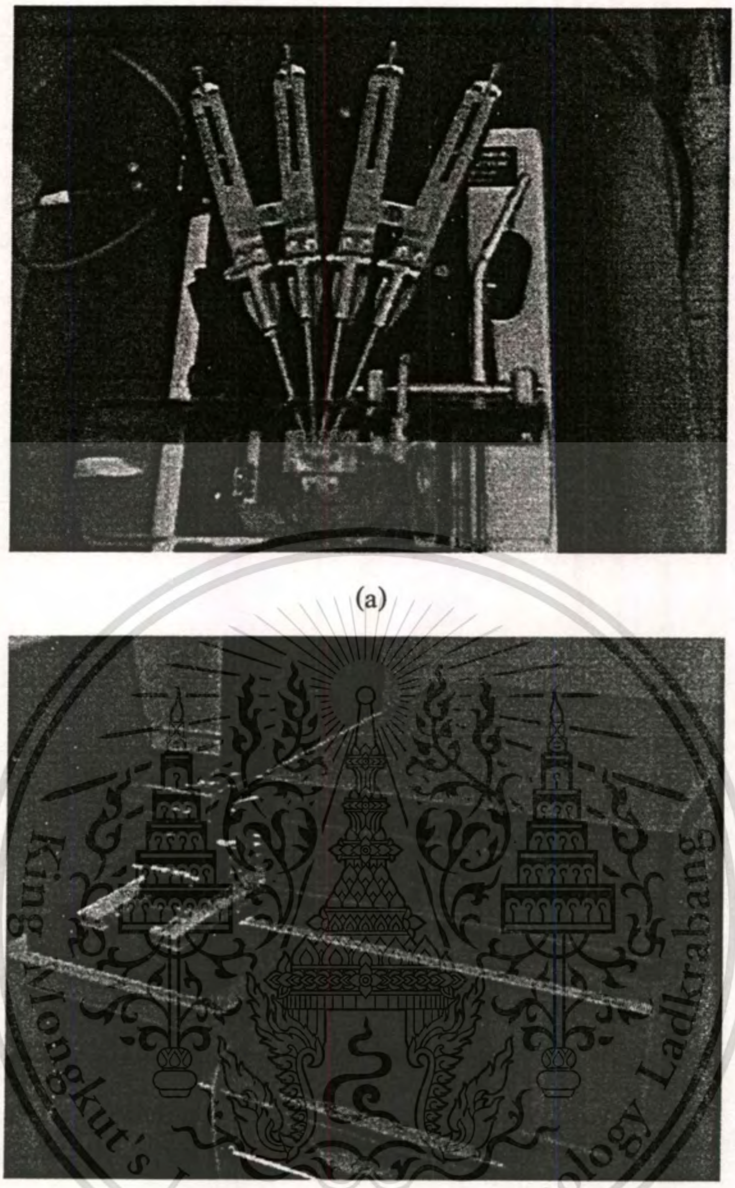

(a)

(b)

**Fig. 5.11** A photograph Linear four point probes instrument; (a) 4 probes and (b) system.

The film conductivity σ is inversely proportional to the product of film resistance and thickness expressed by:

$$\sigma = \frac{1}{\rho}\alpha\left(R_f \cdot d_f\right)^{-1} \tag{5}$$

where $d_f$ is the film thickness.

## 5.4 Chapter Summary

The AlN, InN, ITO and InON thin films grown by reactive gas-timing rf magnetron sputtering in this research were determined by the characterizations methods. The crystallized orientation and surface morphology of thin films were obtained by XRD and FE-SEM, respectively. The optical bandgap energy of thin films was successfully investigated by PR and UV-VIS measurement. The sheet resistance of ITO films was measured by 4 point probes instrument. In additional, the thickness of all films was monitored and measured by thickness monitor and profilometer, respectively.

All measurement gave us to understand our grown films and can apply for devices applications.

## References

[1] Donald L. Smith, **"Thin Film Deposition: Principles and Practices"**, McGraw-Hill, New York, 1995.

[2] David A. Glocker, Ismat Shah, editors, **"Handbook of Thin Film Process Technology"**, Institute of Physics Publishing, Bristol, 1995.

[3] Jiti Nukeaw, Yasufumi Fujiwara, and Yoshikazu Takeda, **"Observation of Electric Field at Surface and Interface of Doped GaAs/Semi-insulating GaAs Structures by Fast Fourier Transformed Photoreflectance"**, Japanese Journal of Applied Physics 36(11), 7019-7023, 1997.

[4] Jiti Nukeaw, Yasufumi Fujiwara, Yoshikazu Takeda, Mitsuru Funato, Satoshi Aoki, Shizuo Fujita, Shigeo Fujita, and Shigeo Fujita, **"Observation of High Electric Field at ZnSe/GaAs Heterointerfaces by Fast Fourier Transformed Photoreflectance"**, Thin Solid Films 334, (1998), 11-14.

[5] D.E. Aspney, **"Third Derivative Modulation Spectroscopy with Low Field Electroreflectance"**, Surface Science, Vol. 37, pp. 418, 1973.

# CHAPTER 6

# GROWTH AND CHARACTERIZATIONS OF AlN THIN FILMS

## 6.1 Introduction

AlN was first synthesized in 1877, but it was not until the middle of the 1980s that its potential for application in microelectronics was realized due to its relative high thermal conductivity for an electrical insulating ceramic (70-210 $W \cdot m^{-1} \cdot K^{-1}$ for polycrystalline material, and as high as 275 $W \cdot m^{-1} \cdot K^{-1}$ for single crystals).

AlN is synthesized by carbothermal reduction of alumina or by direct nitridation of aluminium. AlN is a (mostly) covalent bonded material, and has a hexagonal crystal structure which is isomorphic with one of the polytypes of zinc sulfide known as wurtzite. The use of sintering aids and hot pressing is required to produce a dense technical grade material. The material is stable to very high temperatures in inert atmospheres. In air, surface oxidation occurs above 700 °C, and even at room temperature, surface oxide layers of 5-10 nm have been detected. This oxide layer protects the material up to 1370 °C. Above this temperature bulk oxidation occurs. Aluminum nitride is stable in hydrogen and carbon dioxide atmospheres up to 980 °C. The material dissolves slowly in mineral acids through grain boundary attack, and in strong alkalis through attack on the aluminum nitride grains. The material hydrolyzes slowly in water. Aluminum nitride is resistant to attack from most molten salts including chlorides and cryolite.

Mellor (1928) described the early production of aluminum nitride (AlN), crediting Briegleb and Geuther (1862) as being the first to document a method for its production. Their method involved heating aluminum in a nitrogen atmosphere to yield (impure) AlN according to the nitridation reaction:

$$Al(s)+1/2N_2(g) = AlN(s) \qquad (1)$$

Mellor also reported the commercial production of AlN by Serpek via the carbothermal reduction of alumina using coal and bauxite as starting materials:

$$Al_2O_3\,(s)+3C(s)+N_2\,(g) = 2AlN(s)+3CO(g) \qquad (2)$$

As reactions observed in AlN powder production, (1) and (2) above are by far the most prevalent (Fister, 1985). Purity has been increased over the years by increasing the purity of reactants and by reducing the particle size of the solid reactants.

Another potential application for AlN is as a packaging material for electronic items. Packages made of AlN could reduce cooling problems and allow higher power densities. AlN also shows corrosion resistance to a wide variety of materials. It is wetted by molten aluminum, but does not react with it. It is not attacked by uranium, lithium, many ferrous alloys and some superalloys. It is also stable against molten salts such as carbonate eutectic mixtures and cryolite. AlN is finding increased applications in crucibles and hardware for containing or processing many of these corrosive materials.

Currently there is much research into developing light-emitting diodes to operate in the ultraviolet using the gallium nitride based semiconductors and, using the alloy aluminum gallium nitride, wavelengths as short as 250 nm have been reported. In May 2006 an inefficient LED emission at 210 nm was reported. The bandgap of single crystal AlN has been measured (using vacuum UV reflectivity) at 6.2 eV. This allows a wavelength of around 200 nm to be achieved, in principle. However, there are many difficulties to be overcome if such emitters are to become a commercial reality. Among the applications of AlN: opto-electronics, as a dielectric layer in optical storage media, electronic substrates, as a chip carrier where high thermal conductivity is essential, and in military applications.

Epitaxially grown crystalline aluminum nitride is also used for surface acoustic wave sensors (SAW's) deposited on silicon wafers because of the AlN's piezoelectric properties. Very few places can reliably fabricate these films. Agilent after more than a decade of research now has a RF filter used in mobile phone called the FBAR. This technology is closely associated with engineers working in the MEMS field.

Using on-axis reactive sputtering AlN films have been deposited on different substrates such as glass, Si (100), Si (111), $SiO_2$ and sapphire. The c-axis AlN films are easier obtained at lower pressure (0.75-8 mTorr) and lower pressure [1-6] In Chien-Chuan Cheng's study [7], it is provided that the full width of half maximum intensity (FWHM) of AlN (002) was decrease with increase the $N_2$ concentration. It is also provided that the c-axis AlN films can be improved by increasing the r.f. power and temperature. The effect of r.f. power is similar to the result of M. Ishihara's study [8].

Sputtering is a very versatile process for the fabrication of thin solid films. The subject of this thesis concerns the study of thin films of non-stoichiometric aluminum nitride fabricated by reactive magnetron sputtering with our innovation technique called reactive gas-timing technique. Using gas-timing control in the sputtering process, the argon and nitrogen ions have effectively to yield AlN film. The method allows the deposition of films have orientation in a cubic structure. This deposition technique is shown to be an extremely useful tool in the growth of cubic-AlN polycrystalline structure.

In this thesis, we report the first observation of band-gap energy obtained from room temperature PR measurement on poly-crystalline AlN thin films grown by this new technique. With this approach, the AlN thin films can be performed in cubic structures and nanocrystalline sizes. The crystalline structure, morphology and band gap energy of the samples were characterized by XRD, FE-SEM and PR spectroscopy, respectively.

## 6.2 Experimental Results and Discussions

### 6.2.1 Substrate Cleaning Process

In order to obtain high quality film, it is necessary to clean the substrate thoroughly. Science the condition of substrate surface would influent the quality and adhesion of AlN thin films. The glass slides (Menzel-Glaser German model: SuperFrost) were used as the substrates for AlN thin film growth in this study. The glass substrate cleaning process is as below,

1) Wash the glass surface with detergent solution for 15 minutes in ultrasonic bath cleaner.
2) Rinse with the tap water.
3) Etch the oxide and contamination on the surface with **PIRANHA** process ($H_2SO_4$ +30%$H_2O_2$ with 4:1 by volume) for 30 minutes.
4) Rinse in tap water for 20 minutes.
5) Deep rinse in de-ionized (DI) water for 30 minutes in ultrasonic bath cleaner.
6) Dry out the surface with Nitrogen gas.
7) Bake the substrates in oven at 200 °C.

In this research, the optimized growth conditions of AlN thin films were investigated such as the growth rate with Ar and $N_2$ plasma, the reactive gas-timing sequence, the rf power, and the film thickness discussed in the detail experiment in the next subjects. For result comparison, AlN thin films were grown with and without reactive gas-timing methods.

### 6.2.2 Thin Films Growth without Reactive Gas-Timing

#### 6.2.2.1 Thin Film Growth Rate in Ar Plasma

For primary survey of the growth system with no rf-reflected effect and achieving the require growth rate, the suitable flow rate of Ar as plasma gas was experimented. The aluminium (Al) purity of 99.999% was used as a target material with a diameter of 3 inch. A 500 nm thick of thin film was grown on cleaned substrate. The substrate distance to the target is 7 cm (centimeter) without heating substrate processing. The base pressure of the chamber was $6 \times 10^{-7}$ mbar (millibar). The Ar purity of 99.999% was used to bombard the target with rf power 200 W. Figure 6.1 shows photograph through the chamber window during Ar plasma process in the vacuum chamber, the plasma of Ar gas shows purple visible.

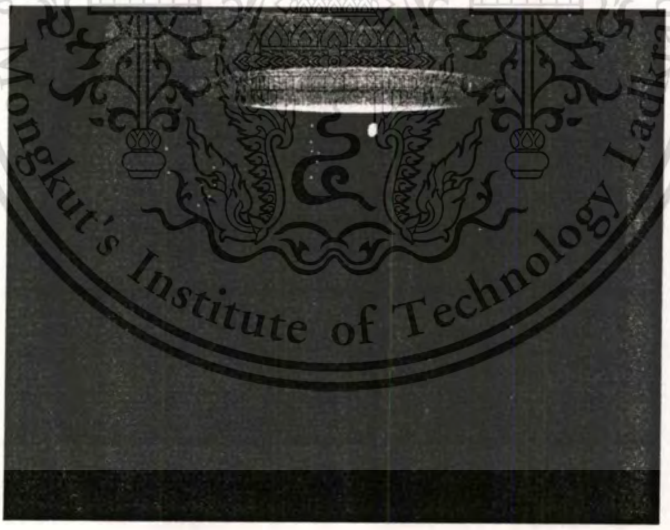

**Fig. 6.1** The Ar-plasma during the sputtering process.

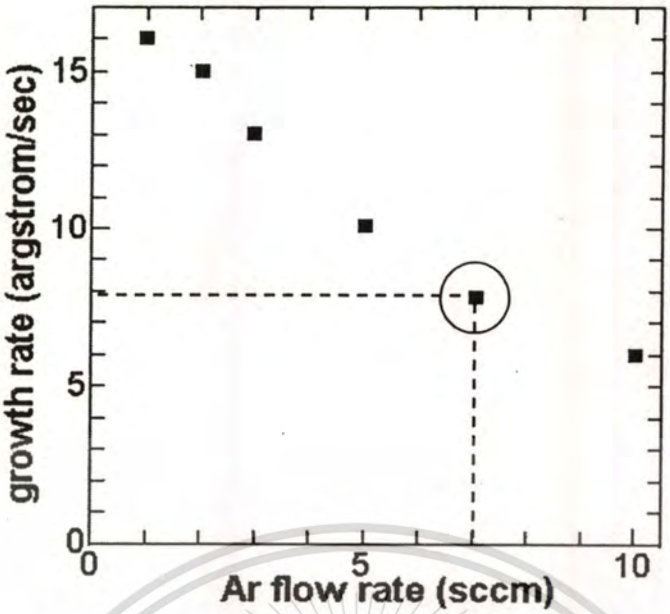

**Fig. 6.2** Relation between growth rate and Ar flow rate of 0-10 sccm.

The flow rate of Ar was varied in rage of 1-10 sccm (standard cubic centimeter per minute) and the film growth rates were recorded. The relation between thin film growth rate and flow rate of Ar was shown in Fig. 6.2.

The excess ions in the chamber may collies each other affected to the decreasing of sputtering yield so the thin film growth rate was decreased when the flow rate of Ar increased as shown in Fig 6.2. From this experiment, the Ar flow rate of 7 sccm was selected because the plasma is stable with no rf reflection effect during the process and the growth rate of 8 Å/sec was achieved.

#### 6.2.2.2 Thin Film Growth Rate in $N_2$ Plasma

The thin films with 500 nm thickness were grown on cleaned substrates at ambient temperature in the chamber. In this experiment, the $N_2$ purity of 99.999% was fed into the chamber and mixed with 7 sccm of Ar gas achieved from the result of 6.2.2.1. Without the rf-reflecting effect, the flow rate of $N_2$ was varied in rage of 0.35-3.0 sccm. Figure 6.3 illustrates during $N_2$ plasma process in the vacuum chamber, the plasma of $N_2$ shows orange light. The relation between thin film growth rate and flow rate of $N_2$ was shown in Fig. 6.4. The importance of this experiment is for the comparison with the thin films grown by reactive gas-timing technique discussed in next subject.

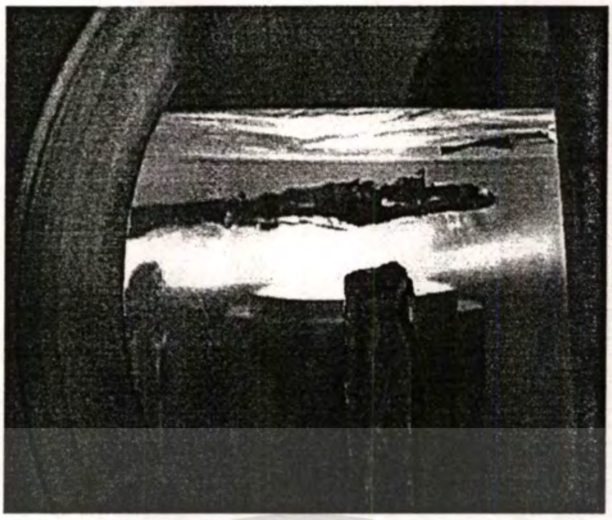

**Fig. 6.3** The $N_2$ plasma during the sputtering process.

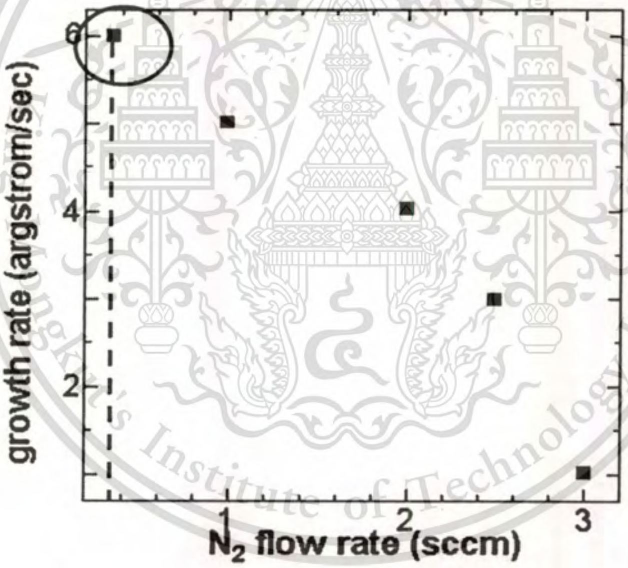

**Fig. 6.4** Relation between growth rate and $N_2$ flow rate of 0.35-3 sccm.

Figure 6.4 shows that the thin film growth rate was decreased when the flow rate of $N_2$ increased. The excess $N_2$ ions in the chamber may collie each other and make high plasma pressure affected to the decreasing of sputtering yield. It found that the $N_2$ flow rate of 0.35 sccm mixed with 7 sccm of Ar achieved the maximum growth rate. The crystallinity, however, of samples were investigated by XRD.

There are not any peaks showed in the XRD results of all samples. Figure 6.5 shows the sample of XRD result of thin film deposited in 0.35 sccm of $N_2$ mixed with 7 sccm of Ar plasma.

It represented that the thin films grown by this growth conditions and gases-mixed technique are amorphous phase of crystallinity.

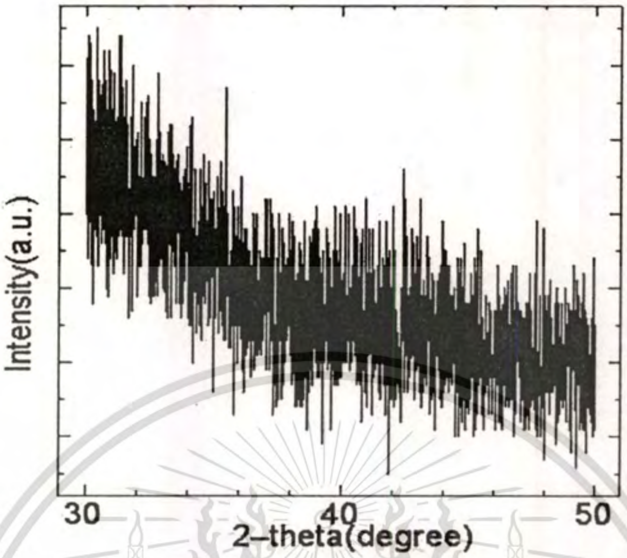

**Fig. 6.5** X-ray 2-2θ scan of 500 nm thick of thin film deposited in Ar and Ar mixed with $N_2$.

We introduced room temperature PR measurement to investigate energy band gap of all thin films in the experiments. Thin films resulted from 6.2.2.1 and 6.2.2.2 show no peak response in PR measurement as shown in Fig. 6.6. PR result confirmed that thin films grown by rf magnetron sputtering without reactive gas-timing technique are amorphous structure in crystallinity.

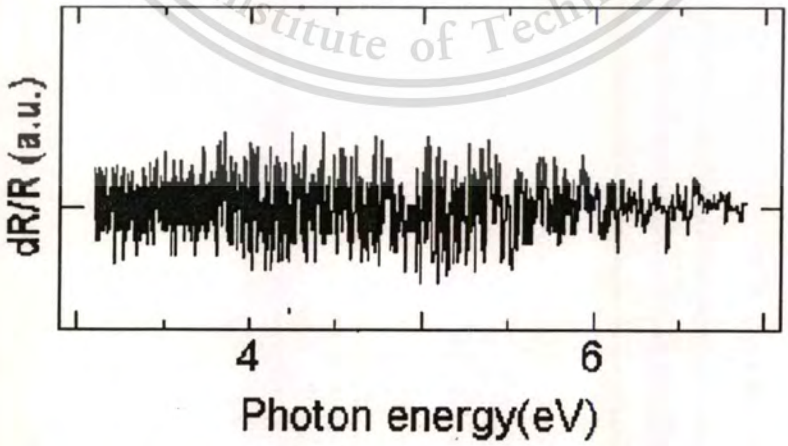

**Fig. 6.6** PR result of thin film deposited in Ar and Ar mixed with $N_2$ without reactive gas-timing technique.

### 6.2.3 AlN Thin Films Growth with Reactive Gas-Timing

In this research, a new technique called **"reactive gas-timing"** will be purposed to grow AlN, InN and their compounds thin films by rf magnetron sputtering at room temperature. Gas-timing technique is a process to control timing sequence of feeding gases (Ar and $N_2$) into the sputtering process. The 99.999 % purity of argon (Ar) and nitrogen ($N_2$) were used to grow AlN thin films. The Ar gas takes advantage of ions bombardment, while $N_2$ gas takes a function of reactive ions. Figure 6.7 is the example of the flow sequence of gases (Ar and $N_2$). The solid line denotes the sequence of 7 sccm of Ar that bombarded the Al target for 60 sec, and the dash line denotes the sequence of 0.35 sccm of $N_2$ that reacted with Al atoms for 30 sec. The period of time sequence depends on thin film thickness requirement.

The aluminium (Al) purity of 99.999% was used as a target material. The base pressure of the chamber was $6 \times 10^{-7}$ mbar while, the sputtering pressure was in range of $1.1\text{-}8.0 \times 10^{-3}$ mbar depended on the flow rate of gas.

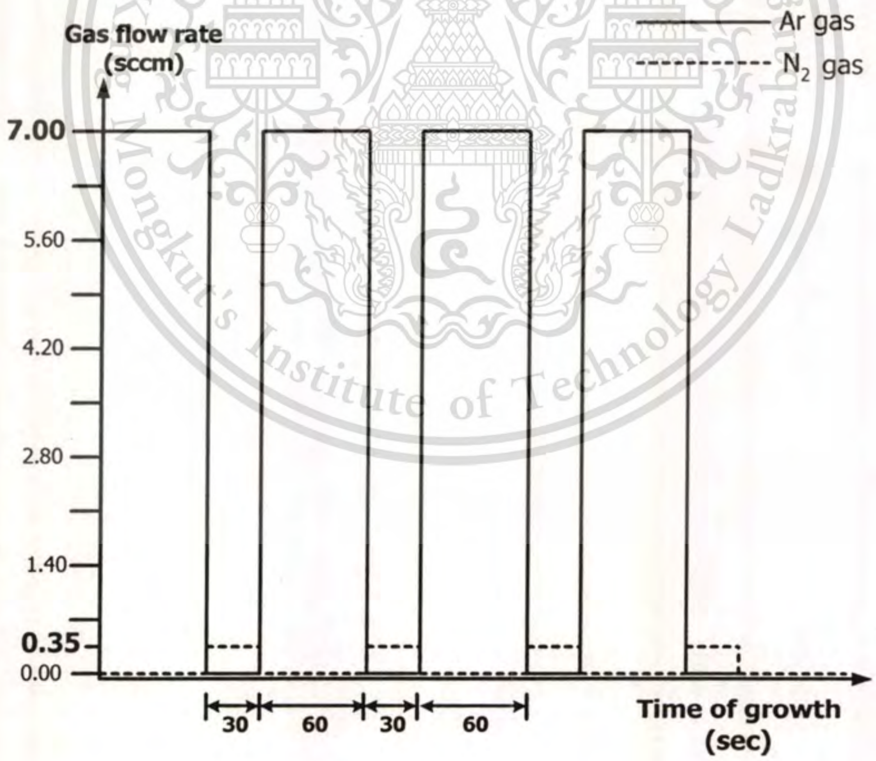

**Fig. 6.7** Gas-timing sequence of Ar and $N_2$ flow for deposited AlN thin film. The flow rate of Ar gas was fixed at 7 sccm and $N_2$ gas was fixed at 0.35 sccm.

### 6.2.3.1 Aluminium (Al) Growth with Different Thickness

For comparison as the reference thin film with AlN thin films, Al thin films were grown by gas-timing technique with varying thickness of 20, 100, and 500 nm, respectively. The base pressure of the chamber was 6x$10^{-7}$ mbar. The rf power was fixed at 200 W and the flow rate of Ar was 7 sccm. Without feeding of $N_2$ gas, the flow timing of Ar was 60 sec and stoped flow for 30 sec as shown in Fig. 6.8. Schematic shows the flow sequence of Ar gas that bombarded the Al target for 60 sec and stoped for 30 sec. The crystalline structure, surface morphology and the band gap energy of samples were investigated by XRD, FE-SEM and PR, respectively.

The Al thin films were grown by reactive gas-timing technique with varying thickness of 20, 100, and 500 nm, respectively. The crystalline structures of all samples investigated by XRD are amorphous phase as shown in Fig. 6.9. The surface morphology of sample with thickness of 500 nm investigated by FE-SEM is shown in Fig. 6.10.

The Al thin films were grown by reactive gas-timing technique with varying thickness of 20, 100, and 500 nm, respectively. The crystalline structures of all samples investigated by XRD are amorphous phase as shown in Fig. 6.9. The surface morphology of sample with thickness of 500 nm investigated by FE-SEM is shown in Fig. 6.10.

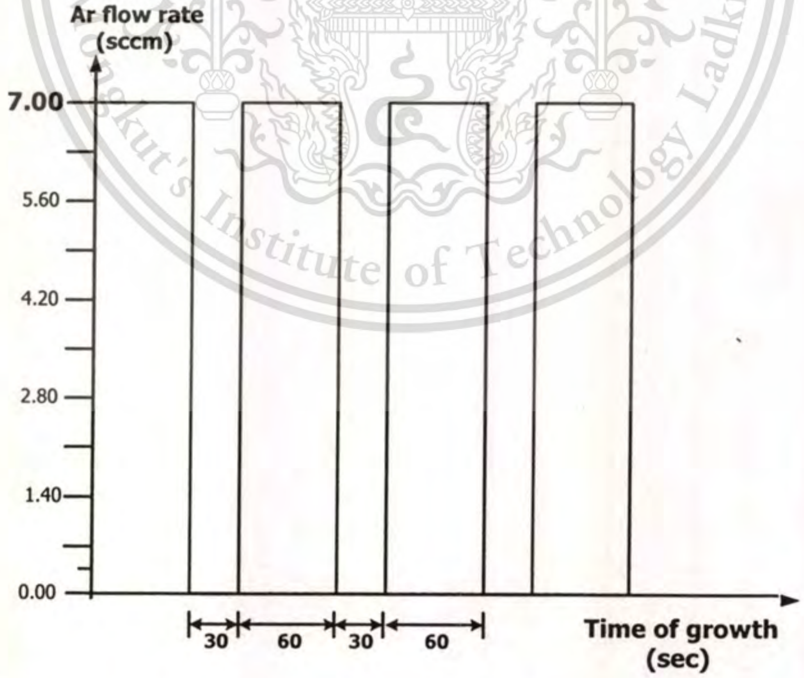

**TFig. 6.8** Schematic of gas-timing sequence of Ar flow for deposited Al thin film. The flow sequence of Ar was 60 sec and stopped for 30 sec.

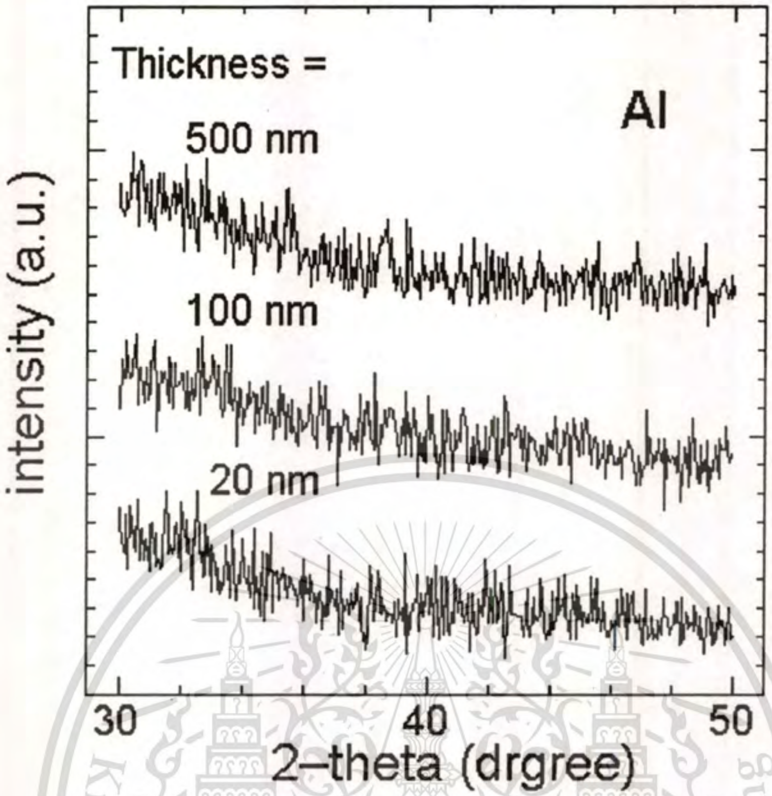

**Fig. 6.9** XRD results of Al thin films grown with difference thickness of 20, 100 and 500 nm.

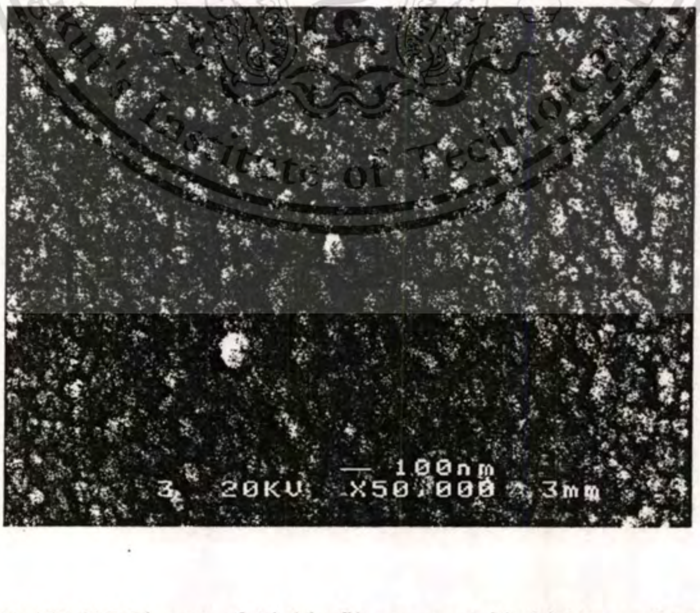

**Fig. 6.10** FE-SEM image of Al thin film grown with thickness of 500 nm.

The PR measurements for deposited Al thin films were conducted at room temperature. The result shows no peak response in PR spectrum as shown in Fig. 6.11.

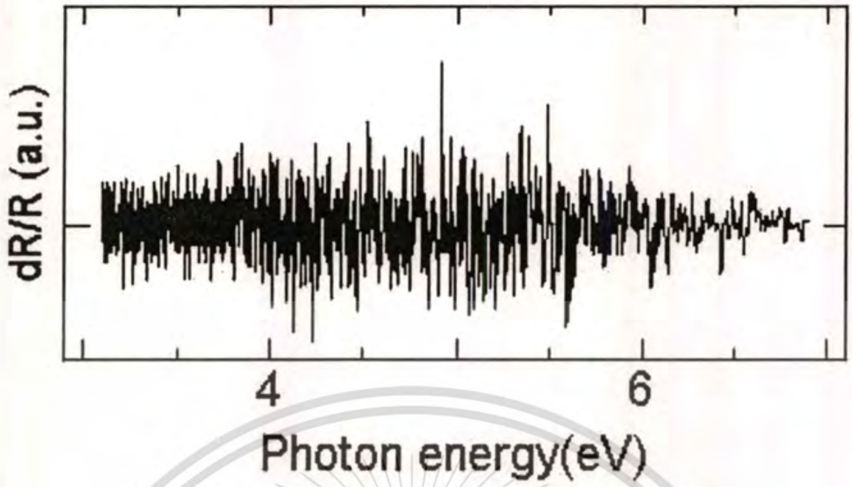

**Fig. 6.11** PR spectrum of Al thin film with thickness of 500 nm.

The XRD, SEM and PR results are in agreement with amorphous Al thin film. Although the thickness of thin film plays an important role to the crystallinity of thin film but the important of this experiment is the PR measurement result of the 500 nm-Al thin film. PR result reveals that the deposited thin films are metal (Al) material, no band gap energy was observed.

#### 6.2.3.2 Effect of Gas-Timing of Ar and $N_2$

According to the experimental results from 6.2.2.1 and 6.2.2.2, the flow rates of Ar and $N_2$ were optimized at 7 and 0.35 sccm, respectively. After the sputtering chamber was evacuated below $6\times10^{-7}$ mbar, Ar and $N_2$ gases 99.999% purity were introduced into the chamber separately and regulated by mass flow controllers. The 500 nm thick AlN thin films were grown on cleaned glass substrates. The rf power was fixed at 200 W. In the sputtering method, the substrate was not heated and the substrate temperature was only dependent on the self-heating of the plasma.

In order to optimize the flow timing of Ar per $N_2$ (Ar:$N_2$) for achieving high quality AlN thin films, the timing sequence of Ar per $N_2$ was varied at 30:30, 60:30, 60:20, and 60:10 sec, respectively. The crystalline structures of all samples were investigated by XRD. Figure 6.12 shows strong XRD peaks at 38.90° and 45.03° in the orientation of (111) and (200) planes, respectively corresponding to the cubic-AlN structure.

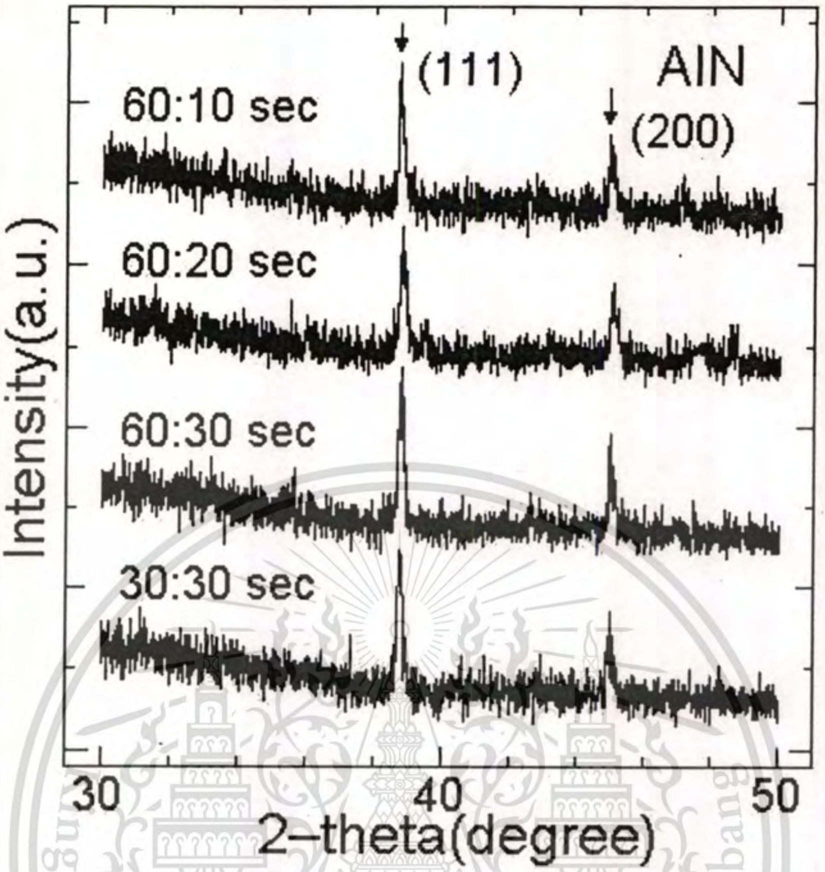

**Fig. 6.12** X-ray diffraction patterns of the AlN films prepared as a function of the gas-timing sequence of of Ar:$N_2$ at 30:30, 60:30, 60:20, and 60:10 second, respectively, rf power: 200 W and film thickness: 500 nm.

Figure 6.12 reveals preferred orientation with two peaks of cubic-AlN for the films deposited with reactive gas-timing by rf magnetron sputtering. It implies that the reactive gas-timing technique in sputtering process is effectively to form AlN in the orientation of (111) and (200) plane as cubic structure. his result can suggest in two steps of mechanism process; the first Ar-ions generated by radio frequency have more effective to bombard atoms in the target surface for x1-time, the second N-ions also generated by radio frequency effectively react with Al atoms yielded from first step for x2-time to form AlN compound. Figure 6.13 illustrates the nitrogen ions are nitride to Al atoms to form AlN on substrate.

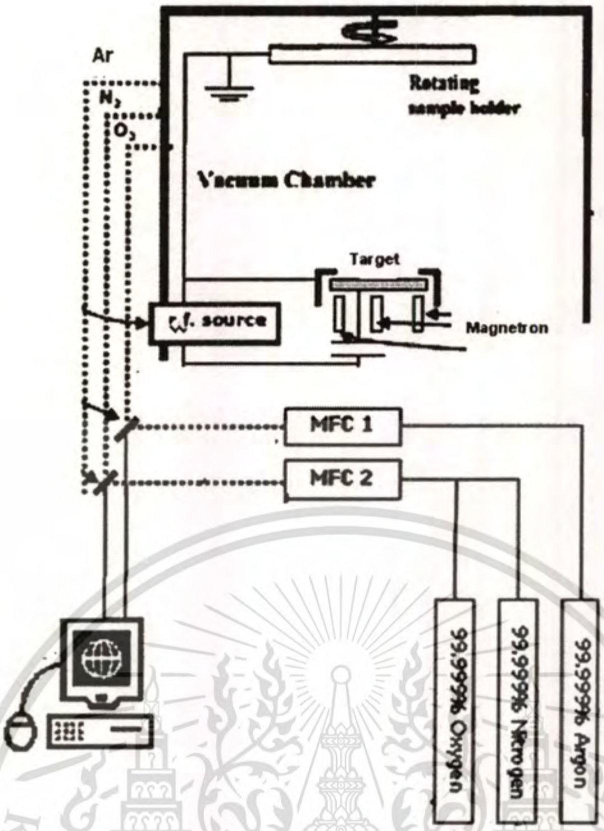

**Fig. 6.13** Schematic arrangement of sputter system used in experiment.

Because of the minimum FWHM and high intensity of XRD peaks, the timing sequence of Ar per $N_2$ at 60:30 sec was selected as fix parameter for growth conditions in the next experiment.

### 6.2.3.3 Effect RF Sputtering Powers

The r.f power of sputtering was varied to achieve the high quality AlN thin films. The 500 nm thick AlN thin films were grown by reactive gas-timing technique on cleaned glass substrates. The base pressure of the chamber was $6 \times 10^{-7}$ mbar. The flow rate of Ar and $N_2$ gases was fixed from the results of 6.2.2.1 (7 sccm of Ar) and 6.2.2.2 (0.47 sccm of $N_2$), respectively. From the result of 6.2.2.3, the optimized flow timing of Ar:$N_2$ (60:30 sec) was used to grow the AlN thin films. In this section experiment, the rf power of sputtering was varied at 100, 150, 200, and 300 watt, respectively. The crystalline structure and surface morphology of all samples were investigated by XRD and FE-SEM.

Figure 6.14 shows XRD results from AlN thin films grown with RF sputtering power of 100, 150, 200, and 300 watts, respectively. The XRD peaks at $38.82^{\circ}$ and $45.11^{\circ}$ of all samples correspond to the crystallinity in plane of (111) and (200), respectively as cubic structure. The surface morphology of all samples was shown in Fig. 6.15. From this experiment, the XRD peak in (111) plane of AlN thin film grown with 200 watts shows the minimum FWHM and high intensity which the high quality AlN thin film was achieved. At hight rf power, the energetic nitrogen ions can enhance the chemical combinations between Al and N atoms and thus lead to more and larger AlN crystal grains but it can cause the defect on the target and deposited thin film thus 200 W of rf power is the optimization power in this experiment.

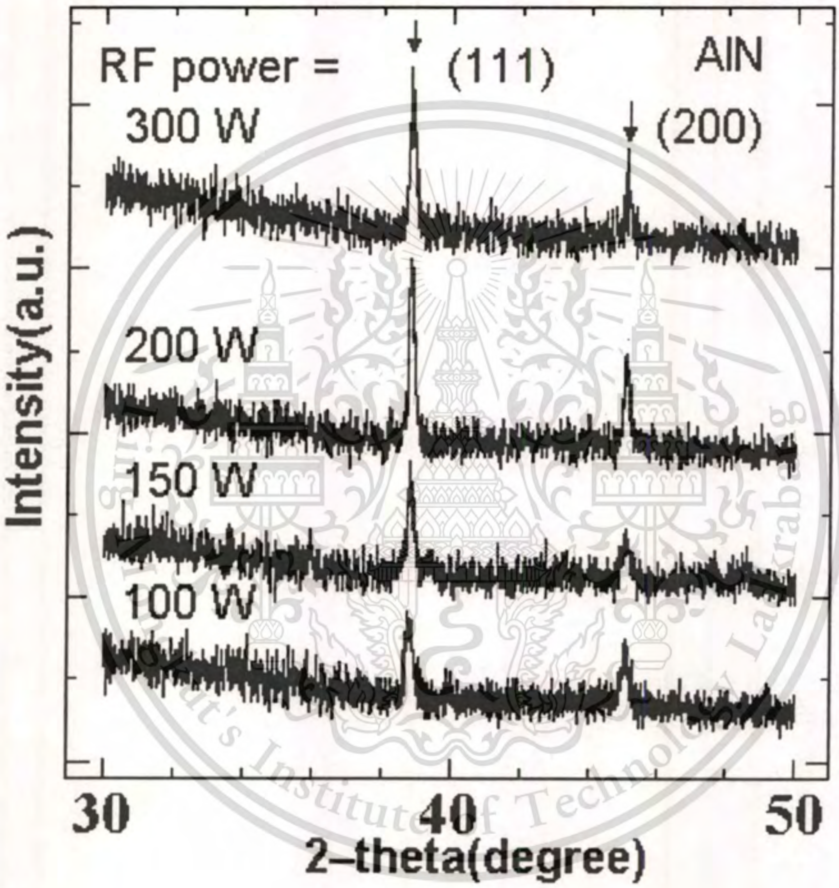

**Fig. 6.14** XRD results of AlN thin films grown with difference RF sputtering power at 100, 150, 200, and 300 watts, respectively.

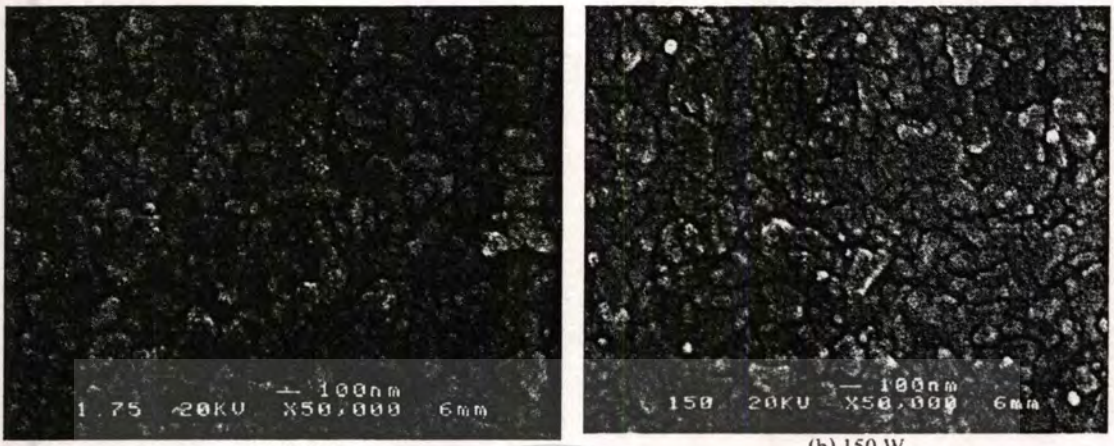

(a) 100 W

(b) 150 W

(c) 200 W

(d) 300 W

**Fig. 6.15** FE-SEM images of AlN thin films grown with difference RF sputtering power at (a)100, (b)150, (c) 200, and (d) 300 W, respectively.

#### 6.2.3.4 Effect of $N_2$ Flow Rates

The 500 nm thick of thin films were grown by reactive gas-timing technique on cleaned substrates. The flow rate timing of Ar:$N_2$, the flow rate of Ar and the rf power resulted of 60:30 sec, 7 sccm and 200 watts were fixed as parameters, respectively. In this experiment, the flow rate of $N_2$ was varied between 0.35 to 1.17 sccm. The base pressure of the chamber was $6\text{x}10^{-7}$ mbar and the sputtering pressure was in range of 1.1-8.0 $\text{x}10^{-3}$ mbar. The crystalline structure, the surface morphology, and the bandgap energy of all samples were investigated by XRD, FE-SEM, and PR, respectively.

Figure 6.16 shows XRD patterns of AlN thin films prepared with different flow rate of $N_2$. All samples show clearly peaks in the orientation along (111) and (200) planes that correspond to the cubic structure of AlN.

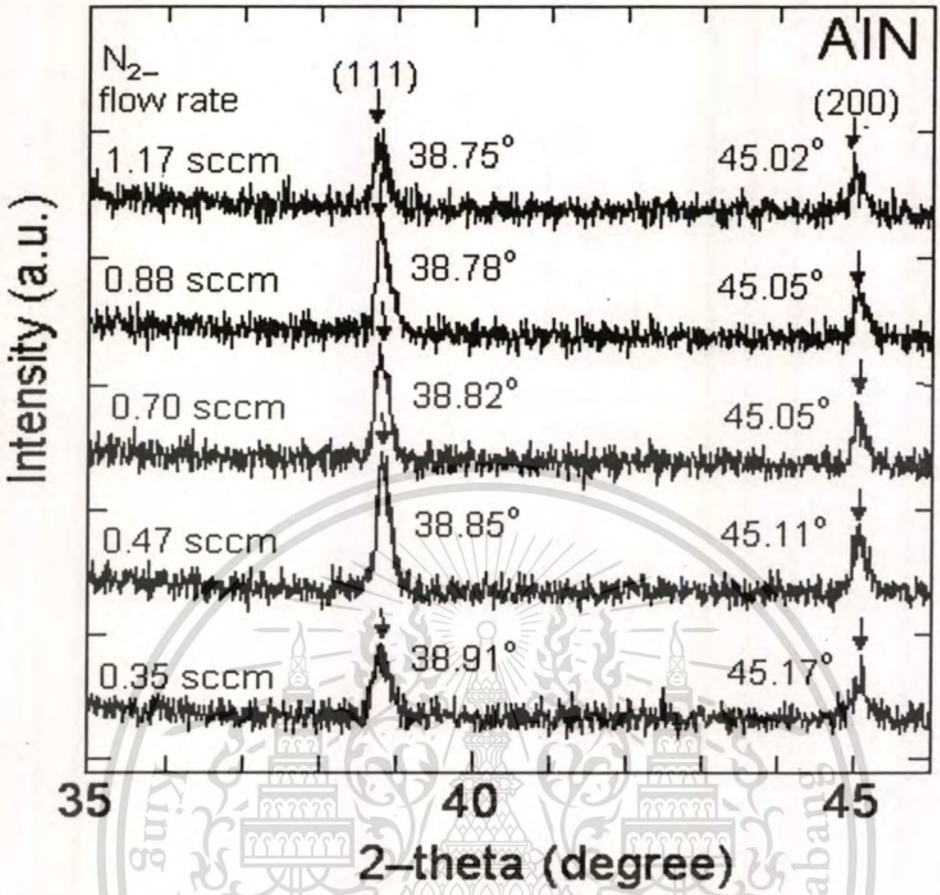

**Fig. 6.16** XRD results of AlN thin films grown with difference flow rates of $N_2$ in range of 0.35 to 1.17 sccm.

**Table 6.1** The relation between the flow rates of $N_2$ and lattice constants (a)

| **$N_2$ flow rate (sccm)** | **$2\theta$ (degree)** | **FWHM** ($2\theta$) | **d** ($\mathring{A}$) | **Plane** **(hkl)** | **a** ($\mathring{A}$) | **D** ($\mathring{A}$) |
|---|---|---|---|---|---|---|
| 0.35 | 38.90842 | 0.27857 | 2.313749 | **(111)** | 4.00753 | 336.1965 |
| | 45.17449 | 0.12143 | 2.006318 | (200) | 4.01264 | 787.6582 |
| 0.47 | 38.84668 | 0.22143 | 2.317283 | **(111)** | 4.01365 | 422.8715 |
| | 45.11276 | 0.18571 | 2.008919 | (200) | 4.01784 | 514.9097 |
| 0.88 | 38.78495 | 0.17857 | 2.320829 | **(111)** | 4.01979 | 524.2687 |
| | 45.05102 | 0.20714 | 2.011529 | (200) | 4.02306 | 461.5357 |
| 1.17 | 38.75408 | 0.20714 | 2.322607 | **(111)** | 4.02287 | 451.9155 |
| | 45.02015 | 0.2000 | 2.012836 | (200) | 4.02567 | 477.9591 |

The XRD main peaks shifted from 38.75° to 38.91° in (111) plane and 45.02° to 45.17° in (200) plane. The increasing of $N_2$ flow rate affected to the main peaks shifted to the low diffraction angles. The lattice constants and crystal grain sizes were calculated from the peak positions and FWHM of the (111) main peaks, respectively. Table 6.1 shows the parameters calculated from XRD spectra. The increasing of $N_2$ flow rate affected to the increasing of crystal lattice constant as shown in Fig. 6.17. The shifting of lattice constant was due to the compressive stress developed in thin films.

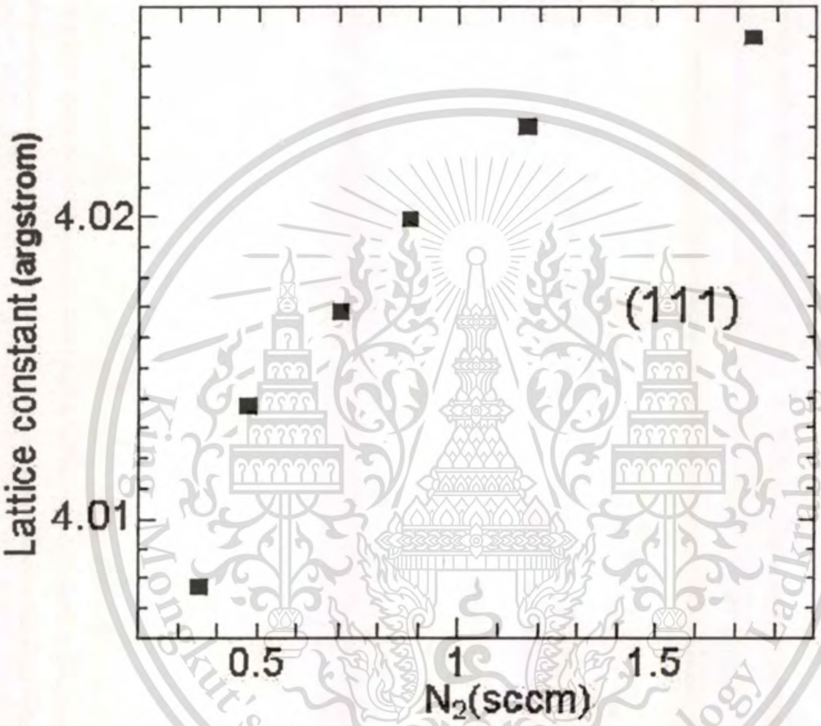

**Fig. 6.17** The relation between the lattice constant of AlN thin films and the flow rate of $N_2$.

In addition, the grain size of AlN thin films grown with different flow rate of $N_2$ obtained from FE-SEM images increased with increasing of $N_2$ flow rate. The nanocrystalline cubic AlN particle sizes determined from FE-SEM were shown in Fig. 6.18. The increasing of grain size with flow rate of $N_2$ was due to the improvement in the degree of crystallinity of thin films.

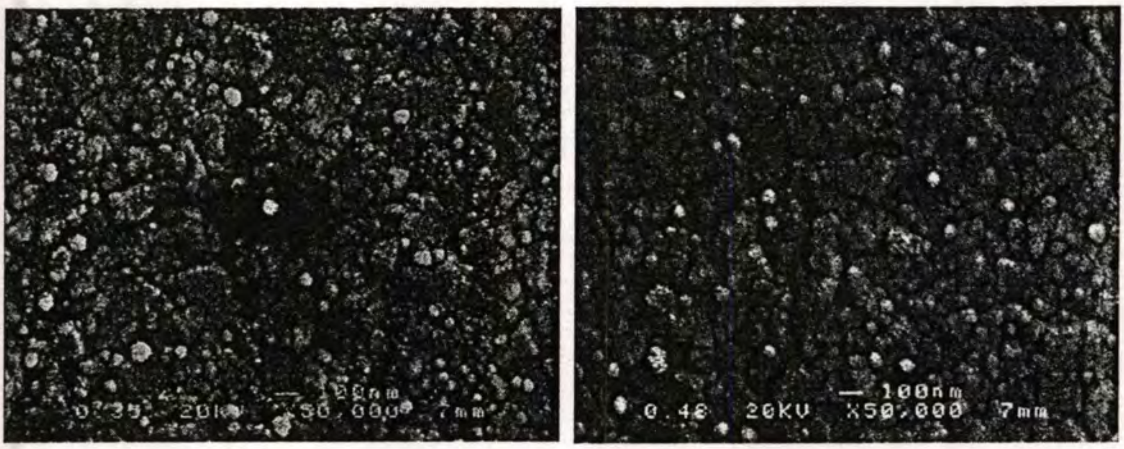

(a) 0.35 sccm

(b) 0.48 sccm

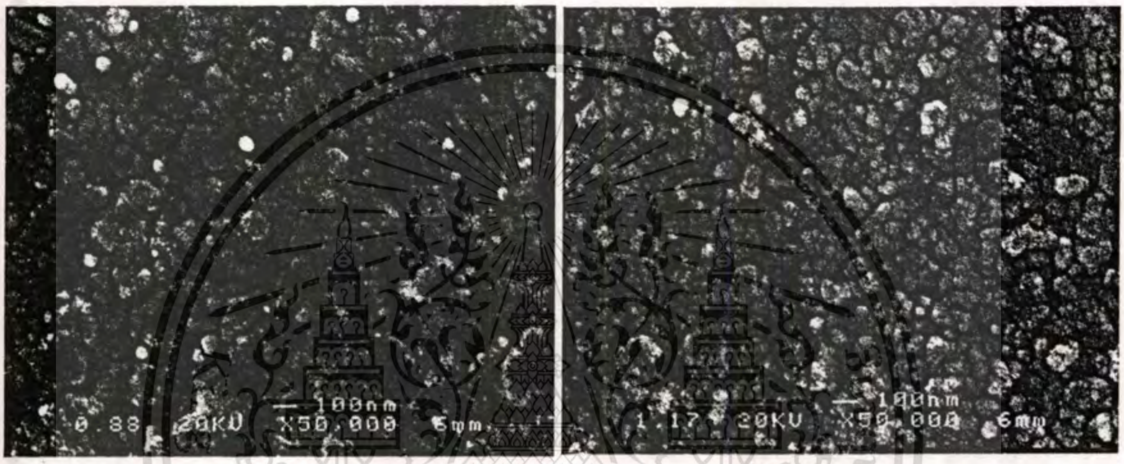

(c) 0.88 sccm

(d) 1.17 sccm

**Fig. 6.18** FE-SEM images of AlN thin films grown with differen1ce flow rates of $N_2$ at (a) 0.35, (b) 0.47, (c) 0.88, and (d) 1.17 sccm, respectively.

Room-temperature PR measurement was conducted to investigate the band gap transition energy of cubic-AlN thin films grown by reactive gas-timing rf magnetron sputtering with difference $N_2$ flow rate. In PR measurements, a modulation light was provided by He-Cd laser. The laser irradiated the AlN sample with a spot radius of about 1 mm. A deuterium lamp was dispersed by a 25-cm monochromator and used as a probe light. The reflected light from the sample was detected by a UV-Si photodetector, and the signal from the detector was fed to a lock-in amplifier. The PR spectra of all samples are shown in Fig.6.19.

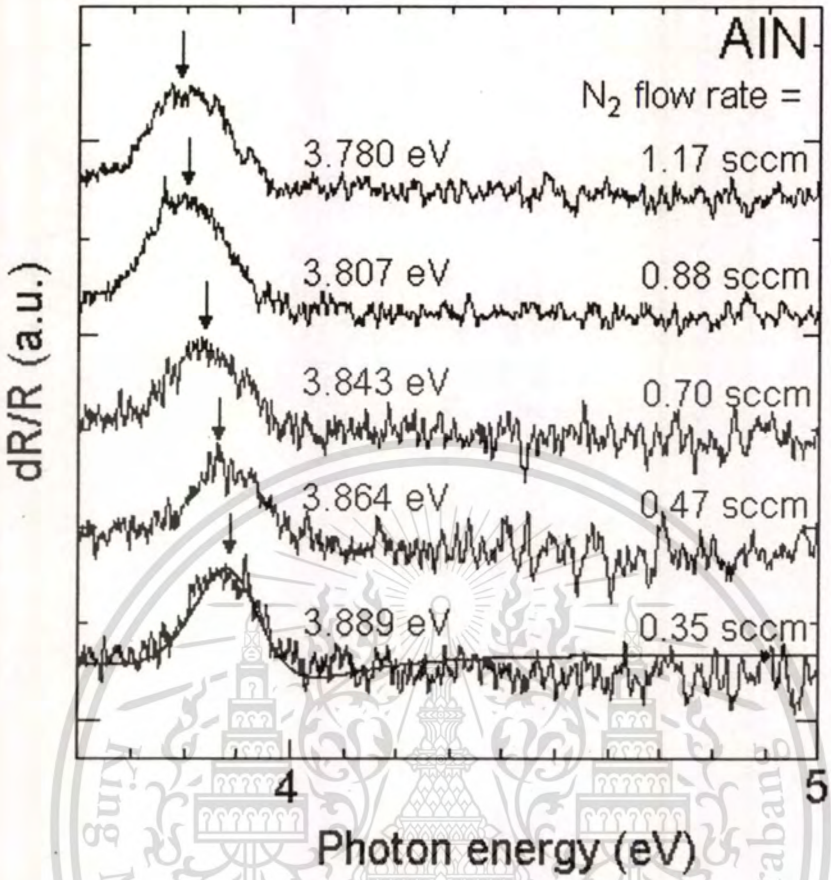

**Fig. 6.19** PR spectra of AlN thin films grown with difference flow rates of $N_2$ in range of 0.35 to 1.17 sccm.

The PR spectra reveal the band-to-band transition in AlN thin films. The clear PR spectra indicate excellent optical quality of these films grown by reactive gas-timing which is firstly developed in our laboratory.The energy levels associated with band-to-band transitions were determined by least-square fitting of Eq. (6.1) to PR spectra obtained experimentally.

The PR spectra (dR/R) as a function of band-gap energy can be calculated using the derivative function in the low electric field limit [6]

$$\frac{dR}{R} = \mathrm{Re} \sum_{j=1}^{p} C_j e^{i\theta_j} \left( E - E_{g_j} + i\Gamma_j \right)^{-n} \tag{1}$$

where $E$ is photon energy, $p$ is the total number of spectral structures to be fitted, and $E_g$ , $\Gamma_j$, $C_j$ and $\theta_j$ are the band-gap energy, broadening parameter, amplitude, and phase of the $j$ th features that correspond with critical points. The parameter $n$ is dimensional critical points.

The least-square fitting is also shown in fig. 6.19 by the black line. In the calculation, the $n$ value is 5/2 for the band gap transition. The band gap transition energies obtained from these fitting are also shown by arrows in figure. Morkok *et al.* [7] have reported photoluminescence determination using eximer-laser excitation on AlN grown on sapphire substrates. The samples exhibit broad peaks at a photon energy of 3.8 eV due to band-to-band energy of AlN thin films. Notice that the band gap energy of AlN in this study is in excellent agreement and which is quite accurate since the spectral difference with flow rate of $N_2$ is clear and temperature is fixed.

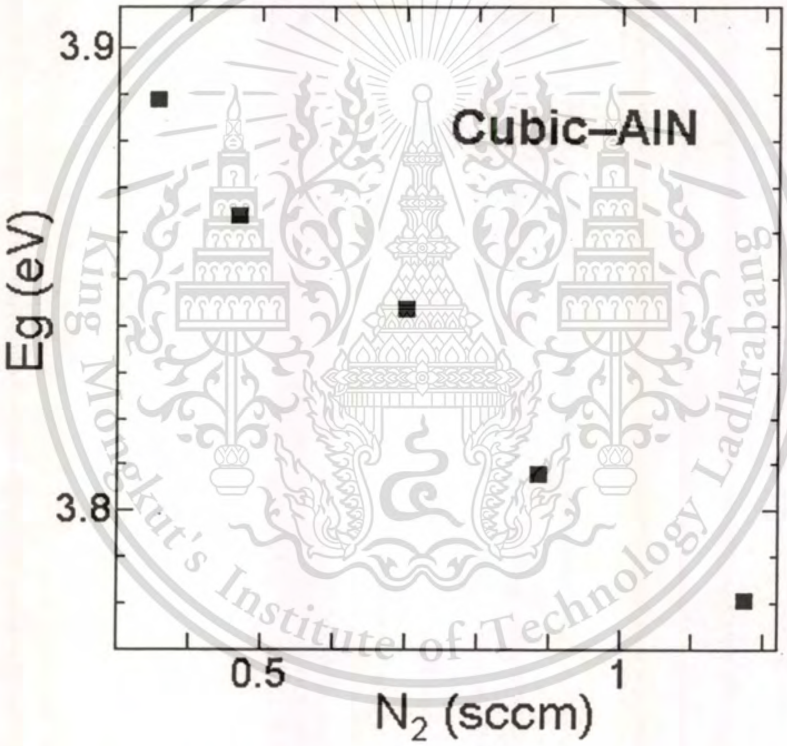

**Fig. 6.20** The relation between bandgap energy of AlN thin films and the flow rate of $N_2$.

In fig.6.20, the band gap transition energies determined from PR measurement are plotted as a function of $N_2$ flow rate. The transition energy decrease with increasing flow rate of $N_2$ might be due to the increase of grain size in addition to the effect of the crystal size on the electronic structure such as quantum confinement energies of electron and holes [8, 9].

### 6.2.3.5 Effect of Film Thickness

The previous experiments above were resulted the optimized conditions for growing cubic-AlN thin films by reactive gas-timing rf magnetron sputtering. In this experiment, the AlN thin films were grown with different thickness on cleaned substrates. The film thickness was varied at 90, 100, 200, and 500 nm, respectively. The crystalline structures and the surface morphology of samples were investigated by XRD and FE-SEM.

The thickness of thin film affects to the formation cubic-AlN due to the improvement of crystallinity as shown in fig. 6.21 and 6.22. Amorphous phase structures are shown in AlN thin films with thickness lower than 500 nm which have no peak observed in XRD spectra. The FE-SEM images show surface morphologies of nanocrystal cubic-AlN in fig. 6.22 (a) and amorphous-AlN in fig. 6.22 (b) and (c).

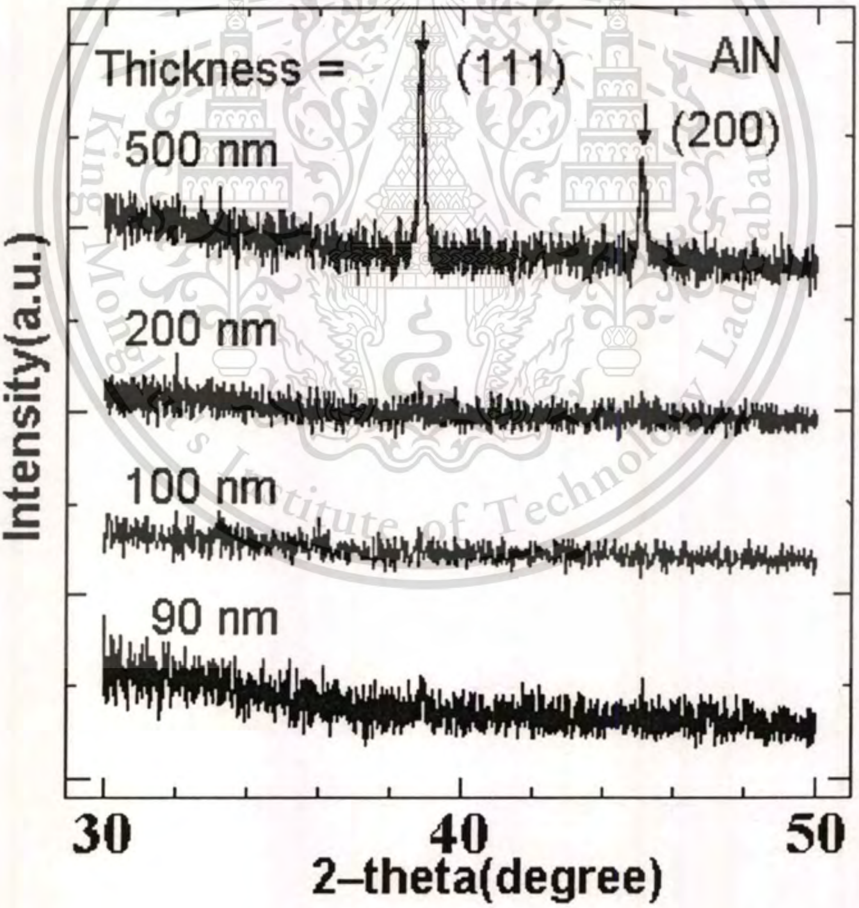

**Fig. 6.21** XRD results of AlN thin films grown with difference thickness.

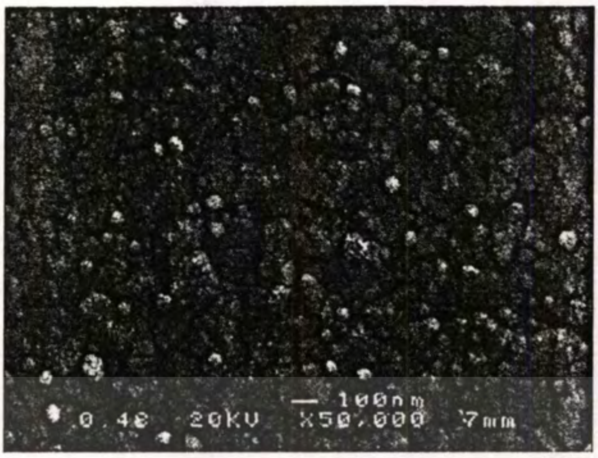

(a) 500 nm

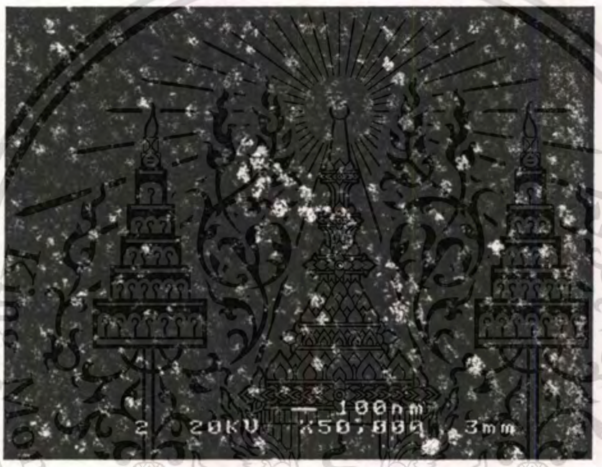

(b) 200 nm

(c) 100 nm

**Fig. 6.22** FE-SEM images of AlN thin films grown with difference thickness of (a) 500, (b) 200, and (c) 100 nm, respectively.

## 6.3 Chapter Summary

This chapter presented the experimental on AlN thin films grown by r.f magnetron sputtering with and without reactive gas-timing and their characterizations. The experiment results show that the reactive gas-timing played an important role in the formation of AlN thin film grown at room temperature and no any annealing during and after the process. The reactive gas-timing technique may increase the opportunity of energetic nitrogen ions to react with Al atom to form AlN compound in cubic structure.

The XRD spectra of AlN indicated a high quality poly-crystalline structure oriented along (111) and (200) as cubic structure. The increasing lattice constant of AlN thin films related with the increasing of $N_2$ flow rate in sputtering process. The shift of lattice constant was due to the compressive stress developed in thin film. The nanocrystalline cubic-AlN particle sizes determined from FE-SEM. The increasing of grain size with $N_2$ flow rate was due to the improvement in the degree of crystallinity of thin films.

PR measurements were used to investigate band-to-band transition energies in AlN grown by reactive gas-timing rf magnetron sputtering. The band-gap transition energies of cubic-AlN were determined by fitting the PR spectra with the values of 3.78 - 3.89 eV depended on the flow rate of $N_2$. The band-gap transition energy decrease with increasing flow rate of $N_2$ might be due to the increase of grain size in addition to effect of quantum confinement energies.

This result is explained by the difference of the sputtering yield of Ar-ions and N-ions. As the mass of Ar-ion was greater than that of N-ion, the sputtering yield of Ar was larger than that of N. In order for the sputtering process to be more efficient, the incident particle has to be of atomic dimensions. A very small particle, such as electron, does not carry enough momentum to be effective, whereas too large and massive particle cannot interact with individual atoms or molecules in the surface. Argon gas tends to be an effective compromise between ion mass and cost, so the Ar gas is the most commonly used sputtering gas. Thus, it seems that the amount of Al atoms sputtered from the Al target decreased with $N_2$ concentration.

## References

[1] L. Wu, S. Wu, and H. T. Song, **"Influence of Sputtering Pressure on Physical Structure of AlN Thin Films Prepared on Y-128° $LiNbO_3$ by RF Magnetron Sputtering"**, J. Vac. Sci. Technol. A Vol. 19, No. 1 (2001) 167.

[2] M. Akiyama, T. Harada, C.N Xu, K. Nonka, and T. Watanabe, **"Preparation of Highly Oriented AlN Thin Films on Glass Substrates by Helicon Plasma Sputtering and Design of Experiments"**, Thin Solid Films 350 (1999) 85.

[3] B. Wang, Y. N. Zhao, and Z. He **"The Effects of Deposition Parameters on The Crystallographic Orientation of AlN Films Prepared by RF Reactive Sputtering"**, Vaccum. Vol. 40, No.5 (1997) 427.

[4] F. Engelmark, G. Fucntes, I. V. Katardjiev, A. Harsta, U. Smith, and S. Berg **"Synthesis of Highly Oriented Piezoelectric AlN Films by Reactive Sputter Deposition"**, J. Vac. Sci. Technol. A Vol. 18, No. 4, (2000) 1609.

[5] H. L. Kao, P. J. Shih, and Chun-His Lai, **"The Study of Preferred Orientation Growth Aluminum Nitride Thin Films on Ceramic and Glass Substrate"**, Jap. J. Appl. Phys. 38 (1999) 1526.

[6] C. H. Wu, W. Y. Chiu, and H. L. Kao, **"Texture and Smooth AlN Films Prepared by Helicon Sputtering System for SAW Device Applications"**, Electronics.

[7] J. W. Soh, and W. J. Lee, **"SAW Characteristics of AlN Films Deposited on Various Substrates Using ERC Plasma Enchanced CVD and Refractive RF Sputtering"**, IEEE Ultrasonic Symposium (1996) 299.

[8] M. Ishihara, S. J. Li, H. Yumoto, K. Akashi, and Y. Ide, **"Control of Preferential Orientation of AlN Prepared by The Reactive Sputtering Method"**, Thin Solid Films 316 (1998) 152.

## CHAPTER 7

# GROWTH AND CHARACTERIZATIONS OF InN THIN FILMS

## 7.1 Introduction

**InN Thin films:**

Until now, InN has been the least studied of nitride semiconductors. This is mainly due to the difficulty in obtaining high quality InN crystals, which is due to the low dissociation temperature, high equilibrium vapor pressure of nitrogen molecules and the lack of suitable substrates for InN. Studies on InN started in the beginning of the 20th century with an attempt to grow bulk InN from a melt [1]. The attempt was not successful because of the low dissociation temperature and high vapor pressure of nitrogen molecules [2]. The next step in growing InN moved beyond the equilibrium. The next-step in growing InN moved beyond the equilibrium approach to the nonequilibrium approach using various substrate materials by various growth methods including d.c., r.f., and magnetron sputtering [3-5]. The InN films obtained by these methods in the 1970s and 1980s were all polycrystalline, some with an aligned orientation along the c-axis; the films also contained an extremely high defect density. The physical parameters of InN were determined using these crystals. The first estimated direct band gap was about 1.9 eV [6]. However, other studies reported values ranging from 1.7 to 3.1 eV [3, 7-11]. The most commonly cited measurement on optical absorption is that of Tansley and Foley [12]; they reported bandgap energy of 1.89 eV at room temperature.

In the late 1980s, improvements in growth techniques have made it possible to obtain single-crystalline InN. Single-crystalline InN was reported by Matsuoka *et al*. [13] for the first time in 1989 using MOVPE. Subsequently, several efforts [14, 15] were made to improve the quality of InN and high-quality films with carrier concentrations on the order of $10^{18}$ $cm^{-3}$ and mobilities of 730 $cm^{2}$/ Vs [16] were obtained. Growth by MOVPE, however, has an inherent disadvantage because it must satisfy the conditions for $NH_3$ pyrolysis and InN dissociation, which impose conflicting temperature requirements. In contrast, MBE equipped with an r.f. plasma source has an essential advantage over MOVPE for obtaining high-quality InN. In this growth method, neutral and ionized excited-state nitrogen atoms and molecules can be generated separately by plasma sources. Thus, the crystal growth temperature can be set independently without considering the nitrogen source. The first attempt to grow single-crystalline InN by the R.F.-MBE method was reported by Hoke *et. al.* in 1991 [17].

Improvements in crystal quality were realized by various techniques such as insertion of low-temperature GaN [18], AlN [19], and InN [20] buffer layers. Within a relatively short period of time, MBE growth studies produced high-quality films with residual electron concentrations of $1.6x10^{18}$ $cm^{-3}$ and a room temperature mobility of 1,180 $cm^2$/ Vs [18]. Such rapid progress is probably due to the inherent advantage of the MBE growth method.

Photoluminescence (PL) and optical absorption were used to study single-crystalline InN films that were grown using MOVPE and MBE. These studies revealed that the fundamental band gap of single-crystalline InN was about 0.8 eV [21-25] instead of 1.9 eV, determined by optical absorption using polycrystalline InN.

This research presented the detailed studies of InN thin films growth by r.f. magnetron sputtering with reactive gas-timing technique. First, fundamental studies on basic growth process are reviewed; these include the initial growth stage, two-step growth processes, the precise control of growth parameters, and the resultant crystal properties of the grown films. This thesis presents the PR spectroscopy measurement for the band gap observation of high-quality InN films. The techniques include XRD, SEM, PR and UV-VIS. Typical results are described in this chapter.

**ITO Thin Films:**

It has been reported that r.f. magnetron sputtering yields ITO thin films with low resistivity and good reproducibility. For the crystallization of ITO thin films, the heating process at an elevated temperature during the film deposition or an addition post-annealing treatment at around 150°C is required. The substrate temperature is an important parameter for several applications, particularly when organic polymer substrates are used.

Sputtering involves knocking an atom or molecule out of a target material by accelerated ions from an excited plasma and condensing it on the substrate either in its original or in a modified form. When this modification is induced by a chemical reaction during the transit from the target to the substrate, the process is referred to as reactive sputtering. In general, most ITO sputter sources consist of hot pressed 90% $In_2O_3$:10% $SnO_2$ compound targets. The sputtering can be achieved by a number of ways which include accelerating the plasma ions by a d.c. field [26] or a d.c. field combined with a magnet (to direct the high velocity emitted electrons away from the substrate), r. f. (with its self induced bias) as well as by ion beams [27]. Hence names such as magentron [28] and reactive r.f. sputtering [29, 30] reflect on the process that has been used for the deposition of the ITO film. The technique used in the course of this study involves reactive r. f. sputtering in an Ar/$O_2$ plasma. This method is reputed for its excellent uniformity, high conductivity and high transparency. The r.f. field ensures that sputtering of non-conductive materials can be achieved at a practical rate. Parameters known to influence ITO quality include sputtering pressure, pre-conditioning, film thickness and r. f. power amongst others. The control of oxygen partial pressure is particularly critical in determining the conductivity and transmittance. However, without the ability to direct unwanted high velocity electrons away from the substrate, damage is associated with this technique; on the other hand, magnetron sputtering yields high deposition rates and minimizes this damage.

In this dissertation, the deposition and characterizations of ITO thin films on PET substrate by RF magnetron sputtering with gas-timing technique are investigated because of their advantages for plastic electronics applications. By our technique, we have succeeded in growing ITO on various substrates at room temperature.

**InON Thin Films:**

High oxide/InN contrast in refractive index is therefore very attractive for photonic bandgap design in photonic device development. A combination of beneficial properties of indium nitride and indium oxide results in a new material indium oxynitride with variable composition and functionality. Changing the oxygen-to-nitrogen ratio in In-O-N in a wide range offers a possibility to tune the film properties by controlling the progress parameters.

In this research, we present an experimental study on the surface structure, the optical bandgap, and the flow rate ratio of nitrogen/oxygen as reactive gases in a series of polycrystalline InN to InO films grown by r.f. magnetron sputtering. The structural and optical properties on InN to InO crystals will be suggested on the XRD, SEM and UV-VIS results.

The innovative reactive gas-timing technique using r.f. magnetron sputtering was used to grow all nitrides thin films in this dissertation experiments.

## 7.2 Experimental Results and Discussions

### 7.2.1 Substrate Cleaning Process

The glass slides (Menzel-Glaser German model: Superfrost) were used as the substrates for all InN, ITO and InON films. The glass substrate cleaning process is as following,

1) Wash the glass surface with detergent solution for 15 minutes in ultrasonic bath cleaner
2) Rinse with the tap water
3) Etch the oxide and contamination on the surface with PIRANHA process ($H_2SO_4$ + 30% $H_2O_2$ with 4:1 by volume) for 30 minutes
4) Rinse in tap water for 20 minutes
5) Deep rinse in de-ionized (DI) water for 30 minutes in ultrasonic bath cleaner
6) Dry out the surface with nitrogen gas
7) Bake the substrates in oven at 200 °C

The plastic substrate (PET) was used as the flexible substrate for depositing ITO thin films. The PET substrate cleaning process is as below,

1) Wash the plastic surface with detergent solution for 15 minutes in ultrasonic bath cleaner
2) Rinse with the tap DI-water
3) Dip in Acetone, Methyl Alcohol and Isopopanol for 5 minutes in ultrasonic bath cleaner, respectively.
4) Dry out the surface with nitrogen gas
5) Cure in the UV light for 30 minutes.

### 7.2.2 InN Thin films Growth without Reactive Gas-Timing

A substrate distance to the target was optimized at the 7 cm. from experimental study of AlN thin film. The indium purity of 99.999% was used as a target material with a diameter of 3 inch. The base pressure of the chamber was $6x10^{-7}$ mbar. The relation of growth rate between Ar and $N_2$ flow rates, the r.f. power of sputtering, the reactive gas-timing sequence, and the film thickness affected to InN thin films were observed and discussed in the next subjects.

#### 7.2.2.1 Indium (In) Growth in Ar Plasma

After indium (In) target pre-sputtering process, 1 μm thick of In film was grown on cleaned glass substrate. The Ar purity of 99.999% was used to bombard the target with r.f. power 50 W.

The flow rate of Ar was 10 sccm, which optimized for our sputtering system with no r.f.-reflected effect. The importance of this experiment is the observation of In crystalline peaks as reference film obtained by XRD. The XRD pattern of In film is shown in Fig. 7.1. FE-SEM was used to investigate the surface morphology of 1 μm thick-In film as shown in Fig.7.2.

The XRD 2-theta (angle) peaks are 32.9°, 36.3°, and 39.1° in orientation of (101), (002), and (110) planes, respectively, as In tetragonal polycrystalline structure. The result pattern (2-theta angle) was matched from XRD spectrophotometer standard database.

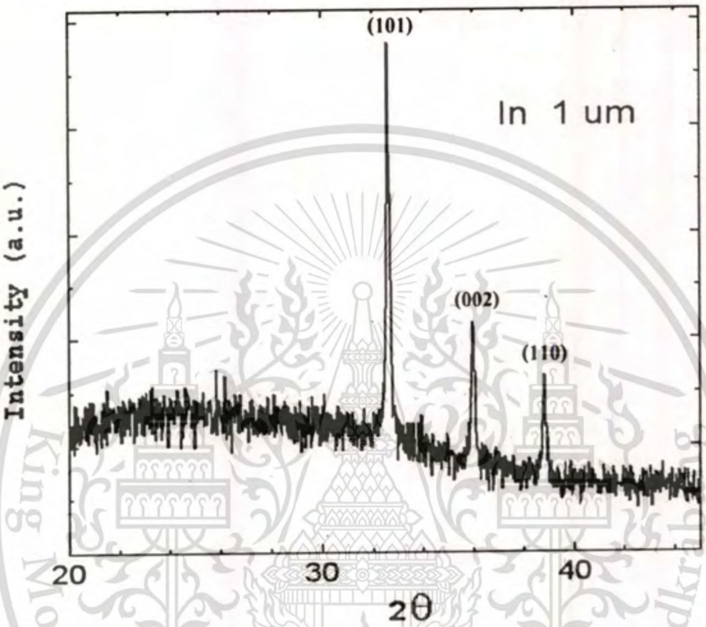

**Fig. 7.1** XRD results of 1 μm-Indium film grown on glass substrate without reactive gas-timing r.f magnetron sputtering.

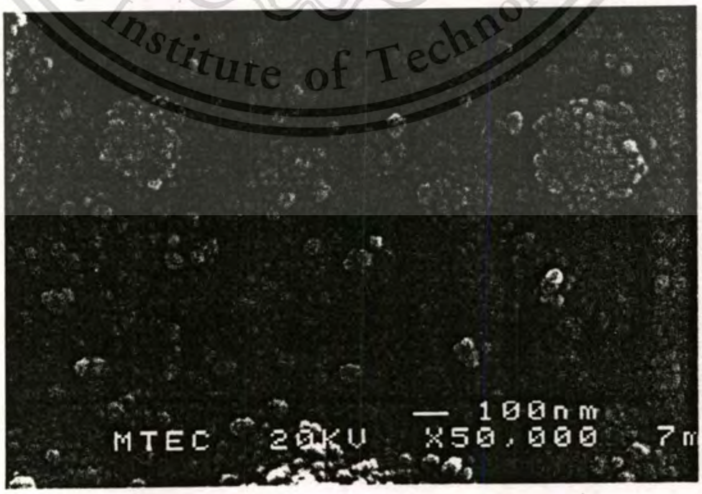

**Fig. 7.2** FE-SEM image of 1μm-In thin film grown on glass substrate without reactive gas-timing r.f magnetron sputtering.

#### 7.2.2.2 Thin Film Growth in Pure $N_2$ Plasma

The $N_2$ purity of 99.999% was fed into the chamber with the flow rate of 9 sccm without r.f reflecting effect. Thin films with thickness of 500 and 1000 nm were grown on glass substrates by r.f. power of 100 W. Figure 7.3 and 7.4 show the XRD results of films grown in pure $N_2$ plasma (without Ar mixed) at r.f. power of 100 W with thickness of 500 and 1000 nm, respectively. The thin film with 500 nm exhibits amorphous phase, while the XRD peaks of 1000 nm film are 32.9°, 36.3°, and 39.1° in orientation of (101), (002), and (110) planes, respectively. The XRD result reveals that 1000 nm film grown with r.f power of 100 W in pure nitrogen plasma without reactive gas-timing technique obtains tetragonal In structure.

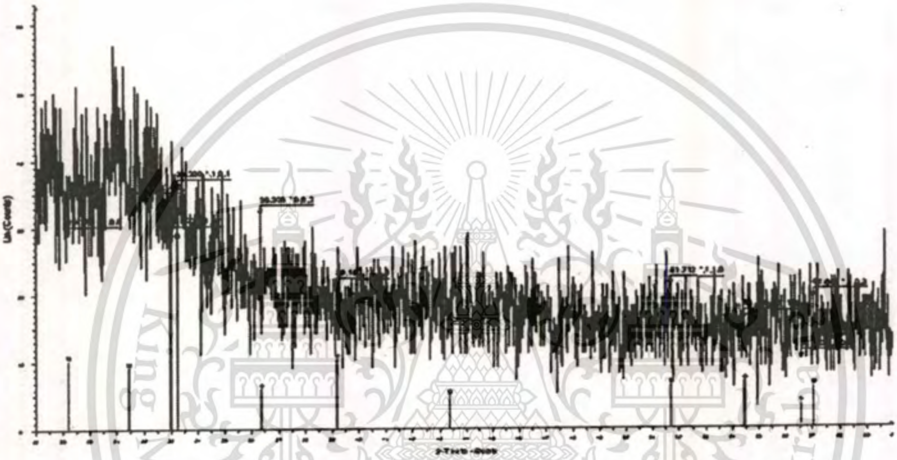

**Fig. 7.3** The XRD result of 500 nm film grown with $N_2$ plasma (without Ar mixed) at r.f power of 100 W.

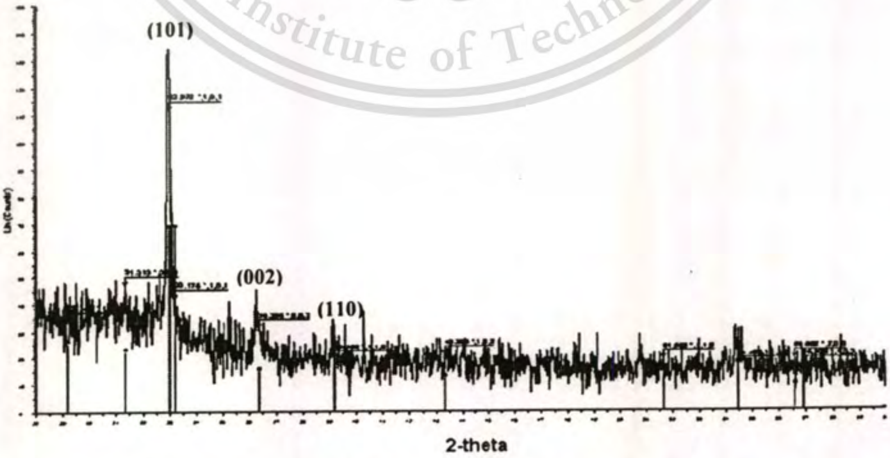

**Fig. 7.4** The XRD result of 1000 nm-film grown with $N_2$ plasma (without Ar mixed) at r.f power of 100 W.

From the results of experiments, it can imply that the nitrogen ions take majority of ion bombardment on indium target and form In thin film on substrate.

### 7.2.3 InN Thin Films Growth with Reactive Gas-Timing

The InN thin films were grown by r.f. magnetron sputtering at room temperature using reactive gas-timing technique. This technique was successfully used to grow cubic-AlN thin films reported in previous chapter. The reactive gas-timing was used to control the flow sequence of Ar and $N_2$ gases. Figure 7.5. shows the schematic of gas flow sequence; the solid line denotes the sequence of ultra high purity (UHP) Ar that takes advantage of bombard ion on 99.999% In target for 30 sec. The dash line denotes the sequence of UHP $N_2$ that takes a function of reactive ion with In atoms for 90 sec in order to form InN compound on the cleaned substrate. The chamber was pre-vacuated to $6x10^{-7}$ mbar, while the sputtering pressure was $4.0 \times 10^{-3}$ mbar. The flow rate of Ar and $N_2$ gases was fixed at 10 and 9 sccm, respectively. This flow rates were used due to no reflected-r.f. power. The period of time sequence depends on the film thickness.

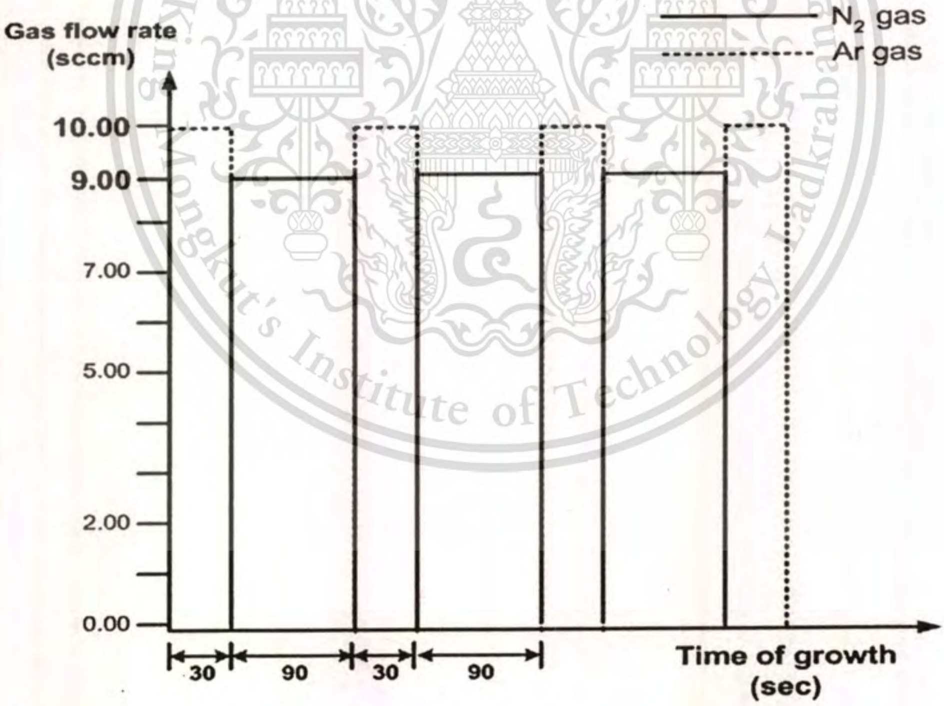

**Fig. 7.5** Time sequence of 30 sec of Ar and 90 sec of $N_2$ flow rate. The flow rate of Ar is fixed at 10 sccm and $N_2$ is fixed at 9 sccm.

#### 7.2.3.1 Effect of RF Sputtering Power

A 500 nm thick of InN thin films were grown on cleaned glass substrates witch varying r.f. sputtering power of 20, 50, 100 and 200 W, respectively by using reactive gas-timing technique. The chamber was pre-vacuated to 6x10$^{-7}$ mbar, while the sputtering pressure was 4.0x10$^{-3}$ mbar. The flow rate of Ar and $N_2$ gases was fixed at 10 and 9 sccm, respectively. Charging effect is not observed during the sputtering process. The crystalline orientation of thin films was investigated by XRD.

Figure 7.6 shows XRD patterns of InN thin films deposited with r.f. sputtering power of 20, 50, 100, and 200 W, respectively. The samples grown with r.f. power of 100 and 200 W appeared strongly peaks at the diffraction angle (2θ) of 30.8° and 33.2° in the orientation along (002) and (101) planes, respectively corresponding to polycrystalline hexagonal InN structure, while the films prepared at 20 and 50 W showed very weak peaks. The results indicate that the activation of plasma gases at 100 and 200 W of r.f power is necessary for efficient growth of InN.

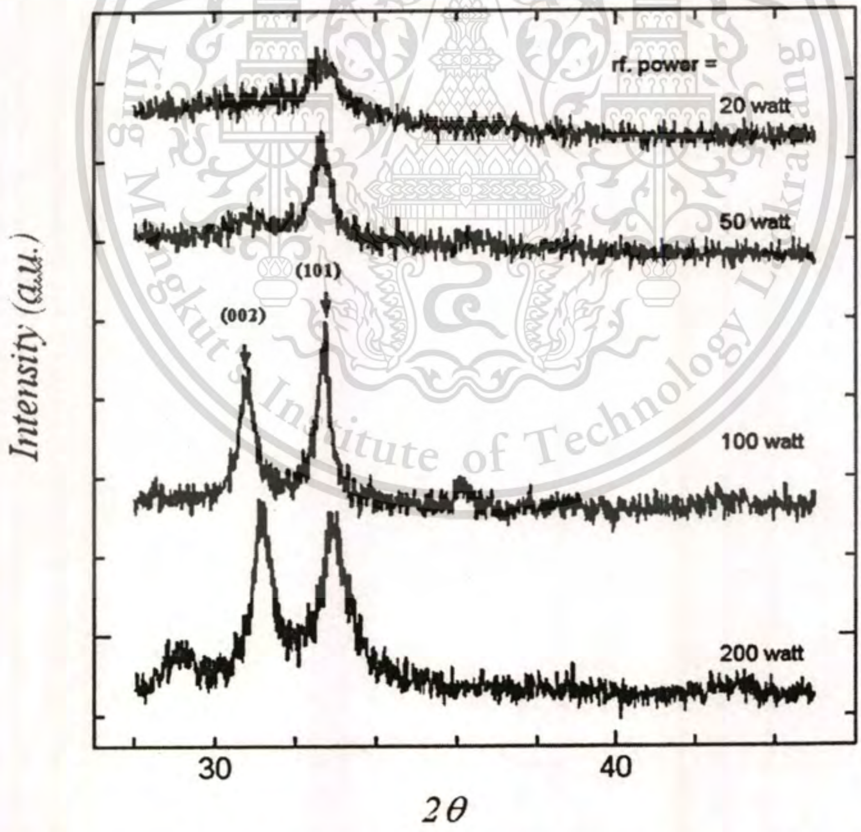

**Fig. 7.6** XRD patterns of InN thin films deposited with difference r.f. sputtering power of 50, 100, and 200 watts, respectively.

The surface morphology of all samples shows in Fig. 7.7. The photon energy of InN thin films obtained from PR measurement shows in Fig. 7.8.

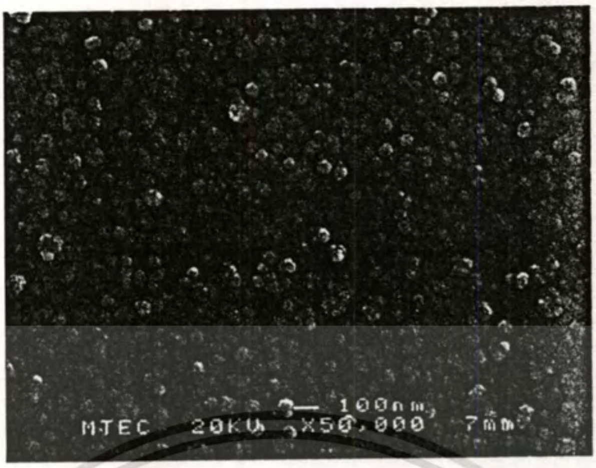

(a) 50 W

(b) 100 W

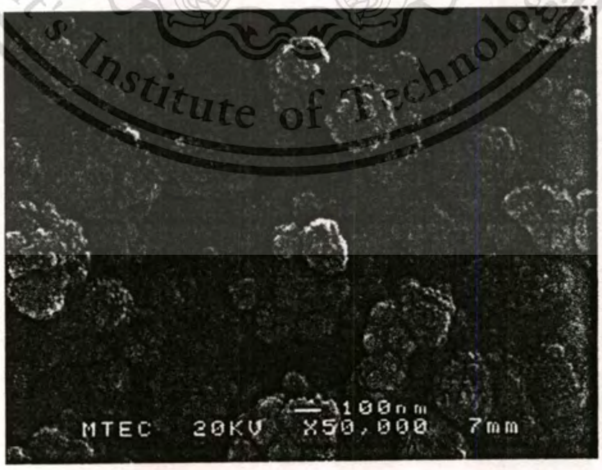

(c) 200 W

**Fig. 7.7** FE-SEM images of InN thin films deposited with difference R.F. sputtering power of (a) 50 , (b)100, and (c) 200 W, respectively.

In PR measurement, the samples exhibit broad peaks at photon energy around 1.18 eV due to band-to-band energy of InN thin films. The PR results confirmed that the high r.f. power was effectively to obtain high quality poly-crystalline hexagonal InN thin films deposited without substrate heating. The r.f. power of 200W is excessively because it damages the target surface caused the defect of In target. Then 100 W of r.f. power was reasonable to deposit InN thin films.

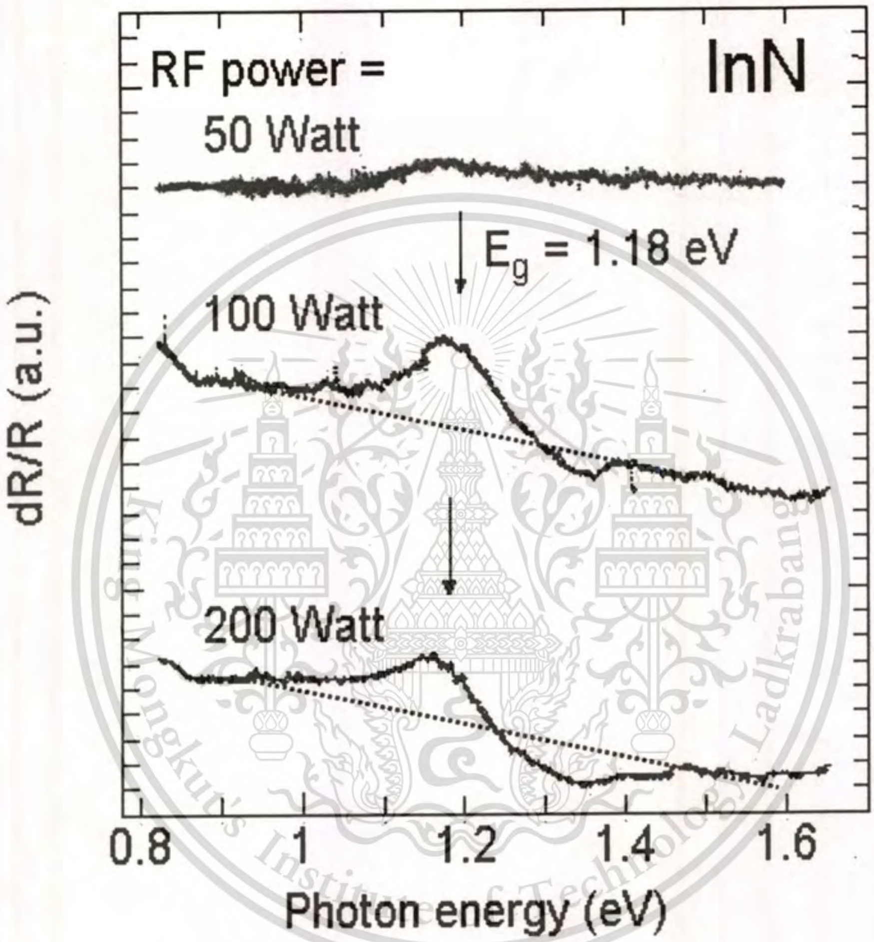

**Fig. 7.8** PR spectra of InN thin films deposited with difference r.f. sputtering power of 50, 100, and 200 W, respectively.

### 7.2.3.2 Effect of Gas-Timing Flow of Ar and $N_2$

The 500 nm InN thin films were deposited on cleaned substrates with reactive gas-timing technique. The 99.999% purity of Ar and $N_2$ were used as sputtering gases. According to the results of previous experiments, the flow rate of Ar:$N_2$ were fixed at 10:9 sccm and the In target was sputtered by 100 W of r.f. power optimized from 7.2.3.1 The base pressure was $6\text{x}10^{-7}$ mbar.

In this experiment, gas-timing sequence of Ar:$N_2$ was varied between 30:30 to 30:210 sec and in pure $N_2$, respectively. Figure 7.9 shows schematic of timing sequence in pure $N_2$ plasma sputtering. The crystallinity of all samples was investigated by XRD.

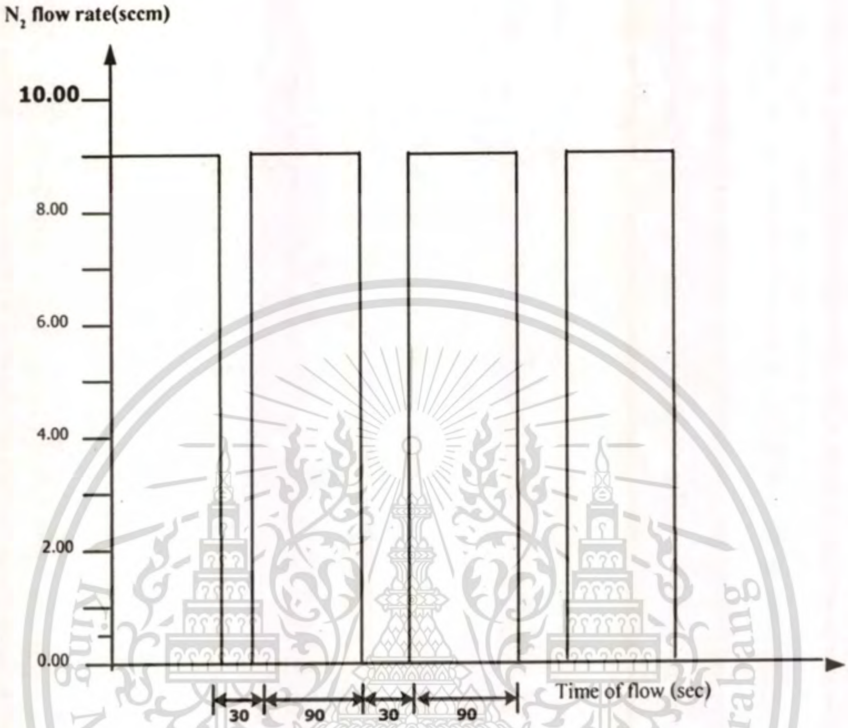

**Fig. 7.9** Diagram of gas-timing sequence of $N_2$ flow. The flow sequence of $N_2$ was 90 sec and stops for 30 sec.

Figure 7.10 shows the XRD patterns of InN hin films deposited with difference reactive gas-timing. The InN thin films grown with the gas-timing of Ar:$N_2$ of 30:30, 30:60 and 30:90 sec have the diffraction angle (2θ) of 30.8° and 33.2° in the orientation along (002) and (101) planes, respectively corresponding to poly-crystalline hexagonal InN structure. While InN thin films grown with Ar:$N_2$ of 30:150, 30:180 and 30:210 sec have decreasing of XRD intensity and shifting from that planes. InN thin film, however, grown in pure $N_2$ plasma shows one strong XRD peak in orientation along (111) plane corresponding to InN cubic structure.

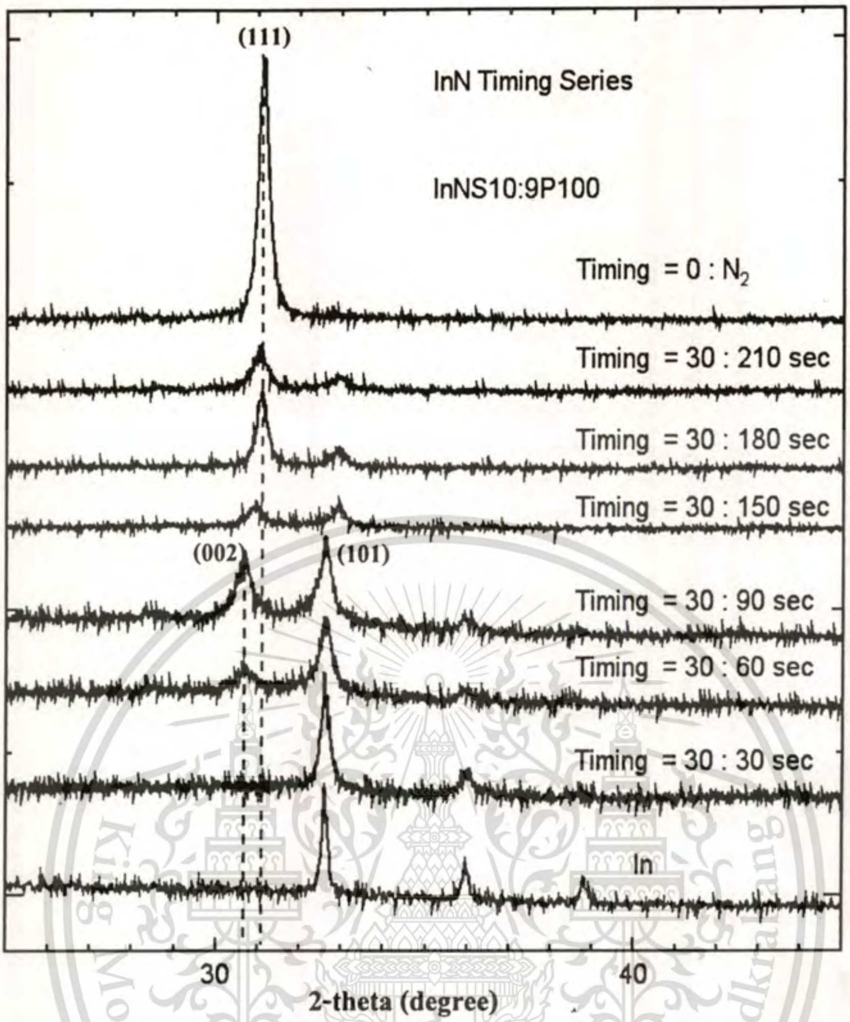

**Fig. 7.10** XRD patterns of InN thin films deposited with difference timing of Ar:$N_2$ flow.

The comparison of XRD patterns of tetragonal-In, hexagonal-InN, and cubic-InN thin films grown with reactive gas-timing r.f. magnetron sputtering shows in Fig. 7.11. With reactive gas-timing technique, the hexagonal-InN, and cubic-InN thin films were successfully obtained by varying timing sequence of gas flow. The morphology of hexagonal-InN, and cubic-InN thin films were observed by FE-SEM and AFM, respectively.

The morphologies of hex-InN and cubic-InN exhibit dramatically difference as shown in Fig. 7.12. It strongly indicates that the reactive gas-timing technique for r.f. sputtering system play an important role to the structure of InN thin film so we can select the growth conditions in order to achieve the InN with preferred structure. The XRD and FE-SEM reveal that the flow gas-timing is a significant growth parameter for the crystalline phase of InN. By the gas-timing technique used in sputtering growth, the InN as hexagonal and cubic structures will be achieved.

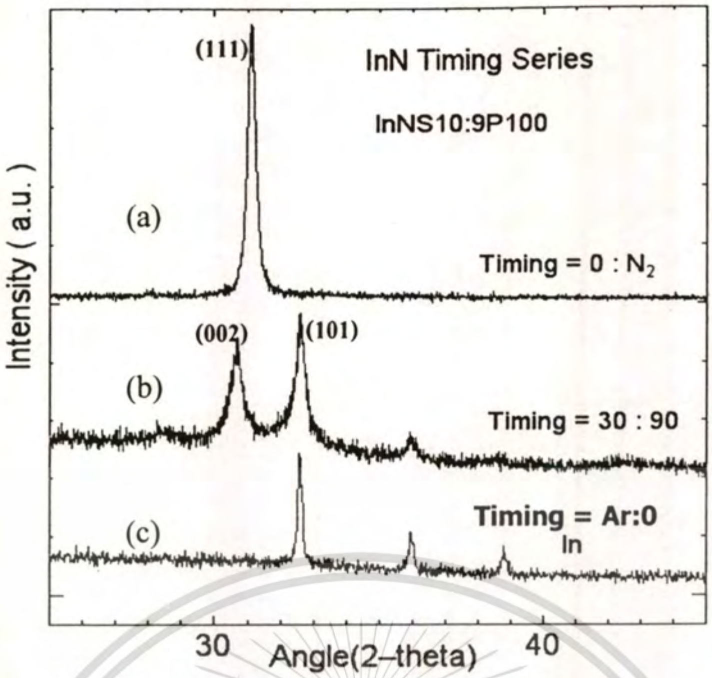

**Fig. 7.11** The comparison of XRD patterns of cubic-InN (a), hex-InN (b), and In (c) thin films

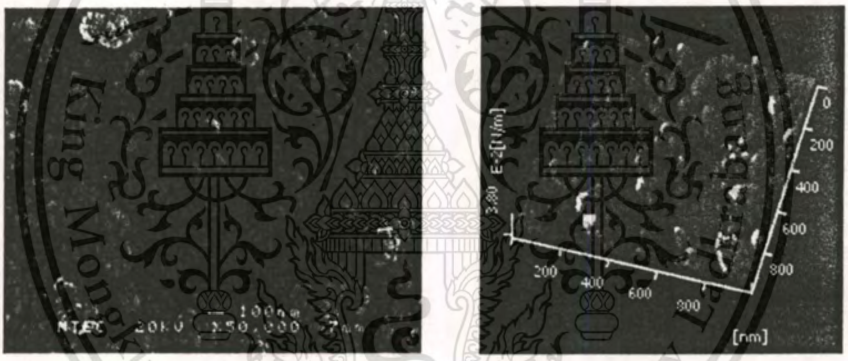

(1) FE-SEM

(2) AFM

(a) InN with timing of Ar:N$_2$=30:90 sec

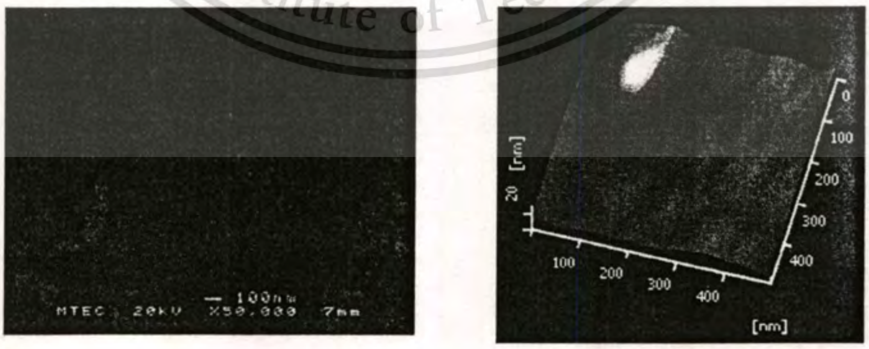

(1) FE-SEM

(2) AFM

(b) InN with timing of stop:N$_2$ = 30:90 sec

**Fig. 7.12** The FE-SEM and AFM images of hex-InN and cubic-InN thin films deposited with (a) timing of Ar:N$_2$=30:90 sec and (b) timing of stop:N$_2$=30:90 sec, respectively.

The bandgap energy of hex-InN and cubic-InN were also investigated by photocurrent spectroscopy (PC) set up in our laboratory. The detail of device fabrication was described in Chapter 8. Figure 7.13 The PC spectrum reveals the bandgap energy of InN grown by reactive gas-timing with different conditions. We found that the hex-InN and cubic-InN films have bandgap energy around 1.2 eV and 1.3 eV, respectively.

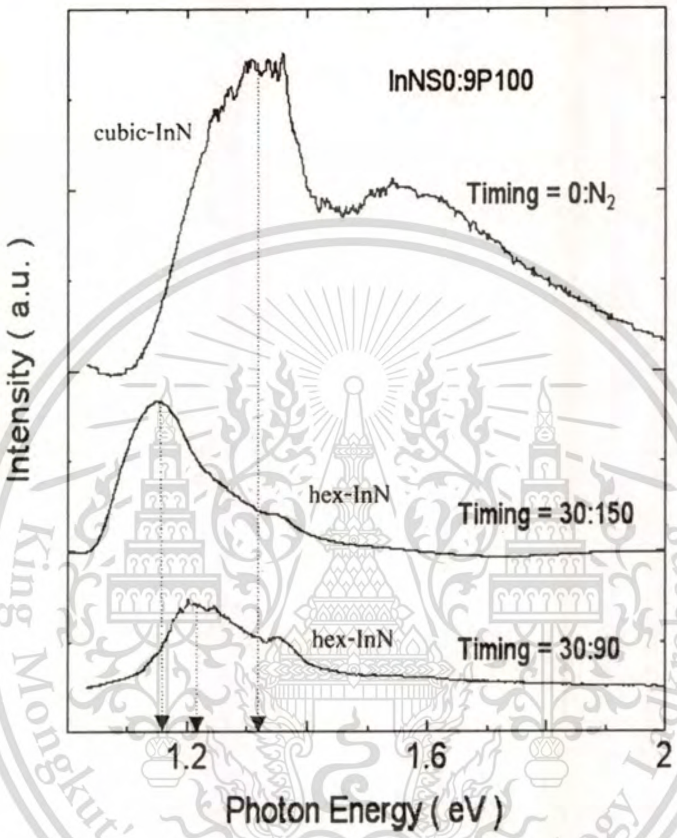

**Fig. 7.13** The PC spectrum reveals the bandgap energy of hex-InN and cubic-InN.

### 7.2.3.3 Effect of Film Thickness

The previous experiments were resulted the optimized conditions such as r.f. power, gas-timing and flow rate of gas, for growing InN thin films by reactive gas-timing r.f. magnetron sputtering. In this experiment, the InN thin films were grown with different thickness on cleaned substrates. The film thickness was varied at 50, 100, 200, 300, 500 and 1000 nm, respectively. The crystalline structures and the surface morphology of samples were investigated by XRD and SEM.

Figure 7.14 exhibits the XRD patterns of InN samples with the thickness of 100, 200, 300, 500, and 1000 nm shown the crystalline orientation along (111) plane as cubic structure. Cubic-

InN thin films, therefore, were achieved with reactive gas-timing technique in pure $N_2$ by r.f. magnetron sputtering. Figure 7.15 shows a photograph of InN thin film samples deposited in our laboratory with hexagonal- and cubic-crystalline structures.

It strongly shows that the cubic-InN thin film can be obtained with reactive gas-timing technique using r.f. magnetron sputtering without substrate heating.

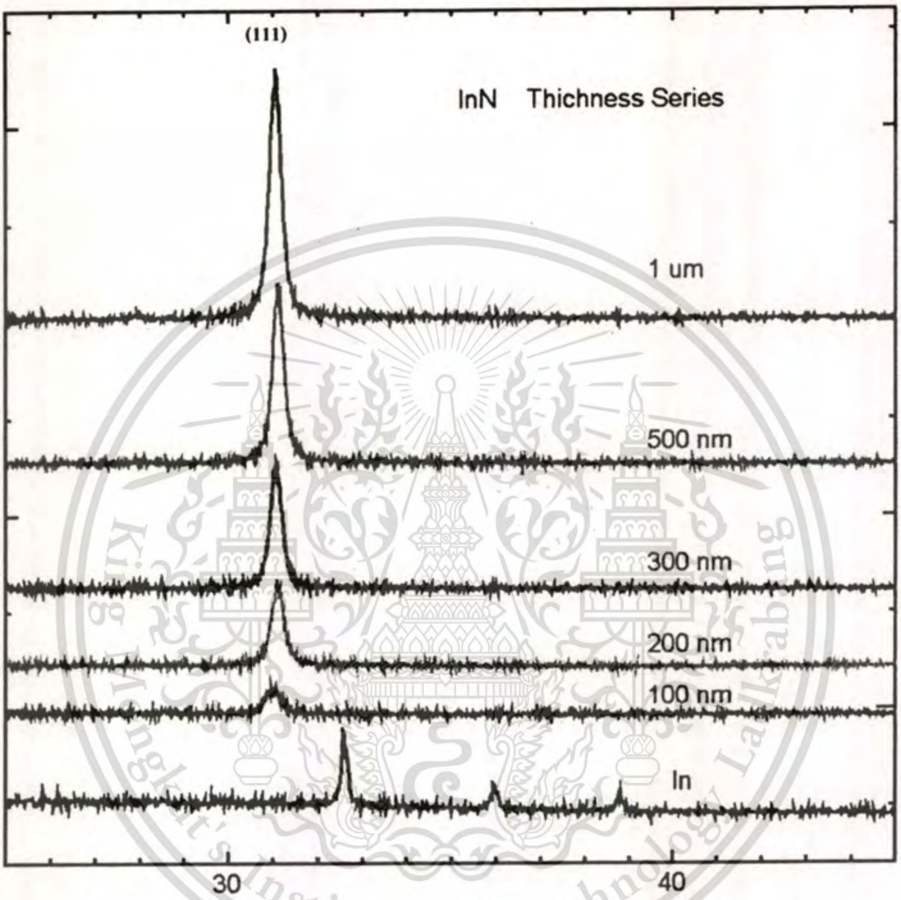

**Fig. 7.14** The XRD patterns of InN thin films deposited in $N_2$ plasma with difference thickness.

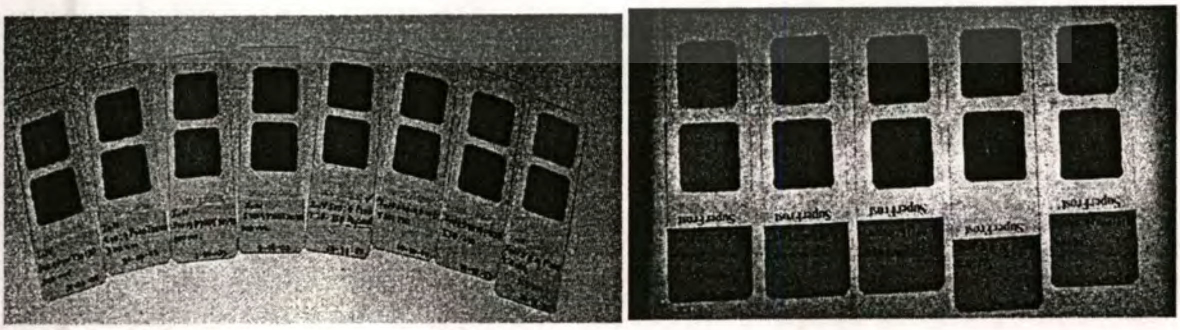

**Fig. 7.15** Illustrates of InN thin films deposited with reactive gas-timing r.f magnetron sputtering, hex-InN (a) and cubic-InN (b) crystalline structures.

The other researcher [22] ,the XRD patterns of hex-InN and cubic-InN in their experiment show in Fig. 7.16, the cubic-InN and hex-InN can achieved from InN nanodots synthesized with and without In droplets catalyst. This XRD patterns correspond to our XRD results.

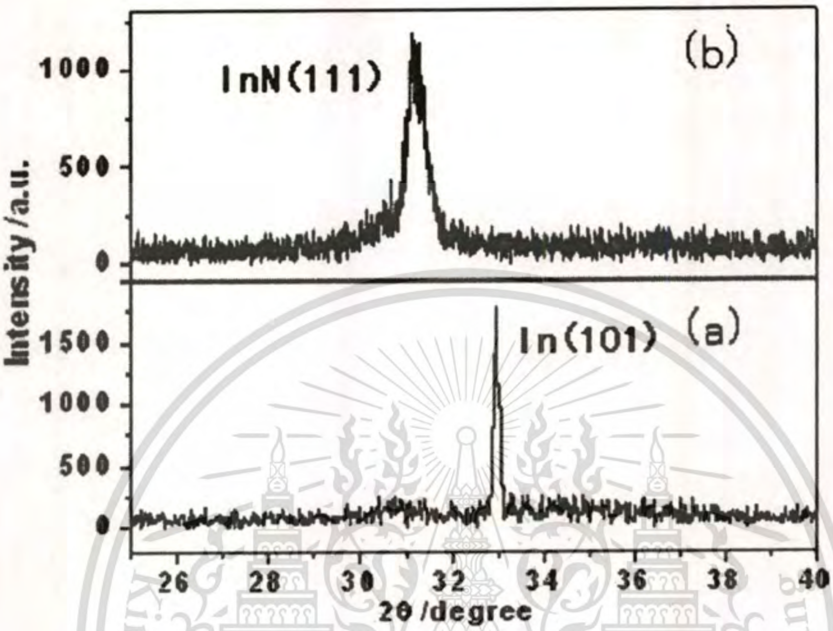

**Fig. 7.16** XRD pattern of InN nanodots synthesized with (a) and without (b) In droplets catalyst

### 7.2.4 ITO Thin Films Growth with Gas-Timing

#### 7.2.4.1 Effect of RF Sputtering Power

Tin doped Indium oxide (ITO) is an *n*-type, highly degenerated, wide band gap semiconductor with relatively low resistivity and high transmittance in visible range region. Due to these properties, it has been widely used as transparent electrodes in various displays, including liquid-crystal display (LCD), electro luminescent display (ELD), and organic light-emitting diode (OLED).

ITO thin films in this experiment take advantage of transparent electrode on flexible substrate. The PET (polyethylene terephthalate) was used as a substrate. By gas-timing technique, we have successfully for growing AlN and InN at room temperature by r.f. magnetron sputtering. The effect of r.f. sputtering power ITO thin film on PET are investigated here.

A ceramic $In_2O_3$:$SnO_2$ (90:10 wt.%, 99.99% purity) from Kurt J. Lesker was used as a target material. PET substrates were cleaned by the process in 7.1. The sputtering system was pump down to 1x10$^{-6}$ mbar for base pressure. Working pressure consisted mainly with high purity Ar (99.99%) gas was $3.2\text{x}10^{-3}$ mbar. The distance between target and the substrate was 5 cm, and the RF power was varied from 10 W to 40 W, whereas the thickness of ITO thin film was 200 nm. The deposition process was carried out at room temperature, i.e. the substrate was not heat during or after the film deposition. The sputtering conditions shows in Table 7.1.

**Table 7.1** Sputtering conditions used for deposition of ITO thin films.

| | |
|---|---|
| Base pressure | $1.0 \times 10^{-6}$ mbar |
| RF power | 10, 20, 30, 40 Watt |
| Substrate-target distance | 50 mm |
| Substrate temperature | Room temperature |
| Sputtering pressure | $3.2 \times 10^{-3}$ mbar, Ar gas activated |
| Ar flow rate | 10 sccm, fixed |
| Ar Gas-timing (on:off) | 50:2 second |

The schematic of Ar fed into the system for bombarding the target is shown in Fig. 7.17 the Ar gas valve was opened then fed into the sputtering chamber for 50 seconds and stopped for 10 seconds (Ar gas valve was closed). The on/off period of Ar gas was controlled by computer until the thickness of thin films is 200 nm.

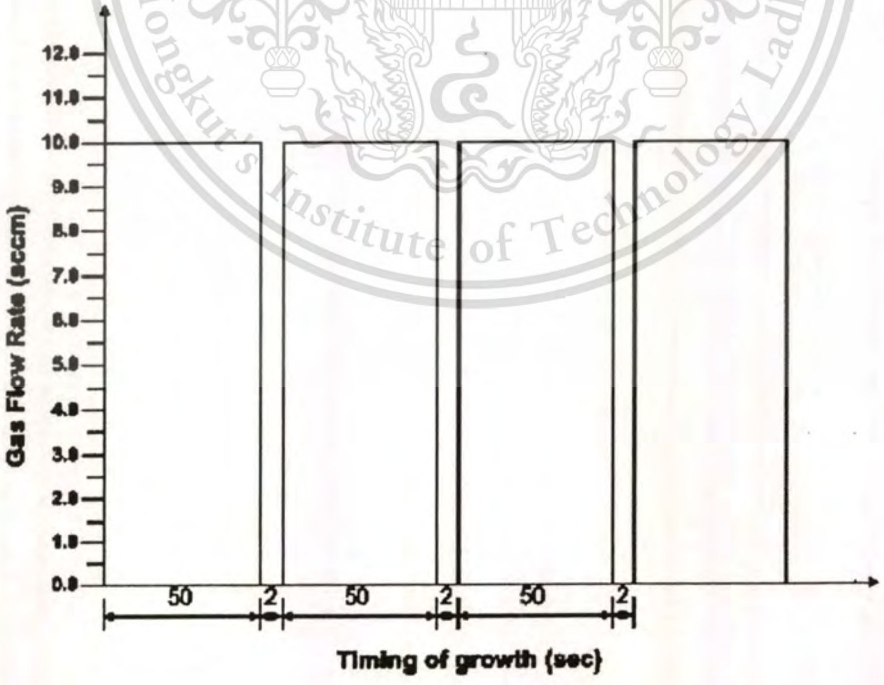

**Fig. 7.17** Diagram of gas-timing technique for ITO thin films growth, the Ar was fed into the sputtering chamber for 50 seconds and stopped for 2 sec.

The crystalline structure of ITO on PET substrate was investigated by a X-ray diffraction spectrometer (D8 Advance, Bruker) using Cu-K$\alpha$ radiation. The surface morphology of the films was observed with a scanning electron microscope. The growth rate and thickness of thin films was determined by crystal monitor. The optical transmission was taken by using UV-VIS spectrophotometer and the electrical characterization was done by measuring the sheet resistance using four point probe measurement.

The XRD pattern of ITO thin films on PET substrate which deposited at various r.f. power was showed in Fig. 7.18 which, (a) shows peak of PET crystallization and (b) shows ITO peak on PET. All deposited ITO thin films with various r.f. power on PET have XRD peaks at $2\theta = 30.273^\circ$ and $35.165^\circ$ which correspond to (222) and (400) planes as polycrystalline cubic bixbyite structure. The SEM micrographs of ITO thin films as a function of r.f power are shown in Fig. 7.19, all ITO samples have the grain size smaller than 100 nm.

The optical transmittance of the films was measured with a single beam spectrophotometer; scanned in the UV-Visible region (300~1000 nm). The optical transmission spectra of ITO thin films with various r.f. power show that the films are highly transparent in visible region, as shown in Fig. 7.20 The average transmission was found over than 90%.

The optical bandgap of the films were determined by extrapolating the linear portion of the hv versus $(\alpha h\nu)^2$ curve to $(\alpha h\nu) = 0)$ (inset of Fig. 7.21). The absorption coefficient ($\alpha$) was determined from the relation, $I=I_0 \exp(-\alpha t)$ where t is the thickness of the sample, I the transmitted intensity at a particular wavelength and $I_0$ the maximum transmitted intensity which is taken to be 100%. This relation give $\alpha = (1/t) \ln(I_0/I)$ [31].

The bandgap of ITO films increase with increasing r.f. power, as shown in Fig. 7.21. The increase in bandgap may due to an increase in carrier concentration with increasing RF power as a result of which the absorption edge shift toward the near UV range [32]. The increasing bandgap with carrier concentration can explain on the basis of Burstein-Moss effect. Assuming that the conduction band and valence band are parabolic in nature and that Burstein-Moss shift is the predominant effect, we can write $E_g = E_{g0} + \Delta E_g^{B-M}$ where $E_{g0}$ is the intrinsic bandgap and $\Delta E_g^{B-M}$ the Burstein-Moss shift due to the filling of low lying levels in the conduction band [33]. An expression for Burstein-Moss shift is given by $\Delta E_g^{B-M} = (h^2/8\pi^2 m^*_{vc})(3\pi^2 n)^{2/3}$ where n is the carrier concentration and $m^*_{vc}$ the reduced effective mass of the carriers. From this expression it is clear that Burstein- Moss shift is directly proportional to $n^{2/3}$. However, at very high carrier concentrations it is seen that there is bandgap narrowing due to electron-electron scattering and electron-impurity scattering [31].

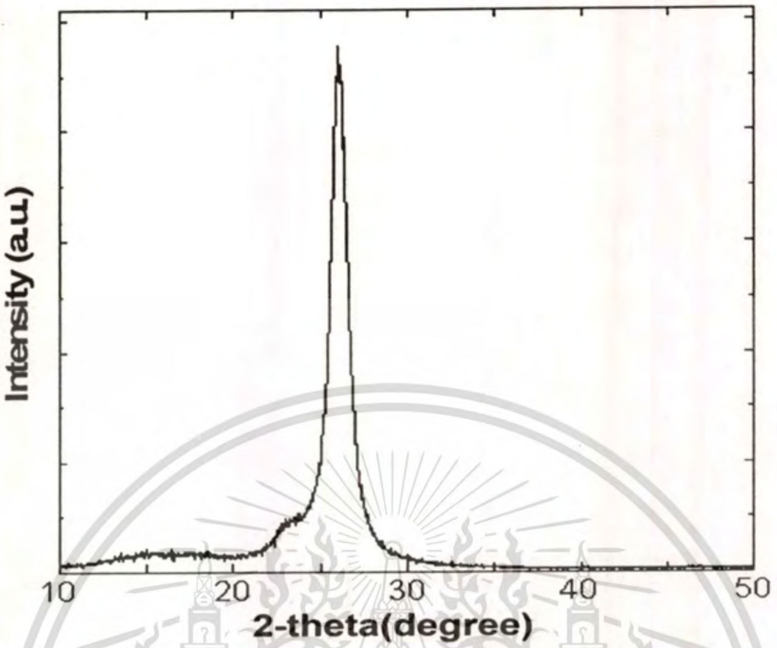

(a) PET substrate

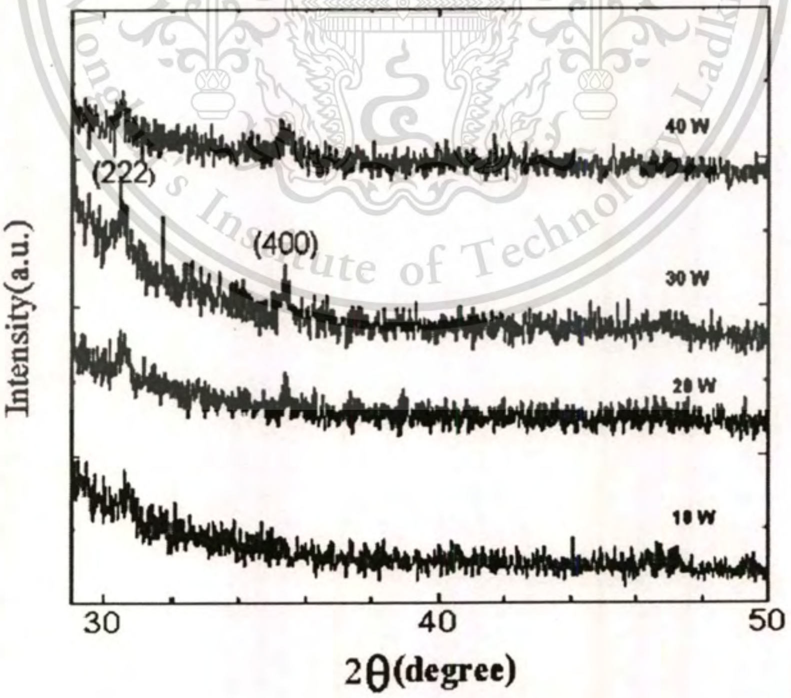

(b) 200 nm thick of ITO on PET substrate

**Fig. 7.18** XRD patterns of (a)PET substrate and (b) ITO on PET.

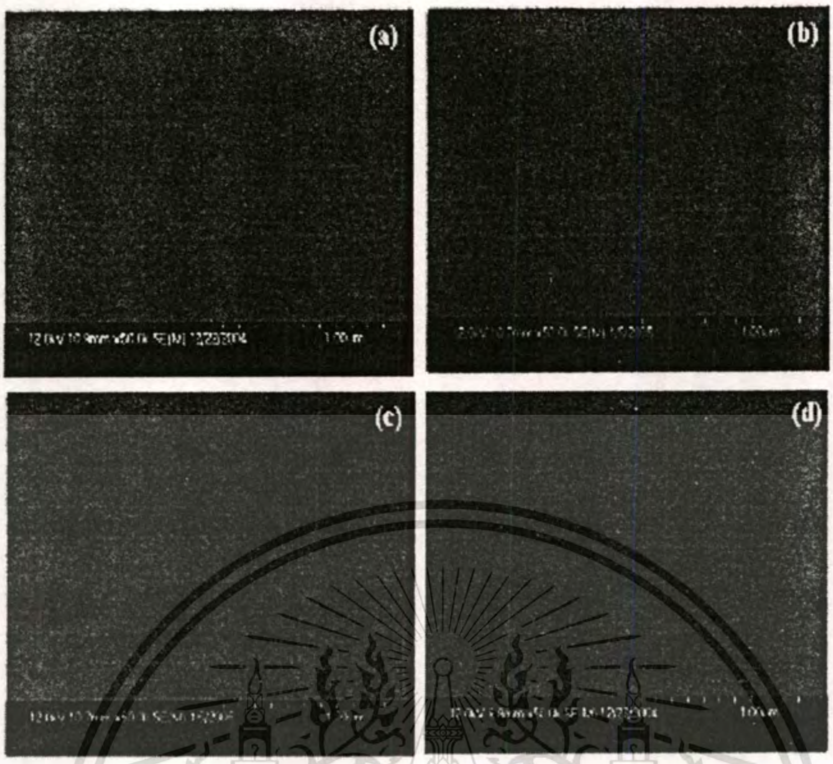

**Fig. 7.19** SEM micrographs of the ITO thin films on PET substrate deposited with the gas-timing technique as a function of RF power; (a) 10 W, (b) 20 W, (c) 30 W and (d) 40 W.

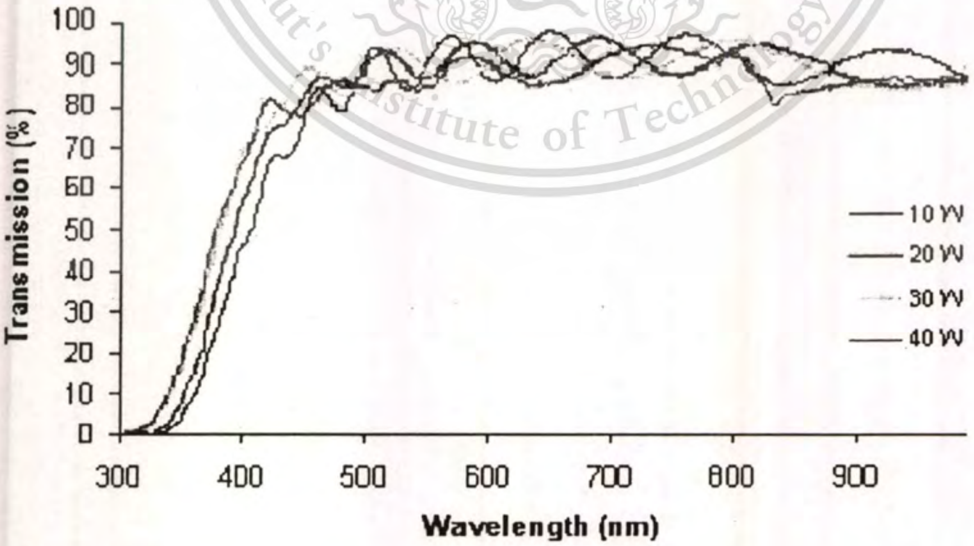

**Fig. 7.20** Transmission spectra of the ITO thin films deposited by gas-timing technique with different r.f power.

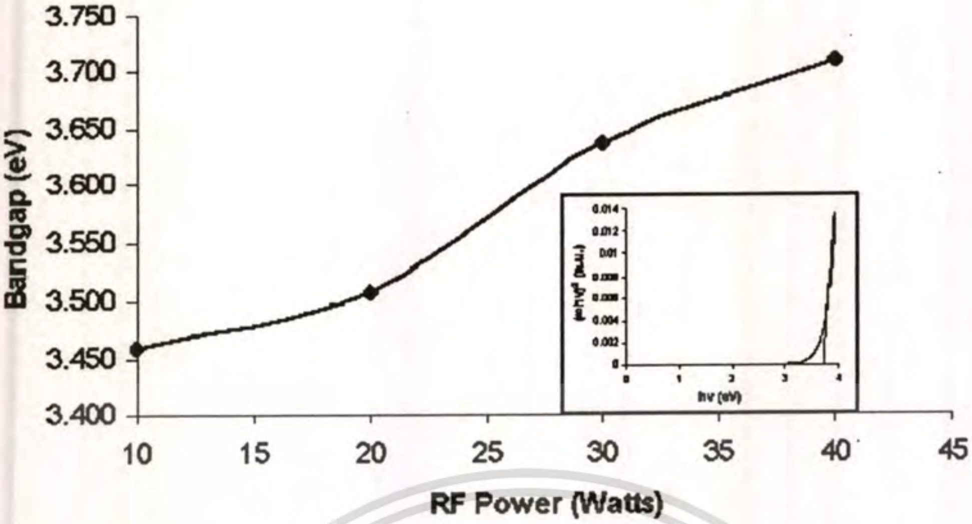

**Fig. 7.21** Variation of bandgap of the ITO thin films on PET substrate deposited with the gas-timing technique as a function of r.f. power. Inset shows a typical plot of hν vs. $(\alpha h\nu)^2$ for the ITO film deposited with the gas-timing technique.

The increase in carrier concentration may be due to an increase in the diffusion of Sn atoms from interstitial locations and grain boundaries into the In cation sites. Since the Sn atom has a valency of 4 and In is trivalent, the Sn atoms act as donors in ITO films [31]. Hence the increase in Sn diffusion with r.f power results in higher electron concentration. In the addition, The gas-timing technique will be increased oxygen vacancy due to decreasing oxygen atoms that distributed from the center of target then it was pumped down when Ar gas turned off. The oxygen vacancy can donate two free electrons for conduction [31]. Hence the increase of oxygen vacancy with gas-timing technique result in higher electron concentration.

The electrical properties of the ITO thin film depend on the film composition and deposition parameters such as r.f power, sputtering pressure, etc [34]. In this study, we found that the sheet resistance decrease with increasing in r.f power. The minimum of sheet resistance was about 8 Ω/☐ at r.f power of 40 W shown in Fig.7.22. This result was supported by the increase of carrier concentration when increased RF power that yields to reduction of sheet resistance [34].

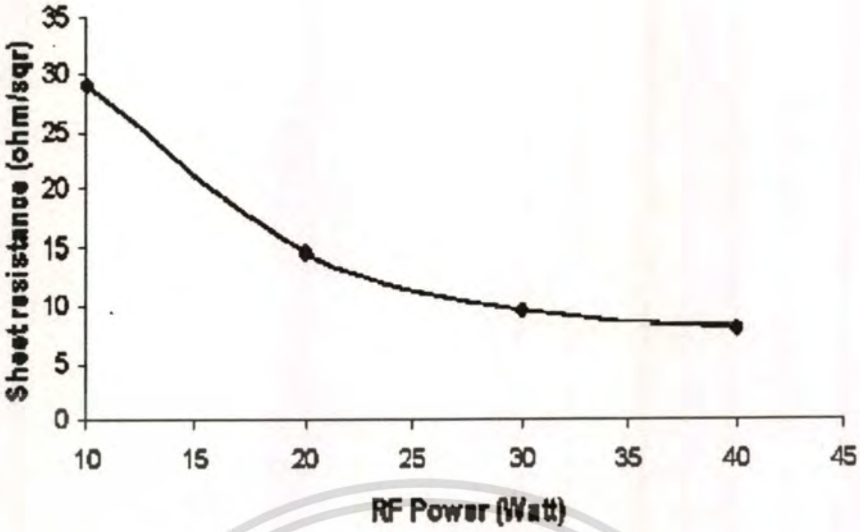

**Fig. 7.22** Variation of sheet resistance of the ITO thin films on PET substrate deposited with the gas-timing technique as a function of r.f power.

By our innovative gas-timing technique used for sputtering without substrate heating and post annealing, the ITO thin films on plastic substrates were achieved with lower resistivity and high transmittance in visible region that suitable for use as transparent electrode.

### 7.2.5 InON Thin Films Growth with Reactive Gas-Timing

#### 7.2.5.1 Effect of $N_2$ and $O_2$ Flow Rates

In this experiment, film samples were grown on substrates without any heating. The 99.999% purity of In was used as the target in the sputtering process. The distance between indium target and substrate was fixed at 5 cm. The two mass flow controllers are used to control the flow rate of ultra high purity (99.999%) of nitrogen and oxygen to the sputtering chamber. The mixed nitrogen-oxygen was fed into the chamber as reactive gas sputtering. The substrate cleaning was done by cleaning process discussed in 7.1. After that, the substrate was set on the substrate holder in the chamber, and then the chamber was evacuated until ~$10^{-7}$ mbar.

The sputtering process began with feeding of nitrogen at flow rate of 10 sccm and then varying the flow rate of oxygen at 0, 0.5, 1, 1.5 and 10 sccm, respectively. The r.f. generator (13.56 MHz) was generated the radio frequency of 100 watt power. The radio frequency excited the nitrogen-oxygen mixed gas, to produce the plasma state. A schematic of gas-timing sequence in sputtering process shows in Fig. 7.23. The thickness of films was 1000 nm which verified by quartz balance thickness monitor. The structural and optical properties of all films were characterized by XRD spectrometer, FE-SEM and UV-VIS spectrophotometer, respectively.

The XRD patterns of all samples exhibited in Fig. 7.24, the films grown with $N_2$:$O_2$ of 0:10, 0.5:10, 1.0:10, 1.5:10 and 10:0 sccm demonstrated difference crystal orientations. The XRD peak ($2\theta = 31.4°$) of film grown in pure $N_2$ plasma determines the crystal orientation along (111) plane as cubicl-InN polycrystalline structures, while the peak ($2\theta = 34.97°$ and $50.71°$) of film grown in pure $O_2$ plasma determines the crystal orientation along (400) and (440) planes, respectively as cubic body-center polycrystalline structure.

The crystal orientations of films grown in $N_2$+$O_2$ plasma exhibit the crystal phase change nearby to InN when $O_2$ flow rate is decreased and to $In_2O_3$ when $O_2$ flow rate is increased. The films between InN and InO are called InON films.

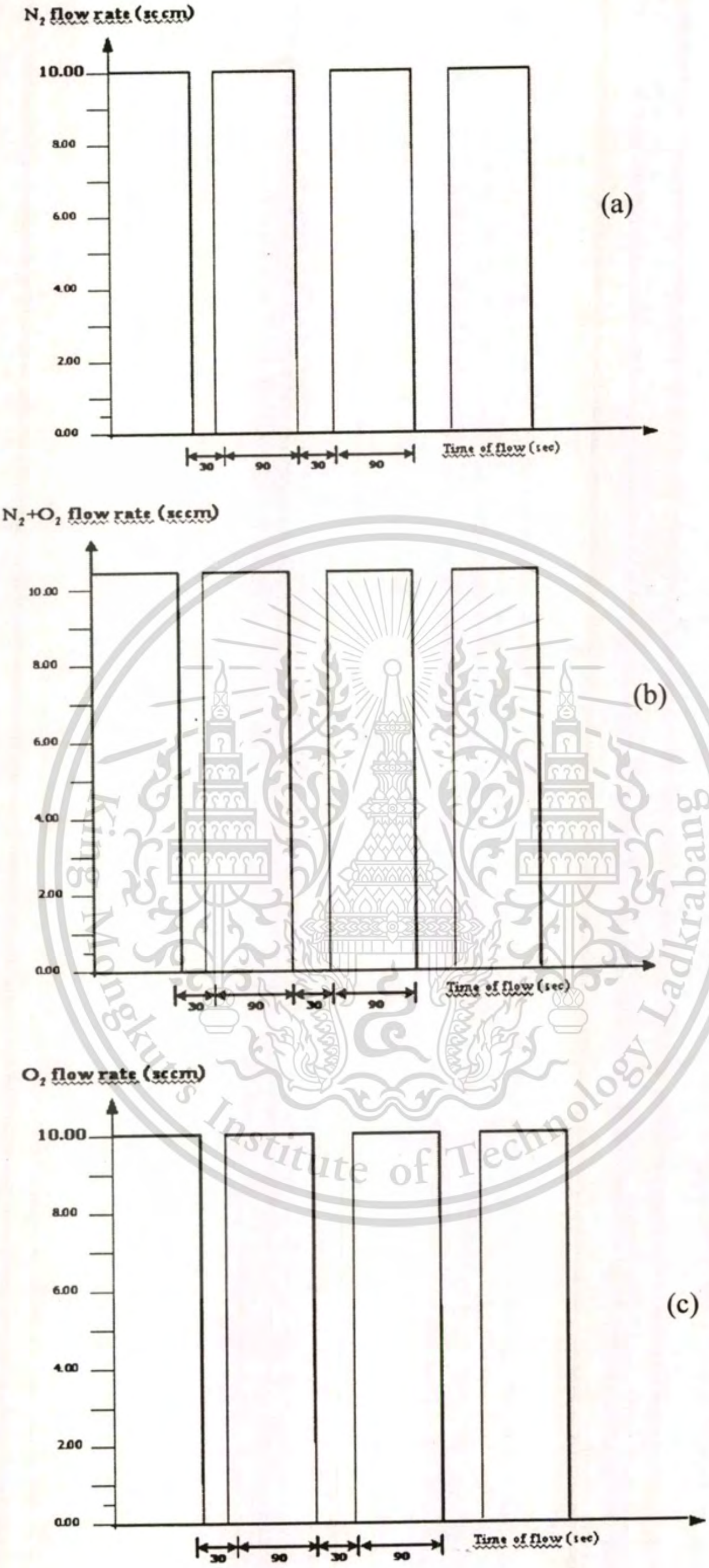

**Fig. 7.23** Diagram of gas-timing sequence of (a) $N_2$ , (b) $N_2$+$O_2$, and (c) $O_2$, flow gases feed for 90 sec and stops for 30 sec.

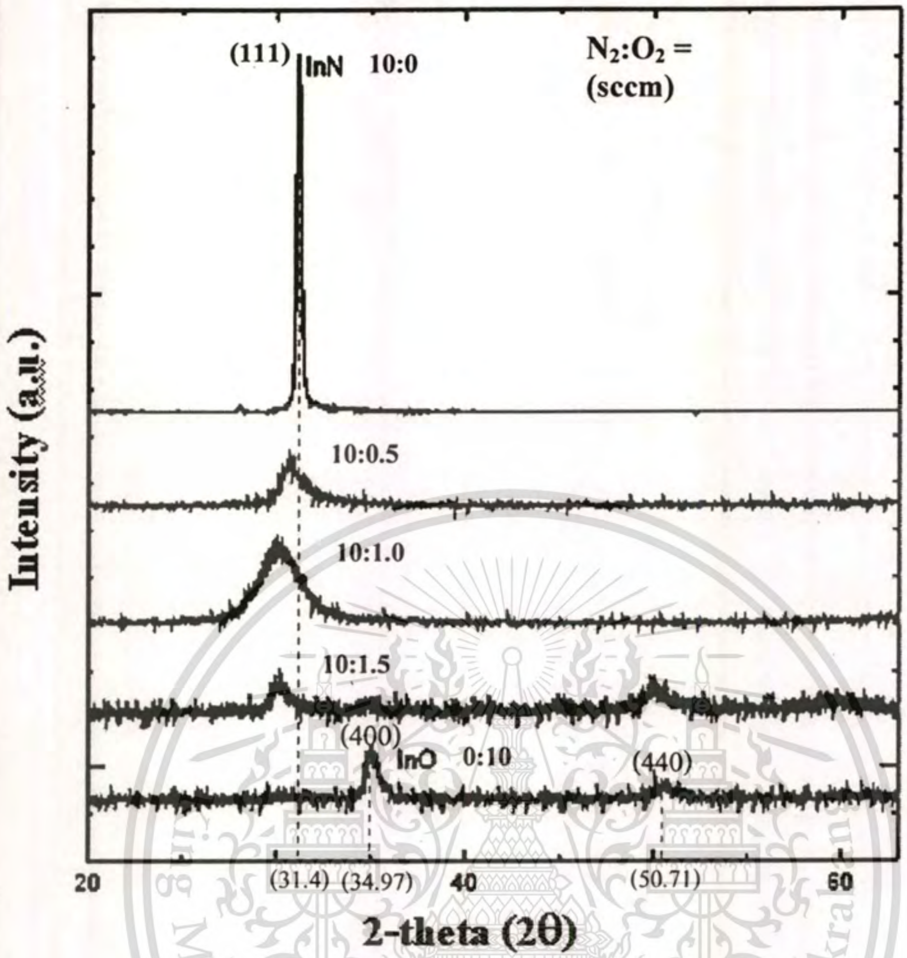

**Fig. 7.24** The XRD patterns of InON films, which deposited on substrates using the reactive mixed-gas of nitrogen and oxygen in difference flow rates.

The surface morphologies investigated from FE-SEM, as shown in fig. 7.25 represent that InN, InON and $In_2O_3$ films grown with gas-timing technique have crystal sizes in nanometer scale. The transmission spectra of all films exhibit in fig. 7.26. The optical properties of InON are depended on the $N_2$:$O_2$ flow rates, significantly. The InON films can be performed in ultraviolet to near infrared regions by the proper sputtering conditions.

The optical bandgap energy in a serie of InON films determined by PUMA method [35] is shown in Fig. 7.27. The film grown in pure $N_2$ plasma has optical bandgap energy of around 1.4 eV that corresponds to cubic-InN bandgap energy of around 1.3 eV obtained from photocurrent spectroscopy, as shown in Fig. 7.13.

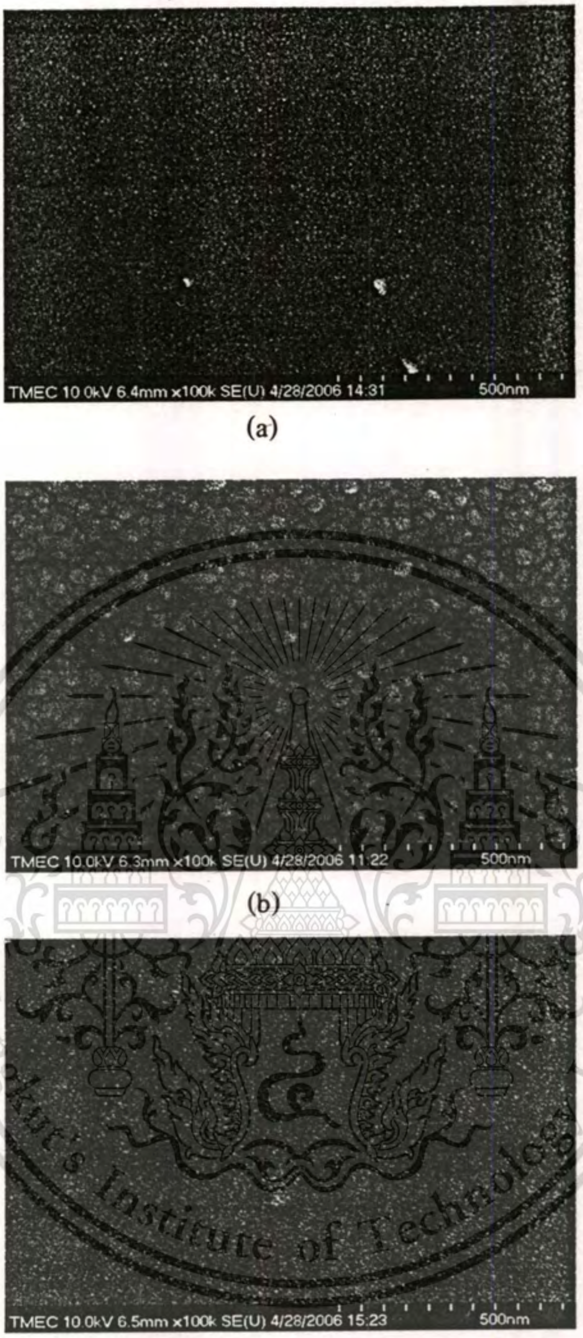

(a)

(b)

(c)

**Fig. 7.25** The FE-SEM images of InN, InON and $In_2O_3$ films, which deposited on substrates using nitrogen and oxygen flow rate control in difference conditions. The magnification is 100K times for all images.

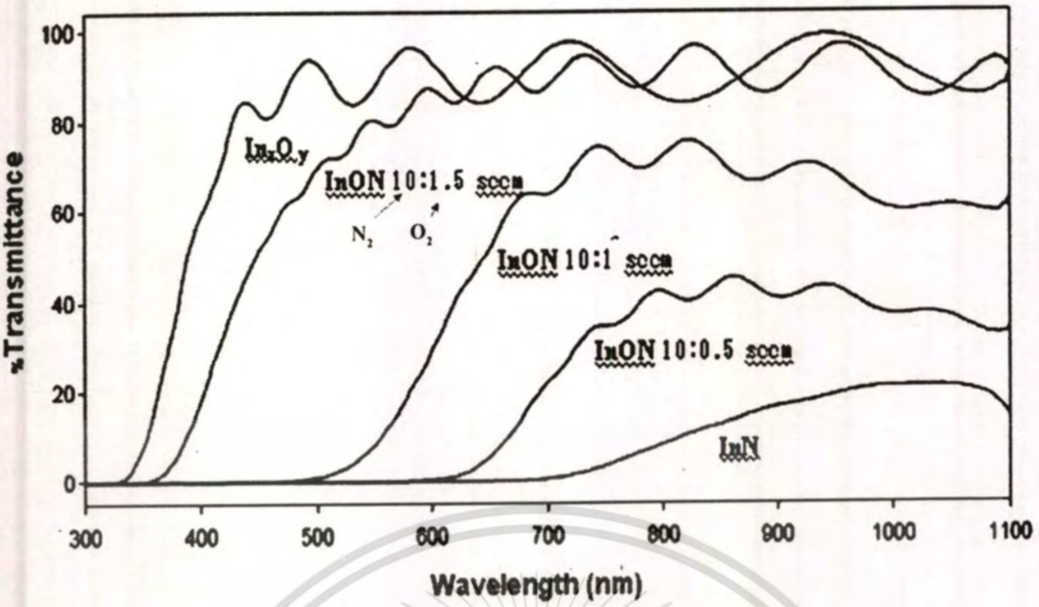

**Fig. 7.26** Transmittance spectra of InON films series deposited by gas-timing technique with different $N_2$+ $O_2$ gas flow rate.

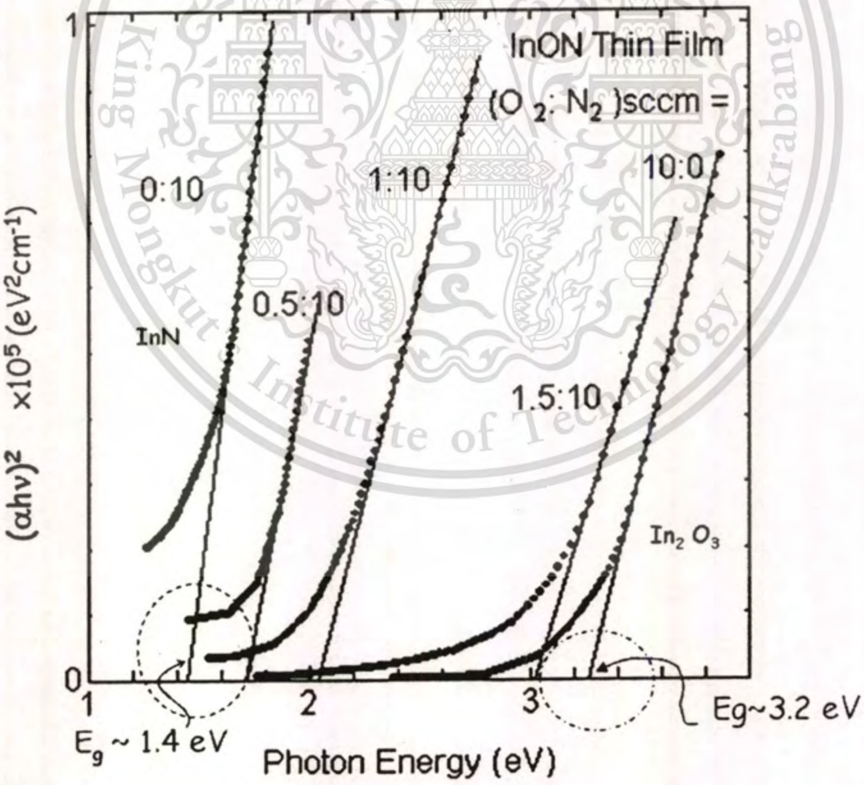

**Fig. 7.27** Variation of bandgap energy of InON films on the substrates deposited with different $N_2$+$O_2$ gas flow rate.

There have a few reports for the growth of indium oxynitride thin films. T. S. Ko *et. al.*, (2006) [36], has synthesized nanoparticles indium oxynitride on a silicon substrate in nitrogen atmosphere using the method involving thermal evaporation of pure indium in a two-zone reactor. These nanoparticles grown at 900 °C could emit a strong PL spectrum centered around 700 nm with a broad full width at half maximum of about 250 nm, spanning the whole red segment. Torbjo¨ rn Lindgrena *et al.*, (2006) [37] reported InN to $In_2O_3$ that was obtained due to dioxygen impurity in annealing gas, temperature range 350-500 °C, absorption at 900 nm (1.4 eV).

InON thin films, however, obtained from our laboratory have different optical properties from the other such as wide transmittance and wide range of energy bandgap (1.4-3.2 eV) that we can achieved by varying the gas-timing of $N_2$:$O_2$.

## 7.3 Chapter Summary

The experiments in this chapter deal with the growth and characterizations of In, InN, ITO, and InON films, which explained in the details on above.

The In film shows XRD peaks are 32.9°, 36.3°, and 39.1° in orientation of (101), (002), and (110) planes, respectively as tetragonal polycrystalline structure. With reactive gas-timing technique, the hexagonal-InN, and cubic-InN thin films were successfully obtained by varying timing sequence of gas flow. The reflection peaks were indexed (101), (102), and (110), in accordance to, the wurtzite-InN polycrystalline structure. InN thin film, however, grown in pure $N_2$ plasma shows one strong XRD peak in orientation along (111) plane corresponding to InN cubic structure. The energy bandgap of around 1.18 eV of hex-InN and 1.4 eV of cubic-InN were investigated by PR and UV-VIS measurements, respectively. From PC measurement of cubic-InN device, the spectrum peaks determined bandgap energy of hex-InN and cubic-InN around 1.2 eV and 1.3 eV, respectively.

All deposited ITO thin films with various r.f. power on PET show XRD peaks at $2\theta$ = 30.273° and 35.165° which correspond to (222) and (400) planes as polycrystalline cubic bixbyite structure. The sheet resistance of ITO thin films is reduced from 30 to 8 $\Omega/\square$ as the r.f. power of sputtering increases from 10 W to 40 W. The ITO thin films on PET substrates have the transmittance of about 90% in visible region. The optical bandgap of ITO films obtained from UV-VIS measurement is about 3.6 eV.

For the experiments of deposited InON films series, the XRD peak at $2\theta = 31.4°$ of film grown in pure $N_2$ plasma determines the crystal orientation along (111) plane as cubicl-InN polycrystalline structures. While the peak at $2\theta = 34.97°$ and $50.71°$ of film grown in pure $O_2$ plasma determines the crystal orientation along (400) and (440) planes, respectively as cubic body-center polycrystalline structure. The crystal orientations of films grown in $N_2$+$O_2$ plasma exhibit the crystal phase change nearby to InN when $O_2$ flow rate is decreased and to $In_2O_3$ when $O_2$ flow rate is increased. The optical bandgap of InON films series determined from UV-VIS measurement is about 1.4-3.2 eV depended on growth conditions. The morphology investigated by FE-SEM identified that all nitride-based films are nanocrystalline.

The gas-timing technique used in the sputtering process is very powerful for achieving nitrides films at substrate room temperature on various substrates without any catalyst or post annealing.

## References

[1] F. Fischer and F. Schröter, Ber. Dtsch. Keram Ges. **43**, 1465 (1910).

[2] J. B. MacChesney, P. M. Bridenbaugh and P. B. O'Connor, Mater. Res. Bull. **5**, 783 (1970).

[3] K. Osamura, S. Nara and Y. Murakami, J. Appl. Phys. **46**, 3432 (1975).

[4] H. J. Hovel and J. J. Cuomo, Appl. Phys. Lett. **20**, 71 (1972).

[5] K. L. Westra, R. P. W. Lawson and M. J. Brett, J. Vac. Sci. Technol. A **6**, 1730 (1988).

[6] K. Osamura, K. Nakajima and Y. Murakami, Solid State Commun. **11**, 617 (1972).

[7] J. W. Trainor and K. Rose, J. Electron. Mater. **3**, 821 (1974).

[8] N. Puychevrier and M. Menoret, Thin Solid Films **36**, 141 (1976).

[9] V. A. Tyagai, A. M. Evstigneev, A. N. Krasiko, A. F. Andreeva and V. Y. Malakhov, Sov. Phys. Semicond. **11**, 1257 (1977).

[10] B. R. Natarajan, A. H. Eltoukhy and J. E. Greene, Thin Solid Films **69**, 201 (1980).

[11] H. Takeda and T. Hada, Toyama Kogyou Koto Semmon Gakko Kiyo **11**, 73 [in Japanese] (1977).

[12] T. L. Tansley and C. P. Foley, J. Appl. Phys. **59**, 3241 (1986).

[13] T. Matsuoka, H. Tanaka and A. Katsui, in Inst. Phys. Conf. Ser. **106**, Int. Symp. on GaAs and Related Compounds, Karuizawa, Japan 1989, (1990), p. 141.

[14] A. Yamamoto, T. Shinya, T. Sugiura and A. Hashimoto, J. Cryst. Growth 189, 461 (1998).

[15] S. Yamaguchi, M. Kariya, S. Nitta, T. Takeuchi, C. Wetzel, H. Amano and I. Akasaki, J. Appl. Phys. **85**, 7682(1999).

[16] A. Yamamoto, T. Tanaka, K. Koide and A. Hashimoto, Phys. Status Solidi B **194**, 510 (2002).

[17] W. E. Hoke, P. J. Lemonias and D. G. Weir, J. Cryst. Growth **111**, 1024 (1991).

[18] M. Higashiwaki and T. Matsui, Jpn. J. Appl. Phys. **41**, L540 (2002).

[19] H. Lu, W. J. Schaff, J. Hwang, H. Wu, G. Koley and L. F. Eastman: Appl. Phys. Lett. **79**, 1489 (2001).

[20] Y. Saito, N. Teraguchi, A. Suzuki, T. Araki and Y. Nanishi, Jpn. J. Appl. Phys. **40**, L91(2001).

[21] T. Inushima, V. V. Mamutin, V. A. Vekshin, S. V. Ivanov, T. Sakon and S. Motokawa, J. Cryst. Growth **227**, 481 (2001).

[22] V. Y. Davydov, A. A. Klochikhin, R. P. Seisyan, V. V. Emtsev, S. V. Ivanov, F. Bechstedt, J. Furthmuller, H. Harima, A. V. Mudryi, J. Adrhold, O. Semchinova and J. Graul, Phys. Status Solidi B **229**, R1 (2002).

[23] T. Matsuoka, H. Okamoto, M. Nakao, H. Harima and E. Kurimoto, Appl. Phys. Lett. **81**, 1246 (2002).

[24] J. Wu, W. Walukiewicz, K. M. Yu, J. W. Arger, III, E. EHaller, H. Lu, W. J. Schaff, Y. Saito and Y. Nanishi, Appl. Phys. Lett. **80**, 3967 (2002).

[25] Y. Saito, H. Harima, E. Kurimoto, T. Yamaguchi, N. Teraguchi, A. Suzuki, T. Araki and Y. Nanishi, Phys. Status Solidi B **234**, 796 (2002).

[26] M. Higuchi, S. Uekusa, R. Nakano and K. Yokogawa, **"Post-Deposition Annealing Influence on Sputtered Indium Tin Oxide Film Characteristics"**, Japanese Journal of Applied Physics, **33**, pp. 302 – 306, 1994.

[27] J. Bregman, Y. Shapira and H. Aharoni, **"Effects of Oxygen Partial Pressure During Deposition on the Properties of Ion-Beam-Sputtered Indium-Tin Oxide Thin Films"**, Journal of Applied Physics, **67**(8), 1990, pp. 3750 – 3753.

[28] M. Buchanan, J. B. Webb and D. F. Williams, **"The Influence of Target Oxidation and Growth Related Effects on the Electrical Properties of Reactively Sputtered Films of Tin-Doped Indium Oxide"**, Thin Solid Films, **80**, 1981, pp. 373 – 382.

[29] J. C. C. Fan, F. J. Bachner and G. H. Foley, **"Effect of Oxygen Partial Pressure During Deposition on Properties of RF Sputtered Sn-Doped $In_2O_3$ Films"**, Applied Physics Letters, **31**(11), 1977, pp. 773 – 775.

[30] K. Sreenivas, T. Sundarsena Rao, A. Mansnigh and S. Chandra, **"Preparation and Characterization of RF Sputtered Indium Tin Oxide Films"**, Journal of Applied Physics, **57**(2), 1985, pp. 384 – 392.

[31] M. Nisha, S. Anusha, Aldrin Antony, R. Manoj, M.K. Jayaraj, Applied Surface Science, 2005.

[32] C.G. Granqvist, A. Hultaker, Thin Solid Films **411**, 1, 2002.

[33] B.E. Sernelius, K.F. Berggren, Z.C. Jin, I. Hamberg, C.G. Granqvist, Phys. Rev. B **37**, 10244, 1988.

[34] H. Kim, J.S. Horwitz, Appl. Phys. Lett. **78**, 1050, 2001.

[35] I. hambouleyron, S. Ventura, E. G. Birgin and J. M. Mart´ınez, **"Optimization Techniques for The Estimation of The Thickness and The Optical Parameters of Thin Films Using Reflectance Data"**, J. Appl. Phys. 92, pp. 3093-3102 (2002).

# CHAPTER 8

# APPLICATIONS OF AlN, InN AND RELATED THIN FILMS

## 8.1 The Application of AlN Thin Films as pH Sensitive Device

According to several literatures mentioned, AlN thin films have several advantages and applications. Based on the results, especially their chemical and thermal properties take on excellent stability, a wide energy gap and superior insulating property. The ISFET sensors from semiconducting technology have the desired feature of low cost, good sensitivity, and convenient from of response. These features have made, and undoubtedly will continue to make, these sensor popular. However, the sensors have problems in reproducibility, stability, drift, hysteresis and temperature dependence. Every improvement in these aspects will undoubtedly increase the usage of the devices. Recently, AlN thin film has received considerable attention as a gate insulator for the pH sensing ISFET device. Many pH-sensitive materials such as $Si_3N_4$, $Ta_2O_5$, a-$WO_3$, and $SnO_2$ have been investigated [1-5]. The ion-sensitive field-effect transistor (ISFET), metal-insulator-semiconductor (MIS), and electrolyte-insulator-semiconductor (EIS) structures of $PbTiO_3$ have been reported [6]. Normally, AlN thin films have a wurtzite structure and growth direction is <0001>. The cubic-AlN thin film is difficult to obtain because of high substrate temperature.

The Ion Sensitive Field Effect Transistor (ISFET) is a chemical sensitive device based on structure of Metal-Oxide-Semiconductor (MOSFET). The ISFET was first demonstrated by Bergveld [7, 8] in 1970. The sensitivity to ions is derived by eliminating the metal gate contact of the MOSFET and exposing the gate insulator to an electrolyte solution. The contact to the electrolyte gate is provided by a reference electrode, and its inclusion was first reported by Matsuo and Wise in 1974. The ISFET sensing principle is based on the charge adsorption at the ion-solid interface between the sensing layer which contains hydroxyl groups and the electrolyte, from which hydroxyls may accept or donate protons. In this process a double-layer capacitance is created with a potential drop, which influences the threshold voltage of the transistor depending on the value of H+ protons concentration (pH). The structure of the ISFET is presented by a cross-section in Fig. 8.1.

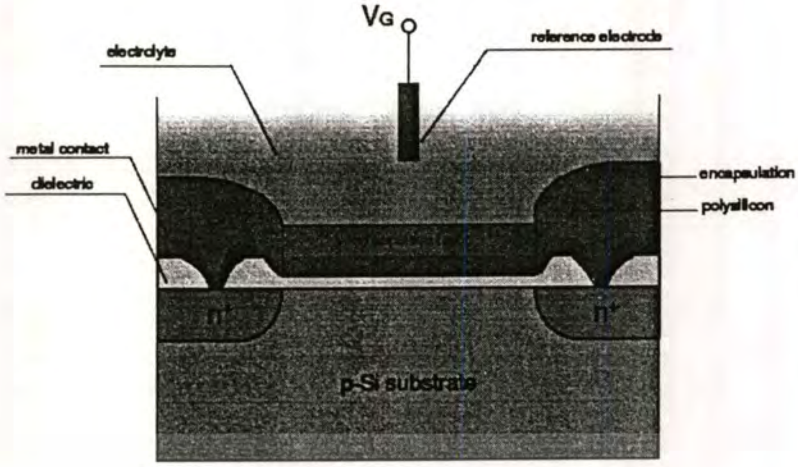

**Fig. 8.1** The cross-section of The ISFET structure.

The pH sensitivity that is observed during the exposure to the electrolyte makes ISEFT a highly useful tool for obtaining measurements in various fields of applications: agricultural, environmental, food, etc. Most important applications are in biomedical engineering, for which the ISFET was initially developed. Some of the examples are in neurosurgery: brain monitoring via CSF, pH measurements in blood; biotelemetry, etc. The ISFET, on the other hand, can become a much more useful detector; sensors are produced commercially, in general, alumina ($Al_2O_3$) or silicon nitride ($Si_3N_4$) as the insulator. Their application in biosensing has been shown great promise.

This thesis will focus on the study of AlN as a novel pH sensitive material advantaged for ISFET devices, and the AlN thin films were prepared by rf magnetron sputtering with reactive gas-timing technique to detect pH response and extract related surface potential. The cubic-AlN thin films were achieved and used as pH sensitive membrane. The AlN/$SiO_2$/Si EIS structure was fabricated for experimental study of pH sensitive device.

**Preparation of AlN thin film:**

The AlN thin film was chosen as the pH-sensing membrane which was deposited on substrates maintained at room temperature by rf magnetron sputtering using reactive gas-timing technique. The 500 nm thickness of AlN thin film was grown on the two types of substrates; glass and Si for thin film and device characterizations, respectively. In addition, the r.f. power was set at 200 W and operated at 13.56 MHz. The thickness of AlN thin films has been prepared at 100, 200, 300, 400 and 500 nm, respectively. The crystalline structures were investigated by X-ray diffraction (XRD). The FE-SEM was used to observe the surface morphology of AlN films in nano-scale. The thickness of the thin films was obtained by surface profilometer.

**Preparation of EIS structure:**

The 500 nm thick of cubic-AlN thin film was grown by reactive gas-timing rf magnetron sputtering on $SiO_2$/p-Si substrate at room temperature. The 200 nm thick of Au was deposited as Ohmic contact, as shown in Fig. 8.2(a). The AlN thin films were deposited on the EIS structure (AlN/$SiO_2$/p-Si/Au).

The EIS structure was made on p-type Si wafer. The thickness of the $SiO_2$ is about 100 nm. The 500 nm thick of cubic-AlN thin films were prepared by rf magnetron sputtering with reactive gas-timing technique presented above. In addition, the Au electrodes were prepared by electron beam evaporator system on the back of the EIS samples. The Au/Pd wire was used as reference electrode. Afterwards, the EIS samples were packaged with epoxy resins, which are commonly used in sensor technology because of their low permeability. Fig. 8.2(b) shows the AlN/$SiO_2$/Si EIS structure, in which the sensitive region is exposed to standard buffer solutions with difference pH values (pH=4,7,10) at room temperature. The current-voltage (I-V) characteristics of AlN/$SiO_2$/Si device and AlN/$SiO_2$/Si EIS were measured.

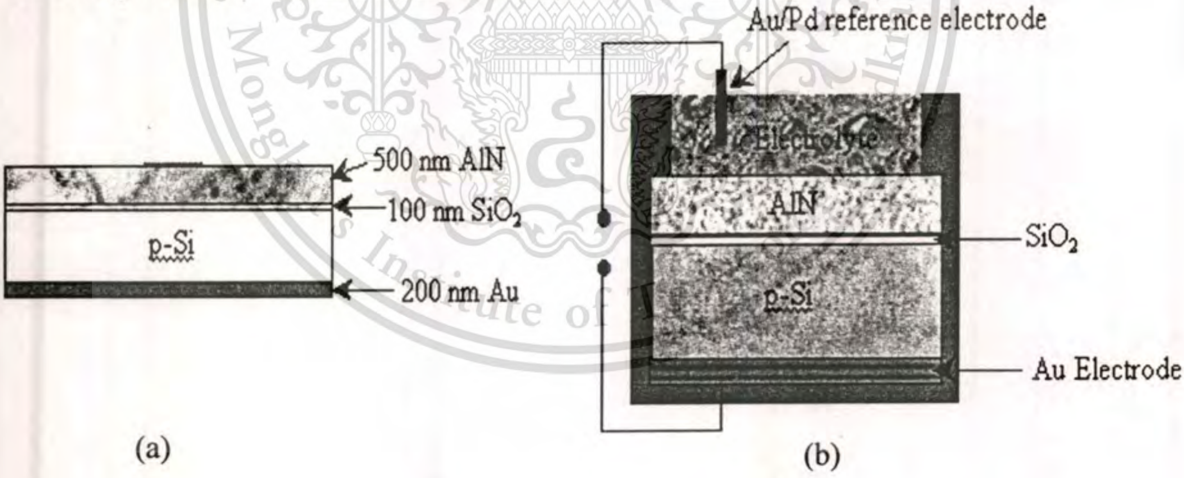

(a) (b)

**Fig. 8.2** The structure diagram of (a) AlN/$SiO_2$/Si (b) AlN/$SiO_2$/Si EIS structure.

**Packaging processes:**

For the measuring convenient and avoid the leakage current to be generated during testing, all samples were packaged with the resin epoxy. A flow chart for packaging processes is shown as Fig. 8.3, and the brief steps of packaging process were described as follows:

(1) Clean samples,

(2) N$_2$ gas to dry and backing in the oven (120$^{\circ}$C, 5~10 min),

(3) Bonding wire with Ag paste,

(4) Baking Ag paste (120$^{\circ}$C, 15 min), for connecting wire and contact,

(5) Packaging with resin epoxy, and backing 15~20 min at 120$^{\circ}$C,

(6) The devices were packaged completely.

After bonding wire and packaging with epoxy, the EIS devices were encapsulated, and the section of packaged device was shown in Fig. 8.4. In which, the sensing area that is the exposed region is close to 1 mm$^2$.

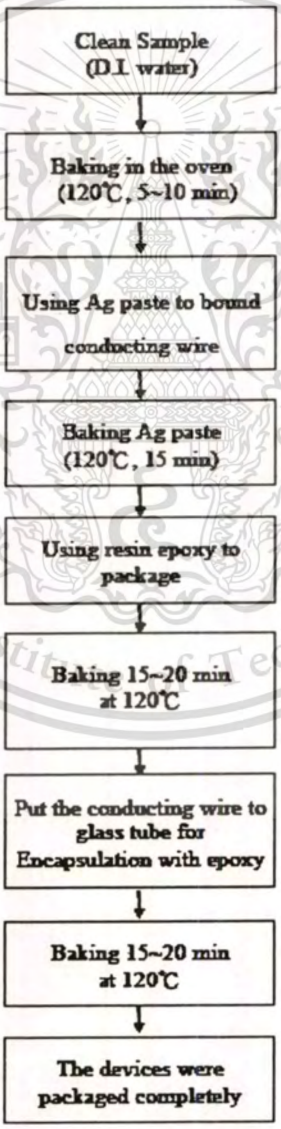

**Fig. 8. 3** A flow chart of packaging processes.

**Current-Voltage (I-V) measurement set-up:**

A Keithley 236 semiconductor parameter analyzer system and a personal computer set up to measure the current-voltage (I-V) characteristics curves. The pH-meter probe and temperature thermocouple probe were used to monitor and ensure that the EIS device electrochemical characteristics were remained at a uniform buffer condition. The I-V measurements, in order to prevent air bubbles from being generated between the sensing membrane and the buffer solution during the testing, the sensor head and the reference electrode were immerse in pH-4,-7, -10 standard buffer solutions for 30 sec before testing. Otherwise, to avoid the light and temperature effects, all of measurements were carried out at room temperature in dark box.

To investigate the pH-sensitivity of AlN/$SiO_2$/Si EIS structure, the I-V characteristics were measured in standard buffer solutions at room temperature, as shown in Fig. 8.4. When the AlN/$SiO_2$/Si EIS device is placed in the difference pH buffer solutions, the surface potential was shifted with pH value due to $H^+$ concentration. The surface potential depends on the pH value [9 10].

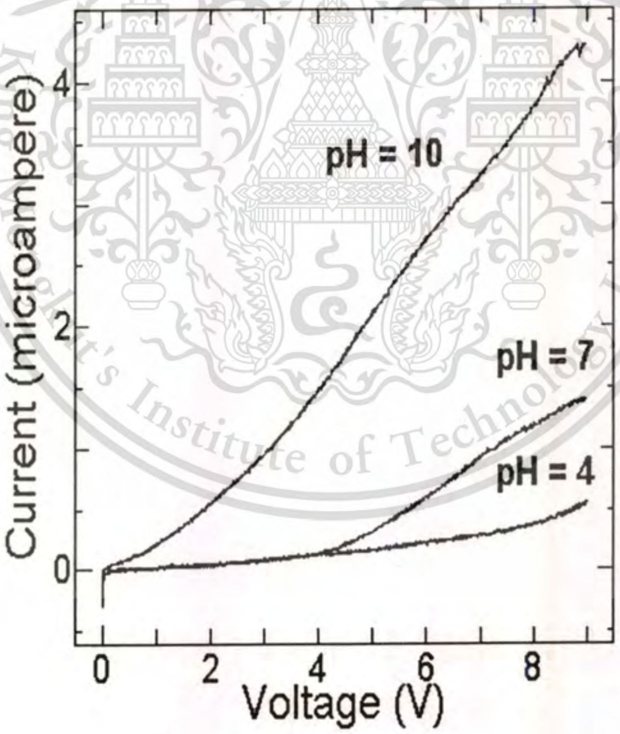

**Fig. 8.4** I-V curves of AlN/$SiO_2$/Si EIS device in difference pH buffer solutions.

According to literature described [11-13], the AlN thin films have been applied not only for surface passivation or insulation layers in integrated circuits, but also in ultraviolet optical devices, acoustooptic devices and surface acoustic wave devices. Because they have some excellent properties such as relatively good thermal conductivity, chemical stability, electrical isolation, a wide band gap, a thermal expansion coefficient similar to that of GaAs, high acoustic velocity and easy to processing.

Because the AlN thin films have been simulated and investigated to analyze pH sensitivity and surface potential which the devices were immersed to a concentration range between pH1~pH11 [14, 15]. Beside, AlN is an attractive material for the optical industry as a dielectric [16, 17] and has a good electrochemical behavior [18]. So we selected AlN as a pH-sensing thin film and try to study its sensing properties. The crystalline structure, morphology and bandgap energy of AlN thin film were investigated by XRD, FE-SEM and PR, respectively described in Chapter 6. The AlN/$SiO_2$/p-Si EIS structure was fabricated for experimental test of pH sensitive device. The photograph of fabricated nanocrystal-AlN EIS device is shown in Fig.8.5.

The AlN thin film was used as pH-sensitive material due to its the mechanical and electronical properties such as hardness and high chemical stability. The cubic-AlN particles are very attractive because of their particularly interesting nanosized structure and their potential in the device applications. In some materials, notably many III-V compound semiconductors, carriers confined to regions smaller than 100 nm begin to show behavior that can be ascribed to the quantized energy levels as a result of such bounding. High temperature superconductors also exhibit a penetration depth typically of about 140 nm so again structures built interesting properties.

**Fig. 8.5** The photograph of nanocrystal-AlN EIS device fabricated in our laboratory.

The effect of semiconductor material sensitive to ion change in electrolyte can imply by Fermi level pinning at surface. J. Nukeaw *et al.* [19] reported the electric fields at surface and linterface of doped GaAs/Semi-insulating GaAs Structures. They observed this effect by Fast Fourier Transformed Photoreflectance. The Fermi surface level pinning of GaAs is shown in Fig. 8.6

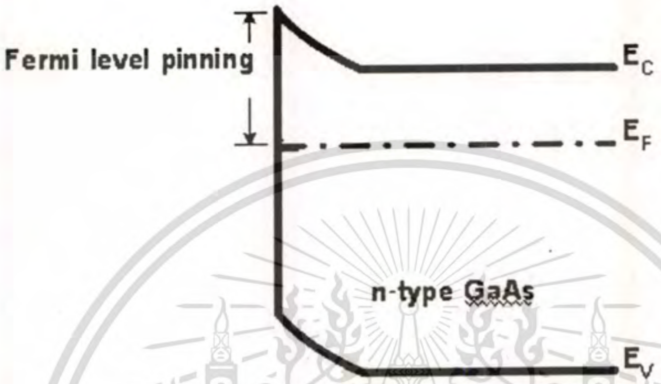

**Fig. 8.6** The Fermi surface level pinning of GaAs.

When the $H^+$ ions in solution have changed (pH-change in electrolyte), the Fermi level at the surface was pinned upper or lower Fermi level of Si depended on $H^+$ ions. The diagram mechanism of Fermi surface level of AlN in electrolyte of pH7, 4 and 10 is shown in Fig. 8.7(a), 8.7(b) and 8.7(c), respectively. The Fermi surface level change of sensitive material affected to the change of voltage of EIS device so the output voltage can calibrate to pH value of solution.

The high quality cubicAlN thin films were successfully grown on substrates at room temperature by reactive gas-timing rf magnetron sputtering. The reactive gas-timing technique played an important role in the formation of nanocrystalline cubic-AlN structure. The properties of nanocrystal cubic-AlN thin film as sensitive material can be effectively investigated using EIS structure for pH sensing. The I-V characteristics show AlN/$SiO_2$/Si EIS structure with good sensitivity suitable for pH sensitive device. In the future, our study on the issues related to the AlN thin films, EIS, MIS and ISFET devices will be fabricated and measured for C-V and I-V characterizations suited for pH sensor applications.

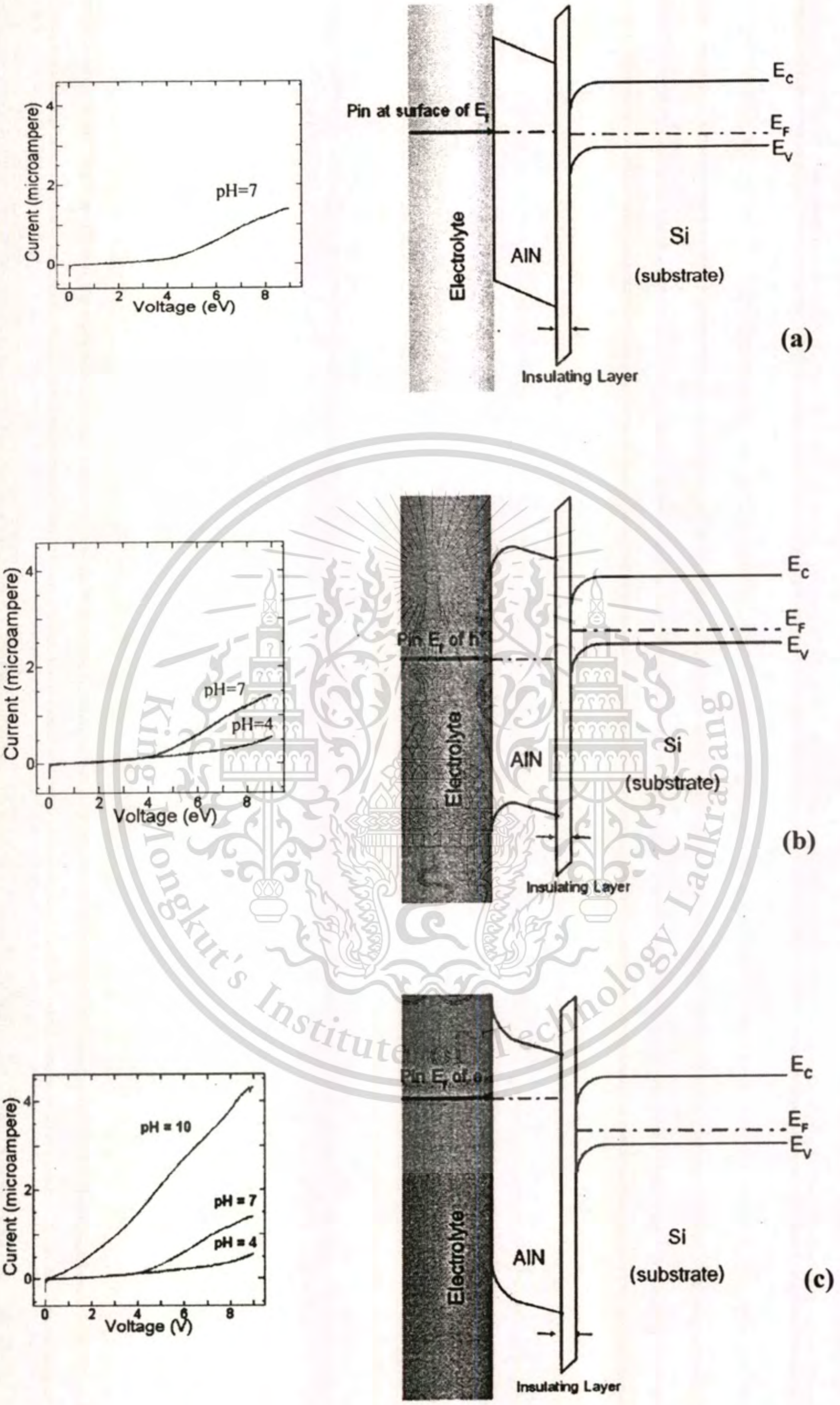

**Fig. 8.7** The diagram mechanism of Fermi surface level of AlN in electrolyte of pH (a) 7, (b) 4 and (c)10, respectively.

## 8.2 Nanocrystal-InN Photodetector

The potential of InN as a photosensitive material was fabricated. The 500 nm thick of InN was deposited on silicon (Si) substrate reactive gas-timing r.f magnetron sputtering. The InN film was selected at the conditions of the flow rate of Ar:$N_2$ = 10:9 sccm and gas-timing of Ar:N=30:150 sec. From XRD characterization, the pattern corresponds to hexagonal-InN polycrystalline structure in the orientation of (101) and (002) planes. The nanocrystal of InN was revealed from FE-SEM. The experimental detail of InN growth and characterization was explained in Chapter 7.

The photodetector structure was made on p-Si wafer. The 200 nm thick of ITO was deposited on InN layer by electron beam evaporator. The 200 nm of Au was deposited on back side of substrate by d.c. sputtering system. The structure of device is shown in Fig. 8.8 The wavelength response of device was measured as shown in Fig. 8.9

**Fig. 8.8** The structure diagram of nanocrystal-InN photodetector.

The bulk p-Si was fabricated as photosensitive material and has the wavelength response peak of about 1100 nm, shown in an inset of Fig. 8.9 which corresponds to the Si bandgap energy of 1.1 eV, while the bandgap energy of nanocrystal-InN film used as photosensitive material of about 1.3 eV as exhibited in Fig. 8.10.The another peak exhibits in curve may due to polycrystalline or phase uniformity. Figure 8.11 shows our nanocrystal-InN phodetector.

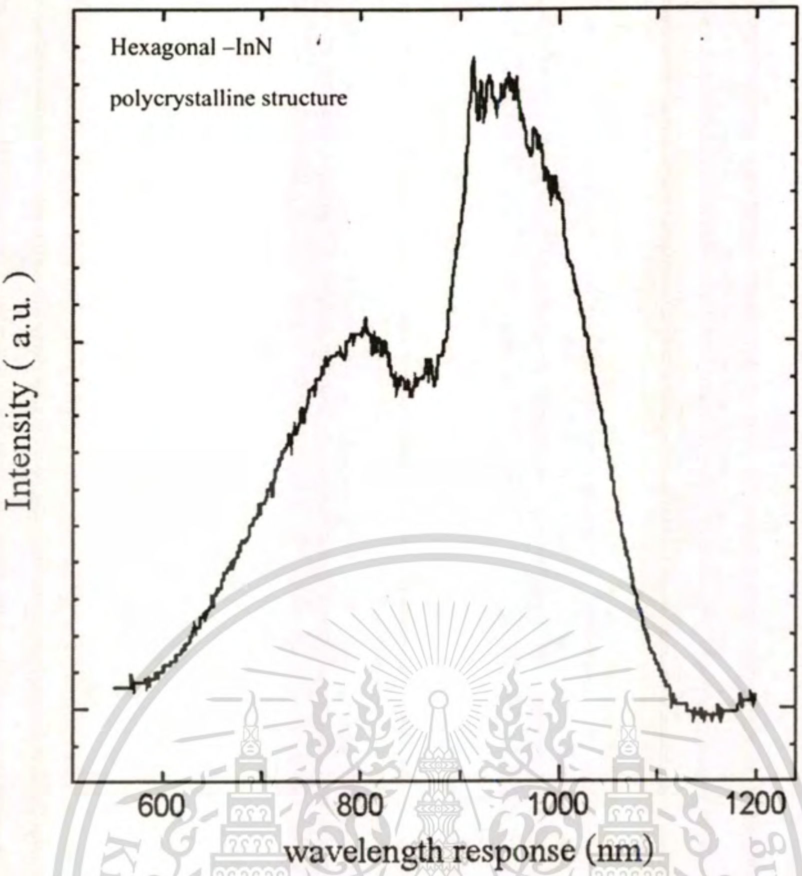

Fig. 8.9 The wavelength response of nanocrystal-InN photodetector.

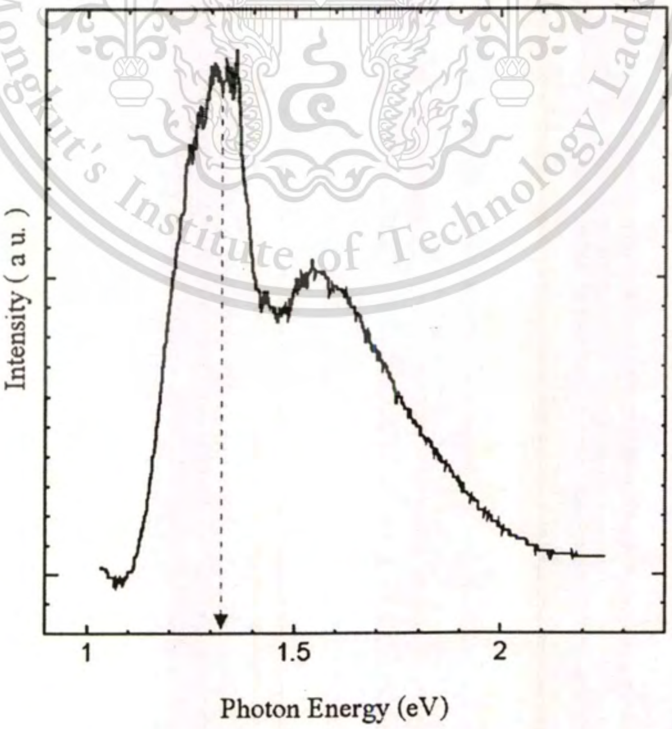

**Fig. 8.10** The bandgap energy of InN hexagonal polycrystalline structure.

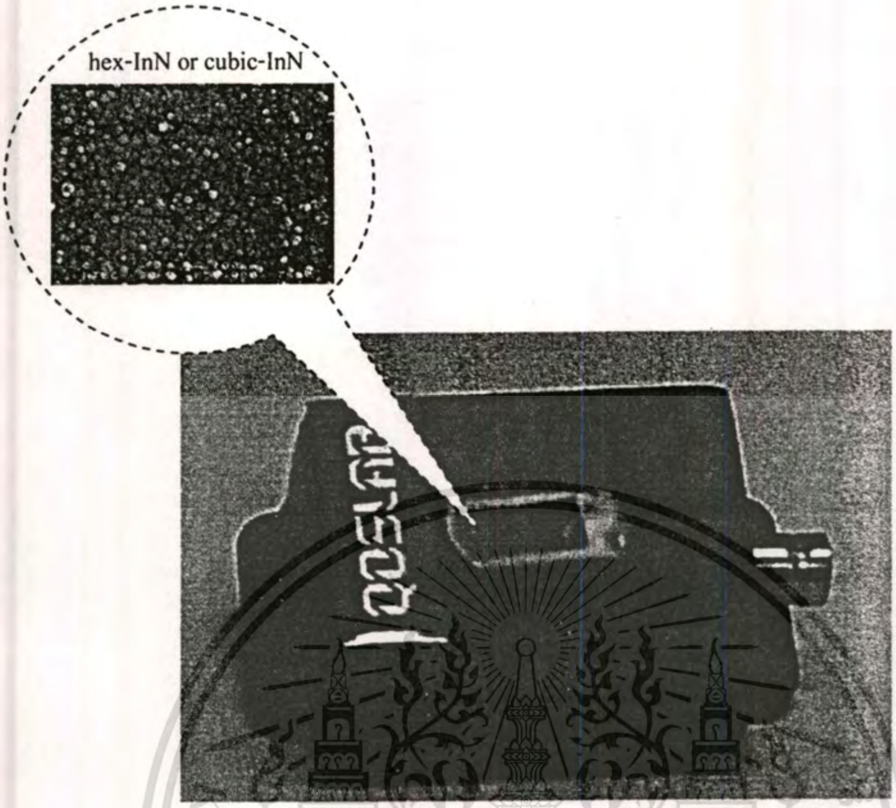

**Fig. 8.11** Photograph of nanocrystal-InN photodetector fabricated in our laboratory.

## 8.3 ITO Thin Film Applications

### 8.3.1 ITO Flexible Transparent Electrode

Due to these properties of ITO, an *n*-type, highly degenerated, wide band gap semiconductor with relatively low resistivity and high transmittance in visible range region. It has been widely used as transparent electrodes in various displays, including liquid-crystal display (LCD), electro luminescent display (ELD), and organic light-emitting diode (OLED).

The PET (polyethylene terephthalate) was used as a substrate for depositing ITO thin film. By our innovative gas-timing technique used for sputtering without substrate heating and post annealing, the 200 nm thick of ITO on plastic substrates were achieved with minimum of sheet resistance was about 8 Ω/□ at r.f. power of 40 W and high transmittance in visible region with average transmission was found over than 90%. The details of experiment on ITO thin film were discussed in Chapter 7.

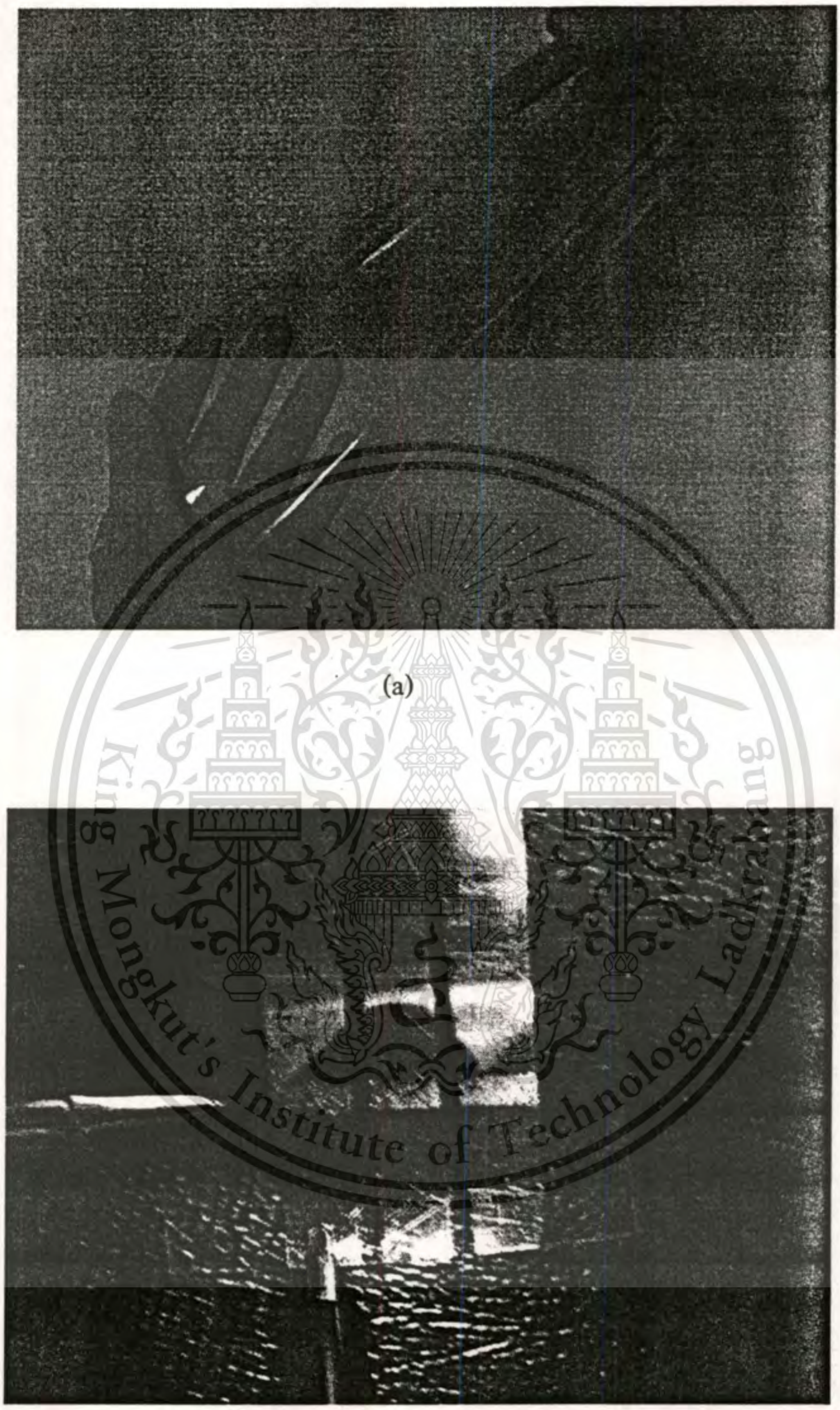

(a)

(b)

**Fig. 8.12** The photograph of transparent ITO thin film, ITO on flexible plastic (a), and ITO on PET used as transparent electrode.

### 8.3.2 ITO Transparent Flexible Antenna

A kind of antenna called film antenna has been available for a few years, it has been used by mounting onto the surface of smooth material such as flat mirror, monitor screen for the purpose of wireless communication, e.g. automotive radio antenna, GPS antenna, wireless LAN film antenna [20]. But those antennas are not transparent when attached to transparent object. In this report, ITO thin film on plastic will be used as the transparent flexible antenna.

ITO flexible transparent film antennas deposited on PET substrate by RF magnetron sputtering with gas-timing technique [21] are proposed that meet the requirements for the wireless systems. The crystallization, surface morphology, sheet resistance and transmittance for the antenna were investigated by XRD SEM, four-point probe and UV-VIS spectrophotometer that implied in Chapter 7.

The geometry of ITO film antenna with the size of 10 cm x 10 cm are depicted in Fig. 8.13. The antenna is electrically small and made of 200 nm ITO thin film deposited on PET dielectric substrate (thickness= 0.1 mm, $\varepsilon_r = 2.2$). The antenna is center-fed by a 50 Ω coaxial cable in the manner of a monopole. To help us understand the performance of the proposed ITO film antenna in terms of its resonant frequency, experiment is carried out. Through many experiments, it is found that the antenna bandwidth is very wide. Resonant frequency can be achieved from very low frequency to UHF [22].

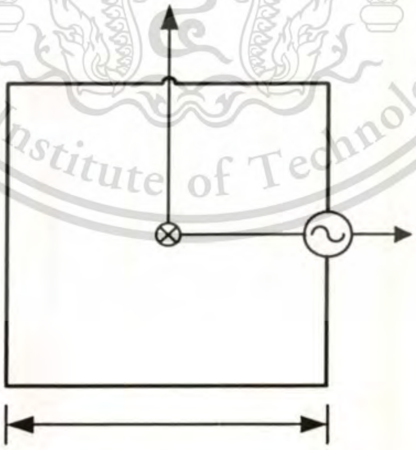

**Fig.8.13** Rectangular ITO transparent flexible antenna.

Fig. 8.14 graphs the measured return loss bandwidth of the ITO film antenna. The bandwidth is very wide, it can operate from very low frequency up to 2.5 GHz. Even though, conventional acceptable return loss bandwidth is -10 dB, the proposed ITO film antenna can be compensated by adding amplifier circuit to obtain acceptable signal. The very large bandwidth is due to inherent surface plasmon phenomenon of ITO film.

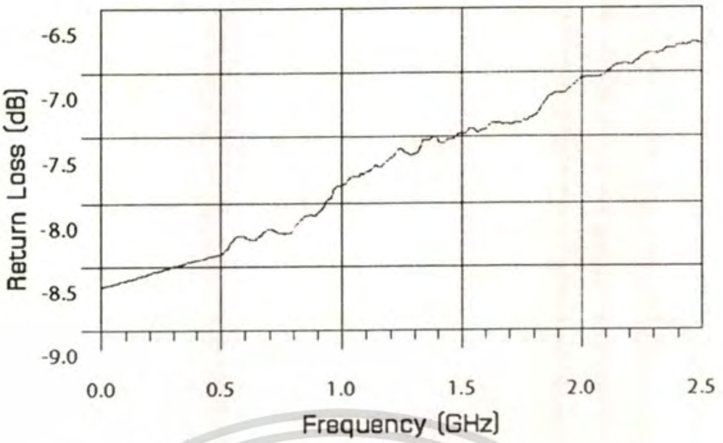

**Fig. 8.14** Measured return loss of ITO transparent flexible antenna.

The terminal impedance is between 25 Ω to 40 Ω (Fig. 8.15) which is comparable match to the 50 Ω and 75 Ω systems. We can obtain good agreement between antenna impedance and system impedance by using impedance matching circuit which currently available in industry called antenna matching-free devices.

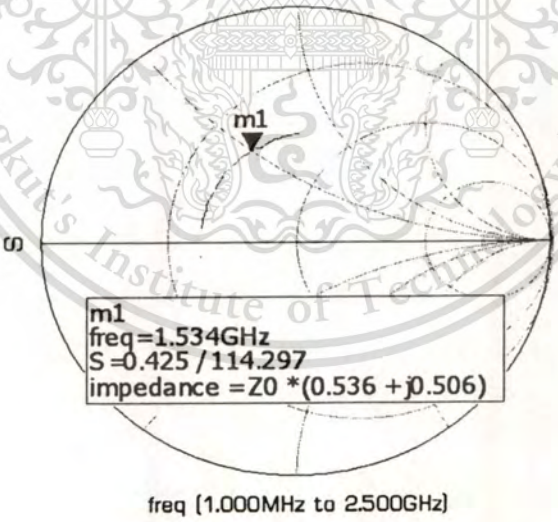

**Fig. 8.15** Measured input impedance at a frequency of 1.534 GHz.

The measured far field radiation pattern for the ITO film antenna is shown in Fig.8.16. It is noted that the radiation patterns in both planes exhibit a well-formed omni-directional pattern. The exhibition of the omni-directional pattern is due to rectangular geometry of the antenna. The measured gain of the antenna was -5 dBd at 100 MHz.

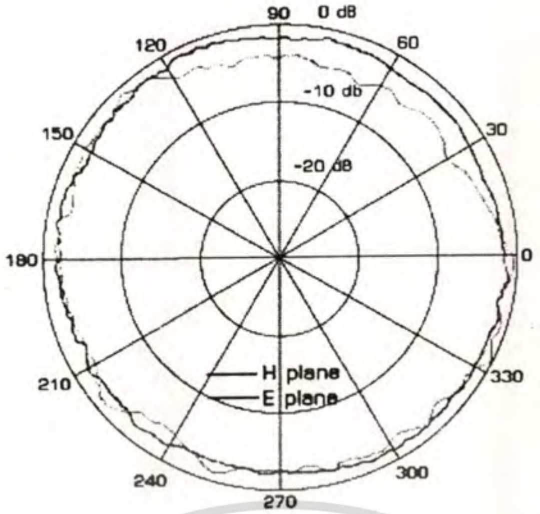

**Fig. 8.16** Measured radiation patterns of ITO transparent flexible antenna at 100 MHz.

The advantage of the use of gas-timing r.f. magnetron sputtering technique to implement optically transparent flexible antennas is that they cost less than conventional antennas do and have light weight. The ITO thin film antenna has the transmittance of about 90% in visible region, wide bandwith which can operate upto 2.5 GHz. Such an antenna could find applications in mobile communication where simplified feed arrangements are required.

## 8.4 Nanocrystal-InON Thin Film Optical Filter

This research has presented an experimental study of the relationship between the structure and the optical bandgap, and the flow rate ratio of nitrogen/oxygen as reactive gases in a series of polycrystalline InN to $In_xO_y$ films. This is the first time report on the growth of indium oxynitride (InON) films by r.f. magnetron sputtering with gas-timing technique, which varied the flow rate of oxygen mixed with nitrogen from In target. The structural and optical properties on InN to $In_xO_y$ crystals will be suggested on the XRD, SEM and UV-VIS results which are presented in Chapter 7.

From the optical property as shown in Fig.7.26, We found that the optical bandgap of films with a thickness of around 1000 nm increases from 1.4 to 3.2 eV depended on the flow rate of $N_2$+$O_2$. A combination of beneficial properties of indium nitride and indium oxide results in a new material-indium oxynitride with variable composition and functionality. Changing the oxygen-to-nitrogen ratio in In-O-N in a wide range offers a possibility to tune the film properties by controlling the progress parameters.

This optical property on a series of InON films can apply as the optical filters. The nanocrystal-InON optical filters were fabricated on of glass, plastic and eyeglass lenses as shown in Fig.8.17. The nanocrystal-InON optical filters have done for examples in medical and forensic science applications which shown in Fig. 8.18 and 8.19.

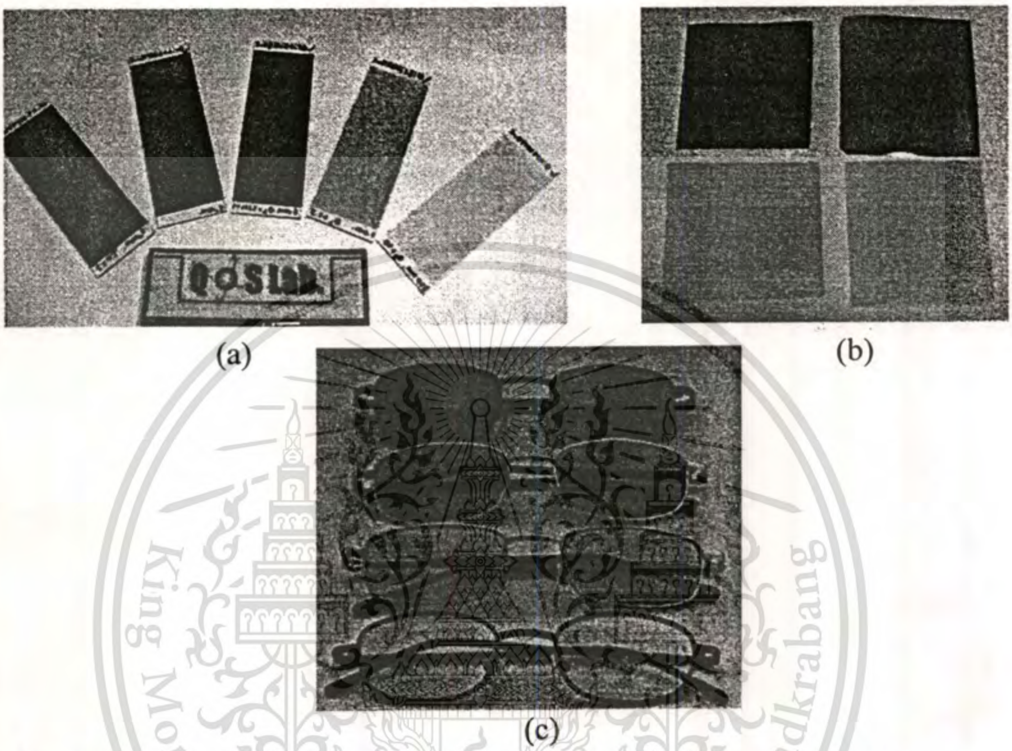

(a) (b) (c)

**Fig. 8.17** The photograph of nanocrystal-InON optical filters on various substrates (a) glass, (b) plastic, and (c) eyeglass lenses.

**Fig. 8.18** The photograph of nanocrystal-InON optical filter use as UV-safety eyeglasses for medical purpose.

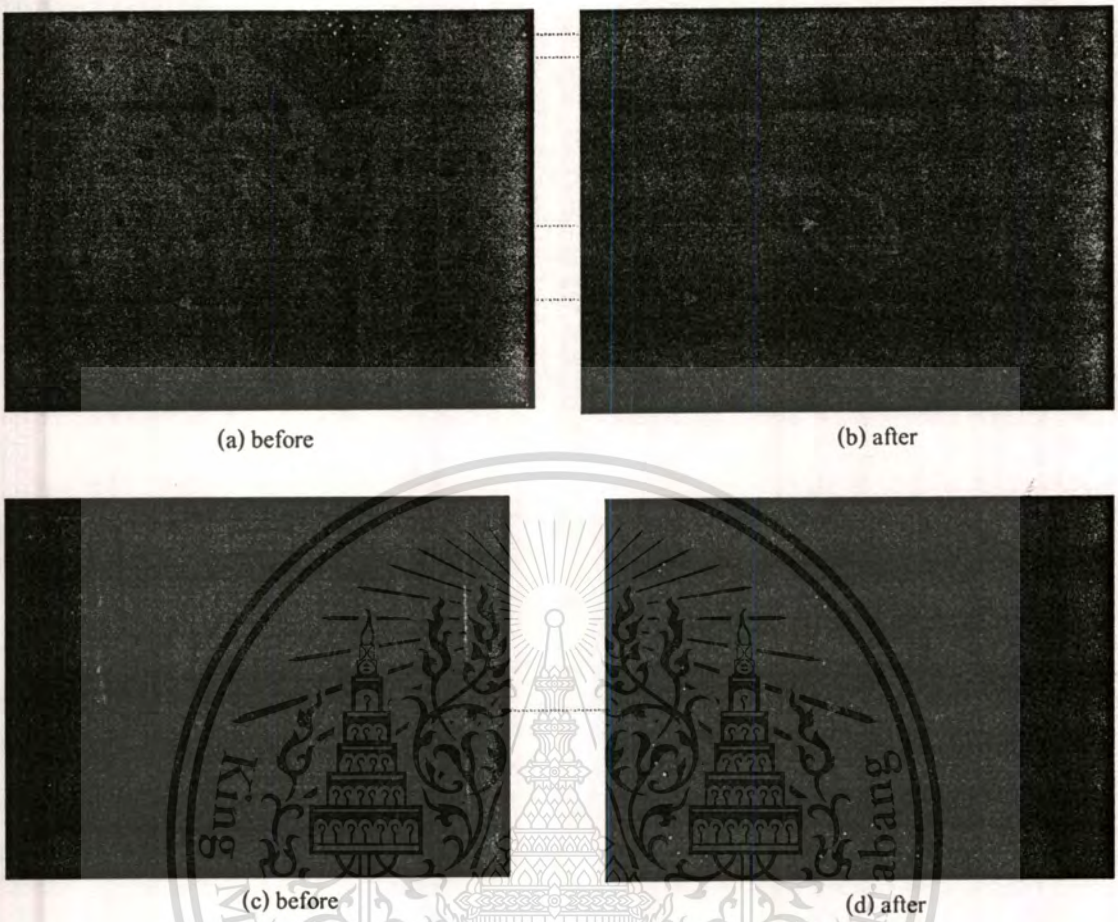
(a) before

(b) after

(c) before

(d) after

**Fig. 8.19** The latent stains from body fluids were exhibited after use the nanocrystal-InON optical filter in crime scene investigation purpose, (a, b) latent sperm (c, d) latent saliva.

## References

[1] H. K. Liao, J. C. Chou, W. Y. Chung, T. P. Sun and S. K. Hsiung: Proc. 3 rd East Asian Conf. Chemical Sensors (EACCS-3), Seoul, Korea, November 5-6, 1997, p. 394.

[2] J. C. Chou, Y. S. Li and J. L. Chiang: Proc. 1998 Annu. Symp. Biomedical Engineering Socitey (BMES'98), National Yang Ming University, Taiwan, R.O.C., December 18-19, 1998, p. 471.

[3] J. C. Chou and J. L. Chiang, Sens. & Actuat. B **62** (2000) 81.

[4] H. K. Liao, L. L. Chi, J. C. Chou, W. Y. Chung, T. P. Sun and S. K. Hsiung, Matter. Chem. & Phys. **59** (1999) 6.

[5] Y. L. Chiang, J. C. Chou, T. P. Sun, W. Y. Chung, and S. K. Hsiung, Sens. & Actuat. B **76** (2001) 582-593.

[6] S. S. Jan, Y. C. Chen, J. C. Chou, C. C. Cheng, and C. T. Lu, Jpn. J. Appl. Phys. Vol. **41** (2002) pp. 942-948.

[7] P. Bergveld, **"Development of An Ion-Sensitive Solid-State Device for Neurophysiological Measurement,"** IEEE Transactions on Electron devices, Vol. BME-17(1), pp. 59-63, 1970

[8] P. Bergveld, **"Development, Operation, and Application of The Ion-Sensitive Field Effect Transistor as a Tool for Electrophysiology,"** IEEE Trans. Biomed. Eng., Vol. BME-19(5), pp. 342-351, 1972

[9] L. Bousse, N.F. de Rooij and P. Bergveld, **"Operation of Chemically Sensitive Field Effect Sensors as A Function of The Insulator-Electrolyte Interface,"** IEEE Transactions on Electron Devices, Vol. ED-30 (10), pp. 1263-1270, 1983.

[10] S.D. Moss, C.C. Thomson and J. Janata, **"Hydrogen, Calcium and Potassium Ion Sensitive FET Transducers: A Preliminary Report,"** IEEE Transactions on Biomedical Engineering, vol. 25(1), pp. 49-54, 1978.

[11] Y.J. Yong and J.Y. Lee, **"Characteristic of Hydrogenated Aluminum Nitride films Prepared by Radio Frequency Reactive Sputtering and Their Application to Surface Acoustic Wave Devices"**, J. Vac. Sci. Technol. A, 15, (1997), 390-393.

[12] D. Monava, V. Dimitrova, W. Fukarek and D. Karquzov, **"Investigation of DC Reactive Magnetron-Sputtered AlN Thin Films by Electron Microscope Analysis, X-ray Photoelectron Spectroscopy and Polished Infra-Red Reflection"**, Surface and Coatings Technol., 106 (1998), 205-208.

[13] E.A. Chowdhury, J. Kolodzey, J.O. Olowolafe, G. Qiu, G. Katuka, D. Hits, M. Dashiell and D. van der Weide, **"Thermal Oxidized AlN Thin Films for Device Insulators"**, Appl. Phys. Lett., 70 (1997) 2732-2734.

[14] S.-S. Jan, J.-L. Chiang, Y.-C. Chen, J.-C. Chou and C.-C. Cheng, **"Characteristics of The Hydrogen Ion-Sensitive Field Effect Transistors with Sol–Gel-Derived Lead Titanate Gate,"** Chimica Acta, vol. 469(2), pp. 205-216, 2002.

[15] J. L. Chiang, S.S. Jan, Y.C. Chen and J.C. Chou, **"Sensing Characteristics of ISFET based on AlN Thin Film"**, Proc. Of SPIE Vol. 4078, Taipei, Taiwan, July 26-28, 2000, pp. 689-696.

[16] T. Adam, J. Kolodzey, C.P. Swann, M.W. Tsao and J. F. Rabolt, **"The Electrical Properties of MIS Capacitors with AlN Gate Dielectrics"**, Appl. Surface Sci., 175-176 (2001) 428-435.

[17] D. Liufu and K.C. Kao, **"Piezoelectric, Dielectric, and Interfacial Properties of Aluminum nitride Films"**, J. Vac. Sci. Technol., A 16(4) (1998) 2360-2366.

[18] V. Dimitrova, D. Monova and R. Djulgerova, **"Element Composition and Electrochemical Behaviour of Polycrystalline AlN Thin Films"**, Surface & Coati. Technol., 123(2000) pp.12-16.

[19] Jiti Nukeaw, Yasufumi Fujiwara and Yoshikazu Takeda, **"Observation of Electric Fields at Surface and Interface of Doped GaAs/Semi-insulating GaAs Structures by Fast Fourier Transformed Photoreflectance"**, Jpn. J. Appl. Vol. 36, 1997 pp. 7019-7023

[20] K. L. Chopra, S. Major, D. K. Pandya, **"Transparent Conductor"**, Thin Solid Films, vol. 102, pp.1-46, 1983.

[21] N. Kietipaisalsophon, W. Bunjongpru, J. Nukeaw, **"Photoreflectance Study of AlN Thin Films grown by Reactive GAS-Timing RF magnetron Sputtering"**, International Journal of Modern Physics B, vol. 16, pp. 4418-4422, November 2002.

[22] E.Terzini, P. Thilakan, C. Minarini, **"Properties of ITO Thin Films Deposited by RF Magnetron Sputtering at Elevated Substrate Temperature"**, Materials Science and Engineering : B, vol. 77, pp. 110-114, 2000.

# CHAPTER 9

# CONCLUSIONS AND FUTURE PERSPECTIVES

## 9.1 Conclusions

This work presents a comprehensive study of aluminum nitride (AlN) and indium nitride (InN) thin films. The InN related thin films including indium tin oxide (ITO) and indium oxynitride (InON) films are also in our study. By our innovative **"reactive gas-timing"** technique, nanocrystal-AlN, nanocrystal-InN, nanocrystal-ITO and nanocrystal-InON thin films have been successfully grown on various substrates by r.f magnetron sputtering system at room temperature. The growth parameters, including gas flow rate, gas-timing, r.f sputtering power, and film thickness, have been adjusted to grow the films. A detailed characterization of thin films has been carried out using x-ray diffraction, scanning electron microscope, photoreflectance spectroscopy, UV-VIS spectroscopy and four point probe measurement. The following sections summarize the growth, characterizations and devices fabrications of AlN, InN, ITO and InON films. The possible future work is suggested.

In order to grow good quality AlN, InN and InON; research groups have tried several deposition techniques. The more common growth methods are metalorganic chemical vapor deposition (MOCVD), molecular beam epitaxy (MBE), Organometalic Vapor Phase Epitaxy (OMVPE) and reactive sputtering. However these methods are limited in their capabilities to produce high quality wide band gap semiconductor thin films. Normally, these growth techniques need to heat substrate and have growth temperature higher than 1000 °C which causes dissociation in InN. Further improvement in the film quality has been achieved by applying new technique which causes these system are complex reactor and more expensive. Radio frequency reactive sputtering (RF-sputtering) is a relatively simple growth technique, cost effective, and widely used for study of nitride films.

In this work, it has been demonstrated that the reactive gas-timing technique used for r.f magnetron sputtering plays an important role to grow AlN, InN, ITO and InON thin films with following conclusions as below.

Crystalline structural and morphological examinations by XRD and FE-SEM show that all deposited films have the polycrystalline form and composed of nanocrystalline grains.

The AlN thin films can be achieved as cubic structure with the orientation along (111) and (200) planes. The band-gap transition energy of cubic-AlN determined by PR measurement is in range of 3.78-3.89 eV depended on the flow rate of $N_2$ and is decreased with increasing flow rate of $N_2$. The increasing grain size with $N_2$ flow rate was due to the improvement in the degree of crystallinity of thin films.

For InN thin films, the reflection peaks of XRD indexed (101), (102), and (110), in accordance to, the wurtzite-InN polycrystalline structure while, InN thin films grown in pure $N_2$ plasma showed one strong XRD peak in orientation along (111) plane corresponding to InN cubic structure. The energy bandgap of about 1.18 eV for hex-InN and 1.38 eV for cubic-InN were investigated by PR and UV-VIS measurements, respectively.

All deposited ITO thin films with various r.f power on PET show XRD peaks at $2\theta$ = 30.273° and 35.165° which correspond to (222) and (400) planes as polycrystalline cubic bixbyite structure. The sheet resistance of ITO thin films obtained by four point probe measurement is reduced from 30 to 8 Ω/□ as the r.f. power of sputtering increases from 10 W to 40 W. The ITO thin films on PET substrates have the transmittance of about 90% in visible region. The optical bandgap energy of ITO films obtained from UV-VIS measurement is about 3.6 eV.

For deposited InON films series, the XRD peak at $2\theta = 31.4°$ of film grown in pure $N_2$ plasma determines the crystal orientation along (111) plane as cubicl-InN polycrystalline structures. While the peak at $2\theta$ =34.97° and 50.71° of film grown in pure $O_2$ plasma determines the crystal orientation along (400) and (440) planes, respectively as cubic body-center polycrystalline structure. The crystal orientations of films grown in $N_2$+$O_2$ plasma exhibit the crystal phase change nearby to InN when $O_2$ flow rate is decreased and to $In_2O_3$ when $O_2$ flow rate is increased. The optical bandgap of InON films series determined from UV-VIS measurement is in range of 1.4-3.2 eV depended on growth conditions.

Finally, the devices fabricated from AlN, InN, ITO and InON thin films for the various applications including nanocrsytal-AlN pH-sensing device, nanocrystal-InN photodetector, ITO flexible transparent electrode and nanocrystal-InON optical filter.

The nanocrystal cubic-AlN thin film was selected as a sensing membrane in electrolyte-insulator-semiconductor (EIS) pH-sensing devices. For experimental study, the pH sensors, EIS, are designed and then fabricated with the reference/electrolyte/AlN/$SiO_2$/p-Si/Au structure. After packaging, the current-voltage (I-V) measurement was utilized to measure a series of the I-V characteristic curves. The threshold voltage can be obtained to evaluate the pH sensitivity in the difference standard pH buffer solutions (pH = 4, 7, 10). From the characteristic results, furthermore, the nanocrystal cubic-AlN thin film is very attractive as a sensing membrane for pH sensing ISFET devices.

The potential of InN as a photosensitive material was fabricated. The photodetector structure was made on p-Si wafer. The wavelength response of nanocrystal-InN phodetector is in range of near-infrared. The bandgap energy of nanocrystal-InN film used as photosensitive material of about 1.2 eV as hexagonal polycrystalline structure.

The transparent flexible plastic electrode and antenna was fabricated. ITO thin film was deposited on flexible plastic substrate at room temperature by gas-timing r.f. magnetron sputtering. By using XRD measurement of the ITO thin film grown by this technique, a cubic nano-crystalline structure with predominant (222) orientation was observed. The technique of gas-timing we used, the ITO thin film on flexible substrate was achieved with high transmittance in visible region of 90% and low resistivity. The ITO films with sheet resistance of about 8 $\Omega/\square$ on plastic have potential as transparent electrode for display devices. The performance of the ITO film antenna was studied experimentally with its return loss and radiation patterns.

InON thin films are used to functional layer for optical high-pass filter. The device can be performed in ultraviolet to near infrared regions by the sputtering conditions. The InON thin film on glass or plastic substrates prepared by gas-timing technique can be achieved without any post-process requirement. XRD results show that the phase of deposited films change from InN to InON and to InO as oxygen content mixed with nitrogen in sputtering are increased. However, the body-centered structures of InON and InO films with preferred orientation depend on nitrogen/oxygen ratio. The FE-SEM micrographs of all deposited films exhibit nanocrystalline structures. The optical properties of nanocrystalline films were recorded by means of UV-VIS absorption spectroscopy, indicating that the optical energy bandgaps of thin films affected by nitrogen/oxygen ratio. Especially, the films were proven to be useful to apply for medical and crime scene investigation in forensic science.

## 9.2 Future Perspectives

In order to future improve the performance of nitride-based devices, significant advances in materials characterization methods need to be made. The device fabrication design and process are suggested for future work to significantly enhance the device efficiency such as ISFET pH-sensor, nitride-based photodetector, oxynitride-based pressure sensor, solar cell and plastic electronics applications.

# BIOGRAPHY

Ms.Nisaporn (Supanit) Porntheeraphat was born on April 30, 1968 in Songkhla, Southern of Thailand. She is the oldest daughter of parents: Mr.Sirideth-Mrs.Chotirot Porntheeraphat. She has one sister and two brothers.

Her educations;

B. Ed. (Second-Honor), Science-Physics, March 1990, from Thaksin University (Srinakarinwirot Songkhla),

M. S., Applied Physics, March 1994, from King Mongkut's Institute of Technology Ladkrabang,

Ph.D., Applied Physics, October 2007, from King Mongkut's Institute of Technology Ladkrabang.

Her experiences;

1990-1991: Lecture Assistant at Mahanakorn University of Technology,

1994-2001: Researcher in Electro-Optics Laboratory, NECTEC,

2005-2006: Researcher in MEMs Laboratory, NECTEC,

2007-present-day: Researcher in TMEC, NECTEC and co-research in Nanotechnology Research Center of KMITL.

Her skills and interests;

More than 7 years experience in production of Embossed Holography including design, lithography, laser exposure, thin film spinning, electroforming, embossing, laminating, cutting and inspection.

Proficient with semiconductor thin film processing techniques including material deposition, various substrates cleaning, etching, and materials characterization methods.

Experience in micro fluidic fabrication processes for lab on a chip devices.